Non-Equilibrium and Finite Temperature Trapped Bose Gases: Interactions and Decay of Macroscopic Excitations

Ashleigh Joy Allen

Thesis submitted for the degree of
Doctor of Philosophy

School of Mathematics & Statistics
Newcastle University
Newcastle upon Tyne
United Kingdom

April 2012

To my brother David

Acknowledgements

First and foremost, I would like to thank my supervisors, Nick Proukakis and Carlo Barenghi, for their enthusiasm, availability for questions and approachability which has made my PhD an interesting and enjoyable experience. I want to extend my gratitude to our collaborators Eugene Zaremba, Anssi Collin and David Hall, as well as Joseph Thywissen for details regarding his experimental trap and Daniel Jackson for his early work on solitons. Further to this, I would like to thank EPSRC for funding this research project.

Within the school, I would like to thank my officemates, and fellow PhD students, in particular those who have been with me from the start, Fred Gent, Anisah Mohammed, Tim Yeomans, Donatello Gallucci and Nathan Barker, for the constant laughter and enlightening conversations. I would like to thank my fellow group members, in particular Stuart Cockburn and Donatello Gallucci for their advice, support and sticking to the policy that no question is a silly question! Also, Rob Pattinson for the use of his 3D GPE code and Anthony Youd for always being available for a chat as well as his enormous amount of help in all things computing, even outside of normal working hours!

Outside of university I want to express my gratitude to my parents, for their constant love and support. To my brother, William, and sister, Naomi, for always being there for me. As well as friends and former housemates, in particular, Trudie Hunter for listening and Kerry Neill for making Newcastle my home and encouraging me to join a gym!

Last but by far the least, I would like to thank Colin Rainey for his constant support throughout all my academic endeavours. For his patience and kindness, particularly whilst I was writing up, and for always being able to put a smile on my face, no matter what!

Abstract

In this thesis we study the dynamics of dark solitons, vortices and Josephson effects, in trapped atomic Bose-Einstein condensates. We firstly demonstrate a novel, sound mediated, long-range interaction mechanism between dark solitons using the Gross-Pitaevskii equation. Then we present the effect of finite temperatures on the dynamics of vortices and Josephson effects using a generalised form of this equation, which additionally includes a source term modelling the coupling of the condensate to a *fully* dynamical thermal cloud, described by a quantum Boltzmann equation. The latter formalism is known as the Zaremba-Nikuni-Griffin scheme (ZNG).

The sound-mediated interaction between dark solitons is such that the speed and trajectory of one soliton in a condensate confined by a harmonic trap can be significantly modified by the presence of a second soliton in the same trap. By confining the two solitons to spatially separated subregions of a double well trap, we show how this effect can be magnified. In particular we find it can be large, and therefore detectable, in experimentally relevant geometries, including high-periodicity optical lattices in which the ability of solitons to act as both *absorbers* and *emitters* of energy becomes apparent.

At finite temperatures, we model the dynamics via the ZNG scheme. Firstly, we give a detailed description of the scheme for numerically solving these coupled equations including all collisional terms. Then we study the effect of a dynamical thermal cloud on vortex dynamics, in particular, focussing on the experimentally-relevant quantities of precession frequencies, decay rates and vortex core brightness. The changes in these are found to increase with increasing temperature for a pancake-shaped geometry, in particular for trapping parameters of a recent experiment of Freilich *et al.* (Science **329**, 1182 (2010)). Particle exchanging collisions between the condensate and thermal cloud are found to be crucial in determining the rate of decay of a precessing vortex. We further show that, rotation of the thermal cloud can be a mechanism for radially translating the position of a vortex, a scenario under current investigation.

Finally, we analyse the effect of finite temperatures on population dynamics in a double well atom chip experiment by LeBlanc *et al.* (Phys. Rev. Lett. **106**, 025302 (2011)). Focussing on the coupled evolution in the *absence* of collisions, we find that it generates significant damping which is, however, less than that observed in the experiment. A detailed comparison in the presence of collisions is beyond the scope of this thesis.

Contents

Part I

Introduction

Chapter 1

Introduction to Bose Gases

Under certain experimental conditions, an astonishing phase transition called Bose-Einstein condensation [1, 2] can occur. Manifestations of this include superfluidity, referring to the property of a fluid to flow without viscosity, and superconductivity which is the ability of materials at low temperatures to conduct an electric current with zero resistivity [3].

The phenomenon of Bose-Einstein condensation was predicted by Satyendra Nath Bose and Albert Einstein in 1924. Bose derived Planck's law of black-body radiation by assuming photons were identical and counting their distribution over energy states. He wrote his findings in a letter to Einstein who immediately saw the importance of it and recommended it for publication [4]. Einstein went on to generalise Bose's work, to develop the quantum statistics of a gas of non-interacting bosons [5] and the Bose-Einstein distribution function was born. It was later in 1938, when London [6] first suggested that the properties of superfluid helium were relevant to Bose-Einstein condensation.

1.1 Bose-Einstein condensation

Particles can be classed into two groups depending on the value of their spin, which is interpreted as the intrinsic rotation of a particle about its axis. Bosons are particles with an integer value of spin, photons for example are bosons and obey Bose-Einstein statistics, while fermions obey Fermi-Dirac statistics and have a half integer spin. An electron is an example of a fermion. The Pauli-Exclusion principle states that two identical fermions cannot occupy the same quantum state. This is because, the total wavefunction of a system can be written as a combination of the two single particle wavefunctions via:

$$\begin{aligned} \Psi &= \frac{1}{\sqrt{2}}[\psi_a(1)\psi_b(2) + \psi_a(2)\psi_b(1)] \quad \text{Symmetric} \\ \text{or} \quad \Psi &= \frac{1}{\sqrt{2}}[\psi_a(1)\psi_b(2) - \psi_a(2)\psi_b(1)] \quad \text{Antisymmetric} \end{aligned}$$

Suppose both the particles are in the same state i.e. $a = b$. The symmetric wavefunction, becomes $\sqrt{2}\psi_a(1)\psi_a(2)$ while the antisymmetric wavefunction vanishes. This means that particles with an antisymmetric wavefunction, fermions, cannot exist together in the same state while particles with symmetric wavefunctions, bosons, can. In fact, if many bosons occupy the same state, the probability of more bosons scattering into that particular state is increased.

The Bose-Einstein probability distribution for a gas of N, non-interacting bosons at temperature T is written as

$$f(\varepsilon_i) \quad = \quad \frac{1}{e^{(\varepsilon_i - \mu)\beta} - 1}, \tag{1.1}$$

where ε_i is the energy of the level i, μ is the chemical potential, with $\mu \leq \varepsilon_i$ since μ is the energy of the lowest energy level, ε_0, and $\beta = (k_B T)^{-1}$, where k_B is Boltzmann constant. The total number of particles of the system is given by the sum of the occupation numbers of all energy levels via $N = \sum_i g(\varepsilon_i) f(\varepsilon_i)$, where $g(\varepsilon_i)$ is the degeneracy of the ith energy level.

At high temperatures, when the quantum statistics of the particles can be ignored, Eq. (1.1) reduces to the Boltzmann distribution $f(\varepsilon_i) = e^{-(\varepsilon_i - \mu)\beta}$. For an ideal gas at absolute zero, all particles are in the ground state, however, when $T > 0$, there is still a macroscopic occupation of the lowest energy level (under the critical temperature for the onset of Bose-Einstein condensation). In all physical systems it is impossible to reach absolute zero, with the lowest recorded temperature of an atomic gas, less than 500 pico Kelvin [7]. Therefore, as well as a macroscopic occupation of the lowest energy level, there is a low occupation of higher energy levels, hence, modelling Bose-Einstein condensation at finite temperatures poses an interesting and important problem.

One can define a particle's thermal de Broglie wavelength as

$$\lambda_{\mathrm{dB}} = \sqrt{\frac{h^2}{2\pi m k_B T}}, \tag{1.2}$$

i.e. λ_{dB} is inversely proportional to the square root of the temperature. At high temperatures, the thermal de Broglie wavelength of a gaseous particle is small, therefore the classical nature of the particle is dominant and one can think of it undergoing so-called 'billiard ball' type dynamics. As the temperature of a gas of bosons is lowered, the wave nature of a particle starts to unravel until the point where the λ_{dB} of neighbouring particles is comparable to the interparticle spacing, and the individual characteristics of the particles are no longer apparent. For bosons, this leads to a macroscopic occupation of the lowest energy level which is termed a Bose-Einstein condensate (BEC). The analogy in fermionic systems, is called a Fermi Sea, where one fermion occupies each energy level

up to the Fermi level (at $T = 0$).

The condition for the onset of Bose-Einstein condensation corresponds to the point where the thermal de Broglie wavelength becomes of the order of the interparticle spacing. For an ideal, three dimensional (3D) uniform Bose gas, this is given as $n\lambda_{\mathrm{dB}}^3 \simeq 2.612$ [1], where $n = N/V$, is the number density of the gas of volume V. Associated with this criterion for the onset of degeneracy or Bose-Einstein condensation, there is a critical temperature, which is the highest temperature at which there exists a macroscopic occupation of the lowest energy level. The critical temperature for a non-interacting gas of bosons is

$$T_c = \frac{2\pi\hbar^2}{mk_B}\left(\frac{n}{2.612}\right)^{2/3}. \tag{1.3}$$

Using this, the fraction of atoms condensed into the lowest energy level can be calculated as

$$\frac{N_0}{N} = 1 - \left(\frac{T}{T_c}\right)^{3/2}. \tag{1.4}$$

To achieve Bose-Einstein condensation, relatively high densities at low temperatures are required[1]. However, it is necessary to avoid the phase transition into liquid or solid that one would expect as a gas is cooled. Therefore, three-body collisions, which bring about the formation of molecules, must be delayed. This can be done by ensuring the density is low enough that elastic binary collisions dominate, but also high enough that the trapped atoms thermalise and condense into the lowest energy level.

It is because of these subtleties required experimentally that a pure Bose-Einstein condensate in weakly-interacting gases was not realised until 1995 [8–10], some 70 years after its prediction.

Due to the weakly interacting nature of these gases, the ideal gas result for the critical temperature for the onset of BEC in the presence of a trapping potential, gives a good estimate for the highest temperature one would expect to find a macroscopic occupation of the lowest energy level. For a harmonically trapped gas in 3D this is defined as

$$T_c = \frac{\hbar\bar{\omega}}{k_B}\left(\frac{N}{1.202}\right)^{1/3}, \tag{1.5}$$

where $\bar{\omega} = (\omega_x\omega_y\omega_z)^{1/3}$ is the geometric mean of the harmonic oscillator frequencies in the x, y and z dimensions.

In the next section we briefly describe the typical methods used to create a BEC, in which we highlight the important role of a trapping potential to cool and trap the gas.

[1]These densities are actually very dilute at around $10^{13} - 10^{15}$ cm^{-3}, when compared with the density of air at room temperature which is around 10^{22} cm^{-3} [1].

1.1.1 Experimental realisation

The initial experiments which produced atomic weakly-interacting Bose-Einstein condensates were performed on dilute vapours of Rubidium by the group of Eric Cornell and Carl Wieman at NIST [8], Sodium by Wolfgang Ketterle's group at MIT [9], and also in Lithium by Randy Hulet's group at Rice University [10, 11]. The Nobel prize was later awarded to Eric Cornell, Carl Wieman and Wolfgang Ketterle in 2001 for

"the achievement of Bose-Einstein condensation in dilute gases of alkali atoms, and for early fundamental studies of the properties of the condensates" [12].

Alkali atoms such as ^{87}Rb, ^{23}Na and ^{7}Li are ideal for producing BECs because they are weakly-interacting and they have one outer electron in the s-orbital which make them ideal for laser cooling and magnetic trapping. They were not the first atoms considered however. The quest for Bose-Einstein condensation initially focussed on spin-polarised Hydrogen since it was predicted to stay gaseous right down to zero temperature as the interactions between two atoms would remain weak enough when their electronic spins are aligned, that no bound state/molecules would form [13]. However, despite the remarkable experimental efforts, spin-polarised Hydrogen was not condensed until 1998 [14], mainly for the very reason it was thought to be a good candidate with which to create a Bose-Einstein condensate. It has such a small scattering length that reducing the temperature enough to realise a BEC at experimentally workable densities, turned out to be extremely difficult. Nevertheless, this work proved instrumental in developing techniques used in the race to produce a BEC since evaporative cooling, routinely used in the final stages of cooling alkali gases, was developed during the effort to Bose-condense Hydrogen [15].

A combination of cooling techniques are required to reach the ultra low temperatures necessary to achieve Bose-Einstein condensation. The advances made in laser cooling since the 1970s are by far the biggest development in cooling methods, which have made the creation of Bose-Einstein condensates possible.

BEC experiments typically begin with 10^9 atoms which are slowed using a laser beam propagating in the direction opposite to the flow of atoms. This is called a Zeeman slower in which the velocity of the atoms typically reduces from 800ms^{-1} to 30ms^{-1} corresponding to a temperature of the order of 1K. The radiative force produced by the absorption of photons has the effect to slow the atoms. They are then transported into a magneto-optical trap in which the magnetic field and optical forces are such that the atoms are trapped and can be further cooled to μK temperatures; it is the laser-induced, Doppler effect that is exploited here to cool the atoms further: if we imagine a laser beam which is 'red' detuned, i.e. it has a frequency slightly *less* than the resonant frequency of the atoms, then if the atoms travel in the direction *opposite* to the direction of the laser beam, due to the Doppler effect, the atoms will absorb photons and lose momentum equal to that

of the photon. They are then in an excited state and will spontaneously emit the photons in a random direction. This spontaneous emission increases the atom's momentum in that direction but as the momentum gain from emitting the photon in the original direction of travel is less than what is lost from absorbing the photon, the overall effect is a loss in momentum on the given direction. Now imagine a gas of atoms surrounded by six counter-propagating laser beams, the overall effect of this absorption-emission process is to cool the gas. This is the general concept behind a magneto-optical trap.

The limit of laser cooling using the Doppler effect is reached when the increase in momentum due to emission of the photon balances out the cooling effect of the laser; this is called the Doppler Limit. To reach the lower, so called recoil limit ($\sim 1\mu$K [1]) a technique called Sisyphus cooling is now typically employed. This method of cooling exploits the polarisation gradient of two counter-propagating, orthogonally-polarised laser beams. When the atoms move up this potential gradient they lose kinetic energy and gain potential energy. When they reach the 'top' of the potential hill, they can be optically pumped to a lower potential energy, where they begin the potential climb again. In this way, the atoms progressively lose kinetic energy.

Evaporative cooling is then required to cool the gas further. It works by effectively lowering the walls of the trapping potential slowly enough that the high energy, high temperature atoms escape the system and the remaining atoms rethermalise and the overall temperature of the system is lowered i.e. the tails of a thermal distribution are effectively 'clipped'. The physical implementation of this involves applying a radio frequency which flips the spins of high energy atoms so they are no longer held in the trap and escape the system. This procedure must be done slowly enough to avoid losing too many atoms so the density remains high enough for the atoms to thermalise and thus form a condensate. The processes is continued until the temperature is reduced to the nano-Kelvin (nK) regime.

At a temperature of $< 10^{-6}$K and density of $\sim 10^{-13}$cm^{-3}, a Bose-Einstein condensate emerges from the thermal component. A characteristic feature of this is a spike in the centre of the velocity distribution of the expanded cloud. This large spike is centred on zero velocity indicating a macroscopic occupation of the lowest energy level.
Since the early realisation of Bose-Einstein condensation, BECs of, for example, ^{85}Rb [16], ^{41}K [17], ^{4}He [18], ^{174}Yb [19], ^{133}Cs [20], ^{52}Cr [21], ^{84}Sr [22, 23], ^{86}Sr [24], ^{88}Sr [25], ^{40}Ca [26], ^{164}Dy [27] have also been formed.

In dilute weakly-interacting atomic gases, the effective radius of the atoms, described by the scattering length, is much smaller than the interatomic distance such that $n^{1/3}a_s \ll 1$ holds; here a_s is the s-wave scattering length which is important since the dominant scattering mechanism is low energy s-wave scattering. In contrast, the strong interactions in superfluid ^{4}He mean that at nK temperature, while $\sim 99\%$ of a typical alkali gases is in the lowest energy level of the system, only $\sim 10\%$ of the superfluid ^{4}He is [28]. This

means the dilute, weakly-interacting atomic BECs are the ideal medium for a 'pure' study of the properties of Bose-Einstein condensation, not least investigating quantum effects on a macroscopic level.

The experimental control of these gases has led to interesting results and the advancement of understanding of the phenomenon of quantum gases. Changing the shape of the geometry of the trap can reduce the dimensionality of the system; for example, when the trap is tightly confined in two of the three cartesian directions (quasi-1D trap), the resulting condensate is highly elongated and can exhibit condensation in one dimension (1D). Atom chips have facilitated the production of quasi-1D systems [29]. When the geometry is tighter in one direction than the other two, the condensate is effectively two dimensional (2D) and its shape is described as oblate or disk shaped. This shape of condensate is regularly used in vortex dynamics experiments since the vortex will stay relatively straight throughout its motion and imaging is easier [30, 31].

The development of double well traps [32] have enabled the study of Josephson oscillations [33]. In particular, in a recent atom chip, double well experiment [34], a tunable barrier between the two wells has enabled the crossover between transport via superfluid flow and quantum tunnelling to be observed. The superfluid to Mott insulator phase has been probed with the use of optical lattice potentials [35]. Persistent flow in a BEC has been observed for timescales of duration $(10-40)$s using a toroidal trap [36, 37]. A simple atom circuit has been created in such a system by the addition of a tunable barrier to the toroidal ring [37]. Rapidly-moving laser beams have been used to create dynamic painted potentials in traps such as these as well as ring and square lattices [38].

The observation of Feshbach resonances in Bose-Einstein condensates [39] has enabled the crossover between Bardeen-Cooper-Schrieffer (BCS) superfluidity (a superfluid state of Cooper pairs which are two fermions bound together at low temperatures) and a Bose-Einstein condensate to be probed [40]. These resonances give the experimentalist a method of control over the strength of interactions between atoms as well as their nature i.e. whether the interaction is attractive or repulsive [16, 41].

Condensate properties such as collective excitations [42–45], interference fringes [46], and the propagation of macroscopic nonlinear excitations such as solitons [47] and vortices [48–50], have also been observed.

In this thesis, we are interested in long-range interactions between solitons as well as the dynamics of vortices and Josephson effects at finite temperatures, therefore, we will now give a brief introduction into the importance of modelling finite temperature effects.

1.2 The role of the thermal cloud

For a system of non-interacting bosons at absolute zero, all atoms are in the condensate and so the total density of the system is the same as the condensate density (Fig. 1.1 (Left)). However, in most experiments involving Bose-Einstein condensates, the system is only partially condensed, therefore, the condensate co-exists with a cloud of noncondensed atoms (see the right part of this figure). These noncondensed atoms are commonly referred

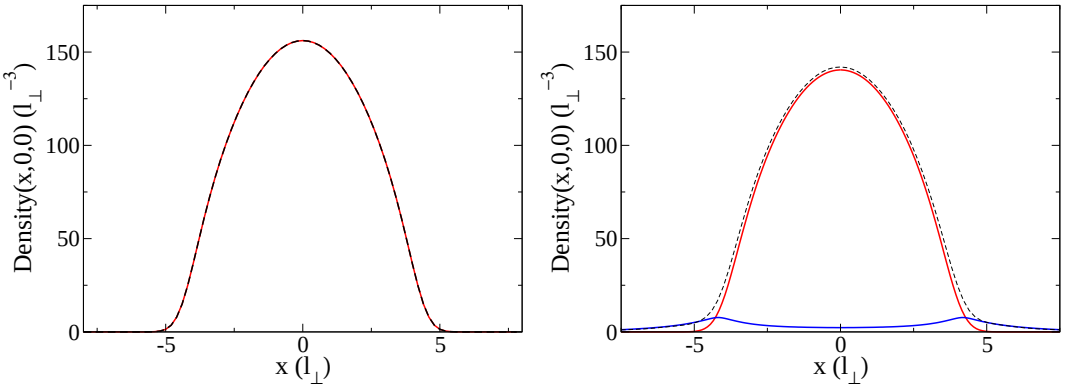

Figure 1.1: Equilibrium condensate (red), noncondensate (blue) and total (black, dashed) densities in the x direction for a system of $N_{\mathrm{TOT}} = 10000$ ^{87}Rb atoms at temperatures of $T = 0$ (left) and $T = 0.5T_c$ (right), for a harmonic trap, $V_{\mathrm{ext}} = (1/2)m(\omega_\perp^2(x^2 + y^2) + \omega_z^2 z^2)$, with trapping frequencies $\omega_\perp = 2\pi \times 129$ Hz and $\omega_z = \sqrt{8}\omega_\perp$.

to collectively, as the noncondensate or thermal cloud (we use these terms interchangeably in this thesis). Since not all the atoms are in the condensate, the central condensate density is diminished. The thermal cloud is repelled by the condensate (for atoms with positive scattering lengths) and so has a higher concentration around the edges of the condensate, therefore, the resulting total density has much broader tails than in the zero temperature case.

The presence of noncondensed atoms in the system mean that thermal excitations can play an important role in the damping of condensate collective modes [45, 51–53] or soliton [47] and vortex propagation [48, 49]. Therefore, when modelling such systems, it is imperative to include, not only the dynamics of the condensate, but also the full dynamics of those atoms which are not condensed. These dynamics include collisions between noncondensed atoms as well as collisions between these atoms and the condensate which result in particles being exchanged between the two 'subsystems'.

The approach which we use, and will explain in detail in the next chapter (Chapter 2), reflects an accurate representation of these combined dynamics, and can therefore fully simulate the back-action of the thermal cloud on the condensate, which is often neglected, treated to lowest order or in linear response (see [54] for a comprehensive review of finite

temperature theories). As this method has been implemented by Zaremba, Nikuni and Griffin (following on from early work by Kirkpatrick and Dorfman [55–58]) we henceforth refer to it as the 'ZNG' method, as described in detail in the recent book of these authors [59].

The strength and frequency of collisions between atoms characterises two distinct dynamical regimes [60]:

- In the collisionless (or mean-field dominated) regime, in which most experiments with ultracold atomic gases have been conducted to date (in stark contrast to helium), the physics tends to be dominated by mean-field effects; nonetheless, an accurate description of collisions is *essential* for correctly describing the system properties, and accounting for changes in condensate atom number. Importantly, a clear separation of timescales (average collision time is longer that the collective mode period), which arises naturally in most experiments with ultracold atoms due to their low densities, enables collisions in this regime to be treated *perturbatively* [54, 61, 62].

- Some recent experiments have been conducted in the crossover to [51] or deep within the hydrodynamic (or collision dominated) [63] regime; in this regime, which has strong analogies to the two-fluid behaviour of superfluid ^{4}He, the high gas density leads to very rapid collisions between thermal atoms, such that the non-condensate enters a *local* hydrodynamic equilibrium (a precursor to true thermodynamic equilibrium), which enables its description in terms of few local hydrodynamic variables (e.g. local density, velocity, chemical potential, temperature, and pressure).

The power of the ZNG equations lies in their ability to successfully describe both collisionless experiments with collective modes [64–66] and macroscopic excitations [67, 68] at finite temperatures (see Chapter 5), and to reduce to the damped two-fluid equations of ^{4}He in the hydrodynamic limit [69–77]. In this thesis, we focus on the collisionless/mean-field dominated regime.

Since the experimental realisation of Bose-Einstein condensation in weakly-interacting inhomogeneous ultracold gases [8–11], there has been great interest in their nonlinear properties [78], including the macroscopic manifestations of vortices [79] and solitons [80]. We now give a brief introduction to each of these.

1.3 Macroscopic excitations and Josephson oscillations

1.3.1 Dark solitons

Solitons are stationary or propagating localised excitations, supported by a unique balance between dispersion and nonlinearity; in particular, dark solitons, on which we focus on in

this thesis, are associated with a localised density dip (see Fig. 1.2 for solitons of different speeds) and a phase shift [81] supported by the repulsive interactions between the atoms. They are of interest in many areas of nonlinear physics and known most widely for their

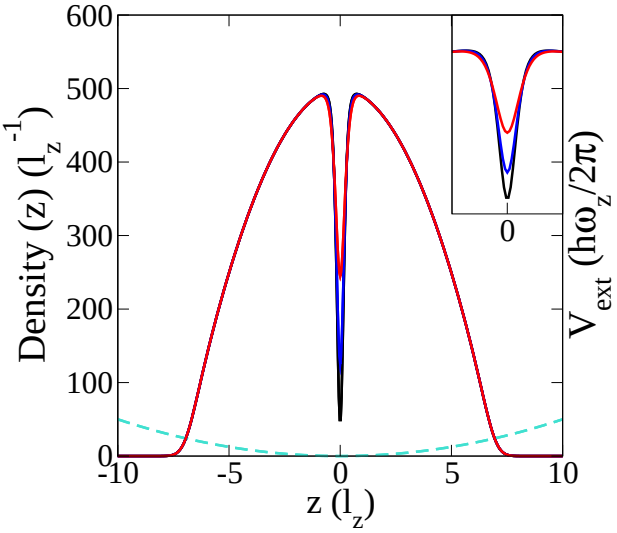

Figure 1.2: (Main) Density of condensate containing a single soliton of speed $v_s = 0.3c$ (black), $v_s = 0.5c$ (blue) and $v_s = 0.7c$ (red) with initial position $z_0 = 0.0$, where $c = \sqrt{\mu/m}$ is the Bogoliubov speed of sound [80] and m is the atomic mass, in a 1D harmonic trap potential (dashed cyan) with frequency $\omega_z = 2\pi \times 63$ Hz and chemical potential $\mu = 25\hbar\omega_z$. (Inset) Zoomed plot around $z = 0.0$ in order to see soliton depths.

applications in optical systems [82]. However, solitons are also a topic of intense research in weakly interacting atomic Bose-Einstein condensates [78, 80], being routinely generated in a number of experiments both in a controlled manner [47, 83–87] and as a result of dynamical processes [88–92].

There is a wide range of interesting analogies between optical systems and Bose-Einstein condensates, as far as solitons are concerned, due to the governing equations. Weakly-interacting atomic Bose-Einstein condensates are well-modelled at low temperatures by a nonlinear Schrödinger equation (known in this context as the Gross-Pitaevskii equation), analogous to the equation arising in nonlinear Kerr optical media [93]. The fundamental difference between these two systems, which is also central to the effects demonstrated in Chapter 3 of this thesis, is the existence of an *inhomogeneous* external potential for ultracold gases (dashed cyan line of Fig. 1.2) which breaks the integrability of the system even in its idealised one dimensional setting, thereby rendering a dark soliton unstable to sound emission along its axis of propagation, as first pointed out in the context of ultracold gases in [94].

Stability and decay mechanisms

Many other dark soliton decay mechanisms have been predicted [95, 96] and observed [47, 88], including the snake instability [95–100], for which three-dimensional solitons decay into vortex rings [101], and thermal dissipation [67, 97, 102, 103]. The role of quantum effects has also been highlighted [104]. However, recent soliton experiments were conducted at such low temperature regimes, where the simplest mean field model, the Gross-Pitaevskii equation was found to accurately describe the observations [105]; in this thesis, we therefore restrict our attention to this regime.

While a dark soliton propagating in an inhomogeneous background tends to dissipate energy acoustically, solitons confined in a harmonic potential can actually reabsorb this sound energy in periodic cycles [106]. Recent work [107] has further highlighted the dependence of the stability of a dark soliton on the homogeneity of the background it is propagating in, revealing the strong role of any anharmonicities present, and demonstrating that the latest soliton experiments [84–86] came extremely close to the regime where this effect would dominate over all other decay mechanisms.

In Chapter 3 we therefore investigate, using the Gross-Pitaevskii equation, the interaction of solitons via the sound mediated by propagation in an inhomogeneous medium.

1.3.2 Vortices

Vortices are a hallmark signature of a turbulent flow. Classical rotational vortices are visible in many areas of nature, from the spiralling flow of a tornado, to the counter-circulating wing-tip vortices which form at the tips of wings on a plane and undergo the Crow instability [108], to the spiralling of our galaxy, the Milky way, characterised by a thin vortex-like, rotating disk.

Quantised vortices in Bose-Einstein condensates are topological defects, see Fig. 1.3 for an example of a condensate containing a vortex. They can arise during condensate formation as a result of broken symmetry, a consequence of a rapid quench through the Bose critical temperature, T_c, via the Kibble-Zurek mechanism [109–111], or as a result of the rotation of a condensate in an anisotropic trap above the critical angular frequency, Ω_c (see [112] and references therein). Below this rotation speed, the condensate remains stationary, whilst above it vortices are nucleated at the condensate edge. These are possible mechanisms for the creation of vortices in condensates [31, 113–116]. Other methods include phase imprinting [117–119] and stirring the condensate with a laser beam [114, 120].

Vortices have been experimentally created in many different configurations such as vortex rings [89, 121], vortex lattices [49, 115, 122], vortex dipoles [30], multiply charged vortices [119, 123] and giant vortices [124] (where the condensate contains many units of

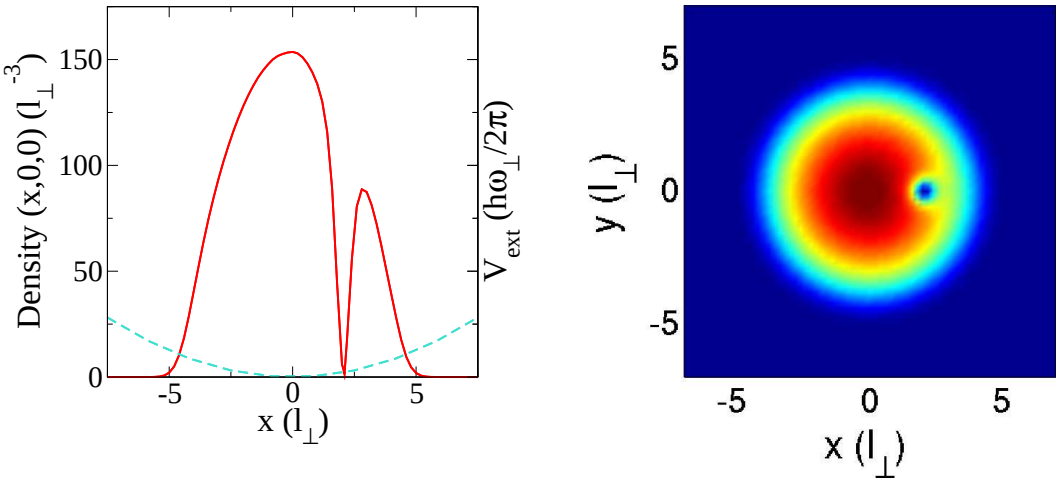

Figure 1.3: Left: Density of condensate (red) containing a vortex in radial position $r_v = 2.1 l_\perp$, in x direction. The harmonic trap in this direction is also shown (dashed cyan) with frequencies, $\omega_\perp = 2\pi \times 129$ Hz and $\omega_z = \sqrt{8}\omega_\perp$. Right: Axial view of condensate density, where the colours range from blue corresponding to zero density, to red, corresponding to high density. $N_c = 10000$ with a negligible thermal cloud ($T \simeq 0$).

vorticity and the density is compressed such that individual vortices are no longer visible). More recently a small vortex tangle has been created [125], increasing the interest in the study of quantum turbulence in BECs by extension to the superfluid helium systems usually probed.

Stability and decay mechanisms

The nucleation of vortices in a rotating condensate is evidently the result of a dynamical instability when the cloud is rotated above a critical angular velocity [126]. The existence of dynamical instabilities of vortices is evident in the nucleation and (when the rotation speed is increased again) subsequent crystallisation of vortex lattices at low temperatures [49, 116, 122, 127].

Vortices, like dark solitons, are unstable to acceleration resulting in the emission of sound waves. The decay of a quantised vortex as a result of this sound emission has been studied quantitatively in [128]. Sound emission and absorption were controlled by embedding a dimple trap in a weaker harmonic trap and by varying the depth of the dimple trap. When the dimple was deep, the vortex was able to re-interact with the energy emitted during propagation and was therefore stabilised, while when the dimple was shallow, sound could escape the embedded trap and the vortex would decay. This is analogous to the decay of dark solitons in anharmonic traps [107].

This radiation-induced decay has also been observed [129] in vortex tangles in su-

perfluid helium and has been investigated theoretically [130, 131]. Reconnections of two vortex lines causes the vortices to accelerate and dissipate energy in the form of sound [132]. It has also been shown that vortex lines lose energy via Kelvin-wave radiation. Kelvin wave excitations along a vortex line/ring change the velocity and decrease the vortex ring size [133].

The lifetime of vortex structures created in the laboratory is approximately 10s. It is thought the reason for their demise is due to thermal dissipation [48, 49]. The interaction of the vortex core with the thermal cloud can cause the vortex to lose energy; this results in the vortex spiralling out of a harmonically trapped condensate, so the lifetime of a vortex is severely inhibited for temperatures approaching T_c [68]. Earlier work on finite temperature vortex dynamics has confirmed the lifetime limiting effect that a cloud of noncondensed atoms has on a vortex [68, 134–139]. In Chapter 5 of this thesis we assess the effect of finite temperature on experimentally relevant vortex quantities.

1.3.3 Josephson oscillations in double wells

When two BECs are weakly linked, there exists a phase gradient which drives transport between the two systems. Theoretically, double well trapping potentials are commonly used to simulate, and therefore understand this transport. If the height of the barrier between the two wells is of the order of the chemical potential, then the density in this region is diminished and quantum mechanical tunnelling can take place. Josephson oscillations are characterised by a sinusoidal oscillation in population imbalance and phase difference between the two wells.

These oscillations were first described by Brian Josephson in the 1960s for transport of Cooper pairs of electrons across an insulating region between superconducting wires [140] when a current is applied. Shortly after this prediction came the first suspected experimental realisation of this tunnelling effect [141].

Josephson oscillations have since been observed in a wide variety of systems including superfluid ^{3}He [142, 143] and ^{4}He [144]. In these systems, pressure detectors have been used to measure changes in the pressure of two containers containing superfluid, connected through small holes comparable in size to the superfluid healing length, in order to determine the density of superfluid in either reservoir and therefore, the population dynamics.

The Josephson effect was predicted for two weakly linked condensates [145] almost a decade before the experimental realisation of Bose-Einstein condensation in 1995 [9, 146]. The trapping geometry outlined in this prediction was in the form of a double well potential. However, experimentally it is difficult to create these traps in the form which the theory predicts necessary in order to observe Josephson oscillations in the experimental timescale. This is because the barrier between the traps must be small in order to allow

tunnelling to take place, but for the typical atom numbers used in experiments (of the order of $N_{\mathrm{TOT}} \simeq 10000$), mean-field effects tend to dominate over quantum effects. As a result, the first experiment in which Josephson oscillations were observed in BECs was not in a double well potential but in an array of Josephson junctions formed on optical lattice potential [147]. In the 1D array of deep wells, an oscillating atomic current was detected which confirmed the presence of tunnelling in the system. However, in this and subsequent experiments of its type, each well tends to be very small with the separation being of the order of 100nm, this makes the direct imaging of each well and measurement of population oscillations very difficult. Therefore, as the abundance of theoretical work suggests [145, 148–152], double well geometries are the ideal geometry in which to directly observe Josephson oscillations.

Albeiz *et al.* were the first group to directly observe, using a double well potential, both Josephson oscillations of the population imbalance and another phenomenon unique to the nonlinearity of BECs, called macroscopic quantum self trapping (MQST) where the population imbalance is large such that it becomes 'self-locked' in one well [33]. They used a small number of atoms, approximately $N_{\mathrm{TOT}} \simeq 1100$, so that tunnelling was not inhibited by the dominance of mean-field effects, and observed these effects over a timescale of 50ms. Further to this, thermal fluctuations of the phase difference have been observed [153] in this type of trap, and found to destroy the Josephson oscillations when the temperature is very high. Thermal effects on the relative phase and imbalance of the atom number in this double well trap have also been investigated theoretically [154] and the damping rate of these oscillations shown to increase with temperature. The presence of thermal atoms in the system has been shown theoretically, to decay the MQST regime until the population begins undergoing Josephson oscillations [155, 156].

Also, double well traps have been experimentally formed on atom chips [157] which has led to the investigation of double well systems in which Josephson oscillations can be observed for larger numbers of atoms. In a recent experiment of this type, by LeBlanc *et al.* [34], the barrier between the two sites of the double well was tunable, therefore, both superfluid and quantum tunnelling transport could be probed. A unique feature of these oscillations is the rapid decay in amplitude which is as of yet unexplained and was the motivation for our study of finite temperature Josephson effects in double well potentials, presented in Chapter 6.

1.4 Outline of thesis and collaborations

At this point we wish to give a general outline of the thesis and highlight collaborative contributions (these will be further noted in the relevant chapter).

The first part of this thesis reviews the zero and finite temperature models we have used, in the subsequent Parts II and III to generate numerical results. The thesis is structured as follows.

Part I - Introduction to Bose Gases

We begin in Chapter 2, by reviewing important theoretical concepts required for the numerical modelling which is carried out in this thesis. This chapter begins with the description of the condensate order parameter and the form of the much celebrated, zero temperature Gross-Pitaevskii equation. The physical importance of modelling thermal effects on top of the condensate is highlighted in Sec. 2.2 which reviews the derivation of the coupled Gross-Pitaevskii equation with a quantum Boltzmann equation for the thermal cloud. This theory is commonly known as ZNG theory, named so after Zaremba, Nikuni and Griffin [69].

Part II - $T = 0$: Sound mediated, Long-range Interactions between Dark Solitons

In Chapter 3, we present results of numerical simulations, obtained by solving the Gross-Pitaevskii equation, of a long-range interaction between dark solitons, which is mediated by the sound which they emit during propagation through an inhomogeneous background. This chapter is an expanded review of work we have previously published on this topic:

Long-range sound-mediated dark-soliton interactions in trapped atomic condensates,
A. J. Allen, D. P. Jackson, C. F. Barenghi, and N. P. Proukakis,
Phys. Rev. A **83**, 013613 (2011).

Following on from the main results of this chapter and to strengthen the general nature of the features present here, Sec. 3.5 briefly presents the findings of a recent paper which investigates a similar effect for vortices in 2D (Figs. 3.14 and 3.15 from this section are taken from [158] and not created by me):

Coherent cross-talk and parametric driving of matter-wave vortices,
N. G. Parker, A. J. Allen, C. F. Barenghi, and N. P. Proukakis.
arXiv:1109.0039v1 (Preprint).

Part III - $T > 0$: Bose-Condensed Gases at Finite Temperatures modelled using ZNG

The numerical methods used to solve the ZNG equations are outlined in Chapter 4, following the procedure laid out by Jackson and Zaremba [159], with the remainder of this thesis giving an overview of work on simulations of finite temperature effects modelled using the ZNG method which are in preparation for publication. An overview of this theory and brief outline of the numerical schemes used is the subject of a recent book chapter:

Dynamical, Self-consistent, Finite Temperature Kinetic Theory (The 'ZNG' Scheme),
A. J. Allen, C. F. Barenghi, and N. P. Proukakis, and E. Zaremba,
To appear in 'Non-Equilibrium Quantum Gases at Finite Temperatures',
N. P. Proukakis, S. A. Gardiner, M. J. Davis, N. Nygaard, M. H. Szymanska (Eds.),
Imperial College Press (2012).

In Chapter 5 we address finite temperature on vortex dynamics. With the initial focus on decay rates in Sec. 5.2, and precession frequencies for the parameters of a recent experiment discussed in Sec. 5.4. The vortex core is studied as a possible thermometer, Sec. 5.5, along with investigations into radially translating a vortex using a rotating thermal cloud in Sec. 5.6. At this point we acknowledge ongoing correspondence with David Hall (Amherst College) regarding his experimental findings which helped shape these questions, and discussions of these issues with Eugene Zaremba (Queen's University, Kingston, Ontario).

In Chapter 6, through collaborative efforts with Anssi Collin and Eugene Zaremba, the effect of finite temperatures on Josephson oscillations of a double well potential are investigated. An idealised geometry, first investigated by Collin and Zaremba using the ZNG scheme [154] is initially analysed in order to understand the nature of Josephson oscillations and the effect of increasing temperature on the population dynamics assessed in Sec. 6.1. Correspondence with the experimental group of Joseph Thywissen (University of Toronto) has enabled us to investigate, in Sec. 6.2, similar dynamics on a more complicated double well with a tunable barrier which is situated on an atom chip. Problems encountered whilst modelling this complicated, double well geometry bring us to the final chapter.

In Chapter 7 we briefly review the main findings of this thesis and discuss opportunities for follow on work.

Chapter 2

Theoretical Models

The common model of dilute, weakly interacting Bose gases at zero temperature is the Gross-Pitaevskii equation (GPE), also referred to as the nonlinear Schrödinger equation (NLSE). The GPE is a mean-field approach, derived independently by Gross [160, 161], and Pitaevskii [162] in the 1960s, which is valid at low temperatures where there is a macroscopic occupation of the lowest energy level and where interaction between particles is weak. In these systems, the scattering length is much smaller than the distance between particles ($a_s \ll n^{1/3}$) and the deBroglie wavelength ($a_s \ll \lambda_{dB}$), therefore, the exact interatomic potential can be replaced by an effective contact potential [1]. The GPE gives a good description of the condensate dynamics, including the oscillations of collective modes, the propagation of macroscopic excitations (solitons and vortices), and interference effects associated with the phase of the condensate's order parameter. In a harmonic trap and in the weakly-interacting limit, it is surprisingly accurate up to temperatures close to $\sim 0.5T_c$, however, it does not account for the interaction of the condensate with the noncondensate atoms and hence the finite temperature effects are ignored.

In most experiments involving Bose-Einstein condensates, the system is only partially condensed, therefore when modelling such systems, it is imperative to include not only the mean-field interaction between the condensate and thermal cloud, but the full dynamics of the noncondensed atoms. This includes particle-exchanging collisions between the condensate and noncondensate, collisions between the noncondensate atoms, as well as the usual mean-field contributions. The accurate representation of these dynamics results in a model which can simulate the back-action of the thermal cloud on the condensate, a property which is often neglected.

The approach used by Zaremba, Nikuni and Griffin (ZNG), which we describe in detail in this chapter, is an extension of the microscopic GPE in which collisions between the thermal cloud atoms, and particle-exchanging collisions between the condensate and thermal cloud are also accounted for.

We begin our discussion of theoretical methods with a description of the zero temperature GPE and follow with a review of the ZNG method to include finite temperature effects by coupling a dissipative GPE with a semiclassical Boltzmann Equation. Finally we briefly remark on other finite temperature theories including the stochastic GPE.

2.1 The Gross-Pitaevskii equation: Methodology of Part II

A system of N interacting bosons can be described by the quantum mechanical wavefunction $\Psi(\mathbf{r}_1, ..., \mathbf{r}_N, t)$ where $\mathbf{r}_i$ denotes the position of atom i. A direct solution for the equation of motion for the full N-body wavefunction is in general not practical, therefore, in practice the method of second quantisation is used to exploit the particle statistics and reduce the wavefunction into a more manageable form. In essence, the N-body bosonic wavefunction is mapped onto an occupation number basis set. The interaction term of the Hamiltonian contains correlations between all the atoms so is difficult to solve for large atoms numbers. In this approach, the Bose field operator $\hat{\Psi}(\mathbf{r})$ ($\hat{\Psi}^\dagger(\mathbf{r})$) for the creation (annihilation) of a particle at position $\mathbf{r}$ evolves according to the Heisenberg equation of motion

$$i\hbar\frac{\partial\hat{\Psi}(\mathbf{r},t)}{\partial t} = [\hat{\Psi}(\mathbf{r},t), \hat{H}], \tag{2.1}$$

where the second quantised form of the many body Hamiltonian is

$$\begin{aligned}\hat{H} &= \int d\mathbf{r}\hat{\Psi}^\dagger(\mathbf{r},t)\left[-\frac{\hbar^2}{2m}\nabla^2 + V_{\text{ext}}(\mathbf{r})\right]\hat{\Psi}(\mathbf{r},t) \\ &+ \frac{1}{2}\int d\mathbf{r}\int d\mathbf{r}'\hat{\Psi}^\dagger(\mathbf{r},t)\hat{\Psi}^\dagger(\mathbf{r}',t)V(\mathbf{r}-\mathbf{r}')\hat{\Psi}(\mathbf{r}',t)\hat{\Psi}(\mathbf{r},t).\end{aligned} \tag{2.2}$$

$V_{\text{ext}}(\mathbf{r})$ is the external trapping potential used to confine the Bose gas, $V(\mathbf{r}-\mathbf{r}')$ is the two-body interatomic potential and the Bose field operators obey the following commutation relations

$$\left[\hat{\Psi}(\mathbf{r},t), \hat{\Psi}^\dagger(\mathbf{r}',t)\right] = \delta(\mathbf{r}-\mathbf{r}'), \tag{2.3}$$

$$\left[\hat{\Psi}(\mathbf{r},t), \hat{\Psi}(\mathbf{r}',t)\right] = \left[\hat{\Psi}^\dagger(\mathbf{r},t), \hat{\Psi}^\dagger(\mathbf{r}',t)\right] = 0. \tag{2.4}$$

For dilute, weakly interacting Bose gases, the exact interatomic potential can be approximated by an effective, contact interaction of the form

$$V(\mathbf{r}-\mathbf{r}') = g\delta(\mathbf{r}-\mathbf{r}'). \tag{2.5}$$

This approximation is routinely made when the particles have elastic collisions (low energy,

$s-$wave collisions), and the interaction strength is defined as

$$g = \frac{4\pi\hbar^2 a_s}{m}, \tag{2.6}$$

where m is the atomic mass and a_s is the s-wave scattering length, hence g is characteristic of the particular atomic species. It is important to note that when $g < 0$ the effective interactions between the bosons are attractive while when $g > 0$ the interactions are repulsive.

Replacing the second quantised Hamiltonian of Eq. (2.2), into the Heisenberg equation of motion Eq. (2.1) we obtain

$$i\hbar\frac{\partial\hat{\Psi}(\mathbf{r},t)}{\partial t} = \left[-\frac{\hbar^2}{2m}\nabla^2 + V_{\text{ext}}(\mathbf{r}) + g\Psi^\dagger(\mathbf{r},t)\Psi(\mathbf{r},t)\right]\Psi(\mathbf{r},t). \tag{2.7}$$

A mean field approach is now used to move the focus to the states which are most highly occupied, and in the case of Bose-Einstein condensates, it is the lowest energy level which is macroscopically occupied. The bosonic field operator is decomposed via

$$\hat{\Psi}(\mathbf{r},t) = \phi(\mathbf{r},t) + \hat{\psi}(\mathbf{r},t). \tag{2.8}$$

Replacing the operator $\hat{\phi}$ by the wavefunction ϕ is done under the symmetry breaking assumption, whereby it is understood that during the formation, the condensate has assumed a single phase and can be described by a single wavefunction. As a consequence of this, the total number of particles is not strictly conserved. However, this procedure can be justified by the argument that the addition or removal of an atom from a condensate containing a large number of atoms, N_0, does not affect the state of the system, i.e. $N_0 \pm 1 \simeq N_0$. It is essentially equivalent to splitting the Bosonic field operator into a part concerned with the macroscopic occupation of the ground state i.e. the condensate wavefunction, defined as the ensemble average $\phi(\mathbf{r},t) = \langle\hat{\Psi}(\mathbf{r},t)\rangle$, and an operator $\hat{\psi}$, which captures all fluctuations around the classical mean-field of the condensate; this often termed the noncondensate operator, and is generally assumed to have zero ensemble average, $\langle\hat{\psi}(\mathbf{r},t)\rangle = 0$[1].

Noncondensate atoms can arise in the system as a result of either quantum or thermal effects. However, for the weakly interacting systems we study ($a_s \ll \lambda_{\text{dB}}$), quantum fluctuations can be neglected and at low enough temperatures, close to absolute zero, thermal depletion may not play a large role, and hence $\hat{\psi}$ can be neglected i.e. $\hat{\Psi}(\mathbf{r},t) = \phi(\mathbf{r},t)$. Therefore, in the limit of zero temperature and weak interactions, the evolution

[1]This is only strictly true if an explicitly number-conserving formalism is used, see [163–165].

equation for the macroscopic condensate wavefunction ϕ, is written as

$$i\hbar\frac{\partial\phi(\mathbf{r},t)}{\partial t} = \left[-\frac{\hbar^2}{2m}\nabla^2 + V_{\text{ext}}(\mathbf{r}) + g|\phi(\mathbf{r},t)|^2\right]\phi(\mathbf{r},t). \tag{2.9}$$

This is called the Gross-Pitaevskii equation (GPE) which has been generally found to provide a very good description of the dynamics of a Bose-Einstein condensate up to temperatures of approximately $T \simeq 0.5T_c$. This equation is of the form of the time-dependent Schrödinger equation with the first term, $-(\hbar^2/2m\nabla^2)\phi(\mathbf{r},t)$ describing the kinetic energy of the system at that particular instant in time, the second term, $V_{\text{ext}}(\mathbf{r})\phi(\mathbf{r},t)$, is the external trapping potential and the final term, $g|\phi(\mathbf{r},t)|^2\phi(\mathbf{r},t)$, is the nonlinear term arising from atomic interactions, therefore, the GPE is also commonly referred to as the nonlinear Schrödinger equation.

2.1.1 Hydrodynamic equations

By expanding the condensate wavefunction in terms of phase and amplitude variables in the following way

$$\phi(\mathbf{r},t) = \sqrt{n_c(\mathbf{r},t)}e^{i\theta(\mathbf{r},t)}, \tag{2.10}$$

where $n_c(\mathbf{r},t) = |\phi(\mathbf{r},t)|^2$ and $\theta(\mathbf{r},t)$ is the phase, it can be shown that the time dependent GPE, Eq. (2.9), is completely equivalent to the following hydrodynamic equations

$$\frac{\partial n_c}{\partial t} + \nabla\cdot(n_c\mathbf{v_c}) = 0, \tag{2.11}$$

$$m\frac{\partial\mathbf{v_c}}{\partial t} = -\nabla\varepsilon_c \tag{2.12}$$

where the superfluid velocity field is defined as the gradient of the condensate phase

$$\mathbf{v_c}(\mathbf{r},t) = \frac{\hbar}{m}\nabla\theta(\mathbf{r},t), \tag{2.13}$$

and the local energy of a condensate atom having potential energy μ_c and kinetic energy $1/2mv_c^2$ is given by

$$\varepsilon_c = \mu_c + \frac{1}{2}mv_c^2. \tag{2.14}$$

In this formalism, μ_c is a position dependent chemical potential, given by

$$\mu_c(\mathbf{r},t) = -\frac{\hbar^2\nabla^2\sqrt{n_c(\mathbf{r},t)}}{2m\sqrt{n_c(\mathbf{r},t)}} + V_{\text{ext}}(\mathbf{r}) + gn_c(\mathbf{r},t). \tag{2.15}$$

2.1.2 Condensate energy and number of atoms

The GPE can also be derived using a variational procedure involving the condensate energy functional [1, 54] which is a function of the condensate wavefunction, $\phi(\mathbf{r})$, and in general is defined as

$$\epsilon[\phi(\mathbf{r})] = \left[\frac{\hbar^2}{2m}|\nabla\phi|^2 + V_{\text{ext}}(\mathbf{r})|\phi|^2 + \frac{g}{2}|\phi|^4\right]. \tag{2.16}$$

The total energy of the condensate is found by integrating $\epsilon[\phi(\mathbf{r})]$ over all space via

$$E[\phi] = \int d\mathbf{r}\epsilon[\phi(\mathbf{r})] = \int d\mathbf{r}\left[\frac{\hbar^2}{2m}|\nabla\phi|^2 + V_{\text{ext}}(\mathbf{r})|\phi|^2 + \frac{g}{2}|\phi|^4\right]. \tag{2.17}$$

By minimising Eq. (2.17) by means of functional differentiation with respect to both real and imaginary contributions of the condensate wavefunction, along with imposing the constraint of fixed atom number, N, the desired optimal form for the condensate wavefunction can then be obtained.
The total number of atoms in the condensate is written

$$N = \int d\mathbf{r}|\phi|^2. \tag{2.18}$$

2.1.3 Obtaining the ground state

Stationary solutions of the GPE can be found by the substitution $\phi(\mathbf{r},t) = \phi_0(\mathbf{r})e^{-i\mu t/\hbar}$, where μ is the chemical potential which characterises the ground state energy of the system (it is associated with the energy required to remove a particle from the system). After rearranging it, Eq. (2.9) becomes

$$\mu\phi_0(\mathbf{r}) \quad = \quad \left[-\frac{\hbar^2}{2m}\nabla^2 + V_{\text{ext}}(\mathbf{r}) + g|\phi_0(\mathbf{r})|^2\right]\phi_0(\mathbf{r}). \tag{2.19}$$

This is the time-independent GPE.

The Thomas-Fermi limit

For repulsive interactions, in the limit of large N, the nonlinear term, $g|\phi_0|^2$, dominates over the kinetic energy term, $-(\hbar^2/2m)\nabla^2\phi_0$ [166], therefore the latter contribution can be neglected in Eq. (2.19). In this limit, the ground state solution can be approximated by:

$$|\phi_{\text{TF}}(\mathbf{r})|^2 = n_{\text{TF}}(\mathbf{r}) = \begin{cases} \frac{\mu - V_{\text{ext}}(\mathbf{r})}{g} & \text{if } \mu \geq V_{\text{ext}}(\mathbf{r}) \\ 0 & \text{otherwise} \end{cases}$$

which is called the Thomas-Fermi solution. In making this approximation for the density, ϕ has arbitrary phase. It is however, very good at large atom numbers but fails close to the condensate edge, $r \simeq R_{TF}$, where it abruptly vanishes rather than gradually diminishing. The Thomas-Fermi radius, $R_{\rm TF}$, is a convenient scaling parameter which we will make use of in the later chapters, and is given by the solution of $\mu = V_{\rm ext}$. For a condensate with trapping potential of the form, $V_{\rm ext} = (1/2)m({\omega_x}^2x^2 + {\omega_y}^2y^2 + {\omega_z}^2z^2)$, the Thomas-Fermi radius in the x direction is given by

$$R_{\rm TF} = \sqrt{\frac{2\mu}{m\omega_x^2}}. \tag{2.20}$$

Although the GPE provides a good description of the dynamics of a Bose gas at temperatures up to $T \simeq 0.5T_c$, if we are interested in the effect of finite temperature on the condensate, we need to include thermal effects in our models.

2.2 The Zaremba-Nikuni-Griffin formalism: Methodology of Part III

When modelling Bose-Einstein condensates at temperatures above absolute zero, it is important to include the effects of finite temperature on the condensate. This means that the approximation made on the bosonic field operator in Sec. 2.1, where the fluctuation term of Eq. (2.8) was neglected, is not sufficient. Therefore, replacing the full decomposition of Eq. (2.8) into Eq. (2.7) and taking the average we obtain

$$i\hbar\frac{\partial\phi(\mathbf{r},t)}{\partial t} = \left[-\frac{\hbar^2\nabla^2}{2m} + V_{\rm ext}\right]\phi(\mathbf{r},t) + g\langle\hat{\Psi}^\dagger(\mathbf{r},t)\hat{\Psi}(\mathbf{r},t)\hat{\Psi}(\mathbf{r},t)\rangle, \tag{2.21}$$

which is *exact* in the context of symmetry-breaking, given that $\langle\psi^\dagger\rangle = \langle\psi\rangle = 0$. Expanding the final term yields

$$\langle\hat{\Psi}^\dagger\hat{\Psi}\hat{\Psi}\rangle = n_c\phi + \tilde{m}\phi^* + 2\tilde{n}\phi + \langle\hat{\psi}^\dagger\hat{\psi}\hat{\psi}\rangle, \tag{2.22}$$

where we have defined the following mean-field 'densities':

- Condensate density: $n_c(\mathbf{r},t) = |\phi(\mathbf{r},t)|^2$
- Non-condensate density: $\tilde{n}(\mathbf{r},t) = \langle\hat{\psi}^\dagger(\mathbf{r},t)\hat{\psi}(\mathbf{r},t)\rangle$
- Pair anomalous density: $\tilde{m}(\mathbf{r},t) = \langle\hat{\psi}(\mathbf{r},t)\hat{\psi}(\mathbf{r},t)\rangle$.

The equation of motion for the condensate therefore reduces to [167–170]

$$i\hbar\frac{\partial\phi}{\partial t} = \left[-\frac{\hbar^2\nabla^2}{2m} + V_{\rm ext} + g(n_c + 2\tilde{n})\right]\phi + g\tilde{m}\phi^* + g\langle\hat{\psi}^\dagger\hat{\psi}\hat{\psi}\rangle. \tag{2.23}$$

It is easy to see that if all the atoms are in the condensate, $\tilde{n}, \tilde{m}, \langle\hat{\psi}^\dagger\hat{\psi}\hat{\psi}\rangle \to 0$, and Eq. (2.23) trivially reduces to the GPE (2.9). From the Heisenberg Equation of motion for the noncondensate

$$i\hbar\frac{\partial\hat{\psi}(\mathbf{r},t)}{\partial t} = [\hat{\psi}(\mathbf{r},t), \hat{H}] = i\hbar\frac{\partial}{\partial t}(\hat{\Psi}(\mathbf{r},t) - \langle\hat{\Psi}(\mathbf{r},t)\rangle), \tag{2.24}$$

we find the corresponding equation for the noncondensate

$$\begin{aligned} i\hbar\frac{\partial\hat{\psi}(\mathbf{r},t)}{\partial t} &= \left[-\frac{\hbar^2\nabla^2}{2m} + V_{\rm ext}(\mathbf{r}) + 2g(n_c(\mathbf{r},t) + \tilde{n}(\mathbf{r},t))\right]\hat{\psi}(\mathbf{r},t) \\ &- 2g\tilde{n}\hat{\psi}(\mathbf{r},t) + g\phi^2\hat{\psi}(\mathbf{r},t) \\ &+ g\phi^*(\mathbf{r},t)\left(\hat{\psi}(\mathbf{r},t)\hat{\psi}(\mathbf{r},t) - \tilde{m}(\mathbf{r},t)\right) \\ &+ 2g\phi(\mathbf{r},t)\left(\hat{\psi}^\dagger(\mathbf{r},t)\hat{\psi}(\mathbf{r},t) - \tilde{n}(\mathbf{r},t)\right) \\ &+ g\left(\hat{\psi}^\dagger(\mathbf{r},t)\hat{\psi}(\mathbf{r},t)\hat{\psi}(\mathbf{r},t) - \langle\hat{\psi}^\dagger(\mathbf{r},t)\hat{\psi}(\mathbf{r},t)\hat{\psi}(\mathbf{r},t)\rangle\right). \end{aligned} \tag{2.25}$$

The equations of motion for the condensate Eq. (2.23), and the noncondensate Eq. (2.25) are coupled to higher order correlations and, therefore, some truncation is required to solve these equations. Attention should be drawn to the triplet contribution in the condensate equation of motion, Eq. (2.23) as this term was often neglected in the early literature but it is pertinent as it can cause condensate growth.

2.2.1 First order effects: Mean-field coupling

In the Hartree-Fock (HF) limit, the only noncondensate terms of Eq. (2.22) which are retained are those involving one creation and one annihilation operator, thereby neglecting both the anomalous averages $\tilde{m}(\mathbf{r},t)$, and $\langle\hat{\psi}^\dagger\hat{\psi}\hat{\psi}\rangle$ in Eq. (2.23). Within the semiclassical approximation, the excitation spectrum can be described in terms of momentum, p, with the kinetic energy term, $-\hbar^2\nabla^2/2m$ being replaced by $p^2/2m$. The local energy of the thermal atoms, $\tilde{\varepsilon}_i$ can be described by Hartree-Fock (HF) energies of the form

$$\tilde{\varepsilon}_i(\mathbf{r},t) = \frac{p^2}{2m} + V_{\rm ext}(\mathbf{r}) + 2g[n_c(\mathbf{r},t) + \tilde{n}(\mathbf{r},t)] \equiv \varepsilon_i + U_{\rm eff}(\mathbf{r},t), \tag{2.26}$$

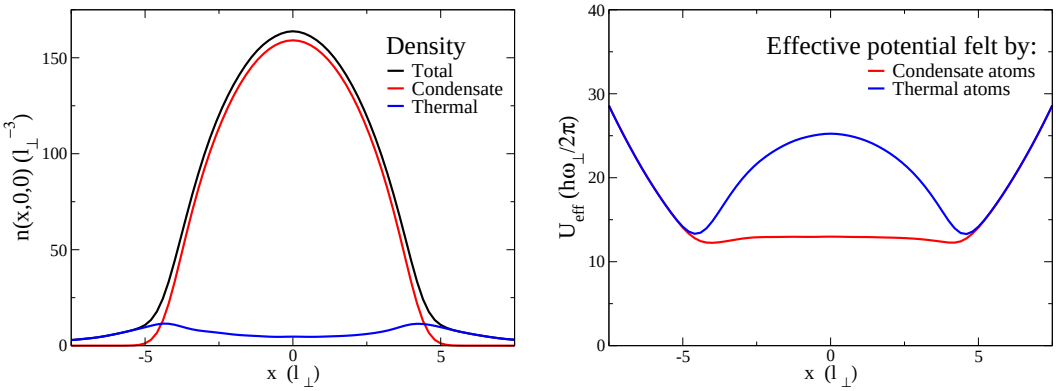

Figure 2.1: Left: Condensate n_c (red), thermal cloud $\tilde{n}$ (blue) and total density $n = n_c + \tilde{n}$ (black) for a system with $N_c = 10000$ condensate atoms and $N_T = 750$ thermal atoms at a temperature of 53.1nK in a harmonic trap ($\omega_\perp = 2\pi \times 129$ Hz, $\omega_z = \sqrt{8}\omega_\perp$). Right: Effective potential felt by condensate atoms, $U^c_{\rm eff}$ (red), and the thermal atoms, $U_{\rm eff}$ (blue).

where the single particle energies are modified by the addition of mean-field of the condensate $n_c(\mathbf{r}, t)$ and noncondensate $\tilde{n}(\mathbf{r}, t)$ i.e.

$$U_{\rm eff}(\mathbf{r}, t) = V_{\rm ext}(\mathbf{r}) + 2g[n_c(\mathbf{r}, t) + \tilde{n}(\mathbf{r}, t)]. \tag{2.27}$$

The corresponding effective potential felt by the condensate atoms is

$$U^c_{\rm eff}(\mathbf{r}, t) = V_{\rm ext}(\mathbf{r}) + g[n_c(\mathbf{r}, t) + 2\tilde{n}(\mathbf{r}, t)]. \tag{2.28}$$

These are both plotted for the case of a harmonic trap in Fig. 2.1 (Right). In the case of repulsive interactions, $g > 0$, the condensate 'repels' the thermal cloud. In the central region where the condensate density is highest (see Fig. 2.1 (Left)), the thermal cloud feels a high potential and the result is a lower thermal cloud density in this region than in the areas in which the condensate mean-field is weaker, i.e. around the condensate edges. This explains the double peaked structure of the thermal cloud density.

The Hartee-Fock-Bogoliubov (HFB) limit is a generalisation of the HF limit in which all quadratic noncondensate operators are maintained in the Hamiltonian, including terms with two like creation or annihilation operators. Such a quadratic Hamiltonian can be routinely diagonalised by a Bogoliubov transformation to a quasiparticle basis. Thus the HFB formalism explicitly considers the anomalous average. However, the homogeneous limit of this theory leads to a gap in the energy spectrum at low momenta, which is prohibited for a symmetry breaking theory by the Goldstone theorem [171]. This inconsistency can be avoided by neglecting the anomalous average altogether, as implemented by Griffin [168, 172]. Predictions of such theories have been presented in [173] and summarised in [174].

The HFB approach forms a good basis for finite temperature theories. The main disadvantage is that the approximations which have been introduced result in neglecting the effect of collisional damping of the condensate motion. In particular, no contribution from the triplet term $\langle\hat{\psi}^\dagger\hat{\psi}\hat{\psi}\rangle$ means important information about condensate collisions with the thermal atoms are ignored. A higher order approximation is needed to maintain higher order correlations, including the effect of collisions with the noncondensate atoms on the condensate dynamics.

2.2.2 Beyond mean-field: Particle-exchange and ZNG

In a similar manner as in Sec. 2.1.1, hydrodynamic equations can be derived by introducing phase and amplitude variables to define the macroscopic wavefunction $\phi(\mathbf{r},t) = \sqrt{n_c(\mathbf{r},t)}e^{i\theta(\mathbf{r},t)}$. Substituting these into Eq. (2.23) and equating real and imaginary parts results in the set of hydrodynamic equations for the condensate wavefunction

$$\frac{\partial n_c}{\partial t} + \nabla\cdot(n_c\mathbf{v}_c) = -\Gamma_{12}[f,\phi], \tag{2.29}$$

$$m\frac{\partial \mathbf{v}_c}{\partial t} = -\nabla\left(\mu_c + \frac{1}{2}mv_c^2\right). \tag{2.30}$$

Physically, the quantity $\Gamma_{12}[f,\phi] \equiv -(2g/\hbar)\mathrm{Im}\left[\phi^*\langle\psi^\dagger\psi\psi\rangle\right] \equiv \Gamma_{12}(\mathbf{r},t)$, arises from particle-exchanging collisions between the condensate and thermal cloud, and will become clear later when defined in terms of collision integrals. To overcome the previously mentioned issues which come with the inclusion of the anomalous average, the analysis of Zaremba, Nikuni, and Griffin (ZNG) [59, 69], neglects the effect of the mean-field associated with the anomalous average, $\tilde{m}(\mathbf{r},t)$. Nonetheless, the role of the anomalous terms is partially taken into account in an implicit manner in the particle-exchanging collision terms.

The final theory is constructed such that, interaction effects are maintained in the chemical potential and excitation energies to first order in g but to second order, g^2 in the treatment of the collision integrals. In this limit the time dependent chemical potential takes the form

$$\mu_c(\mathbf{r},t) = -\frac{\hbar^2\nabla^2\sqrt{n_c(\mathbf{r},t)}}{2m\sqrt{n_c(\mathbf{r},t)}} + V_{\mathrm{ext}}(\mathbf{r}) + gn_c(\mathbf{r},t) + 2g\tilde{n}(\mathbf{r},t). \tag{2.31}$$

Equations (2.29), (2.30) and (2.31) are equivalent to a dissipative Gross-Pitaevskii equation for the condensate order parameter, $\phi(\mathbf{r},t)$

$$i\hbar\frac{\partial\phi(\mathbf{r},t)}{\partial t} = \left(-\frac{\hbar^2\nabla^2}{2m} + V_{\mathrm{ext}}(\mathbf{r}) + g[n_c(\mathbf{r},t) + 2\tilde{n}(\mathbf{r},t)] - iR(\mathbf{r},t)\right)\phi(\mathbf{r},t). \tag{2.32}$$

An important modification of this equation is the inclusion of a non-Hermitian dissipative/source term $R(\mathbf{r},t) \equiv \hbar\Gamma_{12}/2n_c \sim O(g^2)$, which allows the normalisation of the condensate wavefunction ϕ to change with time.
The equation of motion for the noncondensate atoms reads

$$\begin{aligned} i\hbar\frac{\partial\hat{\psi}}{\partial t} &= \left[-\frac{\hbar^2\nabla^2}{2m} + V_{\rm ext} + 2gn\right]\hat{\psi} - 2g\tilde{m}\hat{\psi} + g\phi^2\hat{\psi}^\dagger \\ &+ g\phi^*(\hat{\psi}\hat{\psi} - \tilde{m}) + 2g\phi(\hat{\psi}^\dagger\hat{\psi} - \tilde{n}) + g(\hat{\psi}^\dagger\hat{\psi}\hat{\psi} - \langle\hat{\psi}^\dagger\hat{\psi}\hat{\psi}\rangle), \end{aligned} \tag{2.33}$$

where $n = n_c + \tilde{n}$ is the total density.

The derivation of the kinetic equation for the noncondensate atoms follows from the pioneering work of Kirkpatrick and Dorfmann [56, 57] on uniform Bose gases, as discussed in [69]; here we summarise the main results. The aim of a kinetic approach is to use the microscopic properties of the system, i.e. the particle trajectories, to describe the macroscopic behaviour of the system. It is difficult to define a true phase-space distribution for a quantum mechanical particle because a particle of this type cannot have simultaneously well defined position and momentum, a consequence of the uncertainty principle. To bridge the link between the quantum mechanical operator for the noncondensate atoms, $\hat{\psi}$, to a probability distribution in phase-space, the Wigner distribution function is commonly used [175].

The Wigner distribution function $f(\mathbf{p},\mathbf{r},t)$ for an atom of momentum $\mathbf{p}$, at location $\mathbf{r}$, and at time t is defined as,

$$f(\mathbf{p},\mathbf{r},t) = \langle\hat{f}(\mathbf{p},\mathbf{r},t)\rangle = {\rm Tr}\tilde{\rho}(t,t_0)\hat{f}(\mathbf{p},\mathbf{r},t), \tag{2.34}$$

where $\hat{f}$ is a Wigner operator describing the dynamics of the noncondensate atoms,

$$\hat{f}(\mathbf{p},\mathbf{r},t) = \int d\mathbf{r}' e^{i\mathbf{p}\cdot\mathbf{r}'/\hbar}\hat{\psi}^\dagger\left(\mathbf{r}+\mathbf{r}'/2,t_0\right)\hat{\psi}\left(\mathbf{r}-\mathbf{r}'/2,t_0\right),$$

Tr denotes the trace of the density matrix (see Appendix B), and $\tilde{\rho}(t,t_0)$ satisfies the evolution equation

$$i\hbar\frac{d\tilde{\rho}(t,t_0)}{dt} = \left[\hat{H}_{\rm eff}(t),\tilde{\rho}(t,t_0)\right]. \tag{2.35}$$

The effective Hamiltonian of Eq. (2.35) is chosen to give the exact equation of motion for the noncondensate operator given by Eq. (2.33) and is split as $\hat{H}_{\rm eff}(t) = \hat{H}_0(t) + \hat{H}'(t)$,

such that the unperturbed HF term is defined

$$\hat{H}_0(t) = \int d\mathbf{r}\hat{\psi}^\dagger \left[-\frac{\hbar^2\nabla^2}{2m} + U_{\rm eff}(\mathbf{r},t) \right] \hat{\psi}, \tag{2.36}$$

with $U_{\rm eff}$ as defined in Eq. (2.27). The perturbation term arises from contributions of multiples of noncondensate operators. We do not write these contributions explicitly here but they can be found in Refs. [54, 59, 69]. A more detailed discussion of the treatment of the evolution of Eq. (2.35) was given in Ref. [69].

The identification of the function f allows the determination of nonequilibrium expectation values, such as the noncondensate density via the relation

$$\tilde{n}(\mathbf{r},t) = \int \frac{d\mathbf{p}}{(2\pi\hbar)^3} f(\mathbf{p},\mathbf{r},t). \tag{2.37}$$

Using Eq. (2.35), the equation of motion for f is given by

$$\begin{aligned} \frac{\partial f(\mathbf{p},\mathbf{r},t)}{\partial t} &= \frac{1}{i\hbar}{\rm Tr}\tilde{\rho}(t,t_0)\left[\hat{f}(\mathbf{p},\mathbf{r},t_0),\hat{H}_{\rm eff}(t)\right] \\ &= \frac{1}{i\hbar}{\rm Tr}\tilde{\rho}(t,t_0)\left[\hat{f}(\mathbf{p},\mathbf{r},t_0),\hat{H}_0(t)\right] + \frac{1}{i\hbar}{\rm Tr}\tilde{\rho}(t,t_0)\left[\hat{f}(\mathbf{p},\mathbf{r},t_0),\tilde{H}'(t)\right] \end{aligned} \tag{2.38}$$

The second term on the right hand side of Eq. (2.38) accounts for the change in the particle density due to the collisions. When no collisions are present, this term vanishes while the other term, the free-streaming operator, ensures that the distribution of particles is the same before and after evolution. This is the quantum analogue of Liouville's theorem in statistical mechanics, which states that the local density at a particular point in phase space stays constant with time, and hence no particles are being expelled or admitted. When collisions are present (which is generally the case), and assuming that the collisions time is negligible compared to the evolution timescale of the chosen mean-fields, the evolution of the distribution function $f(\mathbf{p},\mathbf{r},t)$, in the presence of a slowly varying external field $U_{\rm eff}(\mathbf{r},t)$ can be written as a kinetic equation, termed the quantum Boltzmann equation (QBE), see e.g. [176–178],

$$\frac{\partial f}{\partial t} + \frac{\mathbf{p}}{m}\cdot\nabla_{\mathbf{r}} f - (\nabla_{\mathbf{r}} U_{\rm eff})\cdot(\nabla_{\mathbf{p}} f) = C_{12}[f,\phi] + C_{22}[f], \tag{2.39}$$

where the free-streaming term has been expanded in terms of differentials in position, $\mathbf{r}$ and momentum, $\mathbf{p}$. The thermal excitations are assumed to be semiclassical within the HF approximation, i.e. an excitation with momentum $\mathbf{p}$ possesses energy $\tilde{\varepsilon}_i = p^2/2m + U_{\rm eff}(\mathbf{r},t)$. The collision term on the right hand side of Eq. (2.38) has been replaced by collision integrals representing the two types of collisions which can occur.

The collision integrals are written explicitly in terms of binary collisions between two

atoms (obeying Bose statistics), which are assumed to be uncorrelated before and after collision (molecular chaos hypothesis), resulting in scattering from initial to final states. Here $f_i \equiv f(\mathbf{p}_i, \mathbf{r}, t)$ is the single particle distribution function with f_i being the statistical factor for the destruction of a particle in state i, and $(1 + f_i)$ for the creation of a particle in state i.

It can be shown [69] that the resulting collision integrals are thus defined as:

$$\begin{aligned} C_{12}[f,\phi] &= \frac{4\pi}{\hbar} g^2 |\phi|^2 \int \frac{d\mathbf{p_2}}{(2\pi\hbar)^3} \int \frac{d\mathbf{p_3}}{(2\pi\hbar)^3} \int \frac{d\mathbf{p_4}}{(2\pi\hbar)^3} \\ &\times (2\pi\hbar)^3 \delta(m\mathbf{v}_c + \mathbf{p}_2 - \mathbf{p}_3 - \mathbf{p}_4) \delta(\varepsilon_c + \tilde{\varepsilon}_2 - \tilde{\varepsilon}_3 - \tilde{\varepsilon}_4) \\ &\times (2\pi\hbar)^3 [\delta(\mathbf{p} - \mathbf{p}_2) - \delta(\mathbf{p} - \mathbf{p}_3) - \delta(\mathbf{p} - \mathbf{p}_4)] \\ &\times [(f_2 + 1) f_3 f_4 - f_2 (f_3 + 1)(f_4 + 1)]. \end{aligned} \tag{2.40}$$

This refers to a collision involving one condensate atom with one noncondensate atom which results in atom transfer between the two subsystems.

Also

$$\begin{aligned} C_{22}[f] &= \frac{4\pi}{\hbar} g^2 \int \frac{d\mathbf{p_2}}{(2\pi\hbar)^3} \int \frac{d\mathbf{p_3}}{(2\pi\hbar)^3} \int \frac{d\mathbf{p}_4}{(2\pi\hbar)^3} \\ &\times (2\pi\hbar)^3 \delta(\mathbf{p} + \mathbf{p}_2 - \mathbf{p}_3 - \mathbf{p}_4) \delta(\tilde{\varepsilon} + \tilde{\varepsilon}_2 - \tilde{\varepsilon}_3 - \tilde{\varepsilon}_4) \\ &\times [(f + 1)(f_2 + 1) f_3 f_4 - f f_2 (f_3 + 1)(f_4 + 1)]. \end{aligned} \tag{2.41}$$

This refers to a collision involving two noncondensed atoms.

Each of these collision integrals involve a combination of phase space distributions representing the scattering amplitudes for the different possible collision processes. The scattering amplitude for a collision between two thermal atoms is given by $(f + 1)(f_2 + 1) f_3 f_4$, corresponding to two incoming particles in states 3 and 4 which collide, resulting in the final Bose enhanced states of the outgoing particles 1 and 2; the inverse process is also accounted for via $f f_2 (f_3 + 1)(f_4 + 1)$.

For a particle exchanging collision of the C_{12} type, there are two possible outcomes.

- An 'in' collision, denoted henceforth by C_{12}^{in}, in which a particle is scattered *into* the condensate and the scattering amplitudes are given in terms of the 3 thermal atoms which are involved with the collision via $(f_2 + 1) f_3 f_4$, with 3 and 4 representing two incoming thermal atoms colliding, resulting in an atom being transferred into the condensate, and a final Bose enhanced state of the outgoing thermal atom 2.

- An 'out' collision, denoted by C_{12}^{out} results in a particle being transferred *out of* the condensate with scattering amplitude given by $f_2 (f_3 + 1)(f_4 + 1)$, where the incoming thermal atom 2, collides with a condensate atom resulting in two outgoing thermal

atoms 3 and 4 in Bose enhanced states.

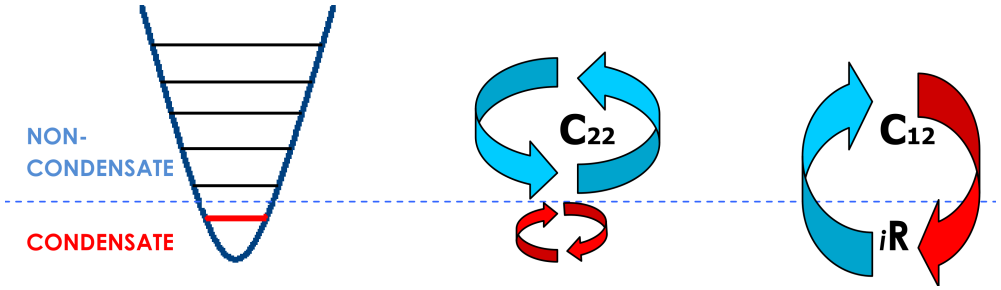

Figure 2.2: Schematic of the collision processes included in the ZNG formalism with the processes modelled by the dissipative Gross-Pitaevskii equation, (2.32), in red and those modelled by the quantum Boltzmann equation, (2.39) are shown in blue for clarity.

If the condensed and noncondensed subsystems are in local equilibrium, then $C_{12} = 0$. When they are out of equilibrium, this term acts to transfer atoms between the condensed and noncondensed parts of the system. Hence, C_{12} is coupled to the source term of Eq. (2.32), as

$$R(\mathbf{r},t) = \frac{\hbar}{2|\phi(\mathbf{r},t)|^2}\int \frac{d\mathbf{p}}{(2\pi\hbar)^3} C_{12}[f(\mathbf{p},\mathbf{r},t),\phi(\mathbf{r},t)]. \tag{2.42}$$

The delta functions of Eqs. (2.40) and (2.41) enforce conservation of energy and momentum. In particular those in the C_{12} term take into account that the condensate atoms have energy $\varepsilon_c = mv_c^2/2 + \mu_c$, and momentum $m\mathbf{v}_c$. However, only the C_{22} term conserves atom number. C_{12} by definition transfers atoms into and out of the condensate but, as a result of Eq. (2.42), the overall theory does conserve atom number.

Equations (2.32) and (2.39) are the closed set of ZNG equations for a condensate coexisting in a trap with a cloud of thermal excitations. A summary of the processes modelled by these equations is shown in the schematic of Fig. 2.2.

The presence of the condensate density $n_c(\mathbf{r},t)$ in the HF mean-field for the noncondensed atoms, and of the noncondensate density $\tilde{n}(\mathbf{r},t)$ in the mean-field for the condensate atoms, indicate that the two equations must be solved self-consistently. Due to the different nature of these equations, two very different numerical methods are required and we will give a detailed explanation of this in Chapter 4.

The underlying nature of the ZNG scheme is that it treats the condensate and noncondensate in qualitatively different ways. The condensate is treated as a quantum-mechanical wavefunction while the thermal atoms are treated within a semiclassical approximation and assumed to move within a HF potential. This theory is built on the difference between a large number of condensate atoms all occupying the same quantum state, and the

thermal atoms occupying many different states with low occupation probabilities, justifying the semiclassical treatment. It is assumed that the dominant thermal atoms in these systems have relatively high energies, and so the HF single particle spectrum gives a good approximation even for low energies [179]. The assumption is made in the derivation of the hydrodynamic Eqns. (2.29) and (2.30), that the variables of amplitude and phase vary slowly in space so that they can be expanded about $\mathbf{r}$ [59]. The consequence of this is that the formalism is unable to describe pronounced phase fluctuations of the condensate and therefore is likely to break down in the regime of critical fluctuations, i.e. very close to the transition temperature T_c in 3D systems, or over more extended temperature range in 1D/2D systems which exhibit enhanced phase fluctuations; in these regimes, other finite temperature approaches can be used. In the next section we briefly discuss a range of closely related methods which yield a description in terms of a classical multimode field which no longer describes only the condensate mode.

2.2.3 The stochastic GPE and classical field approaches

In *classical field* approaches, often referred to as c-field methods, the classical nature of the GPE is exploited for modelling all coherent modes of a finite temperature system (recently reviewed in [180, 181], see also [54] for an indepth review of finite temperature techniques). In these approaches, the assumption is made that at temperatures below T_c, there is a number of highly populated modes with momentum less than a particular value, $k_{\max}$. To obtain an initial condition, the general procedure is to expand the initial wavefunction into eigenstates with coefficients c_k (which are randomised under constraints due to the system) [180, 182],

$$\phi(\mathbf{r}, t = 0) = \sum_{k}^{k_{\max}} c_k \psi_k(\mathbf{r}). \tag{2.43}$$

This initial wavefunction is then propagated in time according to the usual GPE, Eq. (2.9). The nonlinearity of Eq. (2.9) ensures mixing between modes and equilibration to a classical thermal distribution, therefore, the initial condition is generally unimportant. In these approaches, the wavefunction $\phi(\mathbf{r}, t)$ no longer describes only the ground state mode of the system, as in the ZNG approach, but all highly occupied modes up to an momentum cut-off, $k_{\max}$. This momentum cut-off can either be imposed by the numerical grid used in numerical simulations or via a projector, as in the so-called Projected GPE (PGPE), which avoids problems due to aliasing, ensuring that only momentum conserving processes associated with the highly occupied modes are considered [183–185].

The low-lying modes capture *some* of the thermal cloud up to the cut-off; to additionally model the remaining thermal cloud, one may generalise the picture by coupling

these low-lying 'coherent' modes to a set of incoherent modes. This can be done via the stochastic GPE (SGPE), first derived by Stoof [186, 187] and subsequently Davis and Gardiner [188] arrived at a similar equation, in the limit where high-lying modes are treated as a heat bath (i.e. $C_{22} = 0$).

In Stoof's derivation of the SGPE, the probability distribution for the trapped Bose gas, $P[\Psi^*, \Psi, t]$, evolves according to a Fokker-Planck equation. The effects of the coherent, ϕ', and incoherent regions, ψ', are determined by using a Hartree-Fock type splitting of $P[\Psi^*, \Psi, t] = P_0[\phi'^*, \phi', t]P_1[\psi'^*, \psi', t]$: replacing this *ansatz* into the full Fokker-Planck equation and integrating over the noncondensate (condensate) degrees of freedom, lead to evolution equations for the low-lying (high-lying) modes. The high-lying thermal modes (incoherent region), when treated semiclassically, are found to evolve according to the quantum Boltzmann Eq.(4.2), where the Wigner distribution for the noncondensate field operator $\psi'(\mathbf{r}, t)$, is defined

$$f(\mathbf{p}, \mathbf{r}, t) = \int d\mathbf{r}' e^{-\mathbf{p}\cdot\mathbf{r}'/\hbar} \psi'(\mathbf{r} + \mathbf{r}'/2)\psi'^*(\mathbf{r} - \mathbf{r}'/2) = N(\mathbf{p}, \mathbf{r}, t) + \frac{1}{2}. \tag{2.44}$$

$N(\mathbf{p}, \mathbf{r}, t)$ is the thermal occupation of each mode and the addition of $1/2$ ensures that the field now contains quantum fluctuations as well as thermal as in Eq. (2.35). The fundamental difference between the collision integrals here and those used in the ZNG formalism expressed earlier, is the appearance of the multimode field ϕ' in place of the condensate wavefunction in Eqs. (2.40) and (2.41).

The source, $iR(\mathbf{r}, t)$ term in this scheme (associated with the same collision processes as the iR term in Eq. (2.32)) is defined as

$$\begin{aligned} R(\mathbf{r}, t) &= 2\pi g^2 \int \frac{d\mathbf{p}_2}{(2\pi\hbar)^3} \int \frac{d\mathbf{p}_3}{(2\pi\hbar)^3} \int \frac{d\mathbf{p}_4}{(2\pi\hbar)^3} \\ &\times \delta(\mathbf{p}_2 - \mathbf{p}_3 - \mathbf{p}_4)\delta(\varepsilon_c + \tilde{\varepsilon}_2 - \tilde{\varepsilon}_3 - \tilde{\varepsilon}_4) \\ &\times [f_2(f_3 + 1)(f_4 + 1) - (f_2 + 1)f_3 f_4], \end{aligned} \tag{2.45}$$

where $\tilde{\varepsilon}_i = |\mathbf{p}_i|^2/2m + V_{\rm ext} + 2g\langle|\phi'(\mathbf{r}, t)|^2\rangle$ is the Hartree-Fock energy of the thermal atoms. The strength of the collisions between the coherent and incoherent regions is given by the Keldysh self-energy which has the form

$$\begin{aligned} \hbar\Sigma^K(\mathbf{r}, t) &= -4\pi i g^2 \int \frac{d\mathbf{p}_2}{(2\pi\hbar)^3} \int \frac{d\mathbf{p}_3}{(2\pi\hbar)^3} \int \frac{d\mathbf{p}_4}{(2\pi\hbar)^3} \\ &\times (2\pi\hbar)^3 \delta(\mathbf{p}_2 - \mathbf{p}_3 - \mathbf{p}_4) \\ &\times \delta(\varepsilon_c + \tilde{\varepsilon}_2 - \tilde{\varepsilon}_3 - \tilde{\varepsilon}_4) \\ &\times [f_2(f_3 + 1)(f_4 + 1) + (f_2 + 1)f_3 f_4], \end{aligned} \tag{2.46}$$

where this term can be related to the iR term approximately via the fluctuation-dissipation theorem [186, 189, 190]

$$iR(\mathbf{r},t) \simeq -\left(\frac{\beta}{4}\right)\hbar\Sigma^{K}(\mathbf{r},t)[\hat{h}_0 + g|\phi'|^2 - \mu]. \tag{2.47}$$

Within these approximations, the corresponding evolution equation for the low-lying, coherent modes is [186, 189, 190]

$$i\hbar\frac{\partial\phi'(\mathbf{r},t)}{\partial t} = \left(1+\frac{\beta}{4}\hbar\Sigma^{K}(\mathbf{r},t)\right)\left[-\frac{\hbar^2}{2m}\nabla^2 + V_{\rm ext}(\mathbf{r}) + g|\phi'(\mathbf{r},t)|^2 - \mu\right]\phi'(\mathbf{r},t) + \eta(\mathbf{r},t). \tag{2.48}$$

This is typically referred to as the stochastic GPE (SGPE) (a similar form is given by Davis and co-workers [180, 188] (SPGPE)). Here $\eta(\mathbf{r},t)$ is the noise term which has Gaussian correlations and the presence of which provides a 'seed' which can initiate condensate growth (a restriction of mean-field theories is their inability to describe this).

An important observation is that dynamical equilibrium is reached within this theory since an equal combination of 'in' and 'out' collisions between the thermal cloud and condensate will not cause the source term of Eq. (2.47) to become zero, as it does in the dissipative GPE of the ZNG formalism, because in Eq (2.46) such inverse processes are added to each other. The application of this approach involves averaging over many numerical realisations of the noise in order to generate an ensemble average with each numerical realisation modelling in some sense a single experimental run [113, 191].

One important difference between ZNG and the aforementioned methods, is that within the ZNG formalism, the condensate and noncondensate are treated as two distinct parts while, the c-field operator used in these techniques describes the coherent, classical modes which include, but are not restricted to, the condensate mode. Another key difference is that more often than not, approximations are made on the thermal cloud dynamics, hence, the important 'back action' of the full thermal cloud on the condensate is not fully accounted for.

In the present chapter we have stressed the importance of including finite temperature effects when modelling weakly interacting atomic condensates, however, interesting effects can also be modelled within the GPE formalism. In particular, in the low temperature regimes of recent experiments involving solitons [84–86], the most dominant decay mechanism is due to the presence of anharmonicities in the trapping potential, therefore in Part II of this thesis, we describe, using the GPE, a novel long-range interaction between solitons which is mediated by sound emission.

The remainder of this thesis, Part III, focusses on solving the coupled ZNG equations

to analyse finite temperature effects on vortex dynamics (Chapter 5) and Josephson effects (Chapter 6). We begin this part by giving a detailed explanation on the numerical scheme used to solve these equations in Chapter 4.

Part II

$T = 0$: Sound Mediated, Long-Range Interactions between Dark Solitons

Chapter 3

Sound Mediated Dark Soliton Dynamics

Recent experiments have been able to generate appropriate low-temperature conditions in quasi-1D geometries enabling the observation of one or more (undamped) dark soliton oscillations in a harmonically-confined condensate [84–86] as predicted at the mean field level [78, 94, 192]. In general, the presence of the axial confinement in these experiments breaks the integrability of the system, rendering the soliton unstable to sound emission along its axis of propagation, inducing it to decay [94, 106, 193]. Earlier work on this topic has revealed the crucial role of the harmonicity of the underlying trap in stabilising the propagating soliton against decay at low temperatures via continuous cycles of soliton-sound interactions [106, 107], when all other decay mechanisms are suppressed for the timescales of interest [67, 93, 95–98, 100, 102, 104, 191, 194, 195].

In this chapter, we show that soliton-sound interactions also play a key role in the dynamics of two or more solitons in an inhomogeneous atomic condensate, and we identify optimal realistic experimental conditions for observing such an effect. In particular, we analyse the motion of solitons oscillating within either a single harmonically-confined condensate or different spatially-separated sub-regions of a condensate and conclude that, within mean field theory, dark solitons can interact via the emission/absorption of sound waves over a long range, without ever approaching very close to each other. We refer to this interaction mechanism as sound-mediated dark soliton interactions, and suggest an experiment that could probe such an effect.

3.1 Theoretical model

In the limit of strong transverse confinement, when the following conditions are satisfied: $\mu_{3D} < \hbar\omega_\perp$, $k_B T \ll \hbar\omega_\perp$ and $\omega_z \ll \omega_\perp$, where μ_{3D} is the 3D chemical potential, $\omega_\perp$ and

ω_z are the transverse and axial trapping frequencies, k_B is the Boltzmann constant and T is the temperature of the system, a Bose-Einstein condensate can be thought of as being effectively one-dimensional (1D). In this regime, we can model our system by a single complex wavefunction, $\psi(z,t)$ which obeys the 1D Gross-Pitaevskii equation (GPE):

$$i\hbar\frac{\partial\psi}{\partial t} = \left(-\frac{\hbar^2}{2m}\frac{\partial^2}{\partial z^2} + V(z) + g|\psi|^2 - \mu\right)\psi \ , \tag{3.1}$$

where m is the atomic mass, μ is the 1D chemical potential and $V(z)$ is the longitudinal external confining potential. The coefficient g parametrises the interatomic interactions and in 1D takes the form $g = (4\pi\hbar^2 a/m)/2\pi l_\perp^2$, where a is the 3D s-wave scattering length; here $l_\perp = \sqrt{\hbar/(m\omega_\perp)}$ is the harmonic oscillator length in the transverse direction. A dark soliton propagating through a BEC, along the z direction, with speed v_s has the form [196]

$$\psi(z,t) = \psi_{bg}(z)e^{-i\mu t/\hbar}\left(\gamma\left[\tanh\left(\frac{\gamma(z-v_s t)}{\xi}\right)\right] + i\left(\frac{v_s}{c}\right)\right) \tag{3.2}$$

where $\gamma = \sqrt{1-(v_s/c)^2}$ and $\psi_{bg}(z)$ is the wavefunction of the background condensate. It is characterised by a local dip in the density, $n(z) = |\psi(z)|^2$ and a phase slip, S, across the dip's centre defined by $v_s/c = \sqrt{(1-n_d/n)} = \cos(S/2)$, where n_d is the density dip resulting from the soliton and $c = \sqrt{\mu/m}$ is the Bogoliubov speed of sound.

3.1.1 Soliton energy

The energy of the soliton, E_s, turns out to be a useful theoretical parameter for modelling its dynamical properties. It is defined here in the conventional way of calculating the energy of the BEC in the region around the soliton and subtracting the energy of the condensate in this region if no soliton were present [82]. We choose this region, in order to encapsulate the full extent of the soliton, as five healing lengths [107], $\xi = \hbar/(\sqrt{mn_0 g})$, either side of the soliton centre, z_s, with n_0 denoting the peak background condensate density. Thus,

$$E_s = \int_{z_s-5\xi}^{z_s+5\xi}\epsilon[\psi]dz - \int_{z_s-5\xi}^{z_s+5\xi}\epsilon[\psi_{bg}]dz, \tag{3.3}$$

where

$$\epsilon[\psi] = \frac{\hbar^2}{2m}|\nabla\psi|^2 + V|\psi|^2 + \frac{g}{2}(|\psi|^2 - n_0)^2. \tag{3.4}$$

This expression has been used in previous work [99, 106, 107, 197] where it is correctly quoted in [107]. For a homogeneous condensate, $|\psi_{bg}|^2 = \text{constant} = n_0$, and the energy

of the soliton simplifies to the well-known expression [82]

$$E_s = \frac{4}{3}\hbar n_0 c \left[1 - \left(\frac{v_s}{c}\right)^2\right]^{\frac{3}{2}}. \tag{3.5}$$

Therefore, a black soliton, which is a stationary soliton, has more energy than a less deep soliton which is in motion.

We generate each soliton in our simulations locally by multiplying the condensate wavefunction by the soliton form given by (3.2) obtained from the imaginary time evolution of the GPE, via Eq. (3.1). We propagate the GPE using a 4th order Runge-Kutta method (Error $= O(\Delta t^4)$) on a discrete grid with typical spatial step $\Delta z = 0.03 l_z$ and time step $\Delta t = 0.0001\omega_z^{-1}$.

All simulations in this chapter are done in terms of the dimensionless form of Eq. (3.1) (see Appendix A.2 for details), obtained by scaling all physical parameters to harmonic oscillator units; in our present simulations we have chosen a dimensionless 1D coupling constant $g = 0.048\hbar\omega_z l_z$. Our choice was originally motivated by a recent experiment [85] with ^{87}Rb atoms in a harmonic trap with transverse confinement $\omega_\perp = 2\pi \times 408$ Hz. The longitudinal harmonic frequency in Secs. 3.2 and 3.3 was also chosen from that experiment, namely $\omega_z = 2\pi \times 63$ Hz.

3.2 Soliton interactions in a harmonic trap

In a homogeneous background, solitons have the unique ability to remain unchanged in shape and speed during a collision, apart from a slight change in their respective phases [198]. In general, the stability of the soliton depends on the integrability of the governing equation of motion: when the integrability is broken, the soliton becomes unstable and dissipates its energy acoustically. One such case arises when a soliton moves through the inhomogeneous background induced by a trapping potential $V(z)$; in that case, the soliton has the tendency to emit energy to the background in the form of sound waves, an effect visible as ripples in the density profile of the condensate.

We are interested here in exploring the importance of such an effect to the interaction of two solitons. First we give a brief overview of the dynamics in a single trap.

3.2.1 Single soliton in a harmonic trap

In Fig. 3.1 (Left) we have plotted the density of a condensate in a harmonic trap when it contains a central soliton ($z_0 = 0.0$) of three different speeds, $v_s = 0.3c,\ 0.5c,\ 0.7c$. As the speed of the soliton increases, the density dip decreases (see inset of this plot for clarity), this in turn means that during its motion it can probe wider regions of the trap before

it is reflected back in the other direction. This oscillating motion can be seen in Fig. 3.1 (Right), with the larger amplitude oscillations corresponding to the faster solitons.

As is well-known, if there is just one soliton propagating in a harmonic trap, it perturbs the inhomogeneous background motion, setting up a dipole mode, but it also periodically reabsorbs the sound emitted by its own motion [106]; the resulting oscillation exhibits a beating effect due to the different oscillation frequencies of the soliton ($=\omega_z/\sqrt{2}$) [94, 98, 99, 102, 106, 107, 192, 193, 199–202] and the induced background dipolar motion of the condensate ($=\omega_z$). This beating effect can be seen as small modulations on top of the soliton trajectories in Fig. 3.1 (Right).

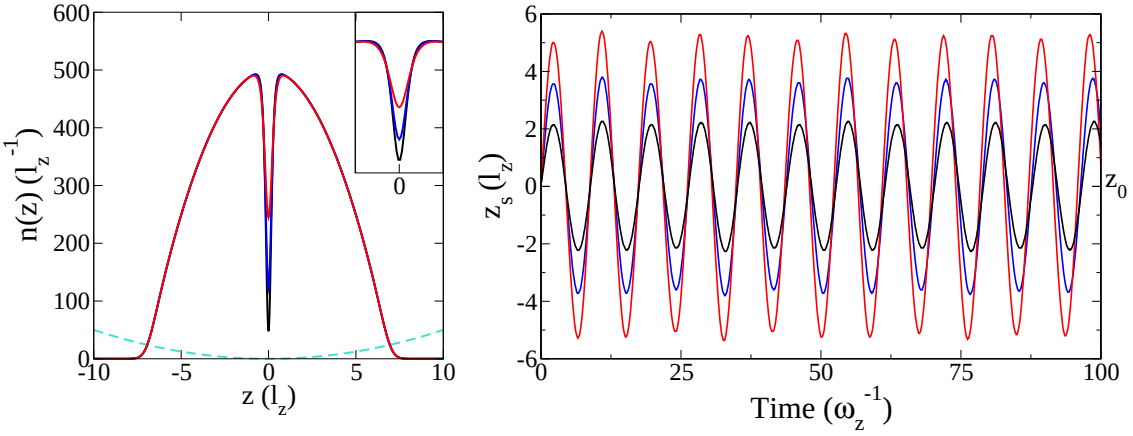

Figure 3.1: Motion of a single soliton in a harmonically trapped condensate. Left: (Main figure) Harmonic trap potential (dashed cyan) and density of condensate containing a single soliton of speed $v_s = 0.3c$ (black), $v_s = 0.5c$ (blue) and $v_s = 0.7c$ (red) with initial position $z_0 = 0.0$. (Inset) Zoomed plot around $z = 0.0$ in order to see soliton depths. Right: Position of these solitons vs. time. $\mu = 25\hbar\omega_z$.

3.2.2 Identical solitons in symmetric setup

Previous theoretical and experimental work [85, 105] has revealed that two identical, low speed, grey solitons displaced equally from the bottom of the harmonic trap and travelling towards each other, are reflected or pass through each other depending on their kinetic energies, indicating that soliton-sound interactions have, at most, a minor effect on their mutual dynamics. Although very small in magnitude, such modulations are actually present even in that context and our simulations reveal such modulations. In Fig. 3.2 (Top) we plot a space time plot of two identical solitons placed at equal distances from the centre of a harmonic trap $z_L = 3l_z$ and $z_r = -3l_z$ (where L and R denote the soliton beginning in the left and right part of the trap), such that they span the depth of the condensate at that point and when time evolution begins, the solitons move towards each other. The space time plot shows us the presence of sound in the system and on the bottom

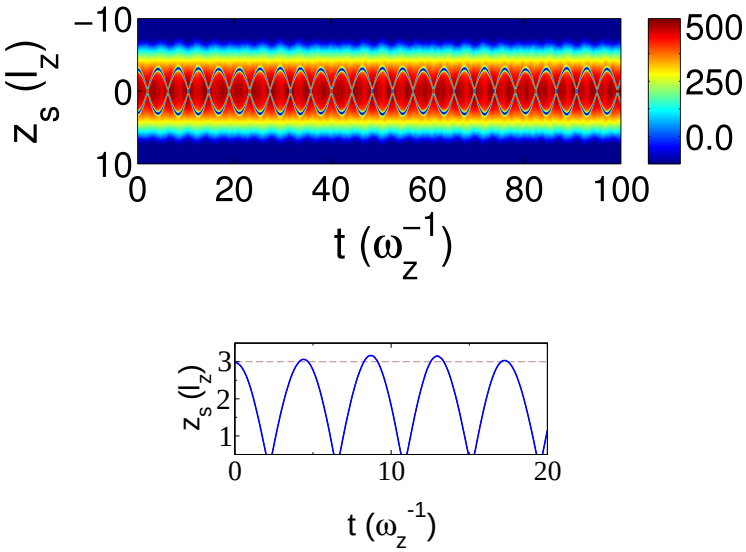

Figure 3.2: Soliton dynamics. Two identical grey solitons placed at equal distance from the centre of the harmonic trap, $z_L = -z_R$, and moving towards each other. Top: Space-time plot of density $|\psi|^2$, showing the soliton dynamics in the harmonic trap. Bottom: Zoomed plot of soliton trajectory showing modulations in the amplitude of oscillation for the soliton beginning at position z_R, where the soliton position is defined as the point at which the soliton is minima. Dotted line at initial z_R to show amplitude oscillations.

part of this figure we have plotted a proportion of this plot for the soliton position in order to see the modulations on top of the solitons oscillations. The effect is only slight in this case. However, this effect does become significant in the case of *non-identical* solitons initially located at non-symmetric locations within a single harmonic trap as discussed below.

3.2.3 Non-identical solitons

In particular, we consider the case of two solitons of speeds $v_L = 0.3c$ and $v_R = 0.1c$ at locations $z_L = -3l_z$ and $z_R = 0$ respectively (see Fig. 3.3). Each grey soliton moves from its initial position, in the same direction in this case, with each emitting sound waves of positive and negative amplitude in counter-propagating directions. The solitons absorb and dissipate sound at *different rates*, as each soliton re-interacts both with the sound it has emitted and with sound emitted by the other soliton. This process, combined with periodic soliton collisions, leads to a much more pronounced modulation of the soliton oscillations than encountered in the case of a single soliton in a harmonic trap (whose corresponding amplitude modulation would typically be a few percent of its initial amplitude [197]).

This effect is shown clearly in Fig. 3.3 (Right): in particular, the fast soliton, initially imprinted away from the trap centre, gains energy, thereby exhibiting oscillations of decreasing amplitude during the initial time period, $t < 70\omega_z^{-1}$. This energy becomes

available from the sound emission originating from the motion of the slower soliton, which in turn exhibits a small increase in its oscillation amplitude; at later times, the change in the relative phase of the two soliton oscillations leads to a reversal of the direction of the energy flow between them. Clearly, however, their mutual energy exchange does not lead to a net decay within a single harmonic trap.

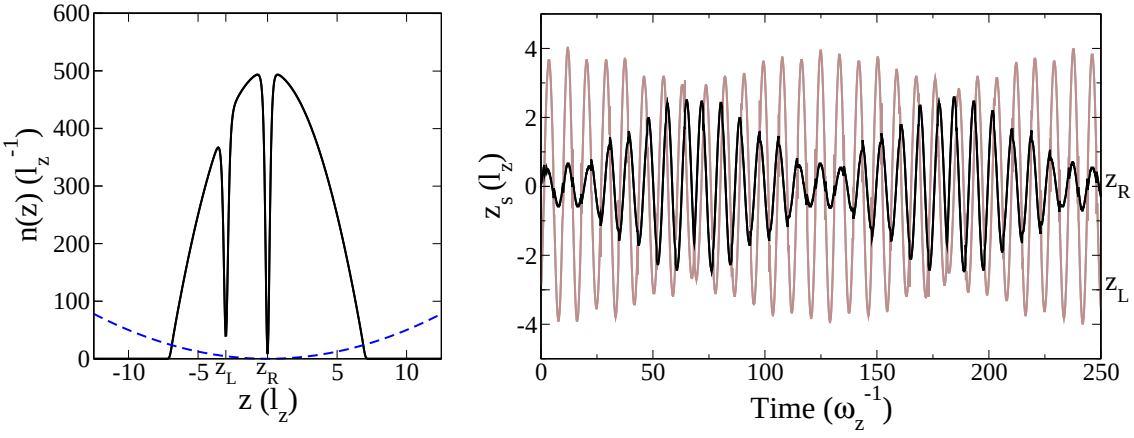

Figure 3.3: Motion of two non-identical dark solitons in a harmonically trapped condensate. Left: Density (black) and potential (dashed blue). Right: Position of left (solid, grey) and right soliton (solid, black) vs. time. (Initial parameters: $z_L = -3.0l_z$, $v_s^L = 0.3c$ and $z_R = 0.0l_z$, $v_s^R = 0.1c$, $\mu = 25\hbar\omega_z$).

However, a more detailed understanding of this process is complicated by the fact that there are two simultaneous competing effects: soliton-soliton collisions [198] and soliton-sound interactions [106], and it is hard to distinguish between the two in this context. In order to isolate these two effects and demonstrate the crucial role of soliton-sound interactions in the coupling of two solitons, we now move to a modified geometry which enables us to restrict the motion of the two solitons in two spatially separated traps. By ensuring that the condensate spans both traps, sound waves can still transfer between the traps and so the solitons can still exchange energy.

We choose to work in a regime of very weak coupling where there is a finite density connecting the two wells. This means that Josephson oscillations are suppressed on our observational timescales and the motion between the two wells is purely hydrodynamic rather than tunnelling (see Chapter 6 for analysis of both Josephson oscillations and hydrodynamic transport in double well traps).

3.3 Soliton interactions in a double harmonic trap

We now consider two solitons on opposite sides of a condensate confined in an idealised double-harmonic potential defined by

$$V(z) = \begin{cases} m\omega_z^2(z+z_0)^2/2 & z < 0 \\ m\omega_z^2(z-z_0)^2/2 & z \geq 0 \end{cases} \tag{3.6}$$

where the value of z_0 identifies both the location of the two density minima and the height of the potential at $z = 0$, via $V_0 = m\omega_z^2 z_0^2/2$, which acts as a 'barrier' between the neighbouring harmonic traps. By changing the height of the barrier between the two traps we can either allow or disallow contact between the two condensates, an effect controlled by the ratio of (V_0/μ). Corresponding initial density profiles with (solid) and without (dashed) contact between the two sides of the well are shown in Fig. 3.4. To demonstrate the energy transfer due to sound-mediated soliton interactions, we initially consider a stationary black soliton at the centre of the right well ($z_R = 7.5l_z$). Choosing a moving (grey) soliton of speed $0.3c$ at the centre of the left trap ($z_L = -7.5l_z$), we can study how the right (black) soliton is perturbed by the sound energy emitted by the soliton in the left trap.

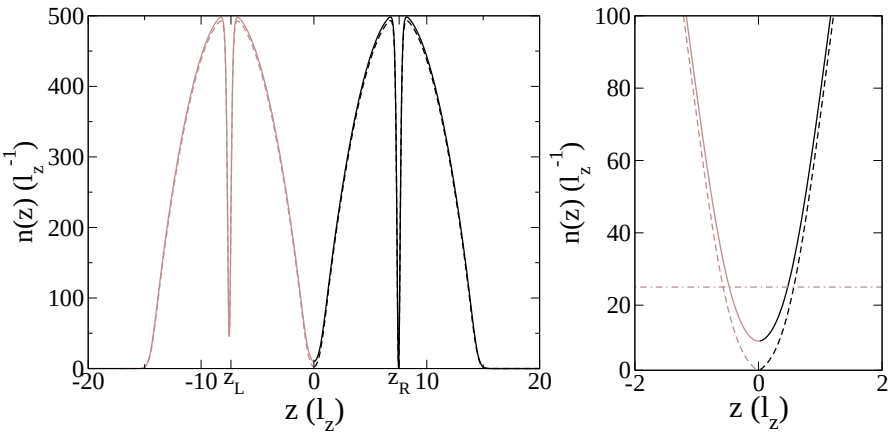

Figure 3.4: Left: Density profiles of a condensate in a double harmonic potential for the distinct cases of no contact i.e. zero density at $z = 0$ ($V_0/\mu = 1.62$, dashed, brown/grey and black line) or contact ($V_0/\mu = 1.125$, solid, brown/grey and black line) between the two wells. Right: Zoomed profile of the central region, with the left (right) well region indicated by brown/grey (black) lines. The chemical potential μ is indicated by the brown/grey dot-dashed line. The two solitons are initially defined by $z_L = -7.5l_z$, $v_s^L = 0.3c$ and $z_R = 7.5l_z$, $v_s^R = 0.0c$.

3.3.1 Identity reversal

Fig. 3.5 plots the paths of the solitons in the two distinct cases of $V_0/\mu = 1.125$ (solid lines) and $V_0/\mu = 1.62$ (dashed). The position of the soliton in the right well is plotted

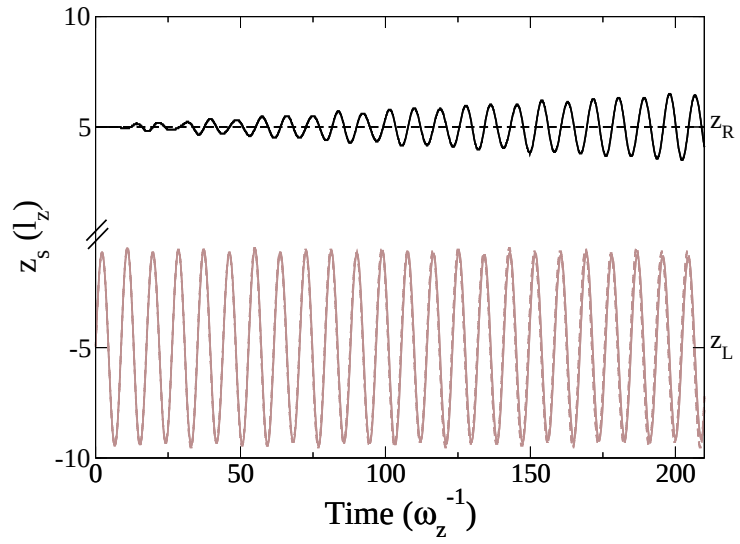

Figure 3.5: Comparison of soliton dynamics in a double harmonic trap for the set-up of Fig. 3.4. for $V_0/\mu = 1.62$ (dashed lines) and $V_0/\mu = 1.125$ (solid lines). Initial soliton positions indicated by z_L and z_R with brown/grey (black) lines indicating the soliton in the left (right) well of the double harmonic trap.

above the position of the soliton in the left (this remains true for the remainder of this paper unless otherwise stated). When $V_0/\mu = 1.62$ the black soliton in the right trap remains stationary as the sound emitted by the moving soliton in the left trap cannot propagate across the barrier (the condensate density is locally zero there) - see dashed (black) line at top of Fig. 3.5. On the contrary, when $V_0/\mu = 1.125$, the sound entering the right well from the left causes the initially black soliton to oscillate (see solid (black) line at the top of Fig. 3.5). In this case, the $0.3c$ in the left trap also becomes affected: as it moves and radiates sound waves, part of its energy which remains confined in the left trap is reabsorbed by the soliton, but some escapes to the right trap and disturbs the initially stationary soliton. However, as the black soliton starts to oscillate in the right trap, it also starts radiating sound, some of which is transmitted back across the barrier which can then be absorbed by the left soliton.

This process of emission, reabsorption and mutual sound exchange between the two solitons continues and results in a periodic reversal of their characteristics. This effect is clearly shown in Fig. 3.6. Note that when the soliton in one well is moving the fastest, its amplitude of oscillation is at a maximum, and the soliton in the other well is stationary (its depth is maximum i.e. it spans the full depth of the condensate), and vice versa.

Energy exchange

To get a better understanding of this effect, we now focus on the respective soliton energies, displayed for different temporal extents in Fig. 3.7. Focusing initially on the 'short'

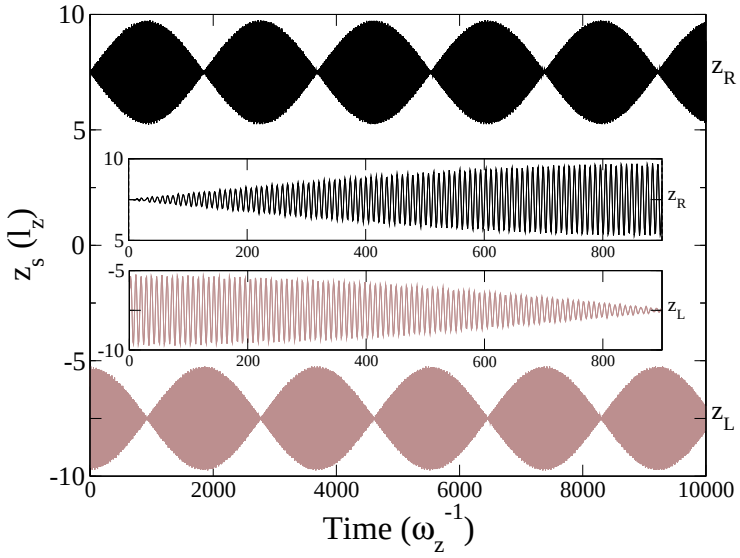

Figure 3.6: Soliton periodic 'identity-reversal' via energy-transfer cycles: Dynamical evolution of the solitons of Fig. 3.5 for $V_0/\mu = 1.125$ over a prolonged period; insets highlight individual soliton oscillations.

timescale ($\sim 200\omega_z^{-1}$) in Figs. 3.7 (a) and (b), we find that for $V_0/\mu = 1.62$, the energy of the black soliton in the right trap remains constant. The left soliton with $v_s \neq 0$ moves through the harmonic background, loses energy, but this energy is periodically reabsorbed, hence the soliton undergoes beating but exhibits no net decay, as shown by the dashed, grey curve (Fig. 3.7 (b)). The case $V_0/\mu = 1.125$ is shown by the solid lines: the initially black soliton loses energy (Fig. 3.7 (a), solid black), and the soliton in the left trap gradually increases its energy while still undergoing modulations. Looking at the energy of these solitons over a longer period (Fig. 3.7 (c)), we notice that the energy is transfered back and forth between each soliton; however this process is still modulated by interactions between each soliton and the sound field generated by its *own* motion (Fig. 3.7 (c), inset).

Until now, we have shown how the energy dissipated by a moving soliton in the left trap affects an initially stationary soliton in its neighbouring trap. This energy transfer occurs also when both solitons are moving: Fig. 3.8 shows the trajectories of two solitons of initial speed $v_s^L = 0.3c$ and $v_s^R = 0.1c$ respectively, placed in the same double trap harmonic geometry, with energy exchange between the two wells enabled by $V_0/\mu = 1.125$. In this case (brown/grey lines), we observe very similar features to those reported earlier (black lines), with the periodic oscillation of the two solitons now restricted to the range between the initial minimum and maximum amplitudes of the two solitons (i.e. never actually leading to instantaneous localisation).

The effect shown here is closely related to the parametric driving of a dark soliton. In particular, in [99] it was reported that appropriate external driving at the edge of a

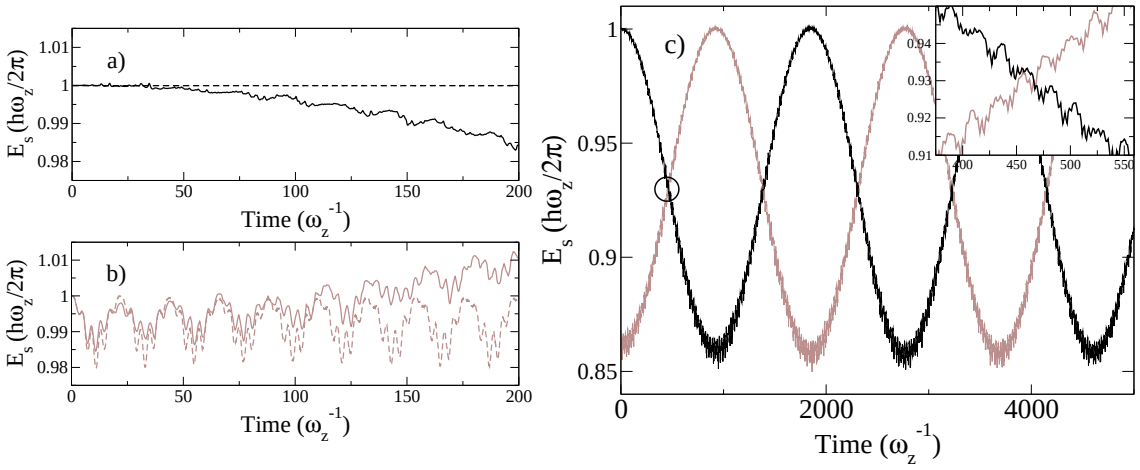

Figure 3.7: Soliton energy, E_s (renormalised by their original values), as a function of time for $V_0/\mu = 1.62$ (dashed lines) and $V_0/\mu = 1.125$ (solid) for the (a) right (black) or (b) left (brown/-grey) solitons of Fig. 3.4. (c) Longer time energy evolution (renormalised by the initial energy of the *black* soliton) for $V_0/\mu = 1.125$. Inset: Evolution around $t = 450\ \omega_z^{-1}$, highlighting the energy beating mechanism due to the interactions of each soliton with their own emitted sound waves.

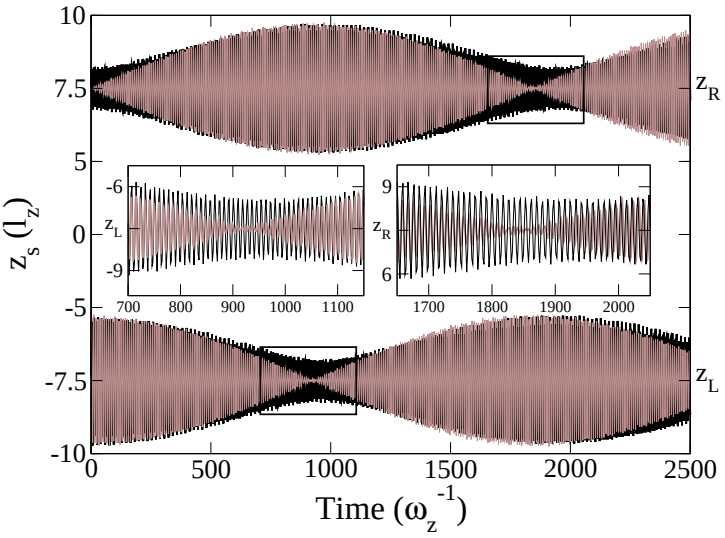

Figure 3.8: Energy transfer cycles for two non-identical initial grey solitons in a double harmonic trap with $v_s^L = 0.3c$ and $v_s^R = 0.1c$ (black) vs. corresponding case of Fig. 3.6 with $v_s^R = 0$ (brown/grey) for $V_0 = 1.125\mu$. Insets: zoomed position plots after the first half and full completed cycles.

harmonically-confined condensate (and outside the region of oscillation of a dark soliton) could lead to a controlled change in the energy of a single dark soliton placed within the condensate. In the idealised case considered here (no additional damping mechanisms), this could lead to periodic oscillations between the original state of the soliton and a black soliton. This effect requires the existence of a background density modulation oscillating at a frequency distinct to that of the soliton under consideration. In the case presented here, the motion of the soliton in the other well acts as a generator of sound waves, which

propagate through the barrier and are seen by the soliton under consideration as the required modulation of its background density. As a result, in each well of our current double harmonic geometry, the distinct frequency between the moving soliton and the sound wave incident onto it from the motion of the soliton in the other trap lead to the necessary beating modulation which changes its respective energetic/motional state. It has also been previously found that the direction of energy transfer from the soliton to the background sound field (i.e. energy emission from the soliton) or from the sound field to the soliton (energy absorption) depends critically on the relative phase of the oscillations of the soliton and the background sound field [203]; when the soliton leads the background sound mode (as happens in the right well), then the soliton sheds energy into the sound field, whereas soliton oscillations lagging behind the sound field (as in the left well) lead to energy absorption. As the process continues, the relative phases change between each individual soliton and the background sound mode, leading to a reversal of the energy emission/absorption cycles between the two solitons.

By changing the ratio between V_0 and μ we can control the amount of energy which can pass between the wells, either speeding it up ($V_0 < \mu$), slowing it down ($V_0 > \mu$) or stopping the contact altogether, ($V_0 \gg \mu$). To speed up the rate of energy transfer we choose a value for V_0 such that $V_0/\mu = 0.98$. Fig. 3.9 compares the trajectories of solitons in this trap geometry when they are alone or when there is another soliton in the other well of the trap. It is apparent from the bottom, black oscillations that a moving soliton alone in this trap geometry will start to lose energy and dissipate. However, the addition of a second soliton into the other well of the trap results in energy transfer between solitons and again characteristic reversal.

The perfect energy transfer between the solitons is more apparent if one plots the position of the left soliton against that of the right soliton at different time periods during their coupled evolution. Fig. 3.10 (top) displays such a sequence of 8 images, each corresponding to a temporal duration of approximately one soliton oscillation in the trap, i.e. $\tau = 2\sqrt{2}\pi\omega_z^{-1}$, with the bottom figure highlighting the times around which these images were taken: initially (top left image) the left soliton amplitude changes continuously from approximately $-9l_z$ to $-5l_z$ and back (oscillating about its initial value of $-7l_z$), while the right soliton is fixed at $z_R \sim 7l_z$, thus generating a horizontal profile. The gradual energy exchange between the two solitons results in this feature becoming more spherical (progression through bottom left to top right images), with the right soliton amplitude increasing at the expense of the left one; their features are perfectly reversed from their initial configuration after a time $t \approx 435\omega_z^{-1}$ (leading to a vertical profile), indicating that the two solitons have entirely exchanged their properties. This trend continues periodically, with the bottom right image revealing that the left soliton once again oscillates with its initial maximum amplitude, while the right one becomes (for a short period of

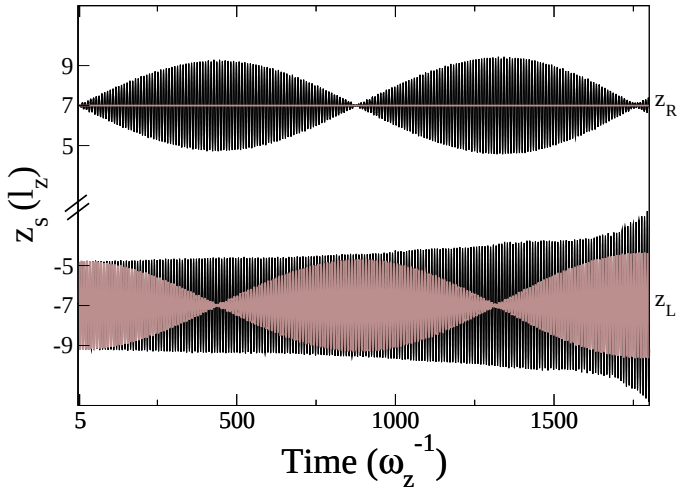

Figure 3.9: Soliton Dynamics for solitons in a double well trap where $V_0/\mu = 0.98$. Top oscillations: Brown/grey line is the path of an initially $0.0c$ soliton in the right well of the double trap geometry when there is no other soliton in the side of the trap. Black line is the path of an initially $0.0c$ soliton when there is an initially $0.3c$ soliton in the other well of the double trap geometry. Bottom oscillations: Black line is the path of an initially $0.3c$ soliton when there is no other soliton in the condensate. Brown/grey line is the path of the initially $0.3c$ soliton when there is also an $0.0c$ soliton in the other well of the trap. Where $V_0 = 24.5\hbar\omega_\perp$.

time) stationary. However, one can see from the brown/grey line in the bottom of Fig. 3.9 that the maximum amplitude of oscillation is actually increasing with time (see the much increased amplitude of the third envelope at $t \sim 1800\omega_z^{-1}$ in comparison to the first at $t = 0\omega_z^{-1}$). This indicates that although for $V_0/\mu = 0.98$ i.e. $V_0/\mu < 1$, the rate of energy transfer is higher, it results in an imperfect energy transfer between the two solitons after a few cycles which later result in the decay of both solitons due to the anharmonicity in the region of the barrier. Now we wish to carry out analysis on the energy transfer for the case in which the two solitons in the double well geometry demonstrate perfect characteristic reversal which continues on a much longer timescale (Fig. 3.5 shows it up until $t = 10000\omega_z^{-1}$).

To quantify the sound-mediated energy transfer, we monitor how quickly the (initially black) soliton in the right trap moves as a function of the initial speed v_s^L of the soliton in the left trap. This is shown in Fig. 3.11 (a), from which it is apparent that the larger v_s^L is, the larger the resulting oscillations of the initially stationary soliton. This arises physically because a faster left soliton is a shallower one, which probes a broader range in the (left) harmonic trap, i.e. experiences more of a gradient in the medium density and therefore emits more energy in the form of sound waves which are thus captured faster by the soliton in the right well.

Parallel to this, the resulting motion of the right soliton leads to its own emission-absorption cycles, which lead to the observed modulation of its own trajectory, an effect

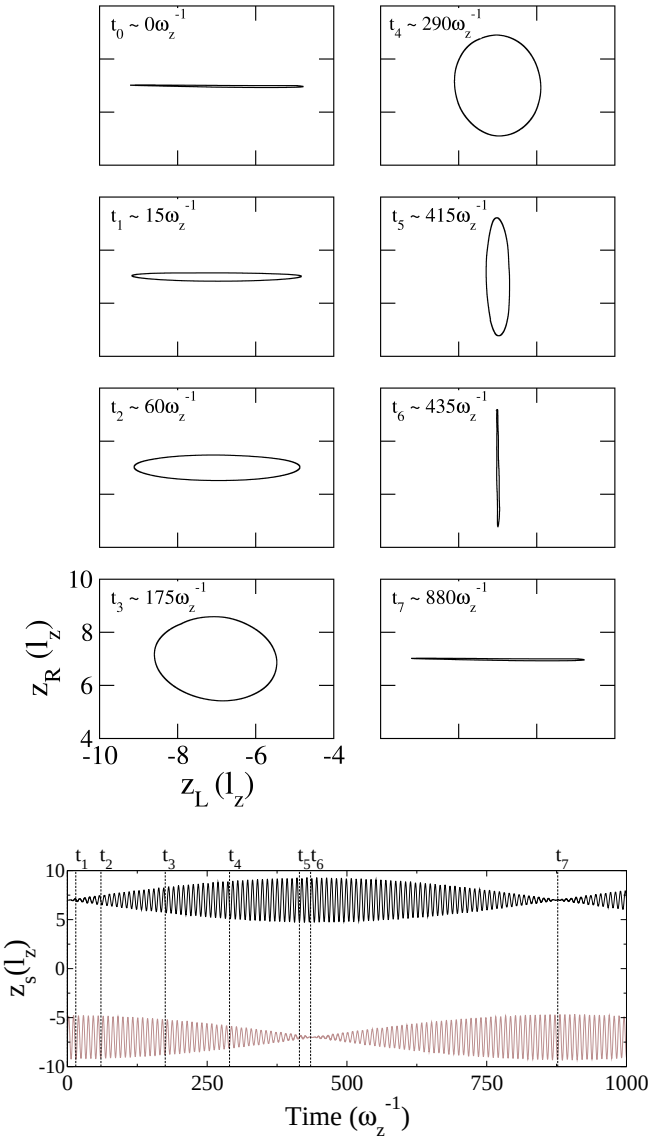

Figure 3.10: Characteristic snapshots of the soliton position in the left trap, z_L, against that in the right trap, z_R, at various time intervals (top images), as highlighted in the position plot (bottom), indicating the complete interchange of the motional properties of the two solitons. Note the different parameters here from those of Fig. 3.6, with $V_0/\mu = 0.98$ and $z_0 = 7l_z$, leading to an approximate doubling of the rate of energy exchange between the two wells, due to the decrease in the distance between their respective minima.

which is enhanced with larger amounts of incident energy from the left well.

To quantify this further, we investigate how the time it takes for the soliton in the right trap to reach a given (arbitrary) point shown by the dashed line in Fig. 3.11(a) depends on the initial speed of the left soliton v_s^L. Fig. 3.11 (b) shows that $\tau = (1/v_s^L)l_z$. Fig. 3.11 (c) shows that the largest oscillation amplitude of the soliton in the right trap, arising after a few tens of oscillations and a timescale $\sim$ few $100\omega_z^{-1}$, increases linearly

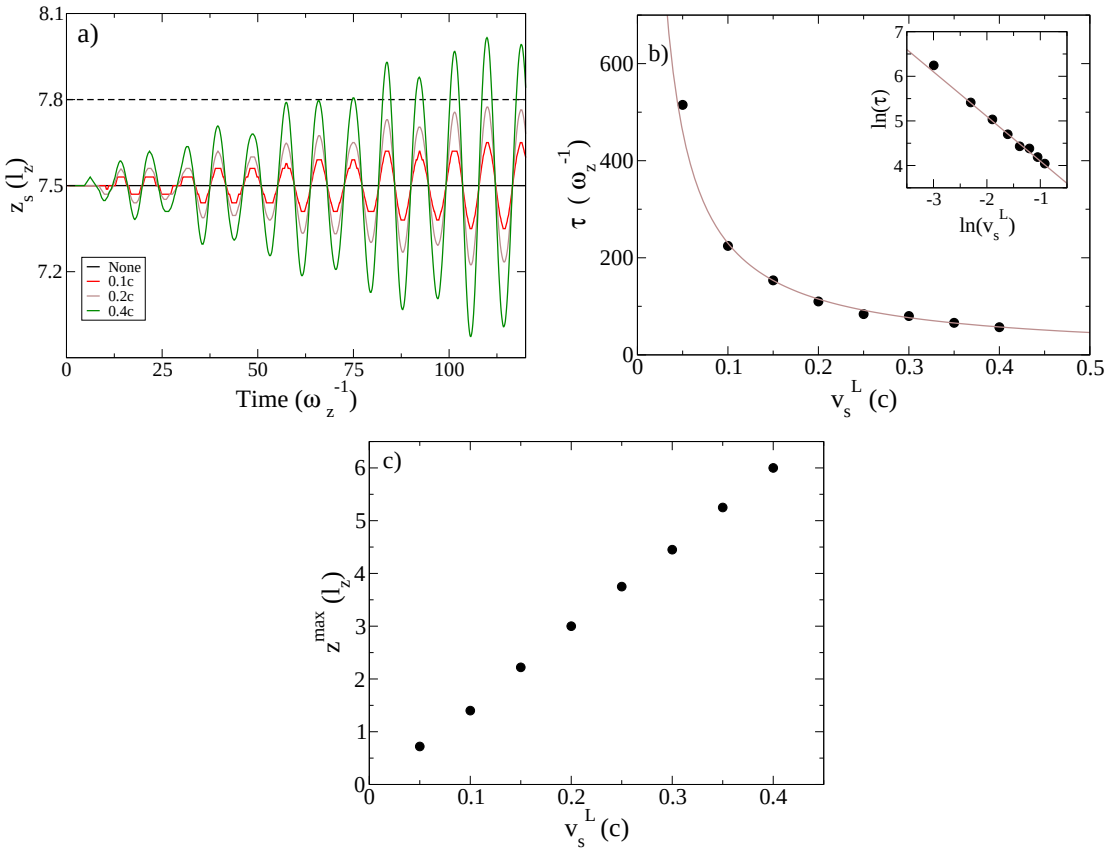

Figure 3.11: (a) Temporal evolution of the position of an initially stationary soliton in the right trap when perturbed by the sound waves generated by moving solitons of variable speeds, v_s^L, in the left trap; largest amplitude corresponds to the highest speed. (b) Dependence of the time τ, it takes for the initially black soliton on the right to reach the arbitrarily chosen position $z_R = 7.8 l_z$, indicated by the dashed line in (a), on the speed v_s^L of the soliton in the left trap. Data points (black circles) fit perfectly on the curve $\tau = 1/v_s^L$ (solid line). Inset: same data plotted logarithmically. (c) Maximum oscillation amplitude, z^{max}, of the initially black soliton in the right trap (arising after a few tens of oscillations, so beyond the time shown in (a)), as a function of the initial relative speed, v_s^L, of the soliton in the left trap. All presented results are based on $V_0/\mu = 1.125$.

with initial soliton speed in the left trap.

We can gain an insight into these graphs by relating the time it takes for the soliton to reach an arbitrary position (τ) to the speed at which the amplitude of the right soliton oscillation increases, which we will denote v_A. This timescale can be approximated by the relation $\tau = z_s/v_A$. However, the speed of increase of the amplitude of oscillation is proportional to the speed of the soliton in the left well, i.e. $v_A \propto v_s^L$, therefore, we obtain the relation $\tau \propto z_s/v_s^L$, which is hinted upon in Fig. 3.11 (b) and (c).

The double harmonic trap geometry of Eq. (3.6) was chosen in order to demonstrate the effect in its most pure, idealised representation, building on previous work [99, 107, 197] in harmonic trap geometries. While double-well geometries can be easily generated experimentally, they actually have a slightly different form (being smoother at/around

$z = 0$), being either formed by a repulsive Gaussian barrier on a harmonic trap [46], or by isolating two sites of a periodic optical lattice potential [204]. We now discuss how the previously analysed effect becomes modified in such realistic geometries, and identify optimal regimes for its experimental observation.

3.4 Experimental considerations: Double/multiple wells

We seek to identify a directly observable effect that could be measured in experiments. Despite the appealing feature of the 'identity-reversal' of the two solitons in the idealised cut-off harmonic trap discussed previously, such an effect is unlikely to be directly observed in an experiment; this is due to the sensitivity of solitons to the locally strongly anharmonic in a small region around the barrier separating the two regions in a realistic experimental double-well geometry. As an alternative, and to make direct links with experiments, we therefore consider the simpler scenario of looking at changes in the motion of a soliton in one well, due to the presence, or absence, of a soliton in the neighbouring well.

Thus, we now discuss experimental geometries in which solitons have been successfully generated, namely Gaussian traps and optical lattice geometries. For simplicity we restrict this study to identical solitons.

3.4.1 Gaussian induced, double-well potential

To enable the experimental observation of the energy transfer between solitons we propose the formation of a double well geometry of the form

$$V(z) = m\omega_z^2 z^2/2 + V_0 e^{-z^2/2d^2}$$

formed by adding a Gaussian dimple to the original harmonic trap (physically this is equivalent to shining a laser in the centre of the harmonically trapped condensate). Here V_0 is the height of the Gaussian and d characterises it's width.

As before, two solitons are placed at the peak densities of the two wells spanned by the condensate, with their respective profiles shown in Fig. 3.12 (Left).

While for many practical purposes each well can be thought of as approximately harmonic, the lack of symmetry about the centre of each well turns out to be quite crucial here, because dark solitons have recently been shown to be extremely sensitive to anharmonicity-induced decay [107], which causes the solitons to quickly de-stablize and dissipate. This effect occurs on a much faster timescale than the corresponding case of a single soliton in a corresponding double harmonic trap. Due to the lack of harmonicity in each well of this trap (and others to follow) we will no longer present our results in harmonic oscillator units but in units of healing length. The relation between harmonic oscillator length l_z

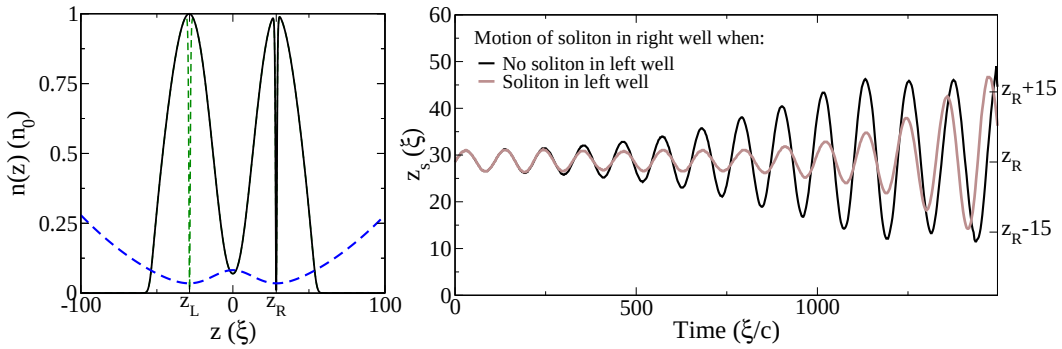

Figure 3.12: Left: Density profile (black and green dashed) and trapping potential (lower dashed blue) of an atomic condensate in a double-well potential, with either a single $0.1c$ soliton in the right well ($z_R = 28.5\xi$, black lines), or also a second identical soliton located in the symmetric position of the left well ($z_L = -28.5\xi$, green dashed). Right: Position of the soliton in the right well when it is the only soliton present in the trap (black) and when there is another soliton in the left well (grey). (Parameters: $V_0/\mu = 0.97$, $d = 14.6\xi$).

and healing length is characterised by

$$l_z/\xi = \sqrt{\frac{n_0 g}{\hbar\omega_z}} \tag{3.7}$$

and for the parameters we are using this conversion factor becomes $l_z/\xi = 4.9$.

Given the rapid decay of a soliton in such an asymmetric trap, we instead investigate the motion of a soliton in the right well depending on whether there is a soliton in the well to the left or not. We find that the addition of a soliton in the left well stabilises the other soliton for a considerable initial period, as shown in Fig. 3.12 (Right); as a result, instead of quickly decaying, it continues oscillating with roughly the same amplitude (i.e. same energy/depth) for a timescale of the order of $800\xi/c$, before eventually decaying. We also note a slight phase difference between the two cases.

The anharmonicity of the trap causes the solitons to decay and this prevents us from seeing as apparent an energy transfer as in the idealised double well case of Sec. 3.3. To improve the lifetimes of the solitons we need to look at a new regime in which the trap is more harmonic. To do this we look at optical lattice trapping.

3.4.2 Solitons in an optical lattice trap

Two lattice sites

To remove the asymmetry of the condensate in which each soliton is propagating (but not the anisotropy), we now consider a symmetric double-well trap formed by two wells of an optical lattice. A geometry of this type has been used, for example to study Josephson oscillations by the Heidelberg group [204]. Intersecting laser beams at an angle can be used

to generate an optical lattice or an array of traps of variable depth and periodicity [205]. To model this configuration we replace the trapping potential given by Eq. (3.6) with

$$V(z) = V_0 \cos^2\left(\frac{\pi z}{d}\right) \tag{3.8}$$

where the lattice spacing d is the distance between two maxima or minima and V_0 is the lattice depth. Again, solitons of equal speed are initially placed at the peak condensate densities.

As before, we initially consider a periodic array of traps of relatively large periodicity [206], in which the condensate however only spans two wells, as shown in Fig. 3.13 (top). We investigate the evolution of an initially propagating soliton ($v = 0.1c$) in one well, when the condensate in the other well does not contain a soliton (black line); this is contrasted to the case when there is an identical soliton in the other well (grey line). It is apparent that the presence of the other soliton leads to a slower decay. This indicates that the soliton in the right well absorbs the sound created by the motion of the soliton through the inhomogeneous background of the left well. The more symmetric nature of the trap results in the soliton experiencing a slower dissipation than in the Gaussian, double-well potential of Fig. 3.12.

3.4.3 Array of optical traps

Finally, we wish to explicitly demonstrate the role of dark solitons as both *absorbers* and *emitters* of sound [106], by investigating the effect of adding further solitons to a condensate spanning a number of lattice sites greater than two.

We consider a condensate spanning 6 lattice sites, and place two identical slowly-moving solitons in the wells at each end of the condensate, as shown in Fig. 3.13 (bottom). The soliton in the right well is found to decay (black lines in Fig. 3.13 (d)) on a timescale of ~ 25 oscillations, due to the partial escape of the emitted sound to the other wells, while the sound from the soliton in the leftmost well arrives too late to stabilise it. This should be contrasted to the case when each intermediate site contains solitons of the same depth. In that case, the solitons in the neighbouring wells clearly have the net effect of partially stabilising the end soliton against decay over a prolonged period, as evident by the grey lines in Fig. 3.13 (d).

Faster solitons were found to decay on a more rapid timescale, as the time required for the oscillating soliton to probe the anharmonic region of the trap decreases rapidly with increasing soliton speed. However, this effect should be observable in carefully controlled experiments, and it does not require identical soliton speeds.

A similar energy interaction has been also theoretically studied for vortices in a double well trap which we will briefly review in the next section.

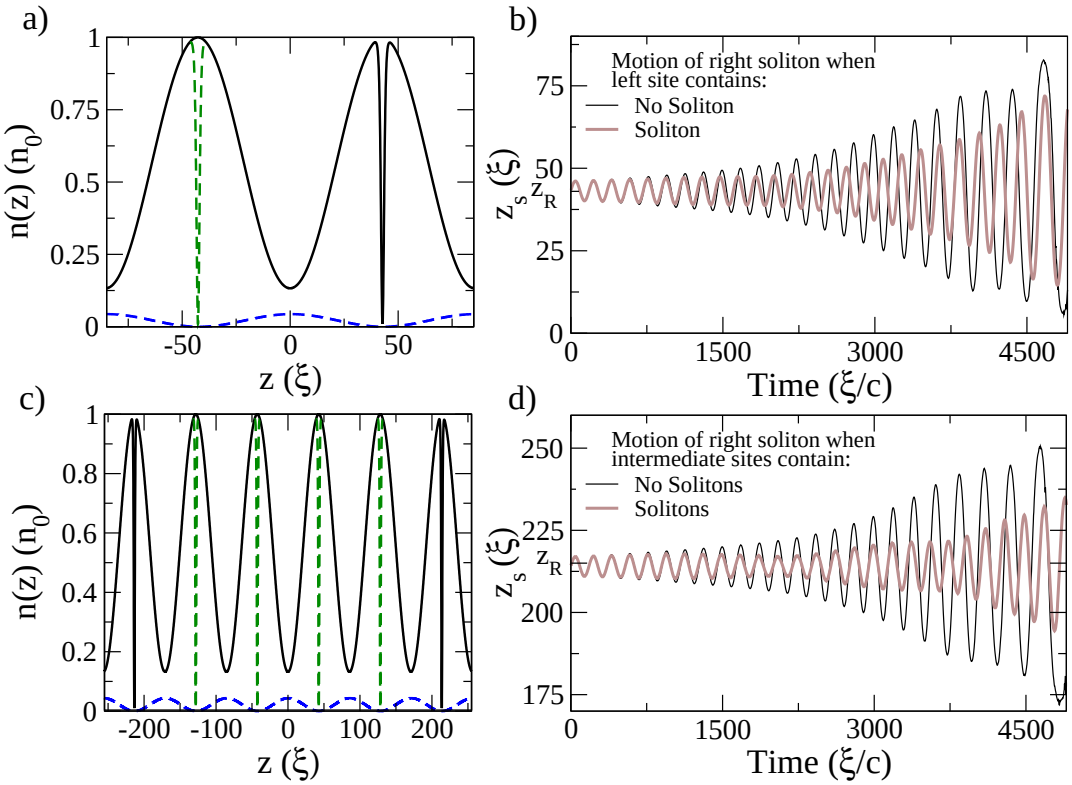

Figure 3.13: Left: Density profiles for a condensate spanning (a) two, or (c) six sites of an array of optical traps. In both cases, the right site contains a $v_s = 0.1c$ soliton (black). In addition, in (a) the left site may or may not contain an identical soliton (green dashed), whereas in (c) the leftmost site also contains an identical soliton, while the condensate in the intermediate sites may or may not contain solitons. Right: Temporal evolution of the soliton in the right well showing clearly that the presence of a soliton in neighbouring wells has a stabilising effect: (b) Comparison of case when there is no soliton in the left well (black) to when this site contains a soliton (grey). (d) Comparison of the dynamics of the soliton in the rightmost trap, when there are no intermediate solitons (black) and when the intermediate sites contain identical solitons (grey). (Parameters: $V_0/\mu = 0.87$ and $d = 170.9\xi$).

3.5 Sound mediated vortex interactions

It is well understood that a vortex in a harmonically trapped atomic condensate is stable and precesses along a line of constant potential [112, 207–209] (See Fig. 5.1, Chapter 5). When a vortex line undergoes reconnections, it loses energy through the generation of sound waves [132] and, similarly to solitons, through acceleration [209, 210]. What is less well understood is the precise mechanism by which a vortex interacts with sound energy and reabsorbs it. Whether two vortices can undergo an exchange of energy which we have studied for dark solitons was the focus of a recent paper of which I have co-authored, however, the simulations were undertaken by Nick Parker [158].

In this work, a double well potential in 2D is exploited to study this sound mediated effect for two identical vortices in either regions of the trap; simulations were based on the

GPE Eq. (3.1) (in this case generalised to 2D). In 2D, a vortex is a point singularity of zero condensate density, with phase winding round the central point in units of 2π. When the phase winds round in the positive (clockwise) sense, the vortex is said to have positive charge and when it winds around in the anti-clockwise direction, it is negatively charged. For more information on the form of vortices and how to numerically 'imprint' one onto a condensate, see Chapter 5.

Analogous to solitons, a vortex in the centre of a harmonic trap is stationary with the maximal energy. Just as a dark soliton loses energy and moves outwards when it accelerates, acceleration of a vortex causes it to minimise its energy by spiralling radially out of the condensate. In Ref. [158], a vortex is placed in the centre of one side of the double well ($r_v^L(0) = 0$) and another, identically charged vortex is placed off-centre in the other well ($r_v^R(0) = 4\xi$) and the subsequent dynamics observed. This is the same procedure as we carried out for solitons in Sec. 3.3. The resulting trajectories are shown in Fig. 3.14 (Left) for an idealised double well trap of the form

$$V(x, y) = \frac{1}{2} m\omega^2 \left[(|x| - x_c)^2 + y^2 \right]. \tag{3.9}$$

where ω is the trapping frequency of either circularly symmetric well, both traps are offset from the origin by the distance $\pm x_c$ and the barrier height characterised by $V_0 = 1/2 m\omega^2 x_c^2$. Units are in terms of the condensate healing length, $\xi = \hbar/\sqrt{mn_0 g}$.

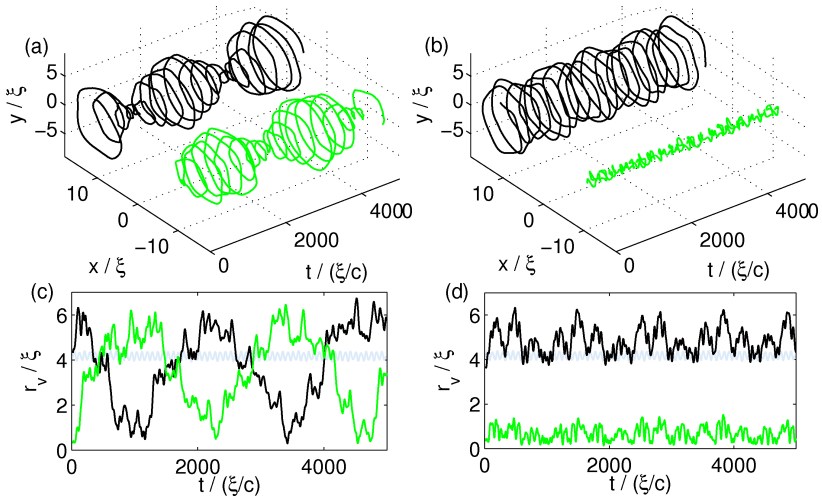

Figure 3.14: Top: Vortex trajectories for two vortices in opposite wells of a double well potential Eq. (3.9) with barrier height $V_0/\mu = 0.6$. The vortex in the right well is initially off-centre with radial coordinate $r_v^R(0) = 4\xi$ (black), and the vortex in the left well is initially central, $r_v^L(0) = 0$ (green). Left: both vortices have the same polarity, Right: the vortices have opposite polarity. Bottom: The evolution of radial coordinates of the vortices and the light grey lines the evolution of a single vortex in a harmonic trap with initial radius $r_v(0) = 4\xi$. With $\mu = 10\hbar\omega$. Figure taken from [158].

In Fig. 3.14 (a) we see the spiralling inwards and outwards of both the vortices. The initially stationary vortex is perturbed and starts to the move outwards radially (also clear from Fig. 3.14(c)); as this vortex is spiralling towards the outer regions of the trap, the vortex in the right well starts to move inwards towards the centre and the vortices continue to oscillate between these positions. This is similar behaviour to that witnessed with two non-identical solitons in Fig. 3.6. This significant motion between the central region of the trap and that closer to the edge indicates that there is transfer of energy between the vortices. What is apparent from Fig. 3.14, is the complete energy transfer between the two vortices happens on a much quicker time scale than for the solitons. The energy transfer happened at around 8 precessions of the vortex in a trap, whereas for the case of the soliton, the characteristic identity reversal took many tens of soliton oscillations to happen (see Fig. 3.6 of Sec. 3.3), hence this effect could potentially be observed experimentally in realistic geometries [158].

What is interesting is that polarity can also be investigated. In Fig. 3.14 (Right), the simulation is repeated but this time the stationary vortex in the left well is of *opposite* polarity to that in the right. We see very little change in their radial coordinates and the slight modulations which we do see are an effect of the sound which is emitted by either vortex modulating the background density of the condensate. These modulations are greater than those experienced by a single vortex precessing in a harmonic trap (see the grey line of Fig. 3.14 (d)) which indicates the presence of a larger sound field in the double well geometry due to the presence of two vortices.

As we remarked in the case of solitons, the presence of the second vortex (of the same polarity) in the double well geometry has the effect to drive energy into the vortex. This means that there could be other possible ways of stabilising a vortex by parametrically driving energy into it. One such way, investigated in [158], is a precessing Gaussian beam of the same angular momentum of the vortex. Physically this corresponds to replacing the vortex in the left well with a blue detuned laser beam moving in a circular path around the condensate. For more details of the form of the precessing obstacle see Ref. [158]. Parameters for the precessing obstacle are chosen to mimic the sound generated by the vortex in the right well. The resulting evolution is shown in Fig. 3.15.

The radial coordinate of a vortex in the right well of the trap is shown in Fig. 3.15 for various scenarios involving the precessing obstacle. When the obstacle precesses in the same direction as the vortex, the vortex radial coordinate decreases indicating an increase in energy as it moves to the central region of the trap. If the precessing obstacle is terminated here, the vortex precesses around the trap with constant radial coordinate. However, if the precessing obstacle is still present, the vortex then proceeds to oscillate between this radial position and its original i.e. there is periodic driving of energy into the vortex, which is analogous to the parametric driving of a dark soliton in Ref. [99]. For

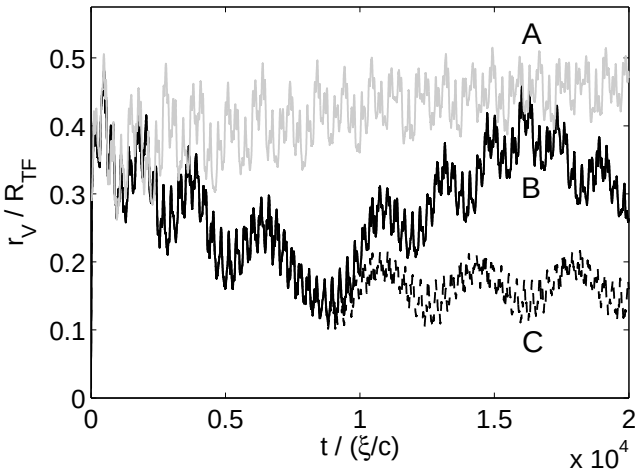

Figure 3.15: Evolution of vortex trajectory under parametric driving by a precessing obstacle when; The obstacle moves in the same direction to the vortex (black line (B)). The obstacle moves in the opposite direction to the vortex (light grey line (A)). The obstacle moves in the same direction as the vortex (dark grey line (C)) but its motion is terminated at $t = 8800(\xi/c)$. Initial position of the vortex and obstacle $r_v(0) = 4\xi$. Figure taken from [158].

completeness, the effect of a precessing obstacle in the opposite direction to the vortex is shown also. No increase in energy is observed, in fact the vortex moves out radially slightly, an effect not observed when the left vortex has opposite polarity to the vortex in the right well. This increase in radial coordinate is associated with a small loss of energy over time however the time scales are much longer than in the case of two solitons.

The timescale over which the precessing obstacle drives energy into the vortex to stabilise it is much longer than when the second vortex is present occurring over ~ 40 precessions compared with 10 in Fig. 3.14. This indicates that the presence of a second vortex is a more efficient way to drive sound into a vortex than a precessing obstacle.

These investigations are repeated for more experimentally realisable geometries in Ref. [158] where the barrier between the wells is not as sharp as that presented here and the wells are no longer circularly symmetric. In these geometries, the energy exchange is still observed within the timescale of other dissipation mechanisms, such as thermal dissipation [68, 134].

3.6 Chapter summary

In this chapter we presented a detailed investigation of the crucial role of sound emission on the direct or indirect interactions between two dark solitons in a low temperature atomic Bose-Einstein condensate. Firstly, within a single harmonic trap, we provided a clear indication of energy transfer between two colliding solitons of different speeds.

We then provided clear evidence of a new *indirect long-range* interaction between two solitons propagating within two non-overlapping regions of the same condensate, which communicate via the propagation of small amplitude sound waves. This effect was demonstrated in an idealised double harmonic trap geometry which allows energy transfer between the two parts of the condensate but contains no anharmonicites to enhance the soliton decay in each individual well. We showed that the periodic sound-mediated soliton interactions led to a perfect periodic exchange of the properties of the two solitons, with an initially moving soliton transferring all its motion to a static soliton in the other well and then returning to its original motional state. Such a complete energy-exchange cycle was found to require a few tens of soliton oscillations, which is a very long time for current experiments due to other decay mechanisms present in such systems.

We then focused on more appropriate experimental geometries, where we showed that evidence of this effect should still be observable in very low temperature condensates on realistic timescales. In particular:

(i) the presence, or absence of a soliton in one half of a double-well potential formed by a harmonic trap split by a Gaussian barrier can significantly change the motion (amplitude, period) of a soliton located in the other half of the trap already within a few oscillations, i.e. on an experimentally relevant timescale as short as a few hundred milliseconds.

(ii) the motion of solitons at opposite ends of an optical lattice filled with a condensate depends sensitively on whether any intermediate sites also contain solitons or not; the solitons in the intermediate sites were shown to act as absorbers and emitters of energy; while this effect is already evident with just three lattice sites (where the middle site either contains, or does not contain, a soliton), increasing the number of intermediate lattice sites to a few (~ 7) is sufficient to amplify this effect so that it can be observed after a dozen oscillations.

Given the current control of dark solitons in atomic condensation experiments, this effect should be observable without major changes to the experimental configurations, provided the experiment is set up in a regime where all other decay mechanism [99] are suppressed [97, 98], which certainly appears within current experimental reach [84–86]. Extensions of this work could include the interplay between soliton-sound interactions and Josephson effects [211] and a deeper investigation of the role of the intermediate states in terms of resonant tunnelling [212, 213].

We have also demonstrated that a similar mechanism of sound emission and absorption is present in double well system containing two vortices of the same polarity, situated at different positions within each trap. This process of transferring energy to a vortex is shown to be more efficient than driving energy into the vortex via a precessing obstacle.

When the two vortices are of opposite polarity, no such identity reversal occurs and the only effect of the second vortex is more pronounced modulations in the vortex trajectory due to the higher density of sound waves in the trap.

The energy exchange between vortices happens over a much quicker time scale than for the case of dark solitons. The vortices are seen to have exchanged characteristics within 10 precessions of the trap whilst the effect takes tens of soliton oscillations before total energy transfer is observed. As a result of this, vortices are likely to be better candidates for the experimental observation of this long-range interaction mechanism between macroscopic excitations in atomic condensates, based on the transfer of sound energy.

In this chapter, we have studied the role of sound in the interactions of solitons and vortices at zero temperature using the GPE, which has been sufficient, since for the case of solitons, dissipation via sound in the presence of trap anharmonicities is the most dominant decay mechanism in the low temperature regime of current experiments [84–86].

In Part III of this thesis, we study the effect of finite temperatures on vortex dynamics (Chapter 5) and Josephson oscillations in double well potentials (Chapter 6). The method we use is the Zaremba, Nikuni and Griffin (ZNG) scheme [69], introduced in Chapter 2, in which the GPE is modified by the inclusion of the mean-field of the thermal cloud as well as a source term, coupled to a quantum Boltzmann equation for the thermal cloud. We begin by giving a detailed explanation of the numerical scheme we use to solve these equations, in Chapter 4.

Part III

$T > 0$: Bose-Condensed Gases at Finite Temperatures modelled using ZNG

Chapter 4

Numerical Procedure for solving the ZNG equations

The two equations which make up the closed set of ZNG equations are very different in nature, therefore, two different numerical methods are used to solve them.

The equations are a finite temperature generalisation of the Gross-Pitaevskii equation (GPE),

$$i\hbar\frac{\partial\phi(\mathbf{r},t)}{\partial t} = \left(-\frac{\hbar^2\nabla^2}{2m} + V_{\rm ext}(\mathbf{r}) + g\left[n_c(\mathbf{r},t) + 2\tilde{n}(\mathbf{r},t)\right] - iR(\mathbf{r},t)\right)\phi(\mathbf{r},t)\ , \tag{4.1}$$

which is modified by the addition of a thermal cloud potential $2g\tilde{n}(\mathbf{r},t)$ and a dissipative/-source term $-iR(\mathbf{r},t)$, and the quantum Boltzmann equation (QBE),

$$\frac{\partial f}{\partial t} + \frac{\mathbf{p}}{m}\cdot\nabla_{\mathbf{r}} f - (\nabla_{\mathbf{r}} U_{\rm eff})\cdot(\nabla_{\mathbf{p}} f) = C_{12}[f,\phi] + C_{22}[f]. \tag{4.2}$$

The meaning of the various terms appearing in these equations has been discussed in detail in Chapter 2. The generalised GPE (4.1) is solved in much the same way as the simpler, $T = 0$ GPE, with the noncondensate mean field and the source term calculated from the QBE at each time step. In this chapter we will outline the numerical procedure for solving the QBE (4.2) in the mean-field-dominated regime, where the full distribution function $f(\mathbf{p},\mathbf{r},t)$ is required to accurately describe the thermal cloud - see [159] for details. After discussing the scheme for solving the QBE, we briefly discuss how the GPE propagation is numerically modified to account for the effect of the collisional processes. This numerical scheme was first implemented by Brian Jackson and Eugene Zaremba who, alongside collaborators provided evidence to show the excellent agreement of this theory with experimental results for condensate modes [65, 66, 214] and even macroscopic excitations such as solitons [67]. The results generated in this thesis are generated from this initial

code with some amendments.

In order to solve the QBE we first need to generate the equilibrium densities for the condensate and noncondensate to use as initial conditions for the full dynamical simulation. To reduce computational time we generate equilibrium densities in a 2D r-z geometry for cylindrically symmetric harmonic traps. As this type of trapping geometry is relevant in most experiments and also used for much of our work, in particular for the vortex analysis presented in Chapter 5, we focus on this type of geometry here. In Chapter 6, we model an experimental double well [34], which is not of this cylindrically symmetric form, hence in this case, we generate 3D densities and subsequent parts of the dynamical procedure are modified accordingly.

The QBE is a complicated six dimensional equation in phase space and the procedure for solving such an equation involves the use of a cloud of phase points which are called test particles. This means, rather than following the evolution of a particle which is dependent of position and momentum separately, the evolution of test particles can be followed in phase space, reducing the computational effort enormously. The number of test particles chosen must be large in order to reduce discrete particle effects in the distribution function and is related to the number of thermal particles by an appropriate weighting factor, denoted by γ. We use approximately $N_{tp} = 275000$ test particles in a typical simulation involving this cylindrically symmetric harmonic trapping geometry.

We need to assign position and momentum to the test particles initially so that they accurately describe the noncondensate density. This is described in Sec. 4.2.1. We again make use of the cylindrical symmetry of the trap to do this, while this is not a necessary condition for numerical simulations and can easily be done in full 3D, our procedure nonetheless increases computational efficiency. In order to carry out the dynamics, the test particles are 'binned' into cells containing equal numbers of test particles both in the radial and axial directions, as described in Sec. 4.2.2. Radially, we use circular cells, which are ideal for the geometry studied; however, depending on the trapping geometry, other cell shapes can be used and may be necessary. For example square cells [215] would be ideal for modelling homogeneous condensates. After this initialisation, the time stepping can begin. Now we will outline the procedure we use to evolve our system during every time step Δt, and highlight the sections of this chapter in which further details can be found.

In Sec. 4.2.3 we describe how to evolve the test particles according to the free streaming terms of Eq. (4.2). Symplectic integration is used to solve Newton's equations for position and velocity, and the test particle positions and momenta are updated accordingly. This particular method conserves phase space and volume unlike other conventional integration schemes such as Runge-Kutta or Euler. To implement this method, the derivative of the effective potential felt by the thermal atoms is required at each time step. This means that

both the condensate and thermal cloud density are also required. The thermal density is obtained from the phase space distribution of the test particles, which can contain large spatial fluctuations thus leading to inaccuracies if differentiated. For this reason a smoothing operation, as described in Sec. 4.2.4 is performed.

After the evolution of free streaming terms of the QBE, the test particles have moved in position, therefore, need to be rebinned into the radial and axial cells. If the collisional terms of Eq. (4.2) are included in the simulations, these cells need to be further reduced in size, as described in Sec. 4.3.1, so there are approximately 100 test particles in each cell (we find that < 30 leads to numerical errors). This is to ensure that when the collisional probabilities are calculated, in particular for the $C_{22}[f]$ collisions, the test particles chosen are in the vicinity of each other and not, in the extreme case, at opposite regions of the trap.

Once this rebinning has been done, for *each cell* the probability that *each test particle* has had a $C_{12}^{\rm out}[f,\phi]$ collision, transferring a particle from the condensate to the thermal cloud, is calculated (Sec. 4.3.3) followed by the probability that that test particle has undergone a $C_{12}^{\rm in}[f,\phi]$ collision, its inverse process (Sec. 4.3.4); for every test particle these probabilities are then compared with a random number to determine which, if any of these collisions the test particle has suffered. Using the information of which test particles have undergone $C_{12}[f,\phi]$ collisions, the dissipative term of the GPE can be calculated (Sec. 4.3.5) and saved for the condensate propagation which is done at the end of the time step. The next step is to determine whether the test particles have undergone a $C_{22}[f]$ collision, associated with the redistribution of two thermal atoms in different modes (Sec. 4.3.6). This is calculated for *pairs of test particles* within the cell and again compared with a random number to determine whether the pair have collided.

At this point, whether each test particle or pair of test particles have undergone a collision in the time step Δt has been determined and as a result of the $C_{12}[f,\phi]$ collisions, there is a set of test particles which need to be removed from the cloud and a set which need to be added. The mechanism by which we do this is outlined in Sec. 4.3.7.

The evolution of the thermal cloud over the time step Δt is complete and condensate propagation can begin. The method in which we evolve the GPE with the addition of the $-iR(\mathbf{r},t)$ dissipative/source term is explained in Sec. 4.4. When the condensate wavefunction has been updated, the evolution can begin again for the next time step with the updated test particle distribution and condensate wavefunction.

This numerical procedure of one time step is summarised on the next page in algorithm form. The total number of time steps is denoted by N_step, the total number of test particles by atom_i and total number of cells in which the collisions take place by N_CELL.

The main body of this chapter contains detailed explanations of the various steps involved in the solution of the ZNG equations for a cylindrically symmetric harmonic trap.

We further summarise this procedure with the aid of a flow chart diagram at the end of the chapter (Sec. 4.5). We must stress that although we make use of cylindrical symmetry to speed up our numerics, the actual evolution of the test particles and condensate is fully 3D and can further be generalised to other geometries which don't have this symmetry, by changing some parts of the algorithm.

```
! Start time evolution over N_STEP time steps.
do t = 1, N_STEP
  do i = 1, atom_i
    Update positions of test particle by half a step
  end do
    Smooth thermal cloud densities
    Calculate effective potential felt by thermal cloud and condensate
  do i = 1, atom_i
    Update velocity of test particle
    Update positions of test particle by further half step
  end do
   rebin test particles to N_CELL phase space cells
   if(C12 and C22) then
   Re-bin atoms into radial and axial bins
   Cut these bins into further smaller cells
! For every cell
    do i_cell = 1, N_CELL
     if(C12) then
! For every atom in the cell
       do i = 1, num(i_cell)
         Calculate condensate velocity and densities at position of i
         Calculate relative velocities
         Calculate final velocities and Bose distributions
         Calculate probability i suffered IN or OUT collision
         Test whether collision has occurred
         Collision occurs - update velocities of products
         Calculate dissipative term of the GPE
       end do
      end if
      if(C22) then
! For every pair of atoms in the cell
         Pair of atoms from each cell selected at random
         Calculate relative velocities
         Calculate final velocities and Bose distributions
         Calculate probability collision has occurred
         Decide whether a collision has occurred
         Collision occurs - update velocities of products
       end if
    end do
   Update total number of test particles
  end if
Update condensate wavefunction
end do
```

4.1 Generating equilibrium solutions

We begin by generating equilibrium condensate and thermal cloud densities for particular system parameters. These will be used as an initial condition for the full dynamical simulations which will be outlined in Sec. 4.2. The densities must be generated self-consistently to fully account for the mean-field coupling between the two subsystems.

At static thermal equilibrium, the rate of change of thermal cloud atom number, as a result of particle exchanging C_{12} collisions is zero, $\Gamma_{12}[f^0, \phi_0] = 0$, hence,

$$R[f^0, \phi_0] = 0. \tag{4.3}$$

The equilibrium condensate density $|\phi_0|^2$, is therefore given as the solution to the time independent GPE Eq. (2.19), with the addition of the mean field due to the equilibrium thermal cloud density,

$$\left(-\frac{\hbar^2}{2m}\nabla^2 + V_{\rm ext}(\mathbf{r}) + g|\phi_0(\mathbf{r})|^2 + 2g\tilde{n}_0(\mathbf{r})\right)\phi_0(\mathbf{r}) = \mu_0\phi_0(\mathbf{r}); \tag{4.4}$$

where the equilibrium noncondensate density, $\tilde{n}_0(\mathbf{r})$, is given by the integral over all momenta of the equilibrium phase-space density, $f_0(\mathbf{p}, \mathbf{r})$ via

$$\tilde{n}_0(\mathbf{r}) = \int \frac{d\mathbf{p}}{(2\pi\hbar)^3} f_0(\mathbf{p}, \mathbf{r}). \tag{4.5}$$

Here $f_0(\mathbf{p}, \mathbf{r})$ is defined as

$$f_0(\mathbf{p}, \mathbf{r}) = \frac{1}{e^{\beta_0(p^2/2m + U^0_{\rm eff} - \mu_0)} - 1}, \tag{4.6}$$

with $\beta_0 = 1/k_B T$, the inverse uniform temperature, μ_0 the system chemical potential and $U^0_{\rm eff}(\mathbf{r})$, the equilibrium effective potential experienced by a thermal atom is defined by

$$U^0_{\rm eff}(\mathbf{r}) = V_{\rm ext}(\mathbf{r}) + 2g[|\phi_0(\mathbf{r})|^2 + \tilde{n}_0(\mathbf{r})]. \tag{4.7}$$

We assume a cylindrically symmetric trapping potential of the form

$$V_{\rm ext} = \frac{1}{2}m\omega_\perp^2(r^2 + \lambda z^2), \tag{4.8}$$

where $\omega_\perp$ is the trapping frequency in the r direction and $\omega_z = \lambda\omega_\perp$ is the trapping frequency in the z direction: We then generate equilibrium condensate and noncondensate densities for a given temperature, T, and total atom number, $N_{\rm TOT}$, in the following way; firstly, we approximate the initial condensate wavefunction with the Thomas-Fermi solution (see Chapter 2), where μ_0 is the ground state eigenvalue. In order to get a more

accurate initial condensate density, the condensate wavefunction is then propagated in imaginary time: in doing so we use Crank Nicholson time stepping method and renormalise the wavefunction by the square root of the condensate atom number, $\sqrt{N_c^i}$, where i denotes the index of the time step. An initial guess of the condensate atom number is made using the ideal gas relation

$$\frac{N_c^0}{N_{\rm TOT}} = 1 - \left(\frac{T}{T_c}\right)^3 \tag{4.9}$$

where T_c is the critical temperature for Bose-Einstein condensation. The number of non-condensate atoms is therefore given at each time step by $\tilde{N}^i = N_{\rm TOT} - N_c^i$.
Bringing all this together, at every time step we have an updated, normalised condensate density, denoted by n_c^i, noncondensate density $\tilde{n}_0^i$ which is obtained via

$$\tilde{n}_0^i = \int \frac{d\mathbf{p}}{(2\pi\hbar)^3} f^0(\mathbf{p},\mathbf{r}) = \frac{1}{\lambda_{\rm dB}} g_{3/2}(z_0^i(\mathbf{r})). \tag{4.10}$$

where $g_{3/2}(z)$ is the Bose-Einstein function and

$$z_0^i(\mathbf{r}) = e^{\beta_0[\tilde{\mu}_0^i - U_{\rm eff}^i(\mathbf{r})]} \tag{4.11}$$

is the local fugacity.

Iteration is performed until the condensate chemical potential and the thermal cloud atom number are within the tolerable limits specified by the user. When performing this iteration we choose here to convolve the condensate and thermal densities with a Gaussian in order to obtain smooth profiles. We do this to ensure that the numerical procedure used to obtain the equilibrium densities will be consistent with the dynamical code; the need for such smoothing in the dynamical code, arises from the numerical modelling of the distribution function via test particles and will be addressed in Sec. 4.2.

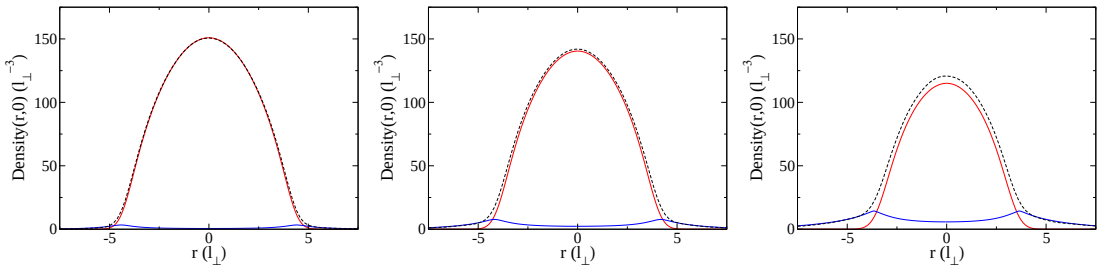

Figure 4.1: Equilibrium condensate (red), noncondensate (blue) and total (black, dashed) densities for increasing temperatures; from left to right, $T = 0.3T_c$, $0.5T_c$ and $0.7T_c$ where $T_c = 177$nK. The system setup is an anisotropic trap with frequency $2\pi \times 129$ Hz and aspect ratio $\lambda = \sqrt{8}$, and with $N_{TOT} = 10000$ ^{87}Rb atoms. Parameters taken from [68]

The equilibrium densities generated using this procedure for the temperatures $0.3T_c$, $0.5T_c$ and $0.7T_c$ where $T_c = 177$nK is the critical temperature of the corresponding non-interacting gas, are shown in Fig. 4.1. We see the distinct double peaked structure of the thermal cloud increasing in density with increasing temperature while the peak of the condensate density is decreasing. We see also how the thermal cloud spans a much wider spatial region than the condensate. For numerical efficiency, we use a larger spatial box for the thermal cloud than the condensate, however, the grid spacing in the example considered is the same. We will use these trapping parameters for examples of the methods used in some parts of this chapter.

4.2 Evolution of the dynamical thermal cloud

Simulating the thermal cloud with a set of test particles, allows a Lagrangian approach to be adopted, whereby the motion of a phase-space element is followed in time, rather than evolving each particle independently in momentum, $\mathbf{p}$, and position, $\mathbf{r}$. These are initially distributed in phase space according to

$$f(\mathbf{p},\mathbf{r},t) \simeq \gamma(2\pi\hbar)^3 \sum_{i=1}^{N_{tp}} \delta(\mathbf{r}-\mathbf{r}_i(t))\delta(\mathbf{p}-\mathbf{p}_i(t)), \tag{4.12}$$

where $\gamma = \tilde{N}/N_{tp}$ is a weighting function between $\tilde{N}$, the total number of noncondensate atoms and N_{tp}, the chosen number of simulated test particles. As test particles are only used in order to accurately sample the distribution, there is no need for their number to match the actual number of thermal atoms, which can be smaller or larger, with the only requirement that N_{tp} needs to be sufficiently large to minimise the effects of discrete particle description. As mentioned previously, we typically use about $N_{tp} = 275000$ test particles for simulations involving a few thousand thermal atoms. When using a graph to illustrate a procedure in this chapter, we may only plot a fraction of the total number of test particles for clarity but this will be highlighted in the caption.
The test particles are evolved according to Newton's equations of motion

$$\frac{d\mathbf{r}_i(t)}{dt} = \frac{\mathbf{p}_i(t)}{m} \tag{4.13}$$

$$\frac{d\mathbf{p}_i(t)}{dt} = -\nabla U_{\rm eff}(\mathbf{r},t), \tag{4.14}$$

thus enabling the phase space distribution to be calculated in time.
We now discuss how the test particles are initially assigned position and momentum in order to describe Eq. (4.12).

4.2.1 Initialisation of test particle position and momentum

Each test particle must be assigned a random position and momentum so that, collectively the distribution of test particles accurately describe the equilibrium noncondensate density. In this subsection, we will describe the use of an acceptance/rejection method for the determination of test particle position and momenta [216]. In the allocation of both position, and momentum to each test particle, we need to use a random number generator [216]; for clarity, every time a new random number is used, we will denote it by '$rand_i$ ', where i is an arbitrary index.

Position

The test particles are first distributed in position space via the following procedure: The position chosen for each test particle must lie within the numerical box with the most probable positions chosen where the equilibrium thermal density is maximum. The equilibrium density we obtained is in two dimensions, hence we begin by choosing two random variates in the r and z direction; if these variates are accepted, they will then be turned into a 3D position vector $\mathbf{r}$ of the test particle, using cylindrical symmetry. A more general 3D sampling could of course also be used for cases outside of cylindrical symmetry.
For **every** test particle (*atom_i*),

- Generate 2 random numbers, $rand_1$ and $rand_2 \in [0, 1]$, and determine positions on the grid in the r and z directions respectively via the random variates:
  temp_pos(1) = PR*$rand_1$
  temp_pos(2) = 2*PZ*($rand_2$-0.5)
  where PR and PZ are half the lengths of the numerical box in the r and z directions i.e. the positive r and z directions.

- Determine the density at the position assigned and use the below inequality to ensure more test particles are assigned positions where the density is higher. This is done using the distribution of positions as shown in Fig. 4.2. In this figure we have plotted the thermal cloud density multiplied by the position in the r direction. This gives us a distribution of the locality of the atoms, with the peak indicating the location in the radial direction where the highest number of thermal atoms are located.
  We choose the maximum of this distribution for comparison and accept or reject the test particles position via,

$$(\tilde{n}_0(r,z) \times r)_{\max} \times \ rand_3 < \tilde{n}(temp\_pos(1), temp\_pos(2)) \ \times \ temp\_pos(1).$$

  If this inequality holds with the positions chosen, *temp_pos(1)*,*temp_pos(2)*, then a test particle with these positions in the radial and axial direction would be a good

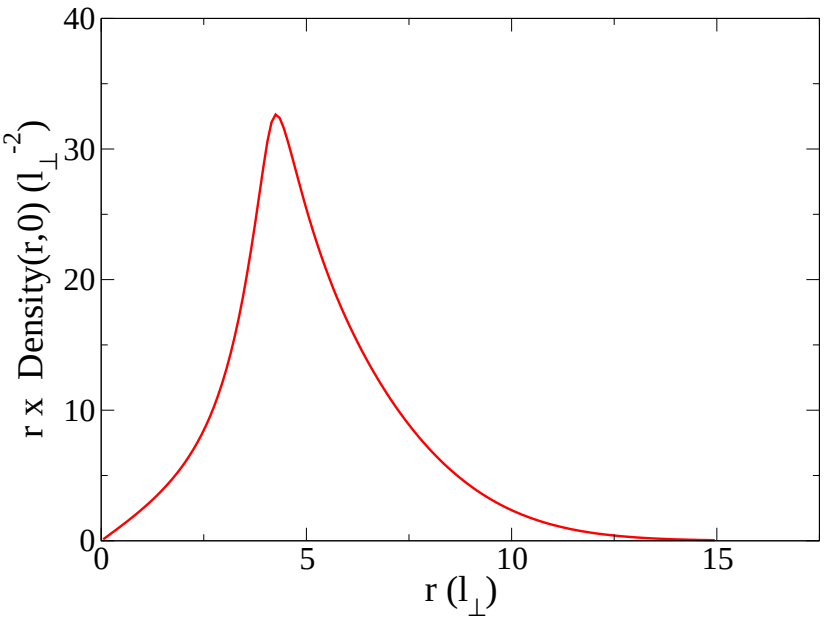

Figure 4.2: A slice through the thermal cloud density multiplied by position in the r direction, to illustrate the distribution of test particles position required in order to aid the binning of test particles in position space. This is generated using the equilibrium density for $0.5T_c$ from Fig. 4.1.

representative point for the thermal cloud density. Also this inequality ensures that more test particles have positions where the density is highest.

We distinguish two cases depending on whether the above inequality holds:
Inequality holds

- Accept this test particle position as viable.
- Assign the x and y positions of the test particles using the first random variate and cylindrical symmetry, the z position is the second random variate.

$$\begin{aligned} Pos(atom\_i,1) &= temp\_pos(1)*\cos(\phi) \\ Pos(atom\_i,2) &= temp\_pos(1)*\sin(\phi) \\ Pos(atom\_i,3) &= temp\_pos(2) \end{aligned}$$

where *Pos(atom_i,dim)* is the position of test particle *atom_i*, in the x, y and z direction, $\cos(\phi)$ and $\sin(\phi)$ are the projections into the x, y plane with angle of rotation $\phi = 2\pi * rand_4$ where $\phi \in [0, 2\pi]$. This is making use of the cylindrical symmetry in our geometry. If the geometry was not of this form, random variates in all three directions could be assigned using the same acceptance/rejection procedure, according to a 3D equilibrium density.

Inequality does not hold

– Procedure is repeated until position for the test particle can be accepted.

This procedure leads to the generation of position of **each** test particle. When we accept the generated positions, we move on to assigning momenta to each test particle.

Momentum

Now we distribute these test particles in phase space by assigning a velocity vector to **each** test particle.
We again start by choosing a random variate ($rand_5 \in [0,1]$) to determine a value of velocity which lies within the physical range of phase space i.e. *temp_vel(1)* $\in [0,\ \mathrm{p_{max}}]$, and, in a similar method to the assignment of test particle position, we use the distribution

$$f_{\max} \geq \frac{z(\mathbf{r})}{1-z(\mathbf{r})} \tag{4.15}$$

where $z(\mathbf{r})$ is the local fugacity generated within the equilibrium code. This inequality ensures the velocity chosen obeys Bose statistics for the thermal cloud and that the square of the velocity chosen is positive.
The procedure for assigning this is as follows:

- Generate a random number $rand_5$ and ensure it lies within allowed phase space i.e. *temp_vel(1)* = (*velbox*/2)**rand*$_5$
  where *velbox*/2 corresponds to the maximum velocity allowed i.e. *velbox* is essentially the "width" of the velocity range. It is not actually required to obtain a distribution of test particles in momentum space since using Bose statistics means only physical numbers are chosen, but it does speed up the numerics since it ensures that only values less than this will be considered. The value of *velbox*/2 chosen is 0.02 ms^{-1} (approximately $\sqrt{10(\mu + k_B T)/m}$ for our choice of parameters).

- The fugacity is extracted at the position of the test particle and the phase space distribution for the velocity of this test particle calculated:

$$f(\mathbf{p},\mathbf{r}) = \frac{1}{e^{(m*\mathit{temp\_vel(1)}^2/2-\mu+U_{\mathrm{eff}})/k_B T}-1} \tag{4.16}$$

- The condition of Eq. (4.15) is tested

$$\mathrm{MAX}\left(\frac{z(r)}{(1-z(r))}\right) * rand_6 < f(\mathbf{p},\mathbf{r})(\mathit{temp\_vel(1)})^2. \tag{4.17}$$

The inclusion of the comparison between $temp\_vel(1)^2$ and a random number, $rand_6$, ensures that more probable values of the velocity are chosen i.e. those where the Bose distribution is largest. If the velocities take on a more uniform distribution in phase space, then, when time stepping starts, problems are caused for the code since more test particles will have high velocities than is physical for the system. This is illustrated in Fig. 4.3 (Left), for a uniform distribution of test particles (black) and one where the more probable velocities are chosen (red). We have only plotted a fraction of the total number of test particles for clarity. Fig. 4.3 (Right), shows the evolution of the thermal cloud density over the first 450 time steps, when the velocities are not distributed via a Bose distribution and just uniformly distributed among the allowed values. Even after the first 50 time steps the thermal density has changed shape and this deformation continues with time exaggerating the importance of correctly assigning velocities to the test particles.

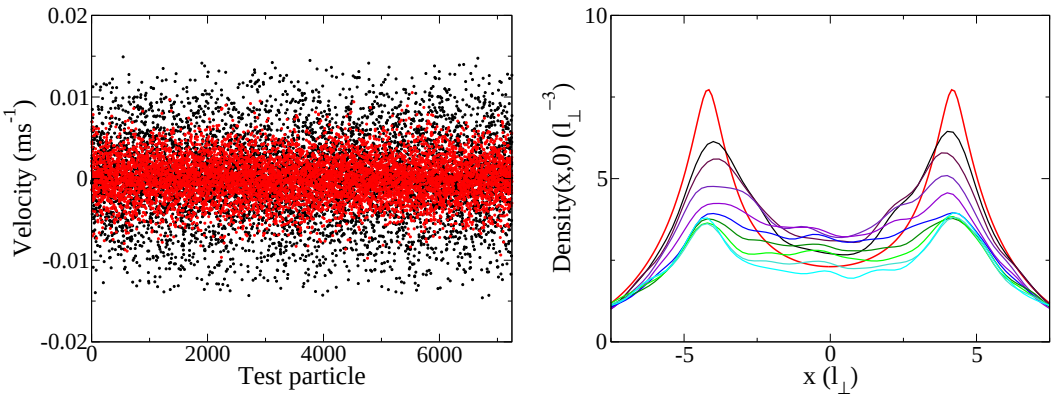

Figure 4.3: Left: Comparison of initial velocities for a sample of 7500 of the test particles ($N_{tp} = 275000$) where the more common velocities are chosen i.e. where the Bose-Einstein distribution is largest (red) and where the test particles are assigned a uniform spread of velocities (black). Right: Equilibrium thermal density (red) and thermal density measured every 50 time steps, evolving over time when the uniform assignment of velocity causes an instability. The evolving density is shown by decreasing strength in colour from black (after first 50 time steps) to cyan (after 450 time steps) with $\Delta t = 0.002\omega_\perp^{-1}$. The parameters used correspond to the $0.5T_c$ case of Fig. 4.1.

We now check whether the inequality of Eq. 4.17 holds and proceed accordingly.
Inequality holds

– Assign velocity to the test particle in the x, y and z directions.

$$Vel(atom\_i,1) = temp\_vel(1)*\sin(\theta)*\cos(\phi)$$
$$Vel(atom\_i,\ 2) = temp\_vel(1)*\sin(\theta)*\sin(\phi)$$
$$Vel(atom\_i,\ 3) = temp\_vel(1)*\cos(\theta)$$

where $Vel(atom\_i,dim)$ is the velocity of the test particle $atom\_i$, in the x, y and z direction and the angles

$\phi = 2\pi * rand_6$ where $\phi \in [0, 2\pi]$ is the angle of rotation in the radial plane,
$\cos(\theta) = 1 - 2 * rand_6$ where $\cos\theta \in [-1, 1]$
$\sin(\theta) = \sqrt{(1 - \cos^2(\theta))}$ where $\theta \in [0, \pi]$ is the angle of projection in the axial direction.

Inequality does not hold

– Procedure is repeated until a velocity for the test particle can be accepted.

The final velocities for a sample of 7500 of the test particles are shown in a histogram of velocity values in Fig. 4.4. This procedure of assigning position and velocity is repeated for every test particle.

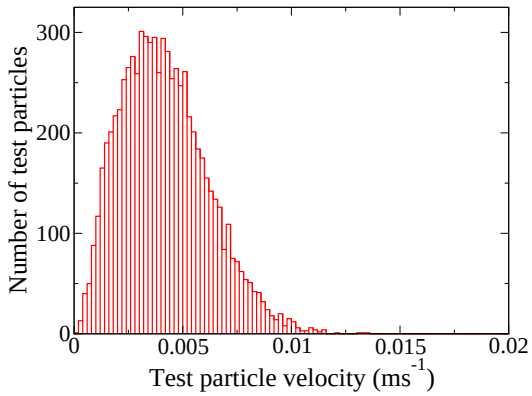

Figure 4.4: Histogram of final velocity values for a sample of 7500 of the $N_{tp} = 275000$ test particles. The bin width of the histogram is 0.0002ms^{-1}.

The test particles are now binned into cells which enable all future dynamics, including collisions to take place.

4.2.2 Test particle binning

We need to place the test particles into cells so that we have a way of sampling the phase space distribution and therefore, the thermal cloud density by essentially counting up the test particles per cell. The shape of the bins can be chosen depending on the shape of the particular trapping geometry. Having circular bins radially is ideal for the cylindrical harmonic trapping potential we have used, but square bins could prove more useful for a highly anisotropic trap [215].

We begin by placing the test particles into equally sized bins both in the radial direction and the axial direction. We choose to have 100 radial bins and define the width of each bin by $\Delta_{\text{bin}} = (2 \times PX)/100$. Determining which cell a test particle resides in is done by (i) comparing the test particle's radial coordinate $Rad_{atom\_i} =$

$\sqrt{Pos(atom\_i,1)^2 + Pos(atom\_i,2)^2}$ with the edges of the radial boxes, beginning from the centre and (ii) repeating the procedure for the axial cells by comparison of the test particle's axial coordinate $Pos(atom\_i,3)$, with the equally spaced axial boxes.

Now the aim is to reduce the number of cells in which the dynamics happen, and have approximately equal numbers of test particles in each box. This ensures an accurate description of the phase space distribution provided that all cells have enough test particles. We typically ensure that at this time, each cell contains approximately 2000 test particles. These cells will be subdivided into more cells and the number of test particles in each will decrease to approximately 100 before the collision algorithm begins.

Since some regions of space are highly occupied with test particles e.g. around the condensate edge, and some are more sparsely populated, e.g. the furthest regions of the box, as shown in Fig. 4.5, we thus use an adaptive spatial mesh. The choice of the number

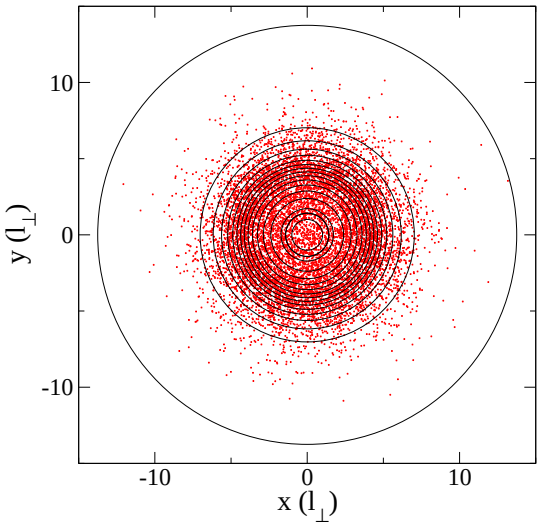

Figure 4.5: We assign 10000 of the total, $N_{tp} = 275000$ test particles to 17 radial bins for the system parameters given in Fig. 4.1. You can see the higher density of test particles where the edge of the condensate is and therefore a higher concentration of radial cells in this region.

of these cells is specified by the user and is of course dependent on the geometry chosen. For example for a harmonic trap with a tight axial confinement most of the interesting dynamics happen in the transverse direction, hence, it is instructive to have more test particle cells in the radial direction than in the axial direction. For example, for the case of Fig. 4.1, we choose 17 cells in the radial direction, and only 7 in the axial direction.

In Fig. 4.5, we show the radial distribution of a sample of 10000 of the total, $N_{tp} = 275000$ test particles for a harmonic trap with tight axial confinement, and the radial cells which have been put in place, each containing approximately equal numbers of test particles. It is easy to see that in the regions where the test particle concentration is

higher, around the condensate edge at $\simeq 4.2l_\perp$, there is a higher concentration of radial cells, and where there are much less test particles, towards the edges of the numerical box, the widths of the cells are much larger. This can be seen more clearly in Fig. 4.6, where the radial and axial cells have been plotted with the thermal cloud density in the x, y and z directions.

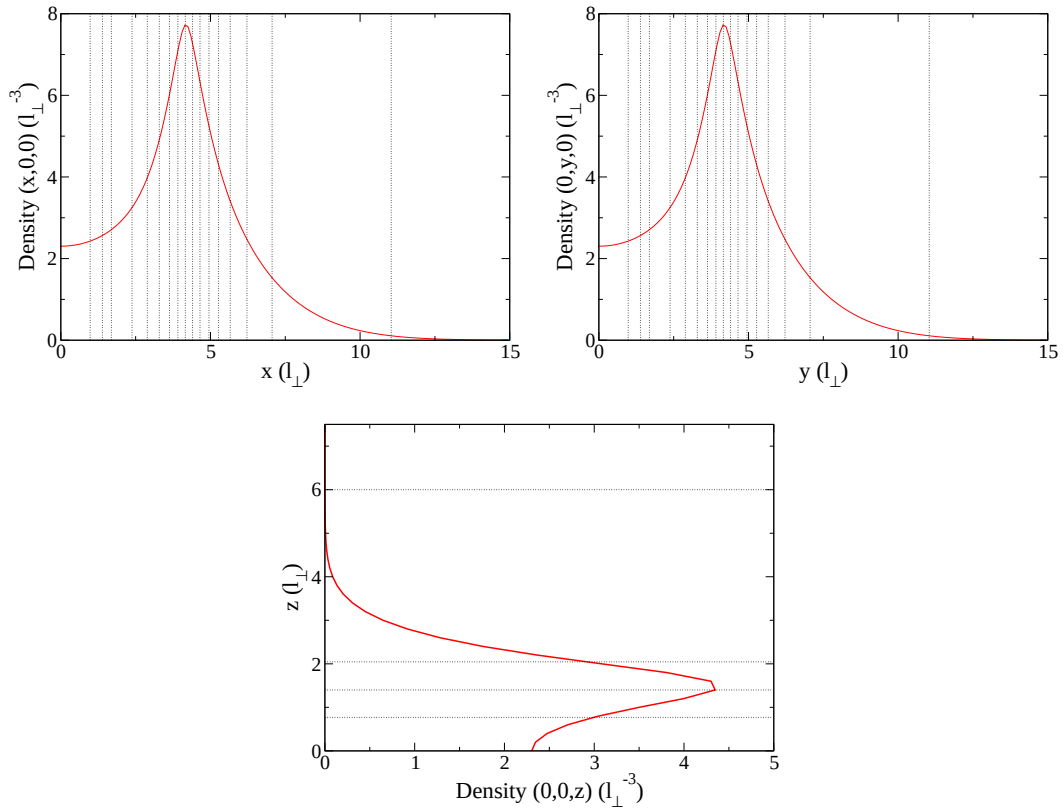

Figure 4.6: Location of bin boundaries (dotted black) in relation to thermal cloud density (red) for x (top, left), y (top, right) and z direction (bottom).

It is important to note here that at the beginning of each time step the test particles will need to be re-binned since as a result of both evolution and collisions, the test particles will have moved positions.
We can now begin the dynamics.

4.2.3 Evolution of test particles

The test particles are allowed to evolve according to Newton's equations of motion Eqs. (4.13) and (4.14); therefore, at every time step, these equations must to be solved. Usual integration schemes such as Euler and Runge Kutta are not efficient at conserving phase space and volume density over long time periods in Hamiltonian systems, therefore Symplectic Integration is used. This is the classical analogue of split operator methods which are

used to solve the dissipative Gross-Pitaevskii equation which we will discuss in Sec. 4.4. Symplectic integrators involve the use of Lagrangian mechanics to combine the conservation of energy laws with the equations of motion. They are typically used for separable Hamiltonians of the form, $H(\mathbf{p},\mathbf{r}) = T(\mathbf{r})+V(\mathbf{p})$, where T is the kinetic energy, a function of position $\mathbf{r}$, and V is the potential energy, a function of momentum $\mathbf{p}$. Poisson brackets are used to express the evolution of the Hamiltonian's phase space coordinate as a single expression

$$\frac{d\mathbf{z}}{dt} = \{\mathbf{z}, H(\mathbf{z})\}\,, \tag{4.18}$$

where the Poisson brackets infer the operation

$$\{\mathbf{z}, H(\mathbf{z})\} = \sum_{i=1}^{N}\left[\frac{\partial \mathbf{z}}{\partial \mathbf{p}_i}\frac{\partial H(\mathbf{z})}{\partial \mathbf{r}_i} - \frac{\partial \mathbf{z}}{\partial \mathbf{r}_i}\frac{\partial H(\mathbf{z})}{\partial \mathbf{p}_i}\right] \equiv i\mathcal{L}\mathbf{z} \tag{4.19}$$

which is equivalent to the use of the Liouville operator $\mathcal{L}$. The formal solution to this set of equations (4.18) is given by

$$\mathbf{z}(t+\Delta t) = e^{-i\mathcal{L}\Delta t}\mathbf{z}(t). \tag{4.20}$$

Since our Hamiltonian is of the separable form ($H(\mathbf{p},\mathbf{r}) = T(\mathbf{r})+V(\mathbf{p})$), we can introduce the Liouville operators $\mathcal{L}_V\mathbf{z} = i\{\mathbf{z}, V\}$ and $\mathcal{L}_T\mathbf{z} = i\{\mathbf{z}, T\}$, and use the Baker-Campbell Hausdorff formula which approximates the product of two exponentials and therefore we split the solution as

$$e^{-i\mathcal{L}\Delta t} \;=\; e^{-i\mathcal{L}_T\Delta t/2}e^{-i\mathcal{L}_V\Delta t}e^{-i\mathcal{L}_T\Delta t/2} + \mathcal{O}(\Delta t^3). \tag{4.21}$$

We update the position and velocity of the test particle numerically by applying the following steps.

- The positions of the particles are advanced half a step (we use $\tilde{\mathbf{r}}$ to denote it is not the final value of position),

$$\tilde{\mathbf{r}}_i = \mathbf{r}_i(t) + \frac{1}{2}\mathbf{v}_i(t)\Delta t. \tag{4.22}$$

- The velocities are updated,

$$\mathbf{v}_i(t+\Delta t) = \mathbf{v}_i(t) - \frac{1}{m}\nabla U_{\text{eff}}(\tilde{\mathbf{r}}_i)\Delta t. \tag{4.23}$$

- Finally the positions are advanced another half step,

$$\mathbf{r}_i(t+\Delta t) = \tilde{\mathbf{r}}_i + \frac{1}{2}\mathbf{v}_i(t+\Delta t)\Delta t. \tag{4.24}$$

The repetition of these steps for each test particle, results in updating the cloud of test particles via the free streaming terms of the QBE over one time step, Δt.
The derivative of the mean-field potential is required to update the velocity (Eq. (4.23)); this in turn implies that the condensate and noncondensate densities are required in order to calculate the mean-field potential. Obtaining the noncondensate density is more involved than finding the condensate density in the locality of the test particle, with details discussed below.

4.2.4 The mean-field potential

The condensate and noncondensate densities are required at every time step for the calculation of the mean field potential experienced by the thermal atoms,

$$U_{\rm eff}(\mathbf{r},t) = V_{\rm ext}(\mathbf{r},t) + 2g[|\phi(\mathbf{r},t)|^2 + \tilde{n}(\mathbf{r},t)]. \tag{4.25}$$

Calculating the phase space density numerically involves sampling the number of test particles in each cell. This method leads to large spatial fluctuations in the resulting noncondensate density, therefore, a more useful method called the 'cloud in cell' method is used [217]. This method takes into account the position of the test particle within the cell by giving each test particle a weighting. In this way, the phase space distribution or the thermal cloud density at a grid point in phase or position space respectively, is an interpolation of the densities of the eight adjoining cells and the result is smoother. This method also allows the phase space distribution and test particle density to vary continuously in time as migration of particles between the cells is allowed which is essential to avoid temporal fluctuations. To relate the density of test particles to the thermal cloud density, the weighting factor γ, between test particle and thermal atom number, is used.

However, the resulting noncondensate density still retains some spatial fluctuations as can be seen from the brown curve of Fig. 4.7. Further smoothing is required since it is the derivative of the mean field potential which is needed to update the velocities of the test particles, (Eq. (4.23)), at every time step. Such smoothing can be achieved by convolving the effective potential with a Gaussian. The smoothed effective interaction then takes the form:

$$U^s_{\rm eff}(\mathbf{r},t) \equiv \int d\mathbf{r}' S(\mathbf{r}-\mathbf{r}') U_{\rm eff}(\mathbf{r}',t) = 2g\gamma \sum_{i=1}^{\tilde{N}_{\rm tp}} S(\mathbf{r}-\mathbf{r}_i), \tag{4.26}$$

where $S(\mathbf{r}) = (\pi\sigma^2)^{-3/2}e^{-r^2/\sigma^2}$ is an isotropic Gaussian of width σ. This is essentially equivalent to replacing a contact interaction $g\delta(\mathbf{r})$ with a finite ranged interatomic potential. The width σ of the Gaussian should of course be chosen to be small with respect to the scale in which the noncondensate density varies.

In practice, instead of smoothing over the full effective potential, we smooth both densities individually, an equivalent procedure to performing the convolution of Eq. (4.7). The effective potential is required at the position of every test particle and the condensate grid points. To avoid having to generate the summation of Eq. (4.26) at all of these points, the densities can be Fourier transformed. This is advantageous since Fourier transform of a convolution is the product of Fourier transforms, therefore, the densities only need to be smoothed once at every time step. Then, by inverse Fourier transforming the smoothed density is obtained, and can be used to generate the potential. The test particles velocities and positions can then be fully updated.

We typically choose the smoothing parameter σ to be approximately 2.5 times the thermal cloud grid spacing, $\Delta x_{\rm th}$ (for the example shown, $\Delta x_{\rm th} = \Delta x_{\rm c}$). The cloud in

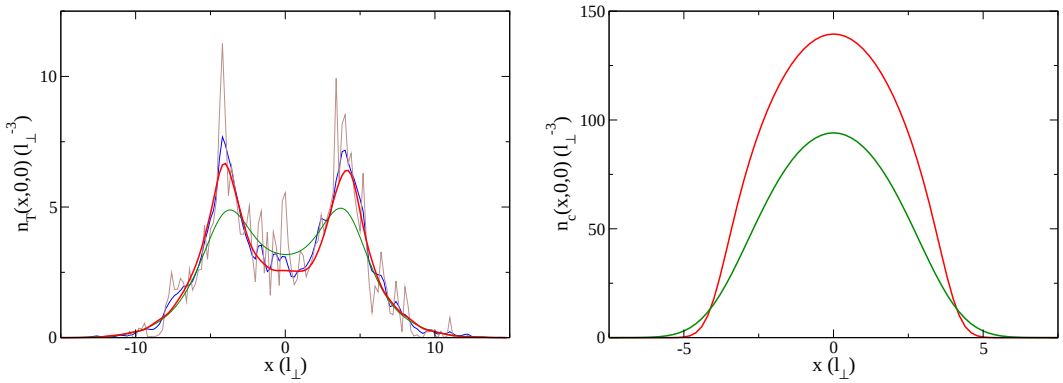

Figure 4.7: Left: Thermal cloud density for the system parameters as described in Sec. 4.1 for $0.5T_c$, before smoothing (grey), after smoothing with $\sigma = 1.2 \times \Delta x_{\rm th}$ (blue), $2.5 \times \Delta x_{\rm th}$ (red) and $6 \times \Delta x_{\rm th}$ (green). Right: Condensate density before smoothing (red), and after smoothing with $\sigma = 6 \times \Delta x_{\rm th}$ (green).

cell extracted thermal density (grey of Fig. 4.7) exhibits large spatial fluctuations. The effect of different levels of smoothing on the thermal cloud is clearly seen in Fig. 4.7 (Left). Clearly the smoothing should happen over more than one grid point. When we smooth with a Gaussian which is only $1.2 \times \Delta x_{\rm th}$ (blue), the resulting thermal cloud density still exhibits spatial fluctuations, therefore, more smoothing is required. However when the thermal density is convolved with a Gaussian of width $6 \times \Delta x_{\rm th}$ (green), the result is that the thermal cloud density has less of the characteristic shape that you would expect, with the central density and the peaks all being of similar magnitude i.e. such pronounced

smoothing lead to unphysical results. We find that a smoothing parameter of $2.5 \times \Delta x_{\rm th}$ (red) generates the 'correct' characteristic shape of the thermal density; we hence choose this smoothing parameter for all future work. It is important to note that changing the size of σ slightly from the chosen value should result in a very similar profile and for all systems, many values of smoothing functions should be tested to ensure an appropriate value is chosen which does not affect the overall dynamics.

For consistency the condensate density is also convolved with the smoothing function, as shown in Fig. 4.7 (Right). For values of smoothing $\sigma = 1.2 \times \Delta x_{\rm th}$ and $2.5 \times \Delta x_{\rm th}$ the condensate profile lies on top of the original unsmoothed profile; however when the smoothing function is large, e.g. for $6 \times \Delta x_{\rm th}$, the characteristic shape of the condensate profile becomes considerably affected (green). In particular, 'over-smoothing' for the condensate density results in a lower central density and broader tails.

Our choice to also smooth the condensate density is motivated by consistency arguments, since both thermal and condensate densities appear in the effective interaction Eq. (4.25). In general, such a procedure does not affect results and so it is simply a matter of choice whether to do so or not. However, it is important to note that if the condensate contains macroscopic excitations, such as solitons and vortices, smoothing of the condensate density is not recommended, since it could result in the loss of definition of the structure being studied which in turn could affect the dynamics of such an excitation.

We have shown in Chapter 3 how 'anti-damping' [94] can be observed for solitons at zero temperature due to sound emission in an inhomogeneous background, and in Ref. [67], the ZNG equations are solved to show how finite temperature effects can also have a dissipative effect on dark soliton dynamics. Fig 4.8 shows how the anti-damped trajectory of a $0.2c$ soliton (obtained by solving the coupled ZNG equations) in an elongated geometry ($\omega_z = 2\pi \times 5$ Hz [67]) is altered by the act of smoothing over the condensate density.

So far in this explanation of numerics, we have only accounted for the free streaming terms of the QBE (i.e. the solution of the left hand side of Eq. (4.2)). In order to deal with the important collisional processes, we follow the procedure outlined by Jackson and Zaremba [159] and earlier work by Jackson and Adams [218], to calculate the Monte Carlo collisional probabilities for each particle, $C_{12}[f, \phi]$ and pair of test particles, $C_{22}[f]$.

4.3 Collisions

The integrals C_{12} and C_{22}, Eqs. (2.40) and (2.41) respectively, describe how the phase space distribution changes with time as a result of collisions. If the timescale between collisions is long i.e. it is only possible for a particle to undergo one collision per time step, then the possibility of a collision happening can be included at the end of each time step. This essentially means that we can treat the evolution of the particle independent

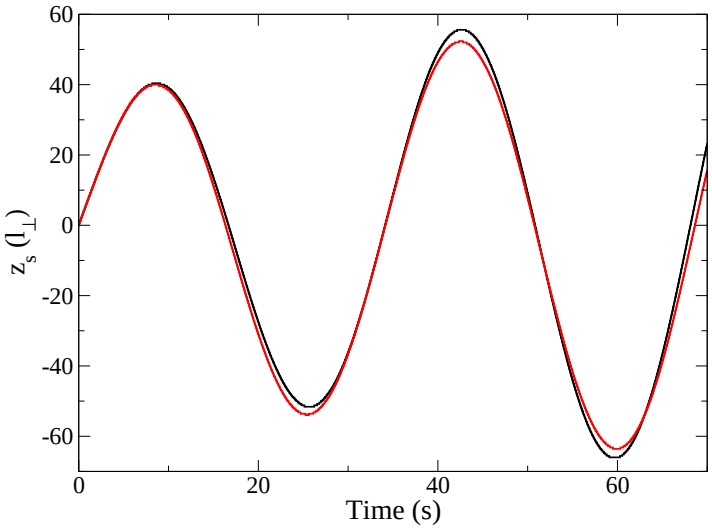

Figure 4.8: Position of $0.2c$ speed soliton in an elongated trap over time (black) and for the same case when the condensate density has been convolved with a smoothing function of width $3.5\Delta z_{\rm th}$ (red). The system parameters are: $N_{\rm TOT} = 10000, T \simeq 0.5Tc$, with $T_c = 166$nK, $\omega_\perp = 1000 \times 2\pi$ Hz and trap aspect ratio $\lambda = 0.005$.

of its collisions. When determining whether a particle has undergone a collision or not, there are four possible collision outcomes which we must consider. We summarise these in the table below.

Event	Colliding Particles	Outcome
$C_{12}^{\rm out}$ Collision	Thermal Atom	Addition of atom to thermal cloud
	Condensate Atom	Condensate atom removed
$C_{12}^{\rm in}$ Collision	2 Thermal Atoms	Removal of atom from thermal cloud
		Addition of atom to the condensate
C_{22} Collision	2 Thermal Atoms	No change to thermal atom number
		No change to condensate atom number
No Collision	N/A	No change to thermal atom number
		No change to condensate atom number

We have discussed the possibility of collisions happening in terms of thermal atoms. While the C_{22} collisions lead to no change in the total number of atoms in the thermal cloud, they do nonetheless cause a redistribution of thermal atoms to different energy levels after the collision.

Within the simulations, we model thermal atoms with a cloud of representative test particles; hence we will further refer to collisions of test particles or test particles with condensate atoms. These test particle collisions alter the phase space density which is multiplied by the weighting factor γ before integrating over momenta to obtain the phys-

ical thermal atom density.
In each case when a collision occurs, the colliding test particle velocities are updated accordingly, and if the collision is of the C_{12} type, i.e. involving a condensate atom (in the initial or final state), the $-iR$ source term of the GPE is also updated before further time evolution takes place.

We now give a detailed description of the numerical algorithm which is used to determine whether a collision event has taken place; we begin by discussing how the test particles are rebinned and the collisional probabilities are assigned.

4.3.1 Re-binning of test particles

To determine the collision probabilities we first need to re-bin the test particles into smaller cells. The algorithm involved in calculating the C_{22} collision probability picks two test particles at random to determine if they collide or not. If this was to happen in every radial and axial cell the test particles reside in from the previous dynamics, this pair of test particles could be spatially very far apart therefore it is intuitive to sub divide the cells further. We do this by further binning the test particles into segments azimuthally as shown for the radial direction in Fig. 4.9. The resulting cells have no less than 30 test

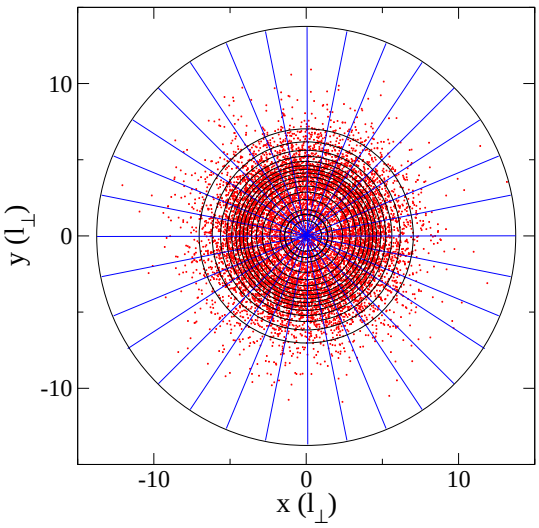

Figure 4.9: A sample of 10000 of test particles from a cloud of $N_{tp} = 275000$ are further binned into cells azimuthally, shown by the blue lines.

particles in each and could have anything up to 140 in the areas around the edge of the condensate where the thermal density is highest.
The algorithm for the collisions begins in one of these cells and calculates the probability

of *each* test particle in this cell undergoing a collision of type $C_{12}[f,\phi]$, and of every *pair* of test particles undergoing a collision of the type $C_{22}[f]$. The algorithm then moves to the next cell and does the same for the test particles residing there. We now define these probabilities and describe the numerical algorithm we use to compute them.

4.3.2 Definition of probabilities

In Appendix C we briefly describe how an expression for the rate of collisions happening in a unit volume per unit time can be derived from the collision expressions of Eqs. (2.40) and (2.41). These expressions all involve integration over momenta which has been approximated in [59, 159] by a Monte Carlo sampling technique. We define the resulting probabilities for each collision case in this section.

The probability that the ith test particle suffered a collision with a condensate atom that will result in an atom being added to the thermal cloud in a time Δt, is given by

$$\bar{P}_i^{\rm out} = \gamma n_c \sigma v_r^{\rm out}(1+f_3^{\Omega_R})(1+f_4^{\Omega_R})\Delta t, \tag{4.27}$$

where $\sigma = 8\pi a_s^2$ is the scattering cross section and $v_r^{\rm out}$ is the relative velocity of the incoming particles in the centre of mass frame. $f_3^{\Omega_R}$ and $f_4^{\Omega_R}$ are phase space distributions for the outgoing pair of atoms 3 and 4 which have a randomly selected scattering angle Ω_R and whose velocities lie on a sphere centred on $(\mathbf{v}_c+\mathbf{v}_2)/2$ of radius $v_r^{\rm out}/2$, where $\mathbf{v}_2$ is the velocity of the incoming atom 2 which collides with the condensate atom. The probability that the ith test particle has a collision with a condensate atom which results in an atom being removed from the thermal cloud, is given by

$$\bar{P}_i^{\rm in} = \gamma \frac{\sigma n_c \mathcal{A}_v}{\pi v_r^{\rm in}} f_4^{\mathbf{v}_\perp^R}(1+f_3^{\mathbf{v}_\perp^{\mathbf{R}}})\Delta t, \tag{4.28}$$

where $\mathbf{v}_r^{\rm in}$ is the velocity of the incoming thermal atom 2 with respect to the condensate velocity in the locality of the test particle, and $\mathbf{v}_\perp^R$ is a velocity vector which is perpendicular to $\mathbf{v}_r^{\rm in}$. The area $\mathcal{A}_v$ is the area of a sphere which compasses all allowed velocity values, i.e. all regions of phase space which are occupied.

The velocity of the other incoming thermal atom 4 is given by

$$\mathbf{v}_4 = \mathbf{v}_c + \mathbf{v}_\perp + \frac{g n_c}{m v_r^{\rm in}} \hat{\mathbf{v}}_r^{\rm in}, \tag{4.29}$$

where $\hat{\mathbf{v}}_r^{\rm in}$ is the unit vector of $\mathbf{v}_r^{\rm in}$. Through conservation of momenta, we deduce that the velocity of the outgoing thermal atom is given by

$$\mathbf{v}_3 = \mathbf{v}_2 + \mathbf{v}_\perp + \frac{g n_c}{m v_r^{\rm in}} \hat{\mathbf{v}}_r^{\rm in}. \tag{4.30}$$

The probability that a C_{22} type collision happens is given for a pair of test particles rather than a single one. That is, the probability that the test particle pair ij suffer a collision in the time interval Δt, is given by

$$P_{ij}^{22} = \gamma \tilde{n} \sigma |\mathbf{v}_i - \mathbf{v}_j| (1 + f_3^{\Omega_R})(1 + f_4^{\Omega_R}) \Delta t. \tag{4.31}$$

where $\gamma = \tilde{N}/N_{\rm tp}$ is the weighting factor between the number of actual thermal atoms $\tilde{N}$, and the number of simulated test particles $N_{\rm tp}$. As in Eq. (4.28), the velocities, and therefore final states, $f_3^{\Omega_R}$ and $f_4^{\Omega_R}$, of outgoing particles are chosen with the use of a randomly selected scattering angle Ω_R. This is sampled numerically by calculating velocity vectors $\mathbf{v}_3$ and $\mathbf{v}_3$ using spherical symmetry and sampling the phase space distributions f_3 and f_4 in the regions of phase space in which these velocities reside.

We aim now to determine whether a collision has occurred for a particular test particle or pair of test particles in a cell: The decision whether a collision has happened or not, and if so what type, is made by calculating these probabilities for each test particle (or pair of test particles in the C_{22} collisional case), and the decision as to which collision, if any, the test particle has experienced is determined at the end of the algorithm through comparison with a random number.

We begin by describing the determination of the particle exchanging C_{12} collisions: Initially we consider those collisions which result in a test particle being added to the thermal cloud distribution and one removed from the condensate, i.e. an 'out' collision; we then discuss collisions which remove a test particle from the thermal cloud distribution with an atom being added to the condensate i.e. an 'in' collision; finally we discuss the calculation of the probability that a C_{22} type collision occurs.

We look at the cells one at a time and within each cell we consider each test particle individually for the C_{12} collisions (and later, in pairs for the C_{22} collisions). This allows us to determine the position of the test particle and therefore quantities such as condensate and noncondensate density, fugacity, condensate velocity and chemical potential at its position which are needed for the collision probability calculation.

Before going into the detailed explanation of the determination of collision probabilities we should point out that numerical calculation of the collisional probabilities for the C_{12} collisions of both types, given below, differ slightly than those defined in Eqs. (4.27) and (4.28). The reason for this is to ensure that the term, $f_2 f_3 f_4$ centred within the difference $(f_2 + 1) f_3 f_4 - f_2(1 + f_3)(1 + f_4)$ of scattering amplitudes in the C_{12} collisional integral cancels also exactly in the numerics, as it should; this is necessary since the numerics involved in determining whether a $C_{12}^{\rm out}$ or $C_{12}^{\rm in}$ collision occurs, differ slightly.

4.3.3 $C_{12}^{\rm out}$ Collisions

The probability of an 'out' collision occurring is calculated as

$$P_i^{\rm out} = n_c \sigma v_r^{\rm out} (1 + f_3^{\Omega_R} + f_4^{\Omega_R}) \Delta t. \tag{4.32}$$

where

$$v_r^{\rm out} = \sqrt{|\mathbf{v}_c - \mathbf{v}_2|^2 - 4(U_{\rm eff} - \mu_c)/m} \tag{4.33}$$

is the relative velocity of the incoming particles in the centre of mass frame. The difference in mean field energy for the condensate and thermal cloud is gn_c, therefore, when a collision of this type takes place and an atom leaves the condensate with the simultaneous addition of an atom to the thermal cloud, the collision results in an increase in potential energy of the thermal cloud of gn_c. To ensure this increase in energy can occur, there is a constraint on the energy of incoming thermal velocities which must be satisfied. This constraint ensures that the incoming thermal atom has an excess of gn_c kinetic energy and so the outgoing thermal atoms will each have energies of *at least* gn_c. In the Thomas-Fermi limit, $gn_c = U_{\rm eff} - \mu_c$. Therefore, the condition for the energy of the colliding pair is,

$$\frac{1}{2} m |\mathbf{v}_c - \mathbf{v}_2|^2 > 2gn_c. \tag{4.34}$$

Since $f_3^{\Omega_R}$ and $f_4^{\Omega_R}$ are the phase space distributions in the vicinity of the outgoing test particles after the collision, we need to calculate the final states of the collision, i.e. the velocities of the outgoing thermal particles 3 and 4. We begin by calculating random variates $\phi, \cos\theta, \sin\theta$ (defined with random numbers in the same fashion as in Sec. 4.2.1), in order to calculate velocity values for the outgoing particles 3 and 4 within the scattering angle centred on $(\mathbf{v}_c + \mathbf{v}_2)/2$. This scattering sphere will have the diameter which is the width of the phase space box, *velbox*.

We use the notation *temp_v3* and *temp_v4* when referring to the outgoing velocities $\mathbf{v}_3$ and $\mathbf{v}_4$ to denote the fact that they will only become the true velocities of these particles if a collision of this type is deemed to happen, in which case one *new test particle will be created*.

We assign the components of the velocity vector for the outgoing particle 3 as

$$\begin{aligned} temp\_v3(\mathrm{x}) &= (v_i(x) + v_c(x))/2 + 0.5{*}v\_rel^2(\mathrm{x}){*}\sin\theta\cos\phi, \\ temp\_v3(\mathrm{y}) &= (v_i(y) + v_c(y))/2 + 0.5{*}v\_rel^2(\mathrm{y}){*}\sin\theta\sin\phi, \\ temp\_v3(\mathrm{z}) &= (v_i(z) + v_c(z))/2 + 0.5{*}v\_rel^2(\mathrm{z}){*}\cos\theta, \end{aligned}$$

and for the outgoing particle 4 as

$$temp\_v4(\mathrm{x}) = (v_i(x) + v_c(x))/2 \text{ - } 0.5 v\_rel^2(\mathrm{x}){*}\sin\theta\cos\phi,$$

$$temp\_v4(\mathrm{y}) = (v_i(y) + v_c(y))/2 \text{ - } 0.5 v\_rel^2(\mathrm{y}) * \sin\theta \sin\phi,$$
$$temp\_v4(\mathrm{z}) = (v_i(z) + v_c(z))/2 \text{ - } 0.5 v\_rel^2(\mathrm{z}) * \cos\theta,$$

where $\mathbf{v}\_\mathrm{rel}^2 = |\mathbf{v}_c - \mathbf{v}_2|^2$ obeys the constraint Eq. (4.33) above, $\theta \in [0, \pi]$ is the angle of projection in the axial direction and $\phi \in [0, 2\pi]$, the angle of rotation about the radial direction.

Now the phase space cells in which outgoing particles 3 and 4 belong to are determined, and, therefore, the phase space distributions $f_3^{\Omega_R}$ and $f_4^{\Omega_R}$ can be calculated (via the cloud in cell method (See Sec. 4.2.4)).

We are now equipped with the information to calculate the probability that a C_{12}^{out} collision has occurred involving the ith test particle, via expression (4.32).

4.3.4 C_{12}^{in} Collisions

The probability of an 'in' collision occurring is

$$P_i^{\mathrm{in}} = \frac{g n_c \mathcal{A}_v}{\pi v_r^{\mathrm{in}}} f_4^{\mathbf{v}_\perp^R} \Delta t. \tag{4.35}$$

where $\mathbf{v}_r^{\mathrm{in}} = \mathbf{v}_2 - \mathbf{v}_c$ is the velocity of the incoming thermal atom 2 with respect to the local condensate velocity and $\mathbf{v}_\perp^R$ is a random, 2D velocity vector which is distributed uniformly over the area $\mathcal{A}_v$ which is the area of allowed phase space i.e. $\mathcal{A}_v = \pi * (velbox/2)^2$. Numerically, we calculate the components of the vector $\mathbf{v}_\perp$ which are perpendicular to $\mathbf{v}_r^{\mathrm{in}}$. Following this procedure for the whole cloud of test particles is a way of obtaining the Monte Carlo estimate of the integral over $\mathbf{v}_\perp$ which appears in the determination of these probabilities (for more detail see [59, 159]). We determine the components of this vector using random variates and begin by defining the unit vector,

$$\hat{\mathbf{v}}_r^{\mathrm{in}} = \frac{\mathbf{v}_2 - \mathbf{v}_c}{\sqrt{\mathbf{v}\_\mathrm{rel}}}. \tag{4.36}$$

The orthogonal vectors, $\mathbf{v}_\perp^{(1)}$ and $\mathbf{v}_\perp^{(2)}$ are defined in terms of their respective components as

$$v_\perp^{(1)}(x) = (\sqrt{r_{\mathrm{vel}}}\cos\theta)\cos\theta_2\cos\phi, \quad (4.37) \qquad v_\perp^{(2)}(x) = -(\sqrt{r_{\mathrm{vel}}})\sin\theta\sin\phi, \quad (4.40)$$
$$v_\perp^{(1)}(y) = (\sqrt{r_{\mathrm{vel}}}\cos\theta)\cos\theta_2\sin\phi, \quad (4.38) \qquad v_\perp^{(2)}(y) = (\sqrt{r_{\mathrm{vel}}})\sin\theta\cos\phi, \quad (4.41)$$
$$v_\perp^{(1)}(z) = -(\sqrt{r_{\mathrm{vel}}}\cos\theta)\sin\theta_2 \quad (4.39) \qquad v_\perp^{(2)}(z) = 0, \quad (4.42)$$

where, $r_{\mathrm{vel}} = rand_7 * (velbox/2)^2$ is the magnitude of the velocity, which is thus constrained within phase space, and $\theta = 2\pi * rand_8$, is an angle of rotation in the plane perpendicular to $\mathbf{v}_r^{\mathrm{in}}$. The following variables then distribute these velocities in 3D cartesian space, corresponding to θ and ϕ from Sec. 4.2.1:

$\cos\theta_2 = \mathbf{v}_r^{\mathrm{in}}(z)$, $\quad \sin\theta_2 = \sqrt{1 - \cos^2\theta_2}$, where $\theta_2 \in [0, \pi]$ is the angle of projection in

the axial direction of the velocity of incoming thermal atom 2 relative to the condensate velocity, and ϕ is the angle of rotation around the radial plane which can be calculated using the relations

$$\cos\phi = \begin{cases} \frac{\mathbf{v}_r^{\rm in}(x)}{\sin\theta_2} & \text{if} \quad \sin\theta_2 > 0 \\ 1 & \text{otherwise} \end{cases} \qquad \sin\phi = \begin{cases} \frac{\mathbf{v}_r^{\rm in}(y)}{\sin\theta_2} & \text{if} \quad \sin\theta_2 > 0 \\ 0 & \text{otherwise} \end{cases}$$

The velocity of the incoming thermal atom 4 can now be calculated,

$$\mathbf{v}_4 = \mathbf{v}_c + \mathbf{v}_\perp^{(1)} + \mathbf{v}_\perp^{(2)} + \frac{g n_c}{m v_r^{\rm in}} \hat{\mathbf{v}}_r^{\rm in} \tag{4.43}$$

as well as the outgoing thermal atom 3 due to momentum conservation, $\mathbf{v}_3 = \mathbf{v}_2 + \mathbf{v}_4 - \mathbf{v}_c$. We now can calculate the probability that the ith test particle undergoes a $C_{12}^{\rm in}$ collision via expression (4.35).

At this point we have the probabilities that the ith test particle has undergone a collision involving a condensate atom which resulted in the removal of an atom from the condensate and the addition of the atom to the thermal cloud, Eq. (4.32), and the reverse process of the addition of an atom to the condensate and removal from the thermal cloud, Eq. (4.35). The next step is to determine which collision, if any, happened for the particular test particle under consideration (this should then be extended to all test particles in the system).

Determination of collisional type

We now test whether a collision of type C_{12} has occurred to the ith test particle or not and if it has, what type of collision it is i.e. 'in' or 'out' collision. Then, we need to update the noncondensate atom number and the dissipative term of the dissipative GPE, (2.32). We assign a random number, $X_i^{12} \in [0,1]$ to the test particle and compare with the probabilities calculated.
We distinguish the following cases

- $X_i^{12} < P_i^{\rm out}$: 'out' collision occurs and a new test particle is now created.
  When an 'out' collision occurs, the ith test particle's velocity is updated to the corresponding value, *temp*_**v**3, which has been calculated in the algorithm to determine the $C_{12}^{\rm out}$ collisional probability of that test particle. The 'new' test particle to be created is added to an array of all test particles which are to be *added* to the cloud as a result of a collision with a condensate atom. These test particles have velocities assigned by their corresponding *temp*_**v**4 values, and positions assigned to where the collision happened i.e. the position of the original ith test particle. This array will be compared by a similar array for the test particles which are leaving the thermal

cloud due to C_{12}^{in} collisions at the end of each time step so that the net change in the number of test particles will be enforced.

- $P_i^{\text{out}} < X_i^{12} < P_i^{\text{out}} + P_i^{\text{in}}$: 'in' collision takes place and a test particle is eliminated. We do this by calculating which phase space cell the test particle with velocity $\mathbf{v}_4$, would reside in and the phase space distribution in this cell. This is the test particle which needs to be eliminated, therefore we look through all the test particles in this velocity cell and if there is one which has not yet collided, we save it in the array of test particles to be eliminated at the end of the time step. If there are no test particles residing in this cell which have not yet undergone a collision, we widen the search by moving the velocity of this test particle to one of the eight adjoining cells in all 3 dimensions. This 'search' is repeated until a test particle in the appropriate cell is found which has not yet undergone a collision and this test particle can be added to the array to be eliminated at the end of the time step.

- $X_i^{12} > P_i^{\text{out}} + P_i^{\text{in}}$ - neither collision occurs.
  The algorithm moves on to the next test particle in that cell.

4.3.5 $-iR(\mathbf{r}, t)$ term updated

The dissipative term of the GPE is now updated via the expression

$$R(\mathbf{r}_{jkl}, t)\Delta\mathbf{r}\Delta t = \frac{\hbar}{2n_c}\sum_i (P_i^{\text{out}} - P_i^{in}). \tag{4.44}$$

This gives the net particle transfer rate at a particular grid point, where jkl denote the 3 axes, near the incoming test particle i's position.
These steps are repeated for every test particle in a phase space cell. Once all of the test particles in the particular phase space cell have been looked at, the algorithm looks at every pair of test particles in the phase space to determine if a C_{22} type collision has occurred.

4.3.6 C_{22} Collisions

The probability of test particles i and j suffering a collision is given by

$$P_{ij}^{22} = \gamma\tilde{n}\sigma|\mathbf{v}_i - \mathbf{v}_j|(1 + f_3^{\Omega_R})(1 + f_4^{\Omega_R})\Delta t. \tag{4.45}$$

Each phase space cell is looked at individually and a pair of atoms are selected at random and the probability that they suffer a collision is calculated.
The temporary velocities of the outgoing thermal atoms are calculated in the same way

as for the $C_{12}^{\rm out}$ collisional probabilities and Bose enhanced phase spaces, $(1 + f_3^{\Omega_R})$, and $(1 + f_4^{\Omega_R})$ are calculated in the usual cloud in cell method.

Determination of Collision Occurrence

To determine if a pair of test particles have suffered a collision, we assign a random number, $X_{ij}^{22} \in [0, 1]$ to each pair of test particles.
We distinguish the following two cases:

- $X_{ij}^{22} > P_{ij}^{22}$: collision has occurred.
  Velocities are updated to the new values, $\mathbf{v}_3$ and $\mathbf{v}_4$ and the next pair of test particles considered.

- $X_{ij}^{22} < P_{ij}^{22}$: no collision occurs.
  The next pair of test particles considered.

These steps are repeated for every pair of test particles in a given phase space cell. Once all pairs have been considered for collision, the algorithm begins again in the next phase space cell to determine whether the individual particles have undergone a C_{12} type collision or the particle pairs have undergone a C_{22} type collision.

When all phase space cells and hence, test particles have been considered, the algorithm can move to the condensate evolution at this time step, but not before determining the collective effect of the $C_{12}^{\rm out}$ and $C_{12}^{\rm in}$ collisions. We describe how this is incorporated into the evolution in the next section.

4.3.7 Updating the number of test particles

As a result of the Monte Carlo algorithm discussed above, at every time step we obtain an array of test particles which our algorithm has decided should be added to the cloud of test particles which we denote *ADD(Out_num)*, and an array of test particles which need to be eliminated, denoted *SUB(In_num)*. To proceed further, we compare the number of test particles that need to eliminated with the number that needs to be added.

Our scheme for efficient numerical incorporation of this effect is as follows:

- If the same number need to be added as subtracted, then we can simply update the positions and velocities of those which need to be eliminated to the positions and velocities which we have assigned to the particles which need to be added; in other words, we implement an algorithm of the form:

  do $i = 1$, *In_num*
  $\mathbf{r}(SUB(In\_num)) = \mathbf{r}(ADD(Out\_num))$

$\mathbf{v}(SUB(In\_num)) = \mathbf{v}(ADD(Out\_num))$
end do

- If more test particles need to be eliminated than added, we update the position and velocities of the required number of test particles as above; for the remaining "excess" test particles which need to be eliminated, we update their positions and velocities to those of another test particle which already exists and update the index of this test particle so that it will be eliminated for the next time step. We do this via:

do $i = 1$, (In_num - Out_num)
$\mathbf{r}(i + Out\_num) = \mathbf{r}(Tot\_num - i + 1)$
$\mathbf{v}(i + Out\_num) = \mathbf{v}(Tot\_num - i + 1)$
end do

where Tot_num is the total number of test particles at that time step.

- However, if more test particles need to be added than eliminated we update those which should be eliminated and are left with an excess number of ($Outnum$ - In-num) test particles, which are then created (indices greater than $Totnum$) with the position and velocities assigned.

do $i = 1$, (Out_num - In_num)
$\mathbf{r}(Tot\_num + i) = \mathbf{r}(In\_num + i)$
$\mathbf{v}(Tot\_num + i) = \mathbf{v}(In\_num + i)$
end do

The total number of test particles now needs to be updated for the next time step,
Total number of test particles = Tot_num + Out_num - In_num.
We can now move on to condensate propagation with the updated $-iR(\mathbf{r}, t)$ source term as a result of $C_{12}[f, \phi]$ collisions (described in Sec. 4.3.5).

4.4 Condensate propagation

The equation we need to solve is the generalised GPE:

$$i\hbar\frac{\partial\phi(\mathbf{r},t)}{\partial t} = \left(-\frac{\hbar^2\nabla^2}{2m} + V_{\rm ext}(\mathbf{r}) + g\left[n_c(\mathbf{r},t) + 2\tilde{n}(\mathbf{r},t)\right] - iR(\mathbf{r},t)\right)\phi(\mathbf{r},t)\ , \tag{4.46}$$

which can be written in operator form as

$$i\hbar\frac{\partial}{\partial t}|\phi(t)\rangle = \hat{H}(t)|\phi(t)\rangle \tag{4.47}$$

where $\hat{H}(t) = \hat{T} + \hat{V}(t)$ is the system Hamiltonian, containing kinetic and potential energy parts where $\hat{V}(t)$ includes the damping/growth term $-iR(t)$. All of the time dependence is maintained in the potential term with the formal solution to this equation given as:

$$|\phi(t + \Delta t)\rangle = \hat{U}(t + \Delta t, t)|\phi(t)\rangle. \tag{4.48}$$

A split operator method is again employed to evolve the condensate wavefunction.

When the condensate numbers become large, the interaction term can cause numerical instabilities. To avoid this, the Hamiltonian can be expanded as a Taylor series and the interaction term approximated by reverse differencing [59]. The expression becomes

$$\tilde{V}(t) \equiv \frac{1}{2}[3\hat{V}(t) - \hat{V}(t - \Delta t)]. \tag{4.49}$$

Therefore, the evolution operator becomes

$$\hat{U}(t + \Delta t, t) \simeq e^{-i\tilde{H}(t)\Delta t/\hbar} + O(\Delta t^3) \tag{4.50}$$

with $\tilde{H}(t) = \hat{T} + \tilde{V}(t)$ where the propagation of the condensate is performed using the Baker-Campbell-Hausdorff, split operator form:

$$|\phi(t + \Delta t)\rangle = \left[e^{-i\tilde{H}(t)\Delta t/\hbar} + O(\Delta t^3)\right] |\phi(t)\rangle, \tag{4.51}$$

where the source term, $-iR(t)$, is included in the potential term, $\tilde{V}(t)$.
Performing a split on the evolution operator results in

$$e^{-i\tilde{H}(t)\Delta t/\hbar} = e^{-i\tilde{V}(t)\Delta t/2\hbar} e^{-i\hat{T}\Delta t/\hbar} e^{-i\tilde{V}(t)/2\hbar} + O(t^3). \tag{4.52}$$

The term $e^{-i\tilde{V}(t)\Delta t/2\hbar}$, is local in real space while $e^{-i\hat{T}\Delta t/\hbar}$ is local in momentum space. This requires that a Fourier transform and its inverse must be applied at each time step.

In brief, to obtain the wavefunction at time $t+\Delta t$ we perform the following operations:

- The potential factor $\tilde{V}(t)$ is applied by multiplication to the wavefunction at time t (which is defined on a spatial set of grid points).
- The wavefunction is then Fourier transformed and the kinetic factor $\hat{T}$, applied in momentum space.
- Applying an inverse Fourier transform brings it back to real space.
- Then the final potential factor is applied.

The wavefunction is evolved over a sequence of time steps with the limiting factor arising from the Fourier transforms. However, efficient Fast Fourier Transform schemes exist for this (see e.g. http://www.fftw.org/).

This concludes our analysis of reviewing the procedure for solving the coupled ZNG equations as originally set up by Jackson and Zaremba [159]. A schematic of this process summarising the main steps in shown in Fig. 4.10.

In the forthcoming two chapters, we implement this numerical scheme to analyse the effect of finite temperatures on vortex dynamics and Josephson effects.

4.5 Numerical procedure summary

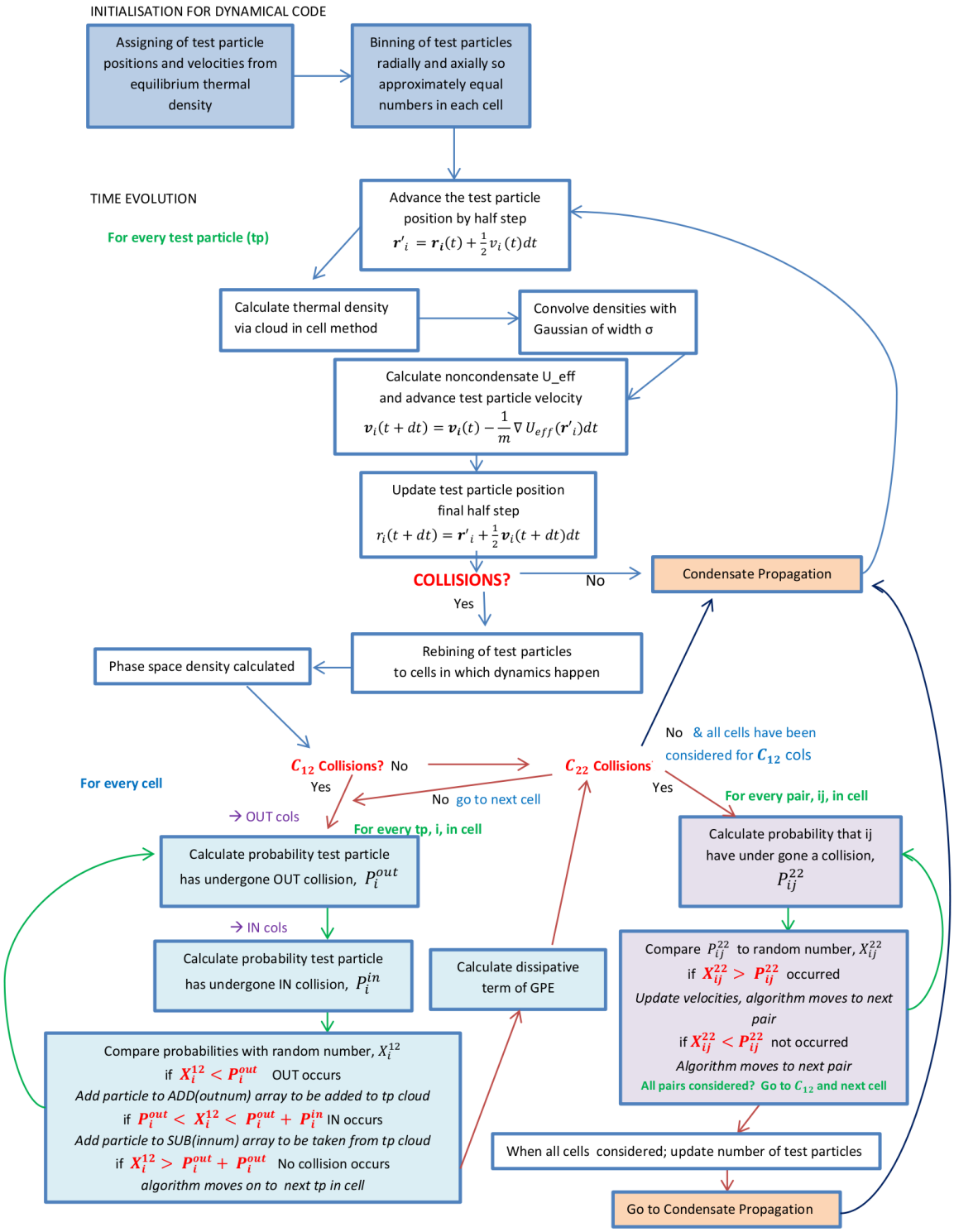

Figure 4.10: Schematic of the numerical implementation of the ZNG scheme.

Chapter 5

Finite Temperature Vortex Dynamics

The existence of quantised vortices in atomic condensates is a feature of the superfluid nature of these systems. In Chapter 2, we defined the superfluid velocity as the gradient of the phase,

$$\mathbf{v}_c(\mathbf{r},t) = \frac{\hbar}{m}\nabla\theta(\mathbf{r},t). \tag{5.1}$$

The curl of this velocity is

$$\nabla \times \mathbf{v}_c = 0 \tag{5.2}$$

indicating that the flow is irrotational. If a superfluid is rotated below a certain *critical* angular rotation frequency, denoted Ω_c, the density profile is the same as when it is at rest. However, in early experiments in the 1940's which involved rotating superfluid Helium II above the critical velocity, the resulting profiles did not agree with predictions for an irrotational flow. This disagreement was explained separately by Onsager [219] and Feynman [220], by the formation of vortex lines, leading to the description of quantisation of circulation, later confirmed experimentally by Vinen in 1961 [221].
Circulation is defined as

$$\kappa = \oint_{\mathcal{C}} \mathbf{v}_c \cdot d\mathbf{r}. \tag{5.3}$$

Since the superfluid velocity is given by the gradient of the phase, Eq. (5.1), we have that

$$\kappa = \frac{\hbar}{m}\Delta\theta, \tag{5.4}$$

where $\triangle\theta$ is the change of phase around a vortex. As the wavefunction must remain single-valued (i.e. must return to the same value after every integer 2π turn around the vortex) we conclude that the circulation must take on integer multiples of $(2\pi\hbar/m)$ i.e.,

$$\kappa = n\left(\frac{2\pi\hbar}{m}\right), \tag{5.5}$$

where $n = 0, \pm1, \pm2, \pm3..$ is the winding number of the vortex, i.e. it is the number of times that the phase, θ, winds through 2π around the vortex. The circulation of a superfluid is therefore quantised in units of $(2\pi\hbar/m)$. Multiply charged vortices have a value of circulation $|n| > 1$; although they have been found to be stable for some interaction strengths [222], in general they decay into a singly charged vortices with circulation $|n| = 1$ via a dynamical instability [123, 223].
The macroscopic wavefunction for a condensate containing a vortex of charge n has the form

$$\phi(\mathbf{r}) = |\phi(\mathbf{r})| \exp(2\pi n i). \tag{5.6}$$

The circulating fluid velocity around a vortex is given by

$$v = n\left(\frac{\hbar}{mr}\right). \tag{5.7}$$

At the very centre of the vortex, the condensate wavefunction vanishes and there is a phase singularity. Quantised vortices in Bose-Einstein condensates are now routinely created in the lab, see e.g. [50, 114, 117, 224] for early experimental realisations.

Vortices at $T = 0$

In a harmonically trapped condensate at zero temperature, an off-centred vortex follows a path of constant potential around the trap centre, moving at constant radius [112, 207–209] (see Fig. 5.1). It has been shown that this vortex precession corresponds to the 'anomalous' mode of the condensate [209], where the excitations of a condensate containing a central vortex have been found by solving the Bogoliubov equations for collective excitations of a condensate [225] (see Appendix A for the derivation of these from the GPE). The trapping potential used to confine atomic gases causes a variation in condensate density (See Fig. 5.2 (Left)), which causes a variation in the energy possessed by a vortex, with the maximum energy obtained by a central vortex. Effectively, it is this inhomogeneity which induces vortex motion in the absence of an external rotation [226, 227], since the vortex experiences a Magnus force which causes it to rotate around the centre of the

condensate [208], Fig. 5.1.

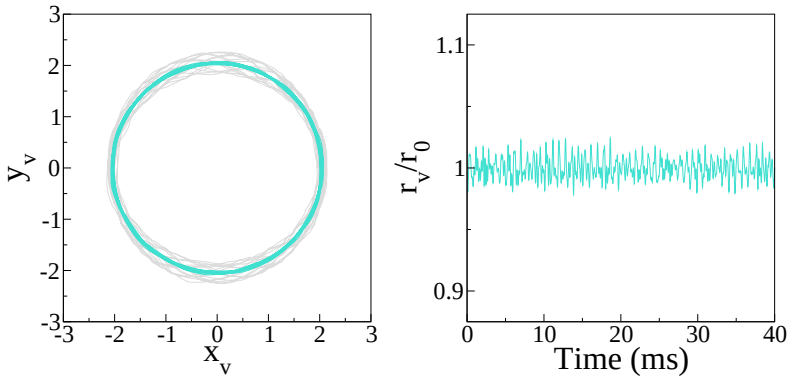

Figure 5.1: Left: Trajectory of an off-centred vortex in a condensate of $N_c = 10000$ at zero temperature (grey), and with respect to the condensate centre-of-mass (cyan) in a pancake-shape harmonic trap with frequencies: $\omega_\perp = 2\pi\times129$ Hz and $\omega_z = \sqrt{8}\omega_\perp$. Right: Radial coordinate of the vortex with respect to the condensate centre-of-mass, as a function of time, where $r_v = \sqrt{x_v^2 + y_v^2}$.

In Figure 5.1 we have plotted the trajectory of an off-centred vortex in a condensate containing $N_c = 10000$ ^{87}Rb atoms at zero temperature using the GPE. During initialisation of a vortex in the condensate, the centre-of-mass is perturbed from its initial position slightly, hence we have induced some centre-of-mass motion of the condensate. This is taken into account when we extract the position of the vortex with respect to the centre-of-mass of the condensate (cyan trajectory of Fig. 5.1). If this motion were not taken into account, the trajectory of the vortex would contain many jitters (grey trajectory of Fig. 5.1). Some jitter still remains, which is clear from the plot of the vortex radial coordinate with time $r_v(t)$, however, this effect is likely to be a numerical artifact of the vortex-tracking algorithm. For the remainder of this thesis, we will assume that all vortex trajectories, are calculated with respect to the condensate centre of mass motion.

Vortices at $T > 0$

At finite temperatures, the presence of a nonrotating thermal cloud induces a frictional force on the vortex, hence the vortex seeks to minimise its energy by radially moving out of the condensate [134, 228], as has been observed experimentally [48–50, 114].
Typically, most theoretical work to date has been based on zero temperature vortex dynamics with only few theoretical works focussing on the finite temperature properties of these systems. Fedichev and Shlyapnikov (FS) [134] describe the dissipation of the vortex in a cylindrical condensate, via scattering of thermal excitations in the vortex core. It is this scattering that provides an energy transfer from the vortex core to the thermal cloud causing the vortex to spiral out of the condensate. Further numerical analysis of vortex

dynamics at finite temperatures has been carried out by Schmidt *et al.* [136]; they used the c-field approach to model a vortex at finite temperature, and found good agreement between the stochastic vortex lifetime as a function of radial position and the analytic formula of FS [134]. Similar agreement was found in the approach by Duine, Leurs and Stoof (DLS) [135] where the dynamics of a vortex in a trapped condensate is described by means of a stochastic equation for its position. This variational equation is derived from the SGPE (see Chapter 2, Section 2.2.3), where the usual GPE is generalised with the inclusion of a damping rate to describe the growth of decay of the condensate and an additive noise term to simulate thermal fluctuations. In Sec. 5.2 we show that, in the limit of a static thermal cloud, our results for vortex decay agree fully with those of DLS.

Other theoretical works relating to finite temperature vortex dynamics include those by Wright, Bradley and Ballagh who, using the *c-field* approach (see [180] for a review), have shown that as the temperature of the system is increased, the angular momentum of the condensed mode decreases while the vortex radial coordinate and the precession frequency increase, until the vortex leaves the system and the condensate becomes irrotational [137, 138]. Precession frequency has also been found to smoothly vary with temperature when the thermal cloud and condensate are in equilibrium using the 'Popov' approximation [229] and the Hartree-Fock-Bogoliubov equations [230].

However, in all the techniques described above, major approximations are made on the thermal cloud dynamics. It has been previously shown that vortex decay in both approaches used by FS and by DLS, do not demonstrate as much dependence on temperature as results found using the ZNG theory [68]. We attribute this discrepancy to approximations made on the dynamics of the thermal cloud. Within the ZNG formalism, we can include all collisional processes involved in finite temperature systems, namely, thermal-thermal collisions (denoted C_{22}) and particle-exchanging, thermal-condensate collisions (C_{12}), see Chapter 2. In the present chapter, we show the necessity of including all dynamical, thermal cloud processes when modelling finite temperature vortex dynamics in experiments.

Outline of the chapter

We begin by setting up the framework for our simulations in Sec. 5.1. The main motivation for this chapter is studying finite temperature vortex dynamics and comparing with experiments, therefore, the largest sections are Sec. 5.2 and 5.4 in which we present results of decay rates and precession frequencies respectively, for finite temperatures. As we frequently use the trapping parameters of a recent experiment by Freilich *et al.* [31], we will gives details of it in Sec. 5.3.

In the remainder of the chapter, we present preliminary studies of two mechanisms which could be used as 'tools' experimentally. The first, in Sec. 5.5 investigates using the

effect of finite temperatures on the vortex core brightness, and the final, in Sec. 5.6 we investigate the radial translation of vortex in a condensate using a rotating thermal cloud.

5.1 Modelling finite temperature vortex dynamics

An advantage of the ZNG method for modelling finite temperature systems and in particular, vortex dynamics, is that the condensate and thermal densities are defined separately; as a result they can be easily observed independently from each other. This means we can gain insight into how the thermal cloud and condensate interact in the region of the vortex.

The density of both are shown for a condensate containing 10000 ^{87}Rb atoms at a temperature of 53nK in Fig. 5.2 (Left), with the corresponding mean-field potentials shown in the right graph. When a condensate contains a vortex (dashed lines), it has a region of zero density associated with the vortex core (see Fig. 5.3 (Left)), this means that the corresponding mean-field potential felt by the thermal atoms also has a dip at this location. The thermal cloud can therefore 'fill in' this region of low potential (similar core filling was found using a classical field approach by Wright *et al.* [137, 138]). This is more

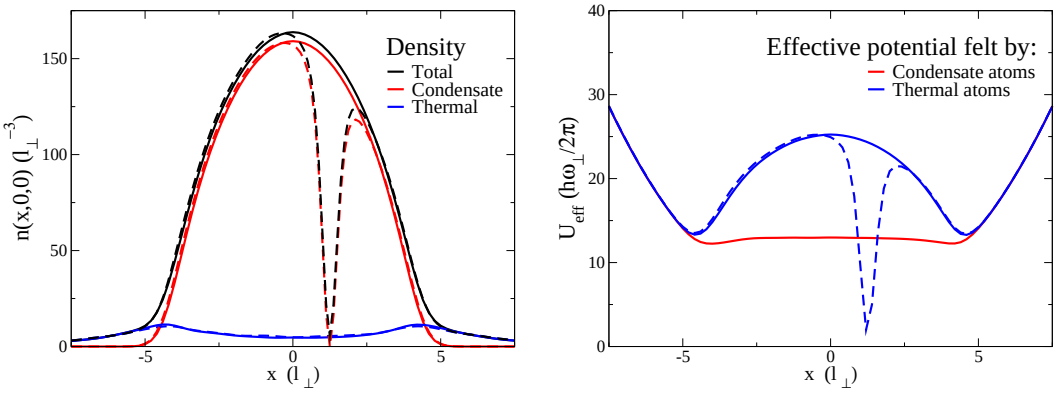

Figure 5.2: Left: Condensate n_c (red), thermal cloud $\tilde{n}$ (blue) and total $n = n_c + \tilde{n}$ (black) without a vortex (solid lines) and with a vortex placed at $0.3R_{\rm TF}$, where $R_{\rm TF} = 4.75\mu m$, (dashed lines) for a temperature of 54nK where $T_c \simeq 177$nK. Right: Effective potentials felt by the condensate (red) and thermal cloud (blue) with no vortex (solid), and effective potential felt by thermal cloud with a vortex at position $0.3R_{\rm TF}$ (blue dashed).

easily seen from the axial view of the thermal cloud density in Fig. 5.3, where the peaks in thermal cloud density are around the edges of the condensate as one would expect, and there is a further peak in the region where the vortex core is located.

The work in this chapter follows on from Brian Jackson's results on the investigation of vortex dynamics at finite temperature via the ZNG method, published in [68]. Much of the results we present will be generated using the same harmonic trapping parameters

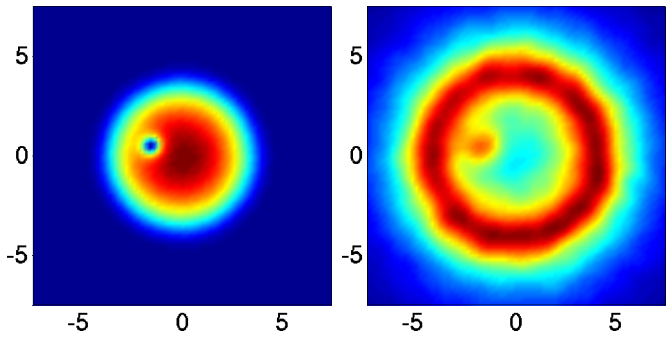

Figure 5.3: Density cross sections of condensate (left) and thermal cloud (right) at $z = 0$, where the colours range from blue corresponding to zero density, to red, corresponding to high density.

as [68] which are

$$\omega_\perp = 2\pi \times 129 \text{ Hz}, \text{ and } \omega_z = \sqrt{8} \times \omega_\perp. \tag{5.8}$$

This trapping geometry results in a pancake or oblate shaped condensate, Fig 5.4, which is advantageous since a vortex line in this geometry remains relatively straight throughout its motion because axial waves, called Kelvin waves [231], are suppressed.

One major difference between the work presented in the following sections on vortex

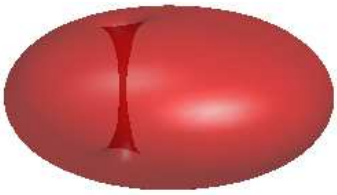

Figure 5.4: Isosurface of the condensate, it is easy to see the hollow, straight, off-centred vortex line.

decay rates and frequencies, and the results given in [68] is that here we fix the number of atoms in the condensate rather than in the system as a whole. Fixing the condensate number means that the condensate shape changes very little with temperature (apart from slight changes due to the mean-field produced by the thermal cloud), hence from a theoretical perspective, we can easily assess the effect that an increasing thermal cloud has on the dynamics.

We generate equilibrium densities as outlined in Chapter 4, for a given condensate number and temperature. We then place a vortex in the condensate by multiplying the condensate wavefunction by the phase factor

$$\phi(\mathbf{r}, t) = |\phi(\mathbf{r}, t)| \arctan\left(\frac{y - y_0}{x - x_0}\right). \tag{5.9}$$

This imprints the velocity field of a straight line vortex at the location (x_0, y_0). We evolve this wavefunction in imaginary time for a short period in order to ensure all density fluctuations and sound excitations generated by the imprinting process have been damped out. In order to fix the position of the vortex, we multiply the condensate wavefunction by the phase factor, as in Eq. (5.9), at every step of imaginary time propagation. This is a somewhat idealised method but it is the standard approach used in numerical vortex simulations.

After imaginary time propagation, this wavefunction is then used as the initial condition for the full dynamical simulation, as outlined in Chapter 4, and the trajectory of the vortex is followed by recording its x_v and y_v coordinates with time.
For a system of $N_c = 10000$ ^{87}Rb atoms, we have plotted the trajectories of an off-centred vortex, initially at position $r_0 = 0.4R_{\rm TF}$ (where $R_{\rm TF}$ is the Thomas-Fermi radius of the condensate, see Chapter 2, Sec. 2.1.3), at three different temperatures in Fig. 5.5. The corresponding radial coordinates, given by $r_v(t) = \sqrt{x_v(t)^2 + y_v(t)^2}$, have been plotted on the bottom of this figure.

At the lowest temperature of 53nK, the vortex radial coordinate increases more slowly than for higher temperatures, hence the vortex suffers less dissipation at lower temperatures. The dissipative effect that the vortices experience increases with increasing temperature, hence it is due to the presence of noncondensed atoms in the system. To see the effect of temperature on the rate of translation of the vortex, we can extract a rate of decay from the vortex radial coordinate. We present the results in the next section.

5.2 Vortex decay rates

In order to quantitatively compare the effect of increasing temperature on vortex lifetimes, we compare the rate at which their corresponding radial coordinate increases with time. This is the process originally used in [68].

From the bottom graph of Fig. 5.5, we can see that the radial coordinate appears to increase exponentially for some initial amount of time, therefore, we can approximate the initial radial growth by

$$r_v(t) = r_0 e^{\gamma t}, \tag{5.10}$$

where γ is the rate at which the vortex radial coordinate r_v increases from initial position r_0, with time, t.
If we plot the natural logarithm of the radial coordinate (see Fig. 5.6 (Left)), we can extract the coefficient of the exponential, which we associate with the rate at which the vortex radial coordinate increases. Since the vortex radial coordinate increases until the

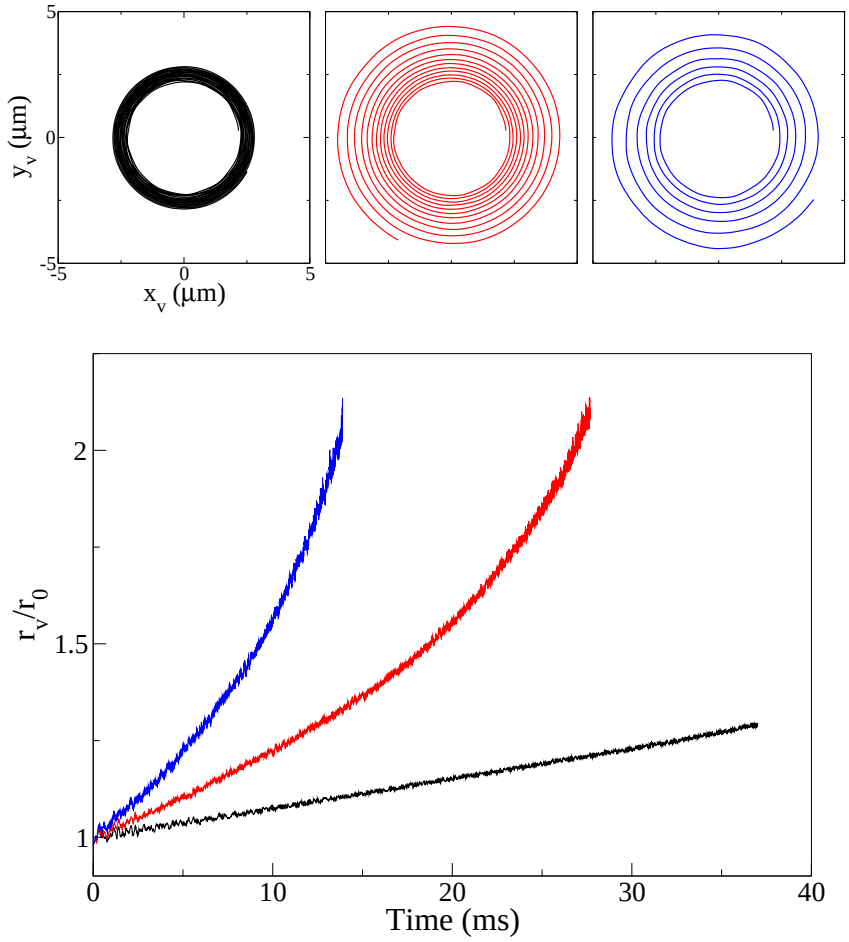

Figure 5.5: Top: (x_v, y_v) Smoothed position of vortex initially at $r_0 = 0.4R_{\rm TF}$ ($R_{\rm TF} \simeq 4.75\mu m$ for each of these temperatures), in condensates of $N_c = 10000$, with a variable number of thermal atoms, at temperatures 53nK (left, black), 89nK (middle, red) and 124nK (right, blue). Bottom: Radial coordinate of vortex over time normalised by initial vortex position, where $r_v = \sqrt{x_v^2 + y_v^2}$ at every instant in time.

vortex is no longer visible as part of the condensate, we shall call this quantity, γ, the vortex decay rate.

It is apparent from the fit of the decay rate in Fig. 5.6 (Right), that for all of the temperatures, the vortex radial coordinate follows exponential behaviour for *at least* 10ms. The exponential behaviour of the vortex at temperature 53nK appears to continue until we stop the simulation. The vortex at this temperature is closer to the centre of the condensate than the vortices at higher temperatures for most of this period of time. Therefore, we attribute this exponential behaviour to the behaviour of the vortex when it is close to the trap centre; similar exponential behaviour has been found in Refs. [68, 134, 135]. Henceforth, we use the time period of 10ms as a guideline for extracting values of the vortex decay rate γ. We initially assess the dependence of γ on the initial position of the

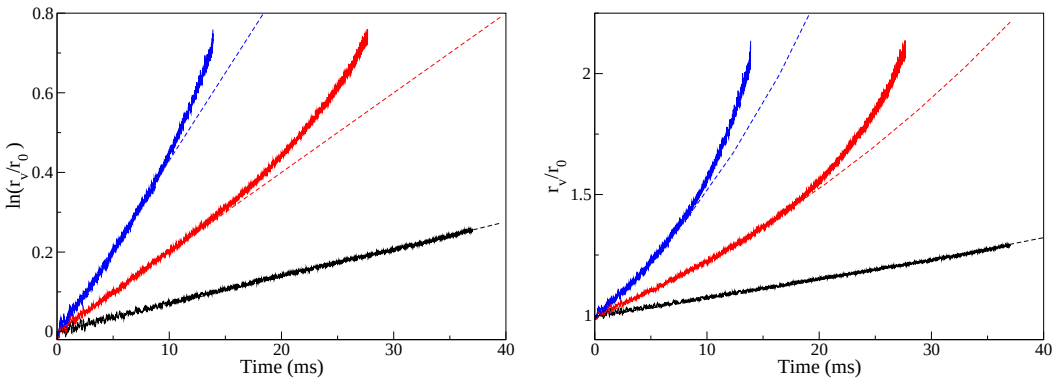

Figure 5.6: Left: Logarithmic plot of vortex radial coordinate normalised by initial vortex position over time to illustrate the extraction of decay rate γ for temperatures 53nK (black), 89nK (red) and 124nK (blue). The dashed lines are the lines $y = 0.007t$ (black dashed), $y = 0.02t$ (red dashed), and $0.044t$ (blue dashed). Right: Plot of the same vortex radial coordinates with the corresponding $r_v(t)/r_0 = \exp(\gamma t)$.

vortex by extracting the decay rate of vortices with different initial positions.

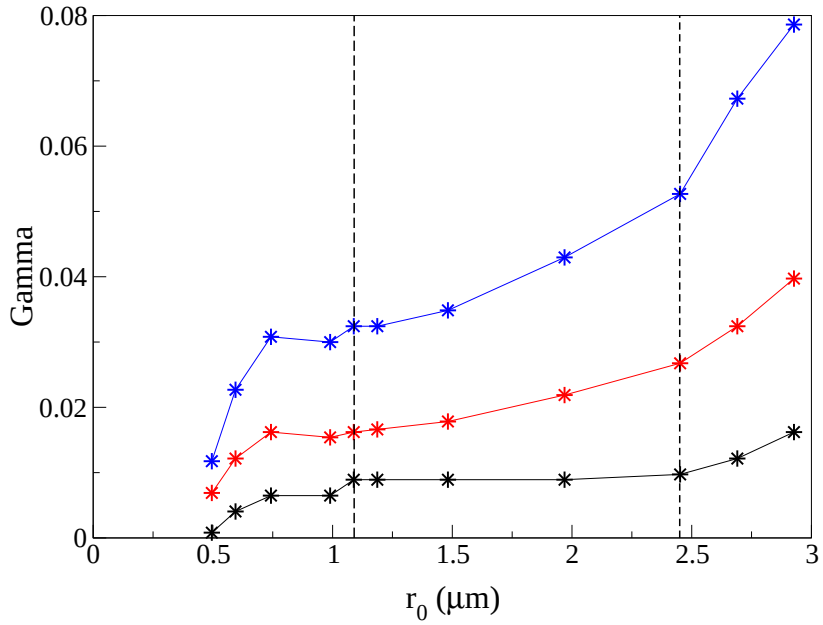

Figure 5.7: Values of decay rate γ for different initial vortex positions r_0, for temperatures 53nK (black), 89nK (red) and 124nK (blue). The decay rate has been extracted as shown in Fig. 5.6

The values of decay rate, γ, for the three temperatures 53nK, 89nK, and 124nK for different initial vortex positions are shown in Fig. 5.7. For all temperatures, increasing the vortex initial radial coordinate r_0 away from the centre and closer to the condensate edge (approximately $R_{\mathrm{TF}} = 4.75\mu m$), results in an increase in vortex decay rate, a feature which

is more pronounced for the higher temperatures. For example, for a vortex with initial position $0.15R_{\mathrm{TF}}$, there is an increase in decay rate of ~ 0.022 between the lowest, 53nK, and highest, 124nK, temperature. The reason for this is the higher thermal cloud density towards the edges of the condensate: since there is less mean-field repulsion, the vortex experiences a higher frictional force and so spirals out of the condensate quicker than if it were placed in the central region. Increasing the temperature increases the number of thermal atoms and therefore this effect is more prominent for higher temperatures.

Experimentally, it is difficult to observe a vortex in the regions of low condensate density, beyond $\approx 0.5R_{\mathrm{TF}}$ [31], therefore we will not analyse vortex dynamics in this region. When the vortex is placed close to the centre, we observe large fluctuations in the vortex position. This suggests that, due to a slowly varying effective potential in this region, a small change in vortex energy will cause the vortex trajectory to change more dramatically than it would in further regions of the trap. Therefore, a vortex placed close to the centre may be more sensitive to numerical, collisional kicks from propagation of the Boltzmann equation: for this reason we are not fully confident in describing the dynamics of a vortex residing in the very central region. For all temperatures, there is a region, bounded by the vertical, dashed lines in Fig. 5.7, in which the rate of decay has an almost linear relationship with initial vortex position. This is the region within which we will we carry out all further vortex dynamics analysis and simulations.

For the lowest temperature of 53nK, the decay rate of a vortex initially placed in this region is uniform and constant throughout. When the temperature is increased from 53nK, the decay rate increases with increasing initial vortex position and for the highest temperature of 124nK, the decay rate increases at a faster rate than for the temperature of 89nK. This means, the decay rate of a vortex, γ, is *dependent* on the initial position of the vortex r_0 and this is an effect which is more apparent at higher temperatures. We also can easily conclude that increasing the temperature results in higher vortex decay rates attributed to a larger thermal cloud, resulting in the vortex experiencing a higher frictional force. This decay could be due to interactions between the vortex core and the thermal excitations.

In Chapter 4, we described how we deal with the collision processes during the numerical simulation of the ZNG method. These collision processes contribute to the rate of change of the phase space distribution of thermal cloud. Since we deal with the collisions separately in our numerics, we can effectively switch them 'on' and 'off' at will. This is a useful tool in determining which collision type has the greater effect on the decay of a vortex, or is it just the thermal cloud mean-field which induces decay.

We repeat the vortex simulations for the higher temperature of 124nK for three initial

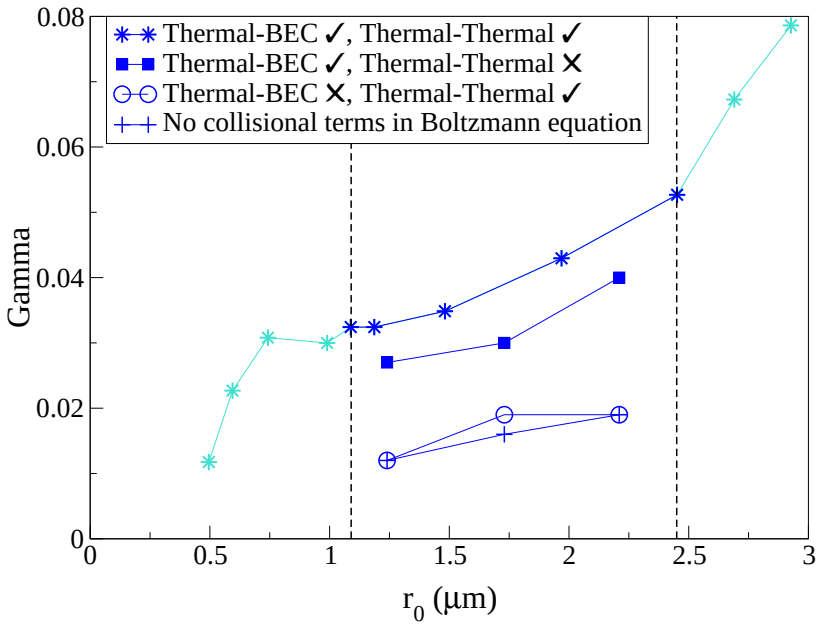

Figure 5.8: Vortex decay rates for a condensate of $N_c = 10000$ at a temperature of 124nK for different initial positions r_0, when all collision terms in the Boltzmann Equation 2.39 (stars), just the particle exchanging, C_{12} collisions are being simulated ($C_{12} \neq 0, C_{22} = 0$, solid squares), just the thermal, C_{22} collisions are accounted for ($C_{12} = 0, C_{22} \neq 0$, open circles), and no collisional terms are included in the Boltzmann equation ($C_{12} = 0, C_{22} = 0$, crosses).

vortex positions within the region outlined in Fig. 5.7. We simulate all possible combinations of dynamics available using the QBE. The results can be seen in Fig. 5.8. It is immediately clear that not accounting for any type of collision has the effect of reducing the decay rate of a vortex. Furthermore, we see that the largest contribution to the decay rate comes from the particle exchanging, C_{12}, collisions. This is apparent since in both cases when the C_{12} collisions are not accounted for, the decay rate is reduced the most. Neglecting to account for the thermal-thermal, C_{22}, collisions has a more significant effect when the particle-exchanging, C_{12}, collisions are included than when they are not. These findings are summarised for one particular initial vortex position ($r_0 \simeq 0.26 R_{\mathrm{TF}}$), within the region outlined in Fig. 5.9 for other temperatures.

This figure shows the nonlinear increase of the decay rate with increasing temperature, clearly highlighting the role of collisional processes particularly at higher temperatures. The process that results in the largest increase in damping rate is the inclusion of the particle-exchanging C_{12} collisions in agreement for all temperatures with Fig. 5.8. Our results are compared to the analytic predictions of Fedichev and Shlyapnikov (FS) [134], which accounts for the scattering of thermal excitations from the vortex core, and the results of Duine, Leurs, and Stoof (DLS) [135], which include the effects of C_{12} collisions within the static thermal cloud approximation. We find the predictions of DLS to

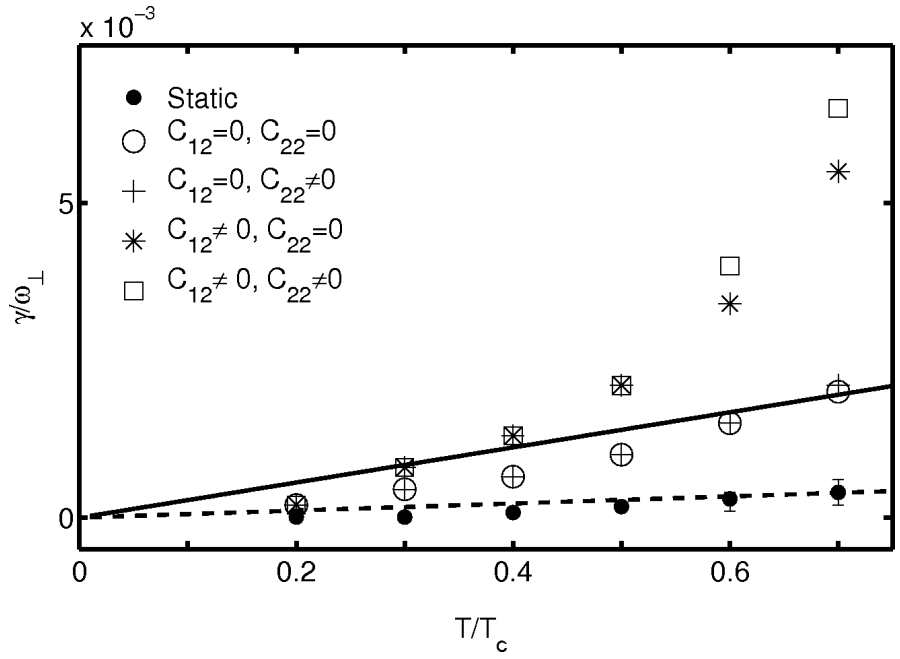

Figure 5.9: Values of γ based on different levels of approximation: static thermal cloud with condensate dissipation, iR, included (solid circles), thermal cloud allowed to evolve within the QBE (Eq. (2.39)) without collisions (open circles), with only thermal-thermal collisions (pluses), with only particle-transferring collisions (stars) or with all collision processes (squares). For comparison, analytic predictions of FS [134] (solid line) and DLS [135] (dashed line) are shown. (Calculations performed at fixed condensate number, $N_c \simeq 10000$, and an initial radial vortex offset $r_0 \simeq 0.26 R_{\rm TF}$ from the trap centre). We have adapted this figure from Ref. [68] to present our results.

be in full agreement with our results, in the corresponding limit where condensate dissipation from a static thermal cloud is included. The enhanced decay predicted by the full theory highlights the importance of including all dynamical processes when modelling experiments.

All further results presented in this chapter for finite temperatures will include all collision terms of the QBE unless otherwise stated.

In this section, we have demonstrated that the rate of decay of a vortex is not only dependent on the temperature of the system, but also on the initial position of the vortex. Due to the procedures used to experimentally generate vortices (see Chapter 1, Sec. 1.3.2), it is difficult to create a vortex in a predetermined position and often when a vortex is generated its position may be random. However, we will demonstrate a mechanism for radially translating a vortex to the desired position in Sec. 5.6.

Our motivation for assessing the temperature dependence on the precession of a vortex as well as investigating the rotation of the thermal cloud, came from a recent experiments by the group of David Hall in Amherst; therefore, we briefly described these in the next section, with further details of both in Secs. 5.4.1 and 5.6.

5.3 Recent experiments in the group of David Hall

In a recent experiment [31], the precession of vortex lines and dipoles were observed in real time. In typical experiments, the vortex core size is smaller than the wavelength of the light used to image it. As a result of this, the common method to image a condensate containing a vortex is to expand the condensate, and so the vortex core size also expands, therefore, enabling it to be identified [114]. However, as a consequence of this expansion the system is destroyed allowing no further time evolution of the vortex to be observed.

In the aforementioned experiment, the vortices arise during evaporation via the Kibble-Zurek mechanism [109–111, 232], and the procedure for imaging is as follows: approximately 5% of the condensate atoms are out-coupled along the z-axis so that they are no longer confined by the trap, and they therefore, fall with gravity (along z). This proportion expands and the position of the vortex can be resolved and measured. This leaves the remaining 95% of the atoms trapped in the condensate and the vortex continues to precess in them. At a later time, this process can be repeated and the position of the vortex at that time also measured. The result is a series of images of vortex position which means that the real time dynamics of the vortex can be assessed.

As a result of this technique, the group were able to observe a single vortex line for 655ms (the image at this time was of the remnant condensate), in a series of snapshots. Using these images, they were able to measure the precession frequency of the vortex line and the observed frequencies were approximately 5% higher than those expected for the geometry and condensate parameters [112]. This result motivated our study of the precession frequency of vortices at finite temperature (see Sec. 5.4).

Through correspondence with the group, we later learned about their early investigations into manipulating the position of a vortex by rotating the thermal cloud of a system at finite temperature. As a result of this, we also began investigating this effect and present preliminary findings in Sec. 5.6.

In the next section, we determine the effect of increasing temperature on the precession frequency of a vortex. Initially, we need to determine the dependence of precession frequency on the initial vortex position r_0, therefore, we begin with a general case (the trapping parameters of the previous section, Sec. 5.2) before presenting result for the experimental parameters.

5.4 Precession frequencies

To assess the dependence of vortex precession on temperature, we extract the precession frequencies of the vortices of Sec. 5.2. We have data for vortices of various initial starting positions, therefore, it is initially important to assess the dependence of initial vortex position on the precession frequency.

We extract the precession frequency by measuring the time taken for one oscillation. In Fig. 5.10, the frequencies of oscillation of vortices, corresponding to various initial positions r_0 (each shown by a different colour), have been plotted as a function of the radial coordinate, r_v for a condensate of 10000 atoms, at a temperature of 124nK.

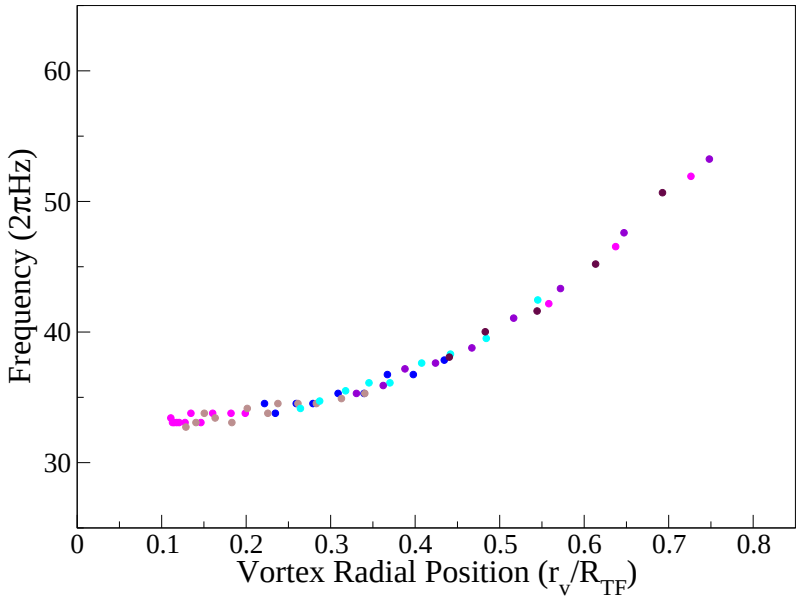

Figure 5.10: Frequencies of vortices with different initial positions r_0 (shown by different colours), in a condensate containing $N_c = 10000$ atoms at a temperature of 124nK. We have plotted the precession frequency of each vortex at different radial positions, r_v, in the condensate.

We can see there is a clear correlation between increasing vortex radial coordinate, r_v, and increasing precession frequency. Also, we note that the frequency appears to be independent of the initial vortex position as the values of the precession frequency lie along the same curve. This means that the frequency of vortex precession depends on *instantaneous* radial position and not on the *history* of how it got there.

We can therefore draw a representative line through these points, shown by the blue line in Fig. 5.11, where this procedure has also been carried out for the lower temperature of 53nK of the previous section. For the sake of comparison, we extract the frequencies of a vortex in a very low, almost zero temperature system too. In the same way in which we can 'turn off' the collisional processes of the thermal cloud in our simulations, we can 'turn off' the thermal cloud propagation. If we do this for a very low temperature, 2nK ($\approx 0.01T_c$), the resulting condensate will only be in the presence of a very slight, static thermal cloud, hence, the vortex will effectively be in a zero temperature system.
As well as the clear dependence of precession frequency on radial position of the vortex, increasing the temperature appears to also increase the precession frequency.

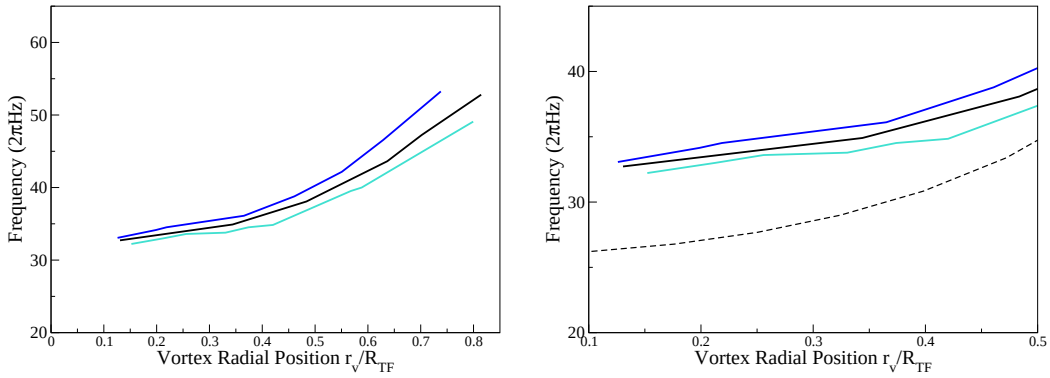

Figure 5.11: Left: Frequencies of a vortex as a function of radial position, r_v, for condensates with atoms number, $N_c = 10000$ at temperatures of 2nK, (cyan), 53nK (black) and 124nK (blue). Right: We focus on the region of interest outlined in the previous section, with the addition of the predicted zero temperature frequency of Eq. (5.11) for comparison (black dashed).

We compare our calculated precession frequency to that predicted in the papers of Fetter [79, 112, 233], and Lundh and Ao [209].
For an axisymmetric trap, the precession of a vortex at zero temperature is given by the formula,

$$\omega_v = \frac{2\hbar\omega_\perp^2}{8\mu(1 - r_v^2/R_{\rm TF}^2)} \left(3 + \frac{\omega_\perp^2}{5\omega_z^2}\right) \ln\left(\frac{2\mu}{\hbar\omega_\perp}\right). \tag{5.11}$$

This prediction is based on a straight vortex in a disc shaped condensate which is within the Thomas-Fermi, i.e. large N_c regime. This means that it is a zero temperature prediction based on the shape of the condensate. It is clear from this formula that as the vortex position, r_v, increases, the precession frequency increases.

We see from Fig. 5.11 (Right), that our results differ hugely from the prediction of Eq. (5.11). This formula approximates the shape of the condensate via the Thomas-Fermi approximation (see Sec. 2.1.3), as well as assuming that all of the atoms are in the condensate i.e. the system is assumed to be at zero temperature.
We have fixed the size of these condensates to be $N_c = 10000$ and the resulting chemical potential for each temperature is $\approx 10\hbar\omega_\perp$. In the Thomas Fermi limit, the number of atoms is assumed to be large with a chemical potential which is $> 10\hbar\omega_\perp$, therefore, the size of condensates which we have considered, are not quite within the Thomas-Fermi regime. This may explain the large deviation from the predicted frequencies. However, at finite temperatures, the shape of the condensate is further affected by the presence of the thermal cloud mean-field, hence the condensate profiles will naturally become less Thomas-Fermi like as temperature increases and the strength of the mean-field produced by the thermal atoms increases.

To assess the Thomas-Fermi nature, we plot the relative difference between the condensate density n_c and the Thomas-Fermi density $n_{\rm TF}$, Fig. 5.12 (Right). In the left part of this figure, we have shown for a temperature of 2nK the density of a condensate of $N_c = 10000$ atoms, with the corresponding Thomas-Fermi profile for comparison. One

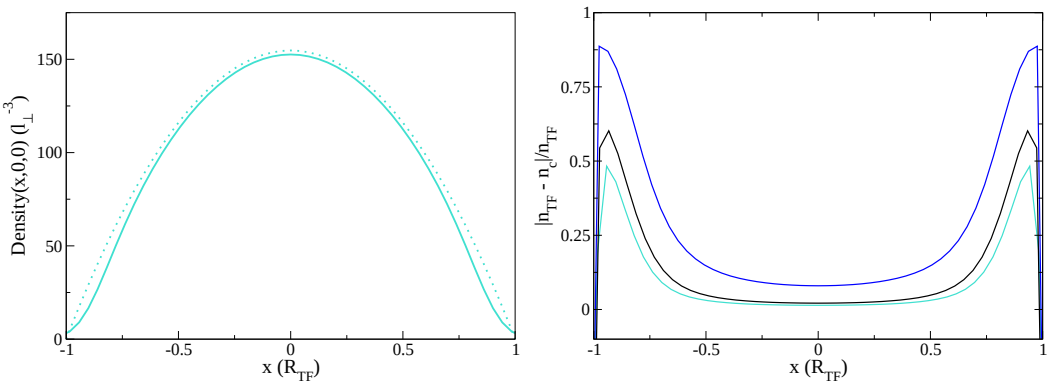

Figure 5.12: Left: Density of condensate, n_c, containing $N_c = 10000$ atoms at a temperature of 2nK (cyan, solid line) and corresponding Thomas-Fermi density, $n_{\rm TF}$ (cyan, dotted line). Right: Thomas-Fermi nature of the finite temperature condensates containing $N_c = 10000$ atoms, given by $|n_{\rm TF} - n_c|/n_{\rm TF}$ for temperatures of 2nK (cyan), 53nK (black) and 124nK (blue).

can see that the overall shape of the Thomas-Fermi density is a good approximation to the 2nK condensate density, with a slight overestimation in the central region and more around the outer edges where the Thomas-Fermi density doesn't take into account the gradual change of shape of the condensate density as the wavefunction reduces to zero. It is apparent that for all temperatures, the Thomas-Fermi approximation somewhat fails at the edges, the effect is greater for a higher temperatures. This is due to the higher density of thermal cloud increasing the mean-field potential felt by the condensate atoms, which effectively *squeezes* the condensate making it taller and thinner. In particular we notice that the highest temperature, 124nK, has the greatest deviation from a Thomas-Fermi profile, both at the edges and in the central region of the condensate.

To test the validity of the formula (5.11), we move to the experimental parameters which involve a much larger number of condensate atoms.

5.4.1 Experimental parameters: Large condensate

In the experiment introduced in Sec. 5.3, vortex precession was observed in a disk shaped condensate [31]. This experiment was conducted with a total atom number of $N_{\rm TOT} \approx 6\times10^5$. This is a large condensate which is well within the Thomas-Fermi, large N_c regime, with a chemical potential for a zero temperature system of $\approx 45\hbar\omega_\perp$. This means, the trapping parameters of this experiment are ideal to assess the validity of Eq. (5.11).

The trapping frequencies are as follows: $\omega_\perp = 2\pi \times 36$ Hz, and $\omega_z = \lambda\omega_\perp$, where

$\lambda \approx \sqrt{8}$, therefore, the aspect ratio is similar to that used in the previous section, which will be useful to make comparisons. Since the total atom number is now fixed, we can express the temperatures in terms of the critical temperature of the system, $T_c \approx 190$nK and in this section we will study vortex precession for temperatures of $0.01T_c$, $0.2T_c$, $0.4T_c$ and $0.7T_c$.

Vortex trajectories and condensate profiles

For the experimental trapping parameters given, we analyse the effect the following temperatures have on vortex precession and in this section, include the profiles at various instants in time for vortices with initial vortex positions given in Table 5.1. For the

T/T_c	N_c	$\tilde{N}$	$x_0(\mu m)$	$y_0(\mu m)$
0.2	590750	9250	3.8	5.5
0.4	514880	85120	3.4	5.9
0.7	260030	339970	0.8	7.7

Table 5.1: Condensate, N_c, and thermal cloud, $\tilde{N}$, atom number at the given temperatures, for the experimental parameters of Hall *et al.* [31]. Initial positions, x_0 and y_0 of vortices for the results presented in Fig. 5.13 are also given.

temperatures and initial vortex positions given in Table 5.1 we plot the first few vortex oscillations in Fig. 5.13 and the corresponding trajectory in the x direction. Since the atom numbers are much larger, the computations are much more labour intensive than our previous parameters and hence, we cannot show as much data as before. The density plots are shown in Fig. 5.14 at various instants in time. This images are similar to those which would be extracted experimentally via the imaging technique outlined in Sec. 5.3. The vortex core is much smaller than for the previous parameters, this is due to the large size of the condensate. This highlights the requirement for expansion to be used in order to image the vortex in real time.

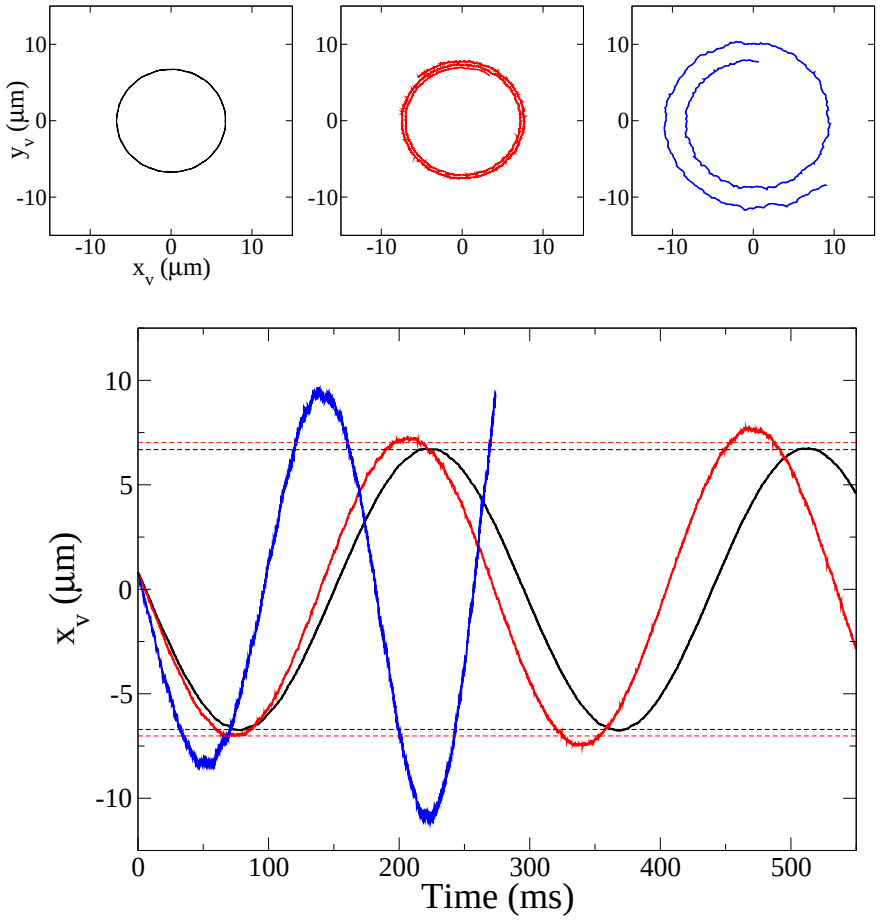

Figure 5.13: Top: Position of the vortex (x,y) in units of μm as it spirals around the condensate for temperatures $0.2T_c$ (black), $0.4T_c$ (red) and $0.7T_c$ (blue). In the latter case the vortex is lost after approximately 280ms. Bottom: x-position of the vortex over time for the temperatures shown. The dashed lines indicate the initial amplitude for $T = 0.2T_c$ (black) and $T = 0.4T_c$ (red) where $T_c \sim 190$nK

Figure 5.14: In situ density cross sections of the condensate at $z = 0$ for indicated times and temperatures. The colours range from red (high density) to dark blue (low density).

It is clear from Fig. 5.14 that with increasing temperature, the condensate contains more density 'ripples'. Since the vortex core is so small for these parameters, we have reduced the amount of smoothing over the thermal cloud density (see Chapter 4, Sec. 4.2.4). This is to avoid losing thermal cloud definition at the vortex core. This means that the resulting condensate density also contains density ripples which are more prominent in the higher temperatures where the thermal cloud density is higher. It is possible to reduce these ripples by increasing the test particle number (we have used approximately $N_{\rm tp} = 275000$ in these simulations). However, these simulations are already computationally expensive and by increasing the number of test particles we would be increasing the computation time even more with the only result being a smoother density profile and vortex trajectory. For this reason, we choose to keep the test particle number as it is for all further simulations in this chapter.

In the interest of comparing results for precession frequencies for these parameters and those used in Sec. 5.4, we repeat the analysis of condensate profiles and subsequent vortex frequency at these temperatures.

Precession frequencies

The low temperature $0.01T_c$ condensate density n_c, and corresponding Thomas-Fermi profile are shown in Fig. 5.15 (Left).

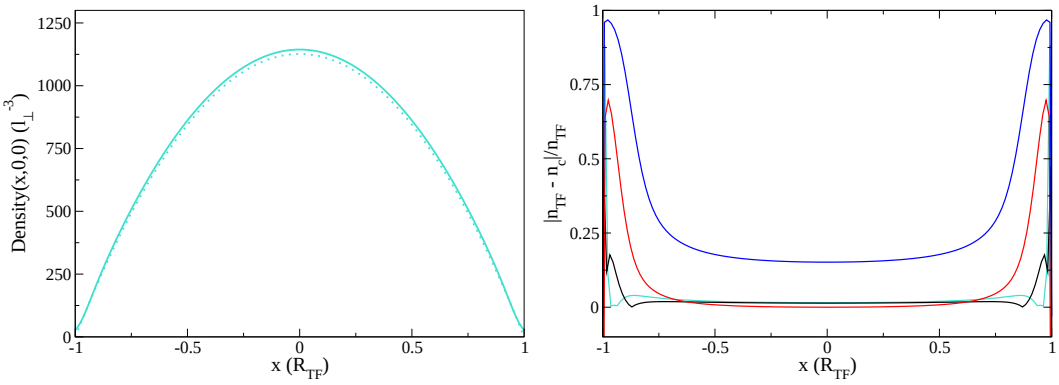

Figure 5.15: Left: Density of condensate, n_c, containing $N_c = 6 \times 10^5$ atoms at a temperature of $0.01T_c$ (cyan, solid line) and the corresponding Thomas-Fermi density, $n_{\rm TF}$ (cyan, dotted line). Right: Thomas-Fermi nature of the finite temperature condensates in a system of $N_{\rm TOT} = 6 \times 10^5$ atoms, given by $|n_{\rm TF} - n_c|/n_{\rm TF}$ for temperatures of $0.01T_c$ (cyan), $0.2T_c$ (black), $0.4T_c$ (red) and $0.7T_c$ (blue).

The Thomas-Fermi profile for these trapping parameters is clearly a much better approximation at this low temperature (see Fig. 5.15 (Left)) than for the smaller condensate of the previous section (see Fig. 5.12 (Left)). In assessing the Thomas-Fermi nature of each temperature in Fig. 5.15 (Right), we see that towards the edge, $R_{\rm TF}$, of the profiles at

each temperature, the densities deviate less from the Thomas-Fermi profile than they do for the condensates containing a smaller number of atoms in the previous section. Again as temperature increases, the condensate density varies from this predicted profile with the largest deviation for the highest temperature $0.7T_c$, as expected.

We extract the frequencies using the same procedure as in the previous section. As the simulations are more computationally expensive due to the large number of atoms, we only present a few data points in Fig. 5.16 for our measured precession frequencies for these experimental parameters.

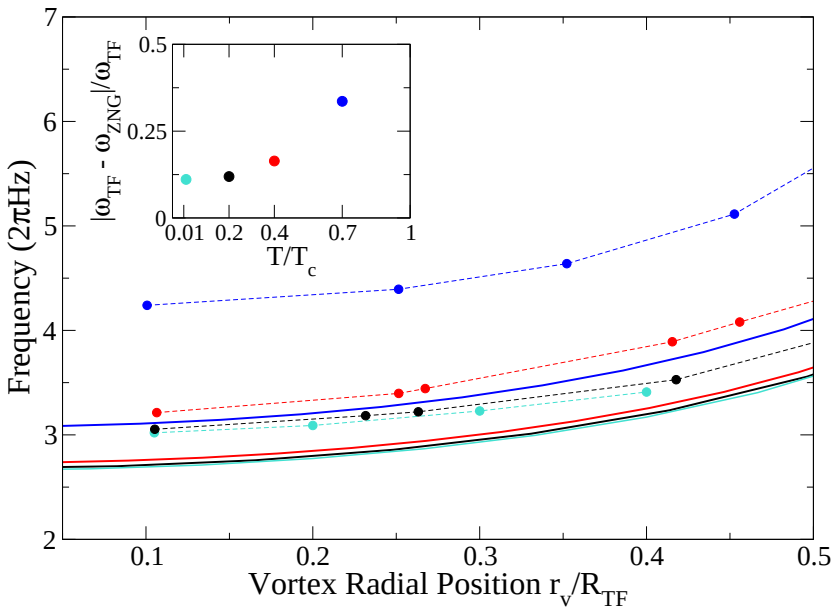

Figure 5.16: Main: Precession frequencies of a vortex, in a system of $N_{\mathrm{TOT}} \approx 6 \times 10^5$ atoms at temperatures $0.01T_c$ (cyan dashed), $0.2T_c$ (black dashed), $0.4T_c$ (red dashed) and $0.7T_c$ (blue dashed), and the respective predicted frequencies from the formula Eq. (5.11) when accounting for the changing number of condensate atoms as a function of temperature (solid lines). Inset: Relative difference between predicted frequencies of Eq. (5.11) and those calculated using the ZNG method at the radial coordinate $0.25R_{\mathrm{TF}}$.

As we have fixed the total atom number, the condensate atom number and chemical potential vary with temperature (unlike in the previous case where the condensate number was fixed). As a result, Fig. 5.16 shows different solid lines corresponding to the predicted frequencies of Eq. (5.11) for each temperature.

As remarked in the previous section, we see a clear trend of increasing precession frequency with increasing temperature. We also clearly see an increasing deviation from the predicted frequencies with increasing temperature. This effect is highlighted in the inset where the relative difference from the predicted frequencies of Eq. (5.11) and the ZNG results have been plotted for each temperature at the radial coordinate $0.25R_{\mathrm{TF}}$.

It is clear that for even a large, Thomas-Fermi like condensate at low temperatures, close to absolute zero, there is $\sim 10\%$ (cyan and black points in inset) deviation from the predicted frequency at this radial coordinate. At the highest temperature we have considered of $0.7T_c$, the relative difference between the ZNG and predicted frequencies becomes as large as $\sim 35\%$.

We have considered a condensate of $N_c = 1 \times 10^4$ atoms as well as one in a system of $N_{\rm TOT} = 6 \times 10^5$ atoms at various temperatures. In both cases, we have found that the resulting precession frequencies do not agree well with the predictions of Eq. (5.11) in the region of radial coordinates which we are interested in. This is even true for the lowest temperatures where we see a deviation in frequency of approximately 10% from the prediction in a zero temperature, large, Thomas-Fermi like condensate. Therefore, the following comparisons to be presented below, will not be made with the Thomas-Fermi prediction, but with the *zero temperature* ZNG result, i.e. the GPE result.

For the purpose of comparison between different trapping frequencies, it is more intuitive (and experimentally relevant) to compare systems in which the total atom number is fixed. In this way, temperatures can be expressed in terms of the critical temperature of the system and therefore, finite temperature effects of different systems can easily be compared.

We have extracted the frequency of the first oscillation of a vortex with position $0.4R_{\rm TF}$ (which lies within the indicated region in Fig. 5.7) and calculated the relative difference between it and the zero temperature precession frequency for the trapping parameters previously used, $\omega_\perp = 2\pi \times 129$ Hz and $\omega_\perp = 2\pi \times 36$ Hz with the same aspect ratio of $\lambda = \sqrt{8}$ in Fig. 5.17 (Left). Two different total atom numbers are compared, $N_{\rm TOT} = 1\times10^4$ and $N_{\rm TOT} = 1\times10^5$. There is an overall trend of increasing relative difference from the zero temperature result for increasing temperature. We also repeat these calculations for a different initial vortex position of $r_0 = 0.1R_{\rm TF}$ and trapping aspect ratio with results shown in Fig. 5.17 (Right). For each trapping parameter, the change in number of atoms does not make a significant amount of difference, however we do see slightly different behaviour when the temperature is increased past $0.5T_c$. This reiterates the accuracy of the GPE at low temperatures.

5.5 Vortex core brightness

Techniques are always being investigated to improve the accuracy and control of experiments; one parameter whose accurate determination is often investigated by alternative methods is the temperature of a system of bosons. Under the critical temperature, it can be extracted by fitting a Gaussian profile to the high energy tails of the velocity distribution of the atoms [234]. These atoms are assumed to be in thermal equilibrium with the

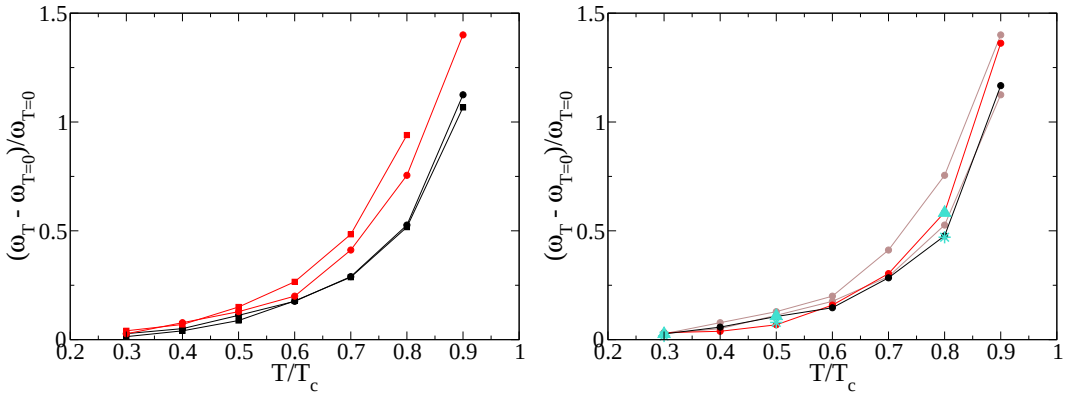

Figure 5.17: Relative difference of precession frequency of a vortex and the zero temperature result for the initial position of the vortex; (Left): $r_0 = 0.4R_{\rm TF}$ for trapping frequencies; $\omega_\perp = 2\pi \times 129$ Hz (red) and $\omega_\perp = 2\pi \times 36$ Hz (black) and a fixed total atom number of $N_{\rm TOT} = 1 \times 10^4$ (circles) and $N_{\rm TOT} = 1 \times 10^5$ (squares). $\lambda = \sqrt{8}$. (Right): $r_0 = 0.1R_{\rm TF}$, $N_{\rm TOT} = 1 \times 10^4$ for trapping frequencies; $\omega = 2\pi \times 129$ Hz, $\omega_z = \sqrt{8}\omega_\perp$ (red, circles), $\omega = 2\pi \times 36$ Hz, $\omega_z = \sqrt{8}\omega_\perp$ (black, circles), $\omega = 2\pi \times 129$ Hz, $\omega_z = 1.5\omega_\perp$ (cyan stars) and $\omega = 2\pi \times 129$ Hz, $\omega_z = 4.5\omega_\perp$ (cyan triangles). Corresponding results from initial vortex position of left graph are shown in grey for comparison.

rest of the cloud and can be described by a Maxwell-Boltzmann distribution, i.e. this high energy tail of the velocity distribution is associated with the high energy, noncondensed atoms in the system. An issue with this mechanism is that it becomes difficult at low temperatures, below $0.4T_c$, when the thermal cloud density is low such that it is difficult to extract any information. One suggestion, investigated by the group of Cornell [235], was that in the region of the vortex core, the thermal density is higher and therefore could serve as a possible new technique for thermometry. In their experiment however, they were not able to consistently get reliable results below this temperature ($0.4T_c$). Nevertheless, we calculate the ratio of thermal density to peak condensate density in this region in the hope that the experimental techniques for extracting the thermal density will improve that this and will result in a new technique to measure the temperature of a system.

As we highlighted in the introduction of this present chapter, the vortex core is a region of zero density in the condensate, and at finite temperatures, due to the low mean-field potential felt by the thermal atoms in this region, thermal atoms can fill in the core. The size of the core is typically of the order of the healing length of the condensate and thus depends on the atom-atom interactions (the interaction strength, g). The aim of this section is to gain insight into the effect of the thermal cloud on the vortex core and to measure the density of the thermal cloud in this region. We initially focus on gaining an insight into the effect of thermal atoms on changing the shape of the vortex core. For ease we look at a stationary central vortex. This is an idealised case which is virtually impossible to realise physically, since the nature of most experimental techniques used to

create vortices produce density fluctuations which inevitably cause an acceleration and therefore, energy dissipation of the vortex. However, in Sec. 5.6 we will look into using the thermal cloud to move a vortex to the desired position by rotation.

We first measure the width of a stationary vortex core for the trapping parameters used at the beginning of Sec. 5.4 ($\omega_\perp = 2\pi \times 129$ Hz and $\lambda = \sqrt{8}$), in order to assess if the presence of the thermal cloud in this region changes the shape of the vortex core. We measure the width of the vortex core in two places, at 90% of the peak density, $0.9n_{c_v}^{\text{peak}}$, and at 50% of peak density, $0.5n_{c_v}^{\text{peak}}$, where $n_{c_v}^{\text{peak}}$ is the peak density of the condensate containing a vortex. We do this for a fixed total number of atoms as well as a fixed condensate number for completeness and we will later compare these results with the experimental trapping parameters of Sec. 5.4.1 ($\omega_\perp = 2\pi \times 36$ Hz and $\lambda = \sqrt{8}$).

5.5.1 Fixed condensate number

Fixing the number of atoms in the condensate enables us to assess the effect of an increasing thermal cloud on the shape of the vortex core. We have plotted the condensate densities for a range of temperatures increasing from 53nK to 225nK in Fig. 5.18 (Left). We see that the shape of the condensate only changes very slightly with increasing temperature, as a result of the stronger mean-field potential felt by the condensate from the increasing density of thermal atoms.

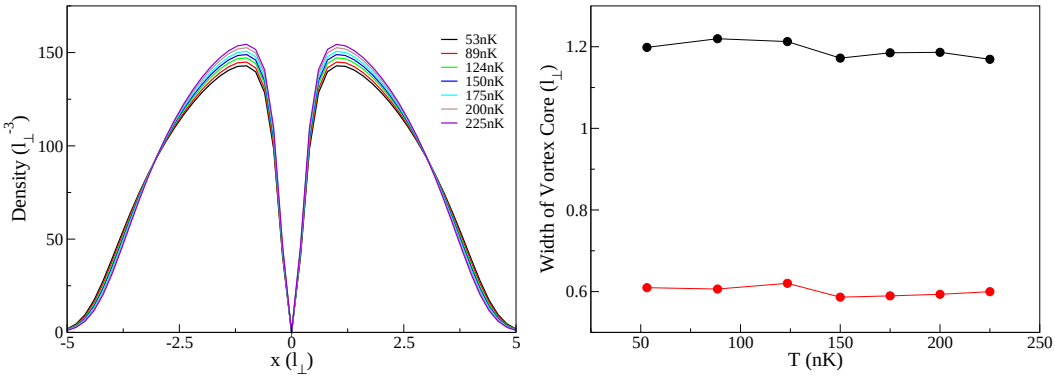

Figure 5.18: Fixed condensate number, $N_c = 10000$. Left: Condensate density, n_c, at finite temperatures. Right: Width of stationary vortex core for densities given in the Left figure, measured at positions $0.9n_{c_v}^{\text{peak}}$ (black), and $0.5n_{c_v}^{\text{peak}}$ (red) as a function of temperature.

In the right part of this figure, we plot the width of the vortex core in the two places specified. As expected, the vortex core is wider, approximately twice as wide, at 90% than at 50% of the peak density. However, we see very little difference in vortex width with increasing temperature, except for a slight unimportant decrease in width at both

positions when the temperature is increased past 125nK which could be due to the mean-field produced by the higher density of thermal atoms. Since this effect is only slight, it means that the shape of a stationary vortex core is relatively unaffected by the presence of thermal atoms. We repeat this analysis for a fixed total atom number.

5.5.2 Fixed total atom number

When the total number of atoms in a system is fixed, increasing the temperature from 0 to T_c has the effect of reducing the number of atoms in the condensate from $N_c = N_{\mathrm{TOT}}$ to $N_c = 0$. We again plot the condensate density, for various finite temperatures in Fig. 5.19 (Left).

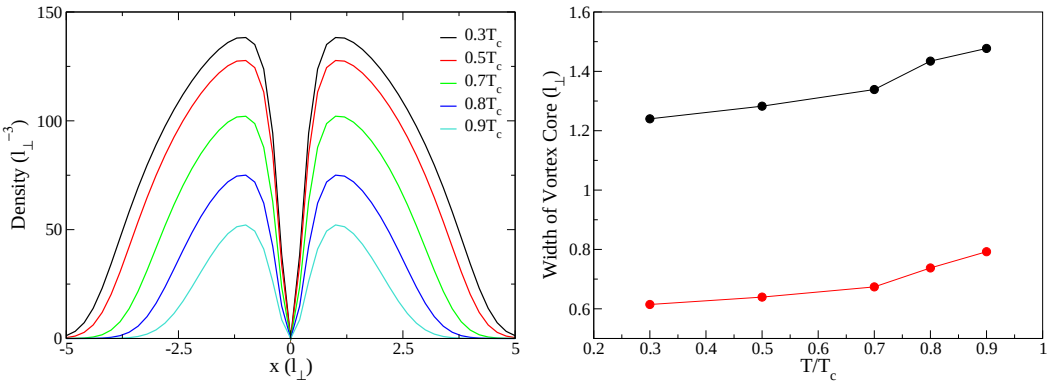

Figure 5.19: Fixed total atom number, $N_{\mathrm{TOT}} = 10000$. Left: Condensate density, n_c, at finite temperatures. Right: Width of stationary vortex core, measured at $0.9n_{c_v}^{\mathrm{peak}}$ (black) and $0.5n_{c_v}^{\mathrm{peak}}$ (red).

We can clearly see the effect of increasing temperature on the condensate; the density not only decreases in height but it also in width due to the mean-field potential of the thermal atoms acting to squeeze the condensate (an effect which is made more clear by plotting the condensate density normalised by the condensate atom number, N_c, see Fig. 5.20).

The effect of this reduction of the number of condensate atoms on the size of the vortex core is clearly seen in Fig. 5.19 (Right), where the width of the condensate at two positions of condensate height, is compared for different finite temperatures. As we noted for the previous case where the condensate atom number was fixed, the width of the vortex core at 90% of peak density is approximately double that at 50% of peak condensate density. In this case however, we see an increase in core width with increasing temperature, in contrast to the slight decrease for the previous case. The fact that the core size only decreases very slightly with an increasing thermal cloud for the case of a fixed condensate number, leads us to believe that this increase which we observe when the *total* is fixed, is

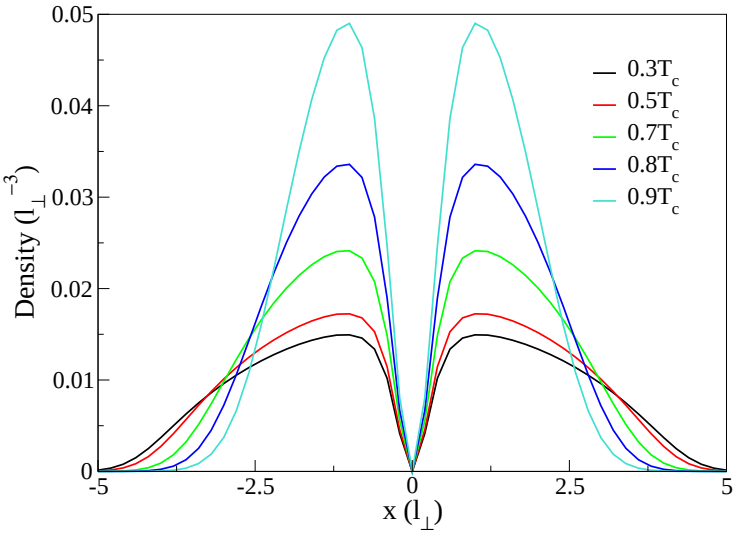

Figure 5.20: Fixed total atom number, $N_{\mathrm{TOT}} = 10000$, condensate density, n_c, normalised by condensate atom number, N_c, at finite temperatures.

in fact due to a decreasing condensate number and not an increasing thermal cloud.

Whether we fix the total or condensate atom number we know that the number of noncondensed atoms in the system increases with increasing temperature, therefore, the thermal cloud density around the condensate edges increases. We would now like to investigate whether the thermal cloud density changes in the *core region* as a result of temperature. We will do this by measuring the thermal cloud density at the centre of the vortex core, $\tilde{n}$, normalised by the peak density of the condensate were no vortex present, n_c^{novort}. We extract n_c^{novort} before imprinting a central vortex onto the condensate. Since the peak density of a condensate with a fixed atom number will only change slightly, we feel it is not important to measure this quantity with increasing temperature whilst fixing the condensate number since we will not benefit in any new knowledge; therefore, in the next section we will investigate the effect of increasing temperature on a system of N_{TOT} atoms on the ratio of thermal cloud density in the vortex core to peak condensate density when no vortex is present.

5.5.3 Thermal cloud density in the vortex core

In an experimental paper by Cornell's group in 2004 [235], equilibrium properties of vortices in Bose-Einstein condensates were investigated. One of the properties they looked

at was vortex core brightness, $\mathcal{B}$, defined as

$$\mathcal{B} = \frac{n_{\rm core}}{n_{\rm cloud}}, \tag{5.12}$$

where $n_{\rm core}$ is the observed atom density, integrated along the line of sight at the core centre and $n_{\rm cloud}$ is the projected integrated density at this point based on a smooth fit of the overall atom cloud. In our simulations, we can measure a similar parameter which we denote B', defined by,

$$B' = \frac{\tilde{n}^{\rm core}}{n_c^{\rm peak}}. \tag{5.13}$$

where, $\tilde{n}^{\rm core}$ is the thermal cloud density in the vortex core region normalised by the peak density of the condensate before it contains a vortex.

We measure this quantity for a stationary vortex and fixed total atom number, for the same geometries of the previous section, $\omega_\perp = 2\pi \times 129$ Hz and $\omega_\perp = 2\pi \times 36$ Hz (aspect ratio of $\lambda = \sqrt{8}$ in both cases).

The results of this analysis are shown in Fig. 5.21 for two different total atom numbers, $N_{\rm TOT} = 1 \times 10^4$ and $N_{\rm TOT} = 1 \times 10^5$ for different temperatures. The overall trend is

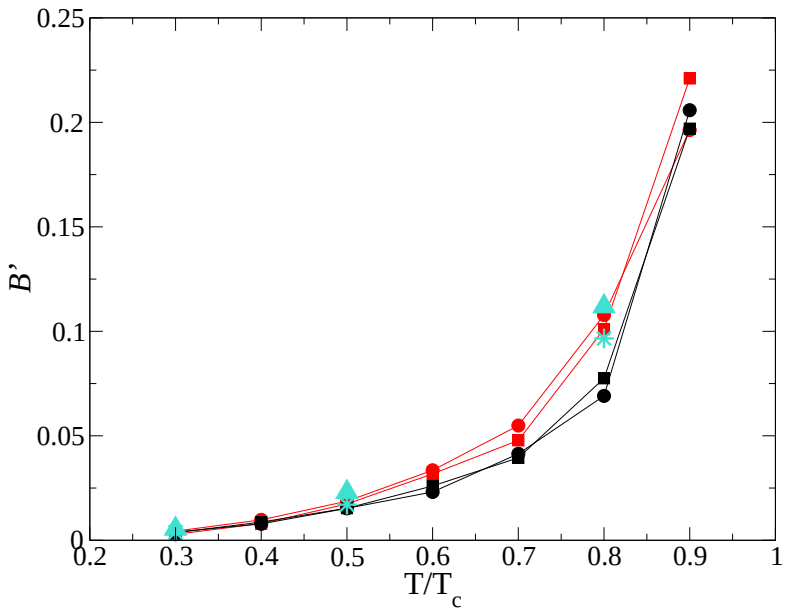

Figure 5.21: Ratio of thermal cloud density in the vortex core (for a central vortex) to the peak density if no vortex were present for various temperatures. The trap aspect ratio in all cases are the same, however there are two different trapping frequencies of $\omega_\perp = 129 \times 2\pi$ (red) and $\omega_\perp = 36 \times 2\pi$ (black) for two different total atom numbers, $N_{\rm TOT} = 1 \times 10^4$ (circle) and $N_{\rm TOT} = 1 \times 10^5$ (square). We include some values for $N_{\rm TOT} = 1 \times 10^4$, $\omega_\perp = 129 \times 2\pi$ with $\lambda = 1.5$ (cyan stars) and $\lambda = 4.5$ (cyan triangles). The errors in calculating this value are less than the size of the symbols used.

clear, with increasing temperature, the ratio of thermal cloud density to peak condensate density increases. Differences in atom number and aspect ratio appear to make very little difference to this ratio; however, at temperatures greater than $0.5T_c$, the values appear to differ slightly for the different parameters. We find an approximate dependence of T^7 above this temperature, however, more testing for different trapping parameters needs to be carried out to quantitatively extract this dependence, not least investigate if this could be a viable measure of system temperature.

The vortex core brightness results we have presented in Fig. 5.21 are determined by a central vortex; since it is experimentally difficult to predetermine the position of a vortex it is difficult to generate the conditions necessary to measure the core brightness of a vortex in an actual experimental. This brings us to the next section which focusses on the manipulation of vortex position using a rotating thermal cloud.

5.6 Vortex manipulation using a rotating thermal cloud

In Chapter 5, Sec. 5.2 we stated that the decay rate of a vortex is dependent on initial position of the vortex. Experimentally, the extraction of this quantity would be difficult however, since it is difficult to create a vortex in a predetermined position due to the procedures used to experimentally generate them (see Chapter 1, Sec. 1.3.2). Often when a vortex is generated, its position may be random, for example when the temperature of a system is quenched through T_c, vortices are generated with random position via the Kibble-Zurek mechanism [109–111, 232]. Therefore, a mechanism which could be used to translate a vortex to the desired position after creation would be useful. Such a mechanism has been suggested and preliminary experimental investigations are underway by the BEC group of Hall in Amherst, the same experimental group introduced in Sec. 5.3. In a recent Master's thesis [236], the group have reported early evidence to suggest translation of a vortex towards the centre (edge) of the condensate when the thermal cloud is rotated in the same (opposite) direction as vortex precession. We illustrate this radial translation initially for a general example before introducing our findings for the particular experimental parameters.

If the thermal cloud is rotated with angular frequency $\Omega_{\rm th}$, then the thermal cloud velocity in the vicinity of the vortex core is given in cylindrical polar coordinates by

$$\mathbf{v}_n = \Omega_{\rm th} r_v \hat{\phi}, \tag{5.14}$$

where r_v is the radial coordinate of the vortex. If the thermal cloud is stationary, then $\mathbf{v}_n = 0$. When the thermal cloud is rotating in the same sense as the vortex, $\Omega_{\rm th} > 0$, collisions between the thermal cloud and the vortex core cause the addition of angular velocity to the condensate, and when it is moving in the opposite sense as the vortex, $\Omega_{\rm th} < 0$,

collisions between vortex core and thermal clouds result in the condensate transferring angular momentum from the condensate to the thermal cloud and thus spiralling further out. Numerically, we impose this rotation by adding $\mathbf{v}_n = \Omega_{\rm th} r_v \hat{\phi}$ to each test particle's velocity [68].

For the trapping parameters ($\omega_\perp = 2\pi \times 129$ Hz, $\lambda = \sqrt{8}$ and $N_{\rm TOT} = 10000$), and similar rotation speeds of [68] we demonstrate the effect of a rotating the thermal cloud on the position and subsequent lifetime of a vortex with initial position $r_0 = 0.4 R_{\rm TF}$.

In Fig. 5.22 we plot the vortex radial coordinate for positive rotation speeds along with the vortex radial coordinate when no thermal cloud rotation is present. Clearly we can see that the vortex radial coordinate increases more slowly with increasing thermal cloud rotation speed and the results for positive thermal cloud rotation speeds leading to longer lifetimes than if no thermal rotation were present. Therefore, rotation of the thermal cloud in the same sense as the precession of the vortex leads to a prolonged vortex lifetime. In

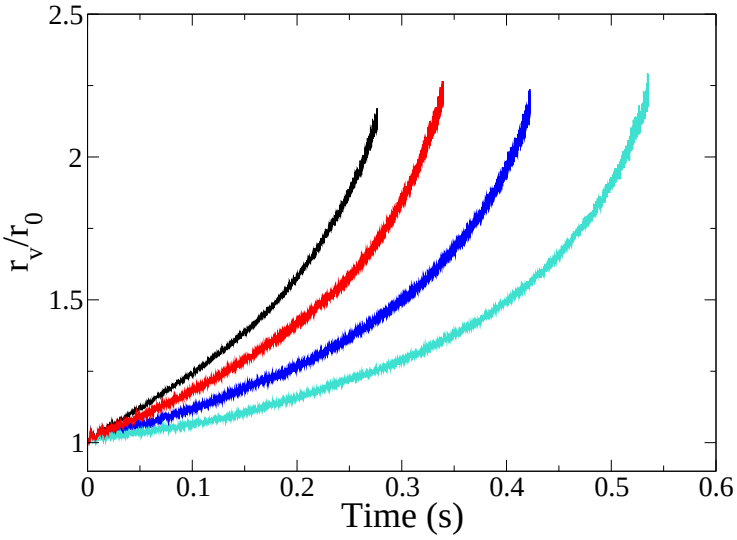

Figure 5.22: Radial coordinate of vortex normalised by initial position, $r_0 = 0.4 R_{\rm TF}$, for no thermal rotation (black), $\Omega_{\rm th} = 0.1\omega_\perp$ (red), $\Omega_{\rm th} = 0.2\omega_\perp$ (blue) and $\Omega_{\rm th} = 0.3\omega_\perp$ (cyan) at $T = 0.5 T_c$ for the trapping parameters $\omega_\perp = 2\pi \times 129$ Hz, $\lambda = \sqrt{8}$ and atom number $N_{\rm TOT} = 10000$.

Fig. 5.23 we show also the effect of rotating the thermal cloud in the opposite sense as the vortex precession. When the thermal cloud is rotating in the opposite sense as the vortex, the radial coordinate increases more quickly with increasing rotation frequency and the time elapsed before the vortex reaches the edge of the condensate (where its position can no longer be measured), is shorter. This means that the lifetime of a vortex is shorter when the thermal cloud rotates in the negative sense with respect to vortex precession.

From Figs. 5.22 and 5.23 it is clear that the presence of rotation in the thermal cloud affects the radial position of a vortex and the result is either a lengthening of its lifetime,

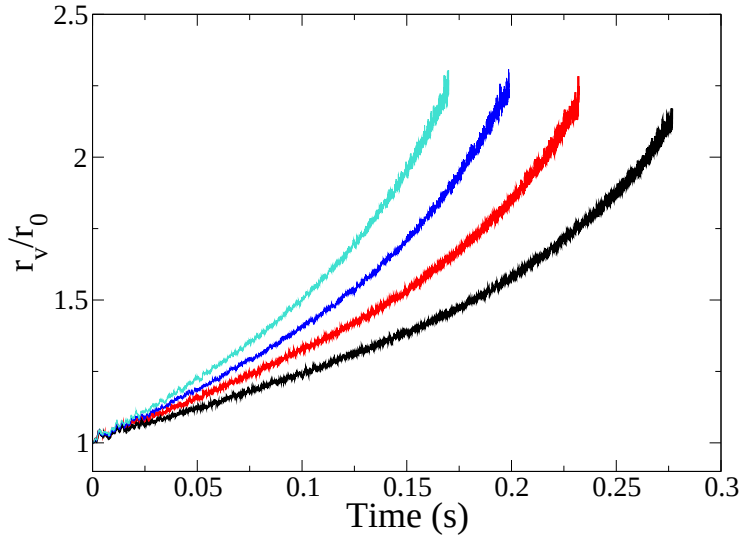

Figure 5.23: Radial coordinate of vortex normalised by initial position, $r_0 = 0.4R_{\rm TF}$, for no thermal rotation (black), $\Omega_{\rm th} = -0.1\omega_\perp$ (red), $\Omega_{\rm th} = -0.2\omega_\perp$ (blue) and $\Omega_{\rm th} = -0.3\omega_\perp$ (cyan) at $T = 0.5T_c$ for the trapping parameters $\omega_\perp = 2 \times 129$ Hz, $\lambda = \sqrt{8}$ and atom number $N_{\rm TOT} = 10000$.

in the case of rotation in the same sense as the vortex, or a shortening of its lifetime, in the case of rotation in the opposite sense. This means that if the thermal cloud is rotated for the right amount of time, a vortex could be moved from its initial position, to a previously specified one. This was the motivation of the experiment by this group for which preliminary data is presented in [236].

5.6.1 Experimental parameters

The trapping parameters are the same as those presented in Sec. 5.4.1 but we state them here also for clarity. The trap frequency in the radial direction is $\omega_\perp = 2\pi \times 36$ Hz and $\omega_z = \lambda\omega_\perp$ and $\lambda = \sqrt{8}$. The atom number in this experiment is $N_{\rm TOT} = 4 \times 10^5$ and initial temperature is $T = 36$nK which is approximately $0.5T_c$. A vortex is generated by quenching from a thermal cloud to a condensate whilst rotating the potential in an elliptically deformed, axisymmetric trap. Then, by ramping up the rotation in the desired direction, the vortex is either moved towards or away from the centre of the condensate.

We focus here on analysing the case of moving the vortex towards the centre of the condensate by rotating the thermal cloud in the positive sense with respect to the vortex, at a rotation frequency of $\Omega_{\rm th} = 0.44\omega_\perp$.

We place a vortex in the position $r_0 = 0.24R_{\rm TF}$ by the method outlined in Sec. 5.1 in a condensate containing $N_c = 389000$ atoms with a rotating the thermal cloud, containing $\tilde{N} = 11000$ atoms, at the angular frequency, $\Omega_{\rm th} = 0.44\omega_\perp$. The radial position of the vortex, r_v, normalised by the initial vortex position, r_0, is shown in Fig. 5.24.

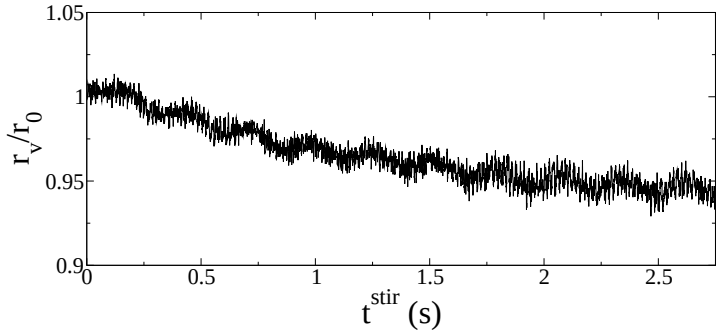

Figure 5.24: Vortex radial position normalised by initial vortex position against time for thermal cloud rotation frequency $\Omega_{\rm th} = 0.44\omega_\perp$. $N_{\rm TOT} = 4 \times 10^5$, $r_0 = 0.24R_{\rm TF}$ and trapping parameters of [31].

The results of Fig. 5.24 suggest a slow translation of the vortex towards the centre of the condensate. The translation observed in the experiment appears to happen much more quickly than this [236], however, from correspondence with the group regarding these results, we have also been made aware of the fact of potentially significant increase in temperature and loss of atoms during the experiment. This could be a possible cause of deviation between our results and the experiment since an increasing thermal cloud could impart *more* angular momentum on a decreasing condensate and hence, the motion of the vortex towards the centre of the vortex could be significantly modified over time. Further investigation needs to be carried out in both respects to minimise these errors and to accurately model the experimental results.

5.7 Chapter summary

In this chapter we have shown that a benefit of using the ZNG scheme to model vortex dynamics at finite temperatures is that the important thermal cloud 'filling in' of the vortex core can easily be observed and thermal density in this region measured. This is because the condensate and thermal cloud densities are defined separately in this scheme and therefore, they can easily be extracted during simulations.

We have shown that, as a result of finite temperature, a vortex spirals radially out of the condensate. By extracting the rate at which the radial position of a vortex increases, we were able to assess the dependence of the decay rate of a vortex on temperature and initial vortex position. In doing so, we have found that the rate at which a vortex decays, increases with increasing temperature *and* initial vortex offset (an effect which becomes more apparent at higher temperatures). We have also demonstrated the crucial role of collisional processes in the decay of a vortex, since when any of the collision terms of the quantum Boltzmann equation are not included in the numerics, the decay rate of the

vortex is significantly reduced. We found that the most dominant contribution to vortex decay is from the particle exchanging, thermal-condensate collisions.

Further to this analysis, we have demonstrated that the precession frequency of a vortex is dependent on the instantaneous vortex position and not on the history of how it got there. We also found that the frequency at which a vortex precesses is greater at higher temperatures, for a general example [68] and for parameters of a recent experiment [31] in which vortices were observed precessing at frequencies higher than those predicted. Through comparison with the predicted frequency of Eq. (5.11) [112, 209], we found at most a $\sim 25\%$ deviation from this prediction at the highest temperature considered, indicating that this is a remarkably good estimate considering it is a zero temperature approximation based on a large, Thomas-Fermi like condensate.

We have investigated the relative difference between the precession frequency of a vortex at finite temperature with the corresponding zero temperature result, for different atom numbers and trapping frequencies. We see similar behaviour with increasing temperature for these parameters especially up to the temperature $0.5T_c$. This reiterates the well known understanding that the GPE as a good estimate of condensate behaviour up to this temperature.

We have further investigated the effect of increasing temperature on the quantity of vortex core brightness as a possible mechanism for determining the temperature of a system containing a vortex. We again found similar behaviour for different atom numbers and trapping frequencies, however, further investigation would be needed to 'fine tune' this for use in experiments.

In the final part of this chapter we described a recent experiment in which rotating the thermal cloud has been shown to be useful to radially translate a vortex towards the centre (edge) of the condensate when it is rotated in the same (opposite) sense as the vortex. When modelling this experiment we find a much slower translation than observed in practice [236]. Through correspondence with the group, we have been made aware of significant increases in temperature and loss of atoms throughout the duration of the experiment and therefore, further investigation is required to determine the source of inconsistency.

Chapter 6

Finite Temperature Effects on Double Well Dynamics

An interesting property of Bose-Einstein condensates is that they have a well defined phase. This phase coherence has been demonstrated experimentally by allowing two separated condensates to interfere and observing the interference pattern formed [46]. When two condensates overlap, there exists a phase gradient across the overlapping region. This phase gradient can drive transport between the two condensates in the form of superfluid flow if the density in the overlapping region is high enough, or via quantum mechanical tunnelling when the density classically vanishes. In this case, Josephson oscillations of the condensate can be observed.

The barrier height, V_0, between the two wells of a double a harmonic trap provides an ideal handle for probing different regimes of transport between the condensates. When the barrier height is low, i.e. $V_0/\mu \ll 1$ where μ is the system chemical potential, superfluid flow takes place. When the barrier height is increased further until the condensate density practically vanishes in this region, i.e. $V_0/\mu \gtrsim 1$, superfluid transport is impeded and only transfer of atoms via tunnelling can prevail.

To understand how the phase difference can drive atomic motion between the two wells when hydrodynamic transport is forbidden, we can derive equations of motion for the wavefunctions of the condensate in either well. Following the method outlined in Refs. [1, 152], the description of the system, in the region of the barrier, reduces to a two-mode model for the time-dependent amplitudes $c_{L,R}(t) = \sqrt{N_{L,R}(t)}e^{i\theta_{L,R}(\mathbf{r},t)}$. Here $N_{L,R}$ and $\theta_{L,R}$ stand for the number of atoms and the quantum mechanical phase of the condensates in the left and right traps respectively with the total number of atoms in the system remaining constant i.e. $N_L + N_R = |c_L|^2 + |c_L|^2 \equiv N_{\mathrm{TOT}}$.

The total wavefunction for the system is expressed in the variational form,

$$\phi(\mathbf{r},t) = c_L(t)\Phi_L(\mathbf{r}) + c_R(t)\Phi_R(\mathbf{r}), \tag{6.1}$$

where $\Phi_{L,R}(\mathbf{r})$ denotes the spatial dependence of the wavefunction for the left and right well respectively.

When there is an overlap of the two condensates, the interaction term of the system Hamiltonian is modified to include a tunnelling term with tunnelling constant κ. It can be shown that, in the region of the overlap, the time-dependent amplitudes of the wavefunctions obey the following equations of motion,

$$\begin{aligned} i\frac{\partial c_L}{\partial t} &= \mu_L c_L(t) + \kappa c_R(t), \\ i\frac{\partial c_R}{\partial t} &= \mu_R c_R(t) + \kappa c_L(t), \end{aligned} \tag{6.2}$$

where $\mu_{L(R)}$ are the respective chemical potentials. By equating real and imaginary parts of Eqs. (6.2) we have

$$\frac{\partial N_L}{\partial t} = -2\kappa\sqrt{N_L N_R}\sin(\theta_L - \theta_R) = -\frac{\partial N_R}{\partial t}, \tag{6.3}$$

where the explicit spatial and time dependence have been assumed. This equation shows that atomic motion between the two wells is therefore purely driven by the phase difference.

The presence of Josephson oscillations across a double well containing a BEC can therefore be characterised by two variables. The first is the *phase difference* between the two wells, given by [149]

$$\theta = \theta_L - \theta_R, \tag{6.4}$$

and the other is the *population imbalance*, calculated as,

$$Z(t) = \frac{N_L(t) - N_R(t)}{N_L(t) + N_R(t)} \tag{6.5}$$

Tunnelling between the two wells results in oscillations of the population imbalance with a mean value of zero, $\langle Z\rangle = 0$, and similarly oscillations of the phase difference with mean value zero $\langle\theta\rangle = 0$. These are called Josephson oscillations, in particular this is analogous to the "d.c." Josephson effect in superconducting wires, and can be induced by an initial offset in the number of atoms in each well, i.e. $Z(0) \neq 0$. When the initial population imbalance is large, above a critical value which is dependent upon the interaction strength, an effect unique to the nonlinearity of Bose-Einstein condensates, can occur. This effect is called *macroscopic quantum self-trapping* (MQST) [149], whereby

large amplitude Josephson oscillations are inhibited, analogous to the "a.c." effect in superconductors. This is where one of the wells contains a large proportion of the total condensate atoms and the population becomes 'self-locked'. Small amplitude oscillations of the population imbalance occur as a result of a rapidly increasing phase difference between the two wells (running phase mode [152]).

The first experiment in which both Josephson oscillations and macroscopic quantum self trapping were directly observed in a double well trap was by Albiez *et. al* [33] in 2005. Since then, both the a.c. and d.c. effects for a BEC have been observed [156], and more recently, the crossover between superfluid flow and quantum transport has been investigated using a tunable superfluid junction on the underside of an atom chip via radiofrequency (rf) potentials which lead to slightly more complicated geometries [34]. In the latter experiment, an unexplained decay of the population imbalance over time was observed. In Sec. 6.2.2 of this chapter, we attempt to model this experiment at finite temperatures using the ZNG equations; however, we begin our analysis of double well dynamics by investigating Josephson oscillations in a simpler double well trap formed by imposing a 1D optical potential in one direction of a 3D harmonic trap [154]. In both traps we quote results at zero temperature for comparison. For consistency, such quoted 'zero temperature' results are obtained using the ZNG code at a very small temperature $\sim$ 5nK (for which the thermal fraction is typically $< 3\%$) rather than a separate GPE code. This is the same procedure as quoted in Chapter 5 in order to get zero temperature, vortex dynamics results.

6.1 Symmetric double well trap

Implementation of such a double-well geometry, for the purposes of studying damping of Josephson oscillations, was first presented in a poster of Anssi Collin at the 2009 FINESS Meeting held in Durham based on joint work with Eugene Zaremba. The discussion presented in this section, which is only a first step towards analysing Josephson oscillations in the atom chip experiment of LeBlanc *et al.* [34], essentially reproduces studies carried out by Collin and Zaremba [154] who have played a key collaborative part in the shaping of this chapter.

System parameters

The trapping potential has the form of a harmonic trap with an additional imposed optical potential in the z-direction to create a double well of the form

$$V_{\rm ext} = \frac{1}{2}m\left(\omega_\perp^2(x^2+y^2) + \omega_z^2(z-z_0)^2\right) + V_0\cos^2\left(\frac{\pi z}{d}\right); \tag{6.6}$$

where z_0 is the initial shift of the harmonic potential relative to the optical potential in the z-direction and has the effect to create an antisymmetric double well with one well having a potential minimum higher than the other. This shift is only in place when generating the equilibrium condensate and noncondensate densities, and has the effect to create an initial population imbalance between the two condensate wells. When $z_0 < 0$ ($z_0 > 0$), the harmonic trap is offset to the right (left), resulting in the left well having a potential minimum at a higher (lower) value than the right (left); therefore, the density of condensate atoms in the left well is less than in the right well and the condensate density is asymmetric. The barrier height between the two wells is controlled by the optical depth, V_0 and the distance between the minima of the two wells is given by $d = \lambda_L/2$, where λ_L is the wavelength of the laser light which forms the optical potential. The harmonic trapping frequencies we choose are $\omega_\perp = \omega_z = 2\pi \times 78$ Hz [33], the optical trap depth, $V_0 = 412$ Hz, and the separation distance, $d = 5.2\mu$m. For these parameters, the ratio of the barrier height to the system chemical potential is $V_0/\mu \simeq 1$, therefore only transport via tunnelling is allowed. The form of the trapping potential and the resulting condensate

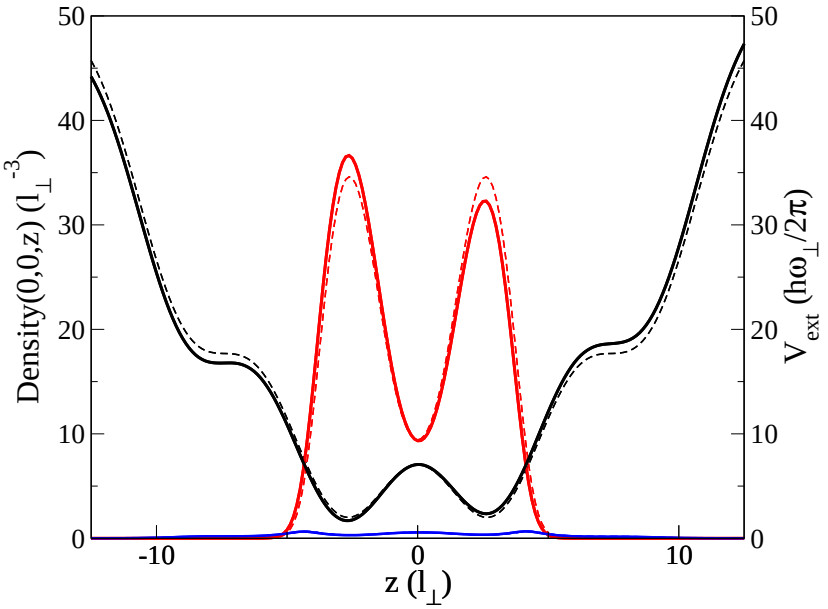

Figure 6.1: Double well potential (black) with equilibrium condensate (red) and thermal cloud density (blue) in the z direction, when $z_0 = 0$ (dashed) and $z_0 = 0.25 l_\perp$ (solid), for a temperature of 30nK with $N_c = 5000$.

density are shown in Fig. 6.1 for the case of (i) no offset between the traps, i.e. $z_0 = 0$ (dashed lines) and (ii) an offset of $z_0 = 0.25 l_\perp$ (solid lines). When there is no offset, the peak densities of the condensate in either well are of equal magnitude and when there is an offset, the resulting condensate density is higher in one well than the other.

In the simulations presented, we have chosen $N_c = 5000$ condensate atoms in the system (with variable total atom number, $N_{\rm TOT}$). In example shown here, the left well contains approximately, 2860 atoms, which is larger than the 2140 atoms in the right well; this leads to an initial value of population imbalance, $Z(0)$, of approximately 0.15. The relatively small thermal cloud densities in both cases are also shown (blue) but the difference between them is indiscernible.

To perform dynamical studies, we first generate equilibrium densities for a specified temperature in this way and then choose time $t = 0$ as the point when we suddenly remove the offset between the traps; since the population imbalance of the two wells remains, this initiates the Josephson oscillations that we wish to study in the ensuing evolution.

6.1.1 Josephson oscillations of the population dynamics

At finite temperatures, the condensate coexists with a cloud of uncondensed atoms. This means in addition to observing the *condensate* population imbalance, $Z_c(t) = (N_{c_L}(t) - N_{c_R}(t))/N_c(t)$, we can also observe the distribution of the *thermal* atoms by measuring the thermal cloud population imbalance, $Z_T(t) = (\tilde{N}_{T_L}(t) - \tilde{N}_{T_R}(t))/\tilde{N}_T(t)$, and the overall *total* population imbalance, $Z_{\rm TOT}(t) = (N_L(t) - N_R(t))/N_{\rm TOT}(t)$.

In Fig. 6.1 shows the equilibrium density (solid, red) generated in a slightly offset trap with $z_0 = 0.25 l_\perp$ (solid, black) for a condensate containing $N_c = 5000$ atoms and a temperature of 30nK. These densities are the initial conditions for the dynamical simulations for which we instantaneously change to $z_0 = 0$. The evolution of the population imbalances and condensate phase are then measured as a function of time for different temperatures and presented in Fig 6.2.

Our results are obtained using the ZNG method for which we have argued collisions play a crucial role (see e.g. Chapter. 5, Fig. 5.9). However, the evaluation of the collision integrals in our present version of the code, which relies on test particle binning based on cylindrical symmetry (as discussed in Chapter 4, Sec. 4.2.2), runs into difficulties - particularly in the highly asymmetric geometry of the atom chip to be considered in the next section. As a result, in the entire analysis presented in this chapter, we do not include thermal-thermal C_{22} collisions and condensate-thermal, C_{12} collisions, and so all finite temperature effects presented henceforth, are a result solely of the *mean-field interaction* between the condensate and a freely evolving thermal cloud. The nature of our numerical problems are briefly discussed in Sec. 6.2.3 where we also propose how they can be remedied - something which however lies beyond the scope of this thesis.

The condensate population imbalance for all temperatures is initially $Z_c(0) = 0.15$ and $Z_c(t)$ proceeds to oscillate between this value and its negative, -0.15. This indicates that the condensate population in either well is essentially oscillating between a maximum and

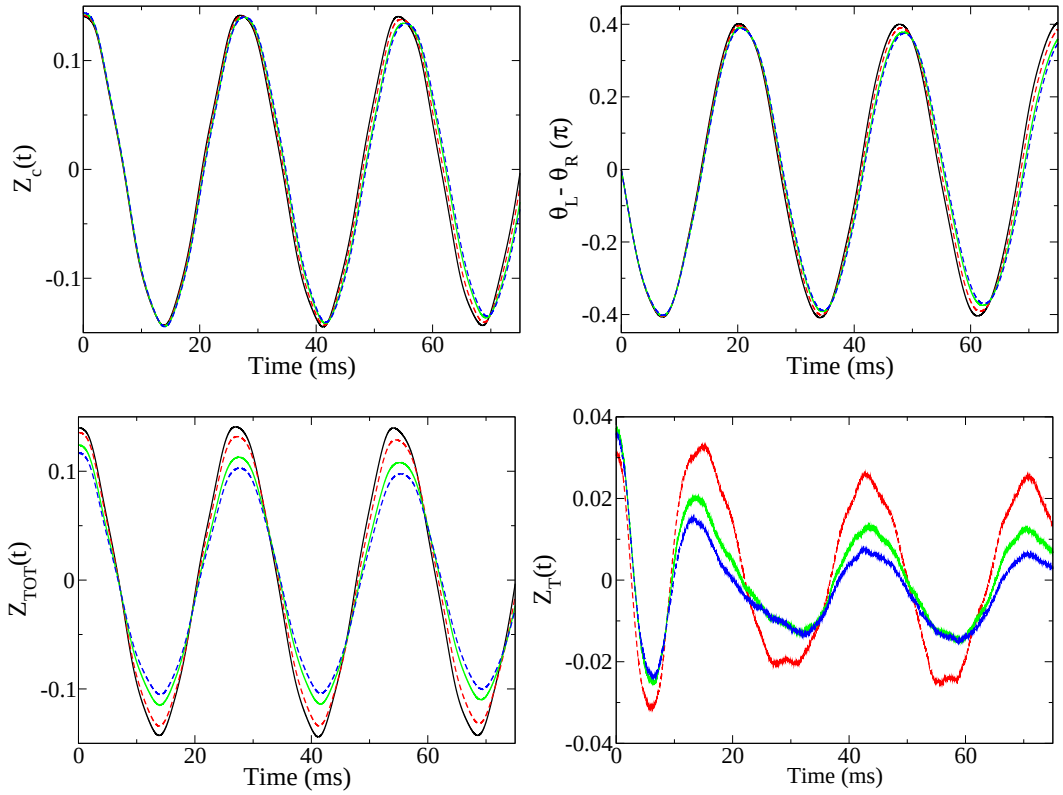

Figure 6.2: Top, Left: Condensate atom number population imbalance, $Z_c(t) = (N_{c_L} - N_{c_R})/N_c$ Right: Condensate phase difference between two wells. Bottom, Left: $Z_{\rm TOT}(t) = (N_L - N_R)/N_{\rm TOT}$. Right: Thermal cloud atom number population imbalance $Z_T(t) = (\tilde{N}_{T_L} - \tilde{N}_{T_R})/\tilde{N}_T$ for temperatures (from top to bottom) 6nK (black solid), 18nK (red dashed), 30nK (green solid) and 48nK (blue dashed). Note: For the lowest temperature 6nK, the thermal cloud is negligible therefore we do not plot the thermal cloud population imbalance for this temperature. System parameters: $V_0/\mu \simeq 1$.

minimum value determined by $Z_c(0)$ with the mean value of the population imbalance zero i.e. $\langle Z_c(t) \rangle = 0$. For example, at the temperature 30nK, the initial, equilibrium profile as shown in Fig. 6.1, had approximately 2860 condensate atoms in the left well and 2140 in the right. When time evolution begins, the condensate atoms start to move from the well with the highest density to that with the lowest, and we see that at 12ms the bulk of the population has moved from the left well, now containing 2140 atoms, to the right which contains 2860 atoms. The number of condensate atoms return to their original values at approximately 25ms. This oscillation between maximum and minimum atom number continues over time.

Following Collin and Zaremba [154], we define the *weighted* average phase of the con-

densate as

$$\theta_{L,R} = \frac{\int_z d\mathbf{r}\ \arg[\sqrt{n_c(\mathbf{r},t)}]n_c(\mathbf{r},t)}{\int_z d\mathbf{r}\ \ n_c(\mathbf{r},t)}. \tag{6.7}$$

The weighted averaged is used to avoid issues with numerical noise when the condensate density is very small. The integrations are over $z \in L$ for the condensate phase of the left well and $z \in R$ to generate the phase of the condensate in the right well. This value is plotted in Fig. 6.2 (Top, Right). The phase difference between the two wells begins at zero for all temperatures and proceeds to oscillate around a mean of zero, $\langle\theta\rangle = 0$, with the same frequency as the condensate population imbalance. From both of these quantities, we infer that the condensate is undergoing Josephson oscillations of its population and phase.

The Josephson oscillations for the condensate appear to change very little in magnitude for increasing temperature, apart from a slight phase shift of both of these oscillations which increases with temperature. However, when the *total* population imbalance, $Z_{\mathrm{TOT}}(t)$ is calculated (Bottom, Left), finite temperature effects begin to emerge.

For the lowest temperature, 6nK, there is a negligible thermal cloud (of approximately 20 atoms), therefore, the total population imbalance is very similar to the condensate population imbalance and with an initial value of $Z_{\mathrm{TOT}}(0) \approx Z_c(0) = 0.15$. As the temperature increases, however, $Z_{\mathrm{TOT}}(0)$ decreases and is less than $Z_c(0)$. The reason for this is the presence of thermal atoms in the system.

In areas where the condensate density is high, the mean field potential felt by the thermal atoms is high, therefore they will be repelled. This means that the thermal cloud density will be higher in the parts of the trap with lowest condensate density, i.e. the edges and the barrier region. Overall, the effect will be more thermal atoms on the side of the potential with less condensate atoms and visa versa.

Initially, for all temperatures, the thermal population imbalance is positive (Fig. 6.2 Bottom, Right), indicating there are more atoms on the left side of the trap than the right. This is an artifact of the offset trap used to generate the equilibrium densities. When the dynamical evolution begins in the trap with no offset, there is a flow of thermal atoms from the left side of the trap to the right where the mean-field potential provided by the condensate density is less. After this initial equilibration period, the thermal atoms oscillate with the same period as the condensate population imbalance with a phase shift of $\pi/2$, therefore when the condensate density in one well of the trap is at a maximum, the thermal cloud density in this region is at a minimum. This is a result of the repulsive mean field exerted by the condensate on the thermal cloud.

By extracting the frequency of the oscillations, we can check if the period of the oscil-

lations are in fact the same. We Fourier transform the population imbalances, $Z_c(t)$, $Z_T(t)$ and $Z_{\mathrm{TOT}}(t)$ for a temperature of 30nK, to extract the dominant frequencies, Fig. 6.3. We

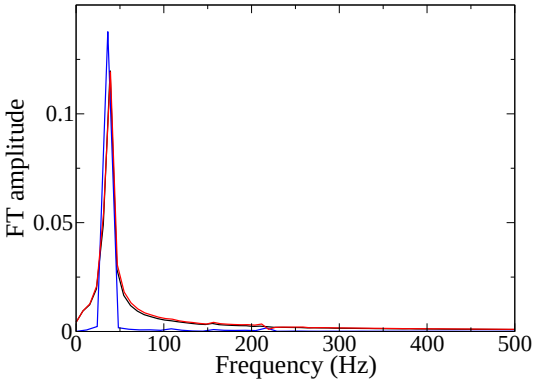

Figure 6.3: Fourier transform of total (black), condensate (red) and thermal (blue) population imbalance for temperature 30nK.

see from this figure, that the frequency of oscillation of all the population imbalances are approximately the same with a value of 40Hz. There is a slight shift in the thermal atom population imbalance which is most likely due to the initial equilibration at the beginning of real time dynamics and this shift could be eliminated by performing the Fourier transform over a longer period of time. We have also taken the Fourier transform of the phase dynamics (Fig. 6.2 Top right) and achieved the same result.

Having reproduced the findings of Collin and Zaremba [154] on the role of finite temperature on the damping of Josephson oscillations, we now move to discuss the more complicated double well trap of a recent experiment [34] and analyse its population dynamics.

6.2 Experiment of LeBlanc *et al.* [34]

In a recent experiment by the group of Thywissen [34], a BEC was formed on the underside of an atom chip [237], in a double well with a tunable junction. The group subsequently investigated transport between the two wells for different barrier heights and initial population imbalances, by measuring the time evolution of the population dynamics. For low barrier heights, $V_0/\mu < 1$, they found two peaks in the frequency spectrum of the population imbalance, indicating that the superfluid hydrodynamic regime undergoes rich and interesting population dynamics, where two modes were excited as a result of the anharmonic nature of the trap. When the barrier height was increased such that the condensate density in this region was negligible, $V_0/\mu > 1$, quantum tunnelling takes place and analysis of the frequency spectrum revealed only one dominant frequency in this regime. An unexplained feature of their results is the decay of the population imbalance over time

(see subsequent Fig. 6.7). In order to discuss whether this decay could be a result of finite temperature damping, we will investigate finite temperature effects on the population imbalance in Sec. 6.2.2. We begin however by analysing the shape of the trapping potential and corresponding condensate density at a low temperature with a negligible thermal cloud.

6.2.1 The atom chip, double well trap

In this experiment, ^{87}Rb is cooled on the underside of an atom chip in a static, Ioffe-Pritchard style magnetic potential, $\mathbf{B}_S(\mathbf{r})$ and by slowly applying radiofrequency (rf) magnetic fields. The atoms follow the new, dressed states and a smooth transition is made to a double well. The advantage of this method for 'splitting' a condensate, is the control over the width and height of the barrier between the two wells, enabling or suppressing tunnelling between both condensates.

The approximate analytic form of the potential is written as [238],

$$V_{\rm ext}(x,y,z,\delta) = \frac{1}{h}\sqrt{(\mu_B B_{\rm dc}(x,y,z) - 2h(\delta+\nu_{TB})^2) + \left(\frac{\mu_B B_{{\rm RF},\perp}(x,y,z)}{2}\right)^2} - \frac{1}{h}\sqrt{(2h\delta)^2 + \left(\frac{\mu_B B_{\rm RF}}{2}\right)^2} + \frac{1}{2}m\omega_{z0}^2 z^2. \quad (6.8)$$

whereby rapidly rotating terms of the Hamiltonian have been neglected following the rotating-wave approximation (see for example, Ref. [239]). The long form of $B_{\rm dc}$, the strength of the static magnetic field for an Ioffe-Pritchard style trap, and $B_{{\rm rf},\perp}$, the oscillating field strength, are given along with more details about the trapping potential in Appendix D (see also [240]). When the rf-dressing is turned on, the shape of the trap in the x-direction becomes less quadratic than the usual harmonic trap and becomes 'flat bottomed'. As the strength of the rf-dressing is increased the barrier between the two wells increases. The rf-detuning, δ, is zero when the radio frequency, $\omega_{\rm rf}$, is on resonance with the trap bottom. The shape of the trap in all three directions is shown in Fig. 6.4. The effect of changing the value of detuning, δ on the geometry in the x-direction is also shown in Fig. 6.5 with the remainder of the experimental trapping parameters summarised in Table 6.1.

From Fig. 6.4 we see that the trapping frequency in the x-direction is indeed a double well; however, although there is a weak harmonic trap in the z-direction, required to prevent the atoms falling under gravity, the trapping potential in the y-direction has also changed and is no longer harmonic. It has become a flat bottomed, weak double well which is raised so that its minimum corresponds to the height of the barrier in the x-direction

ω_z	Axial trapping frequency	$2\pi \times 10$ Hz
ω_{z0}	Axial trapping frequency, with Gaussian beam	$2\pi \times 95$ Hz
ω_r	Radial trapping frequency	$2\pi \times 1310$ Hz
ν_{TB}	Trap bottom frequency	787000 Hz
m_F	Magnetic quantum number	2
g_F	Lande g-factor	0.5
h	Planck's constant	6.626×10^{-34} J $\cdot$ s
μ_B	Bohr Magneton	$9.2741 \times 10^{-24} J/T$

Table 6.1: Summary of experimental trapping parameters used to create the double well potential [240].

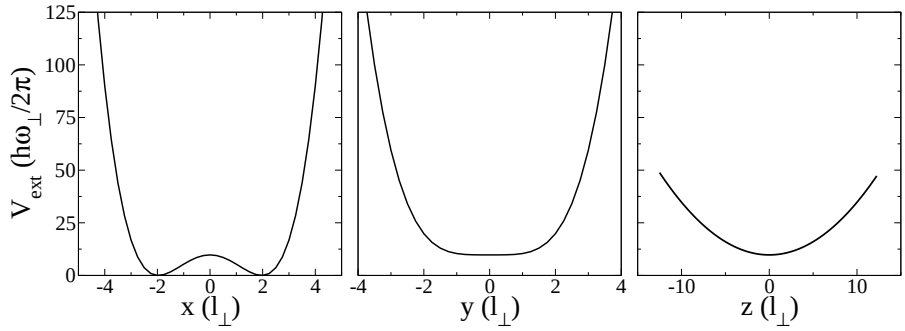

Figure 6.4: Trapping potential in the x, y and z directions for $\delta = 0$ kHz

(likewise for the minimum of the harmonic trap in z). This means the geometry is much more complicated than that investigated in Sec. 6.1. The double well manifests itself (mainly) in the x-direction and so we focus on the population dynamics in this direction and analyse the effect of changing the detuning, δ.

Fig. 6.5 shows the trapping potential in the x-direction for three different values of detuning, $2\pi \times (-5)$ kHz, 0 kHz, and $2\pi \times 5$ kHz along with the corresponding condensate densities for an atom number of $N_c = 8000$ at $T = 10$nK with negligible thermal cloud. Below resonance, $\delta < 0$, the barrier between the two wells is low and the density in the region of the barrier is nonzero whilst well above resonance, $\delta \gg 0$, the barrier is high and increasing the detuning any further would result in the condensate density in the barrier region approaching zero (when $V_0/\mu \gtrsim 1$). In order to bias the population into one well, a linear optical bias is applied across the double well in the experiment. This bias is then turned off before the population dynamics begin. We simulate this by applying a slope

across the double well in this direction using the loop over $x-$coordinate,

$$\text{do} \quad i = 0, NNX \tag{6.9}$$

$$V_{\text{linear}}(i) = \alpha \frac{V_0}{(i_{\min})\Delta x}(i - i_{\min})\Delta x \tag{6.10}$$

$$\text{end do} \tag{6.11}$$

where, α is the slope of the linear ramp, V_0 is the height of the potential at the barrier and $i_{\min}$ is index of the $x-$coordinate at the minimum of the right well, NNX is the total number of grid points in the $x-$direction and Δx is the grid spacing.
Here we have used a slope with gradient $\alpha = 0.4$ and the corresponding population imbalances for these condensates are shown in Fig. 6.5 (Bottom).

In summary, our numerical procedure is a follows: We create the equilibrium densities in the potential, $V_{\text{ext}}(x, y, z) + V_{\text{linear}}(x)$, where $V_{\text{linear}}(x)$ is the linear slope with specified gradient, applied in the x direction in order to bias the population towards one of the wells. When we have generated the equilibrium densities the linear slope is removed and the population dynamics of the resulting asymmetric state are studied along the x direction of the trap $V_{\text{ext}}(x, y, z)$.

Fig. 6.5 (Bottom) shows the evolution of condensate population dynamics for the displayed potentials. For the condensates in the trapping potentials which have a value of detuning $\delta \leq 0$, the populations are undergoing oscillations with a mean value of zero, $\langle Z_c(t) \rangle = 0$. When the detuning is $2\pi \times (-5)$ kHz, the initial population imbalance and the subsequent amplitude of oscillations are much smaller than when $\delta = 0$ kHz. This is because the barrier height is low compared with the system chemical potential and tunnelling is suppressed. For a value of detuning of $\delta = 2\pi \times 5$ kHz, the population is macroscopically trapped with population imbalance oscillations below its initial value of $Z_c(0) \approx 0.275$. For this value of detuning the barrier is high compared with the system chemical potential, so the majority of the population has become self-locked in one of the wells, this is phenomena referred to as *macroscopic quantum self trapping* (MQST). It is characterised by a large number of atoms in one well, a much smaller number of atoms in the other, and rapid tunnelling across the barrier. The phase difference between the two wells in this self-locked system, rapidly increases with time (running phase modes [152]). MQST is predicted to decay at finite temperatures [154–156], however, an analysis of this effect is beyond the scope of this thesis.

A significant difference observed between the population dynamics for this atom chip trap and the previous double well investigated in Sec. 6.1, is the complicated nature of the oscillations which appear to have more than one frequency. We can gain more of an insight into the frequency of the population imbalance oscillations by performing a Fourier transform to extract the dominant frequencies. From Fig. 6.6, it is clear that the population

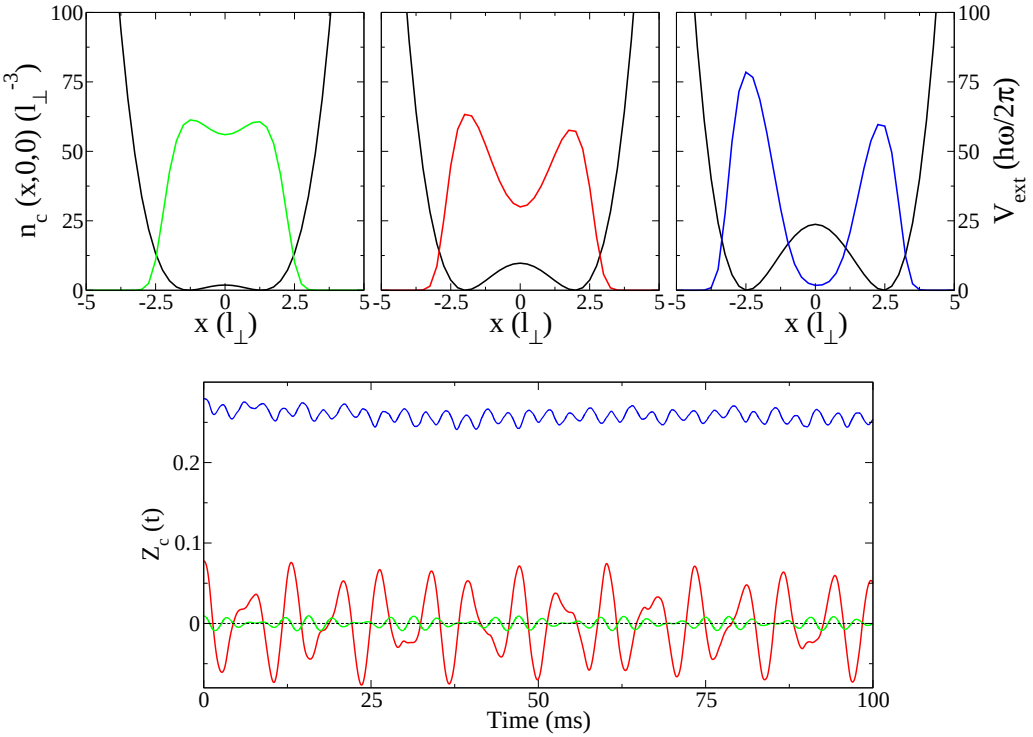

Figure 6.5: Top: Trapping potential (black) and condensate density in the x-direction for $N_c = 8000$, for values of detuning, $\delta = 2\pi \times (-5)$ kHz where $V_0/\mu \simeq 0.1$ (Left, green), $\delta = 0$ where $V_0/\mu \simeq 0.5$ (Middle, red), and $\delta = 2\pi \times 5$ kHz where $V_0/\mu \simeq 1.1$ (Right, blue) with the applied linear potential of slope $\alpha = 0.4$. Bottom: Corresponding condensate population imbalances, $Z_c(t)$ at $T \simeq 10$nK and $N_c = 8000$ atoms, showing Josephson oscillations (green, red) and MQST (blue).

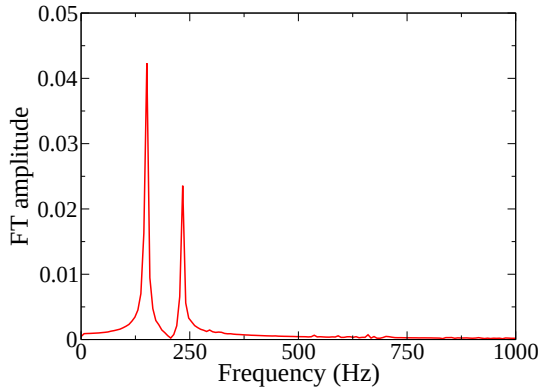

Figure 6.6: Fourier transform of population imbalance for $T = 10$nK when $\delta = 0$ kHz. Dominant frequencies given by peaks at 150Hz and 235Hz.

dynamics for the trapping potential with a value of $\delta = 0$ kHz, has two dominant frequencies. This is in agreement with the findings and analysis of the experimental group [34] who state that the appearance of two frequencies is a consequence of the anharmonic as well as anisotropic nature of the trap and interactions. This is in contrast to the single

mode which was excited in the previous example.

Experimental Considerations

To compare our results with the exact experimental parameters we turn to notes given in the supplementary material of this paper [34]. In these notes, reference is made to the difference in the full potential and the analytic potential derived as a result of the rotating wave approximation. A shift in the value of detuning must be made to account for this difference; for example, to account for the difference between the full potential which has a detuning value of $\delta = 0$ kHz and the rotating wave approximation potential of Eq. 6.8, a shift of $\delta_{\text{shift}} \approx 2\pi \times (-1.85)$ kHz must be used (see the supplementary material provided for [34] for analysis). We will take this shift into account in all further analysis.

In [34], damping of the population imbalance is observed. A detuning of $\delta = 2\pi \times (0.1 \pm 0.5)$ kHz is used with an atom number of $N_c = 6800 \pm 400 \pm 1700$, with the first error arising from shot to shot variations and the second is uncertainty in measured atom number of each run. In order to measure the population imbalance, the clouds are allowed to expand and absorption imaging is used. For these parameters, the population imbalance measured is shown in Fig. 6.7 (Left). The frequencies are extracted by performing a decaying 2-mode fit to the experimental points and applying a Fourier Transform to this, see Fig. 6.7 (Right). In the experiment, when the barrier is low such that $V_0/\mu < 1$ (as is the case for

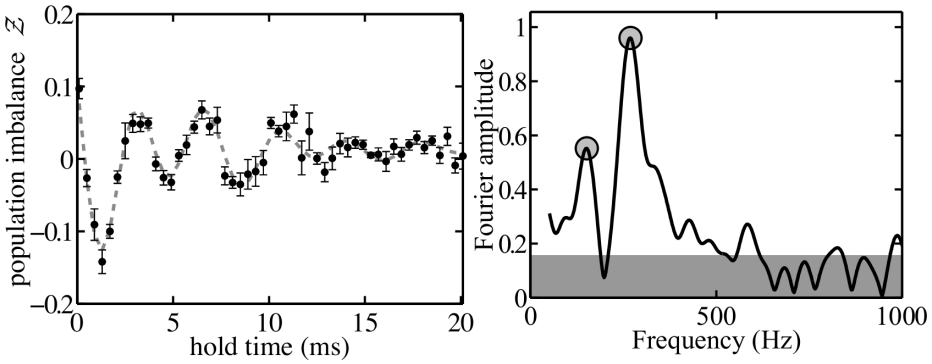

Figure 6.7: Figure taken from Ref. [240]. Left: Experimental points of population imbalance, $\mathcal{Z}(t)$ for $\delta = 2\pi \times (0.1 \pm 0.5)$ Hz. Dashed line is a decaying GPE, two frequency sinusoidal fit. Right: Frequencies of this fit extracted via a Fourier Analysis. The dominant frequencies are 268 ± 6Hz and 151 ± 13Hz.

these trapping parameters), two dominant oscillation frequencies are observed indicating that two modes have been excited as a result of the complicated nature of the trap. The unexplained decay of the population imbalance observed in Fig. 6.7 (Left) remains an open question for the experiment. In order to assess if it can be explained by finite temperatures, we can use the ZNG theory to model the experiment at various temperatures. Firstly, we will get results for these parameters at low temperature when there is no discernible

thermal cloud.

The trapping potential and resulting condensate densities are shown in Fig. 6.8. Although, the number of condensed atoms in the experiment is $N_c = 6800 \pm 400 \pm 1700$ we will continue to use an atom number of $N_{\rm TOT} = 8000$ as was recommended to us in order to gain results to best match the experiment [240, 241]. We investigate oscillations corresponding to a physical choice of $\delta = 0$ kHz, which translate to the shifted value of detuning of $\delta_{\rm shift} = 2\pi \times (-1.85)$ kHz. We increase the slope of the linear bias to $\alpha = 0.7$ in order to obtain an initial population imbalance of $Z_{\rm TOT}(0) = 0.07$, which is close to the experimental value. In Fig. 6.8 we have also plotted the condensate density for a later

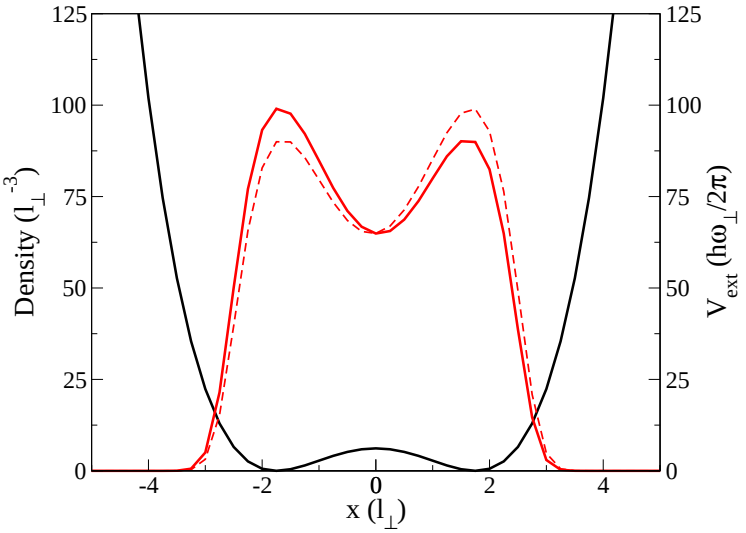

Figure 6.8: Trapping potential (black) and equilibrium condensate density (red, solid) in the x-direction for a shifted value of detuning of $\delta_{\rm shift} = 2\pi \times (-1.85)$ kHz, corresponding to a physical value of $\delta = 0$ kHz. The condensate density is also shown at a later time of $\approx$ 2ms to demonstrate the oscillation of population between the wells (red, dashed). This point in time is also highlighted in the plot of the population imbalance shown in Fig. 6.9. Here $V_0/\mu \simeq 0.3$, $N_{\rm TOT} = 8000$ at $T = 10$nK with negligible thermal cloud.

time of 2ms when the bulk of the population has shifted from the left well to the right well. At this time, the oscillation of the population imbalance, shown in Fig. 6.9 with this point highlighted, has reached its most negative value before it increases again as the population oscillates back again. The remainder of the population imbalance undergoes complicated oscillations and the dominant frequencies of these oscillations are given by the Fourier Transform of the population imbalance, Fig. 6.9 (Right).

Dominant frequencies appear with values 184 Hz, and 264 Hz, similar to the experimental values quoted in [34] of 151 ± 13Hz and 268 ± 6Hz. We can use these values to come up with an approximate fit to the population imbalance.

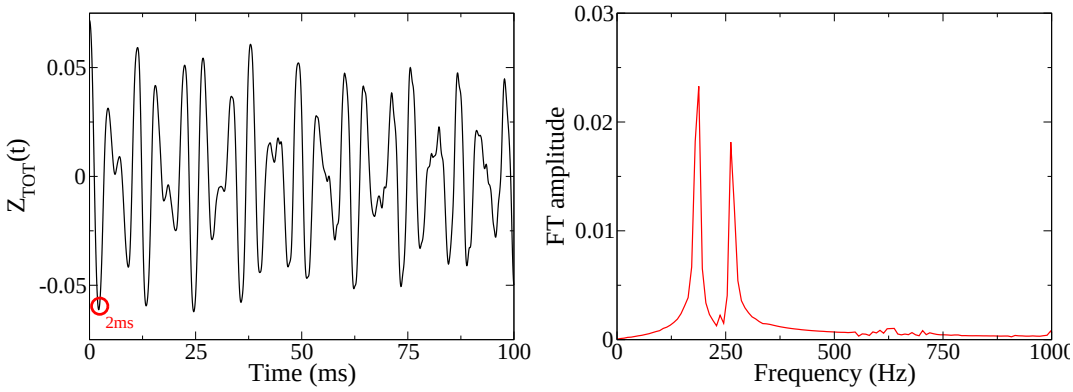

Figure 6.9: Left: Population imbalance, for a system of $N_{\mathrm{TOT}} = 8000$ at 10nK with no discernible thermal cloud and $\delta_{\mathrm{shift}} = 2\pi \times (-1.85)$ kHz where $V_0/\mu \simeq 0.3$. The red circle highlights the point at which the bulk of the population has moved from the left well to the right. Right: Fourier Transform of total population imbalance $Z_{\mathrm{TOT}}(t)$ with dominant frequencies 184 Hz, and 264 Hz.

Population Imbalance Fit

Since the population imbalance decays so rapidly in the experiment, see Fig 6.7 (Left), in order to extract the dominant frequencies, a 2-mode sinusoidal fit is made to the experimental points. Then resulting Fourier spectrum is shown in Fig 6.7 (Right). In our simulations, we do not find the population imbalances decay over this short timescale; so we extract the frequencies directly, as we have done in Fig. 6.9 (Right), and then use the fit

$$Z_{\mathrm{TOT}}(t) = a_1 \sin(2\pi\omega_{z_1}(t - t_1)) + a_2 \sin(2\pi\omega_{z_2}(t - t_2)) \tag{6.12}$$

where $\omega_{z_{1,2}}$ are the frequencies of each component with amplitudes $a_{1,2}$, and $t_{1,2}$ are the phase shifts for each. The population imbalance in shown in Fig. 6.9 (Left) with the Fourier transform plotted in the right part of this figure. We extract the dominant frequencies, ω_{z_1} and ω_{z_2}, from this in order to calculate the fit of expression (6.12) for these parameters. This fit is shown by the dashed lines of Fig. 6.10 on top of the population imbalance.

From Fig. 6.10 we see there is a slight damping of the population imbalance. We will now assess the effect of the presence of a thermal cloud on the population dynamics by presenting results for the same trapping potential as in Fig. 6.8 and total number of atoms, $N_{\mathrm{TOT}} = 8000$ for higher temperatures.

6.2.2 Finite temperature effects on the population imbalance

We now repeat these calculations for higher temperatures. Due to the very asymmetric nature of this trap i.e., each well is not symmetric about its minimum and the trap differs in the x and y directions, the numerical manner in which we currently find the solution

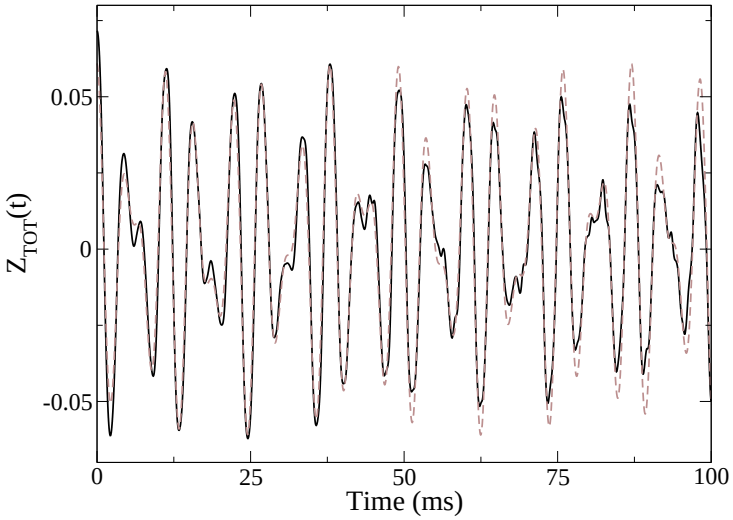

Figure 6.10: Fit of Eq. (6.12) (brown/grey) to the population imbalance (black) for $\delta_{\text{shift}} = 2\pi \times (-1.85)$ kHz where $V_0/\mu \simeq 0.3$ at $T = 10$nK.

of the collision integrals for the Boltzmann equation are not suited to this problem and tend to run into numerical problems. For this reason, which will be outlined further in Sec. 6.2.3, all further finite temperature results are obtained without the inclusion of the C_{12} and C_{22} collision integrals. Therefore, any finite temperature effects reported here are the result of mean-field interaction between the condensate and thermal cloud and will consequently *underestimate* the amount of damping actually present in the physical system.

The equilibrium condensate and thermal cloud densities in the x-direction for a temper-

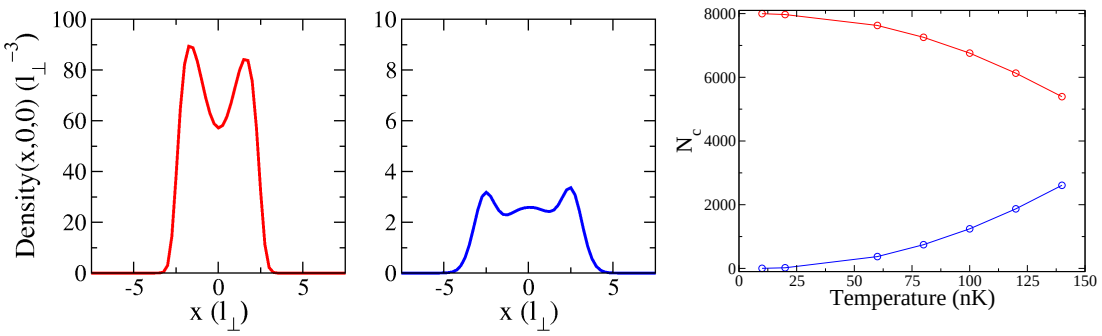

Figure 6.11: Left: Condensate (red) and Middle: thermal cloud (blue) densities for $T = 120$nK for the experimental trap with shifted value of detuning of $\delta = 2\pi \times (-1.85)$ kHz where $V_0/\mu \simeq 0.3$. The resulting atom numbers for this temperature are $N_c = 6130$ and $\tilde{N}_T = 1870$. Right: Condensate (red) and thermal (blue) atom numbers for a range of temperatures for total atom number $N_{\text{TOT}} = 8000$.

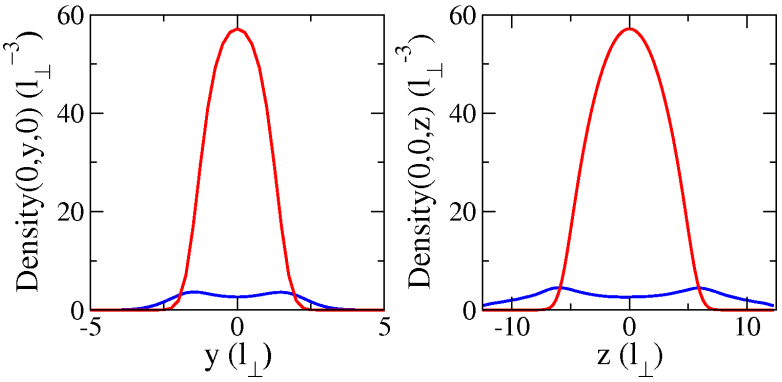

Figure 6.12: Condensate (red) and thermal cloud (blue) densities for $T = 120$nK in the y (left) and z (right) direction, for the experimental trap with shifted value of detuning of $\delta = 2\pi \times (-1.85)$ kHz where $V_0/\mu \simeq 0.3$. The resulting atom numbers for this temperature are $N_c = 6130$ and $\tilde{N}_T = 1870$.

ature of 120nK are given in Fig. 6.11 (Left), with the resulting condensate and thermal cloud atom numbers as a function of temperature given to the right of this figure. We do not simulate temperatures higher than 140nK because the resulting atom numbers of such temperatures are no longer consistent with the experiment. The condensate density has the usual two peaked structure expected in a double well potential and, due to the mean field interaction between the condensate and thermal atoms, the normal double peaked structure of the thermal cloud is somewhat increased in the central region than if the trap were harmonic. This is due to the lower mean-field repulsion felt by the thermal cloud due to the dip in the condensate density. We also plot the resulting densities in the y and z direction in Fig. 6.12.

For the temperatures 60nK and 120nK we plot both the *total* and *condensate* population imbalance in Fig. 6.13 for the same system of $N_{\rm TOT} = 8000$ atoms. It is clear from

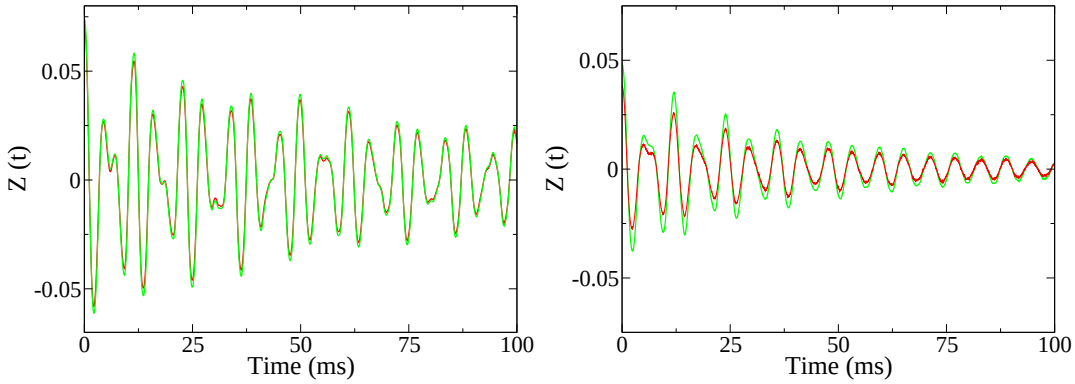

Figure 6.13: Total, $Z_{\rm TOT}(t)$ (red) and condensate, $Z_c(t)$ (green) population imbalance for $T = 60$nK (left) and 120nK (right). $\delta_{\rm shift} = 2\pi \times (-1.85)$ kHz where $V_0/\mu \simeq 0.3$ and the slope of the linear bias is $\alpha = 0.7$.

these population imbalance graphs that at low temperatures, the condensate and total population imbalance are very similar, however, when the temperature is increased from 60nK to 120nK, they differ slightly. In particular, the amplitude of the total population imbalance oscillation is smaller than that for the condensate. This is due to the presence of thermal atoms in the system and the effect is more apparent for the temperature of 120nK since there are more thermal atoms in the system. When the total population imbalance is measured, the thermal atoms on either side of the trap are also counted and since there is repulsion between the thermal cloud and condensate, there will be more thermal atoms where there are less condensate atoms and visa versa, as previously discussed in Sec. 6.1.1. Since in the experiment no differentiation has been made between these two quantities, and we see such little difference we will henceforth study the *total* population imbalance and refer to it as $Z(t)$.

A feature which is absent from the zero temperature results in the previous section, is the damping of the population imbalance which we can see in Fig. 6.13. This damping is much more enhanced in this geometry than in the previous case becoming more apparent in the higher temperature of 120nK; however, even at that temperature, where there are approximately $\tilde{N}_T = 2000$ thermal atoms in the trap (which is the limit allowed by the experimental measurements), the damping occurs over a longer timescale, $\sim 100ms$, than in the experiment, $\sim 10ms$ (see Fig. 6.7). Although the decay of the population is not as rapid for our results as was observed in the experiment, it is suggestive that some of the damping observed experimentally could be due to the presence of an undetected, small number of thermal atoms in the system. It is crucial here to note once again that our present analysis neglects the effect of thermal cloud collisions as well as collisions between the condensate and thermal cloud. We have shown for the case of a vortex in Chapter 5, Sec. 5.2, that neglecting any of these collisional types leads to a significantly slower decay time for the vortex. We suspect the same to be true here, that is to say, the population dynamics may suffer from more damping if we include the effect of these collisions, something which is however left to future work.

We now assess the dependence of the damping in the absence of collisions on temperature by extracting a decay rate of the population imbalance, initially for the temperature 120nK. To modify the sinusoidal fit of Eq. (6.12) to include damping, we can multiply it by a decaying exponential function, as is done in the analysis of the experimental data [240]. The expression becomes

$$Z(t) = e^{-t/\tau} \left(a_1 \sin(2\pi\omega_{z_1}(t - t_1)) + a_2 \sin(2\pi\omega_{z_2}(t - t_2))\right), \tag{6.13}$$

where $1/\tau$ is the damping rate. We have also extracted this rate for other temperatures and plotted these in Fig. 6.14. From this we see a clear dependence of the rate of damping on the temperature of the system.

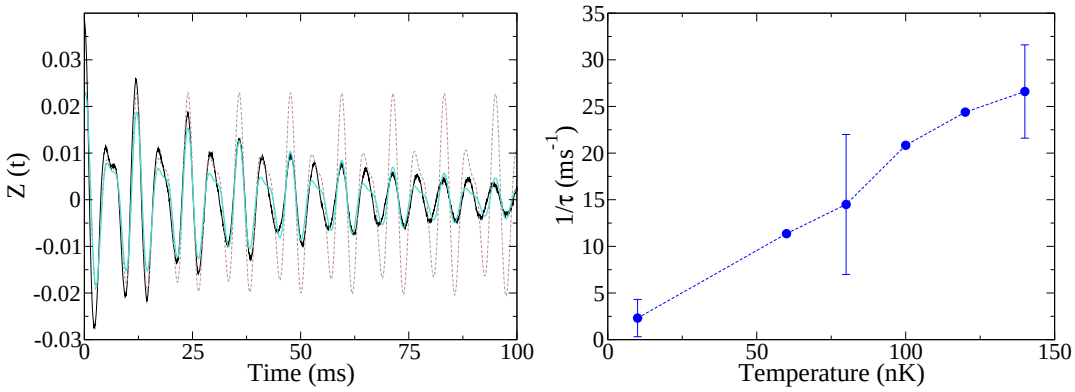

Figure 6.14: Left: Total population imbalance for $T = 120$nK (black), fit of expression (6.13) without damping (brown/grey dashed) and with a damping rate $1/\tau = 24.4$ (cyan). Right: Damping rate, $1/\tau$ plotted as a function of temperature with error bars for 3 of the temperatures.

In the experiment, very little dependence was found on the decay rate with temperature and therefore it was suggested that temperature was not likely to be the principle cause for the decay observed. We have extracted the rate of decay as a function of temperature, as shown in Fig. 6.14, and find a clear dependence on temperature; however we reiterate that the decay we find in our simulations without collisions is much slower than in the experiment. We therefore suggest that the decay observed in the experiment could be, at least, partially due to the presence of thermal atoms in the system, although other reasons could contribute further and even more dominantly, for example damping arising from the motion of the condensate in this large anharmonic double well trap.

6.2.3 Numerical issues

In Chapter 4, we discussed how the collision integrals of the Boltzmann Eq. (2.39) are calculated in our numerics. In particular, we assume when we initialise the test particles according to the equilibrium density, that the trapping potential in the x and y directions are symmetric. This means that for complicated geometries, or any geometry in which the trapping potential in the x and y direction are not symmetric, the initialisation of the test particles is not accurate for that geometry. Further to this, the test particles are also binned into cells radially at every time step which is not optimal for an asymmetric geometry and other shapes of cells should be used, for example square cells [215].

We show an example of the numerical difficulties encountered in Fig. 6.15 for the geometry of Fig. 6.2.2. The total number of atoms in the thermal cloud is initially $\tilde{N} = 1250$ (635 in the left well and 615 in the right), when the dynamics begin, the population of the thermal atoms in each well decreases with time (numerical drift) due to inaccuracies in the initialisation of the test particles and the positioning of the cells.

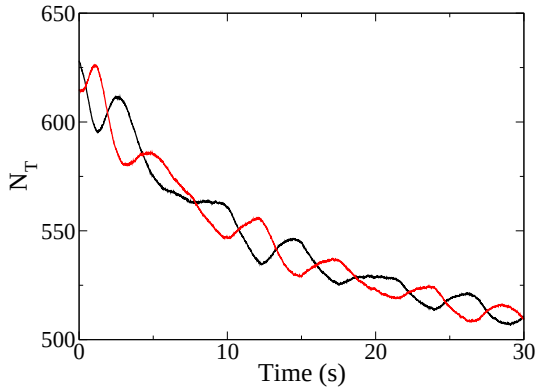

Figure 6.15: Number of thermal atoms on the left (black) and on the right side of the trap (red) for 100nK when all collisional terms are included in the numerical calculation of the QBE using symmetric test particle binning for this non-cylindrically symmetric geometry.

We will address how we propose to deal with geometries of this kind in the next chapter.

6.3 Chapter Summary

In this chapter we have studied oscillations of population and phase dynamics in both a symmetric double well geometry, formed by the superposition of a one dimensional optical lattice and a harmonic trap first discussed by Collin and Zaremba [154], and a more complicated geometry corresponding to a recent experiment in which a double well is formed on the underside of an atom chip [34]. The analysis of such oscillations is based on numerical simulations of the ZNG equations at finite temperatures, in which however, the effect of collisions has been neglected due to 'technical' reasons.

In the first case, we demonstrated oscillations of population dynamics, including *condensate*, *thermal* and *total* atom population oscillations of the same frequency around a mean value of zero; the condensate phase oscillates also with the same frequency. The dependence of temperature on the total and condensate population imbalance has been assessed, revealing that the thermal cloud also has a population oscillation which is out of phase with that of the condensate. This is a result of the mean-field repulsion between the two subsystems. The resulting effect on the total population imbalance, is to decrease the amplitude of the oscillation, therefore the thermal cloud has a balancing effect on the total population imbalance. Furthermore, with increasing temperature we see an increasing phase shift in the population imbalance.

We then investigated similar dynamics for a more complicated double well geometry with a tunable barrier, situated on the underside of an atom chip, as recently realised experimentally [34]. By increasing the value of detuning one can change both the barrier height and well separation enabling population dynamics to be studied for a range

of different initial conditions. Depending on the height of the barrier between the wells either one or two dominant frequencies of the population dynamics were observed experimentally corresponding to the existence of the excitation of two condensate modes in the hydrodynamic regime as a result of the anharmonic nature of the trap. Another feature of the observed population dynamics, was damping which occurred over the short time of 10ms.

We again used the ZNG equations to investigate this trapping geometry at low and finite temperatures. When we modelled the specific trapping parameters from the experiment at low temperatures, we found very little damping occurred over a long time scale. However, we also found rather more complicated population dynamics, as already observed numerically by Smerzi and co-workers [34], with two dominant frequencies showing reasonable quantitative agreement with experiment. When we increased the temperature the damping of the population dynamics increased, indicating a noticeable, linear like increase of the decay rate with temperature; however, the damping we observed, occurred over a much longer timescale of 100ms. We stress the fact that the decay of the population imbalance obtained in our simulations is only due to the mean-field interaction between the condensate and thermal cloud with the Boltzmann equation solved in the absence of collisions for 'technical' reasons. In Chapter 5 we showed that the rate of decay of a vortex increased significantly when both collisional types were simulated, and the most dominant mechanism for decay was in fact the collisions between the condensate and thermal cloud. This gives us reason to believe that the damping rate of the population dynamics would also be greater if all collisional processes were included in these double well simulations.

The experimental group investigated the effect of finite temperature on the rate of decay of the population dynamics and found little to no correlation; therefore, we suspect that the observed decay, while partially due to finite temperature effects, may also arise due to another, apparently more dominant mechanism possibly pronounced by the complicated geometry of this experiment.

We also reported the limiting factor in our simulations of this kind at the moment, which is the symmetry assumed when calculating the collision integrals of the Boltzmann Eq. (2.39). We will address how we plan to implement changes to this computation so that asymmetric geometries can be dealt with in the future, in the next chapter.

Chapter 7

Summary of Conclusions and Future Work

In this thesis, we have presented investigations into weakly-interacting atomic Bose-Einstein condensates at zero and finite temperatures. In particular, we have studied dark soliton decay via sound emission due to propagation in an inhomogeneous background at zero temperature. We have demonstrated how two or more solitons can interact over a long-range, mediated by the energy dissipated in the form of sound as a result of this decay. At finite temperatures we have studied the dynamics of vortices, their decay rates and the role collisions involving the thermal cloud play in this decay, precession frequency and core brightness. We further investigated a method for increasing or decreasing the angular momentum of a vortex by rotating the thermal cloud in the same or opposite sense as vortex precession. We also studied the effect of the mean-field interaction between the condensate and thermal cloud on Josephson oscillations of the population in an atom chip, double well experiment.

We began in Part I by giving an overview of the theory involved in the study of weakly-interacting Bose-Einstein condensates, highlighting the important concepts involved in the derivation of the equations used to model these systems at zero and finite temperature.

In Part II, the results presented on soliton dynamics were obtained by numerically solving the Gross-Pitaevskii equation which is known to be accurate for the description of the condensate wavefunction for temperatures up to $\simeq 0.5T_c$. The low temperatures probed in recent soliton experiments are well within this regime [84–86].

In the remainder of this thesis, Part III, we focussed on the effect of finite temperature of the dynamics on vortices and Josephson effects. The scheme we use to model the presence of a thermal cloud in the system is the Zaremba-Nikuni-Griffin (ZNG) scheme [69]. In this formalism, the Gross-Pitaevskii equation is modified by the mean-field of the thermal cloud, as well as a source term coupled to a quantum Boltzmann equation for the ther-

mal cloud. The quantum Boltzmann equation contains the usual free streaming terms, describing the free evolution of the thermal atoms, the collision term representing binary collisions between two thermal atoms as well as the inclusion of another collision term describing particle-exchanging, thermal-condensate collisions. Therefore, the thermal cloud in this scheme is *fully dynamical*.

This part of the thesis began in Chapter 4, with a detailed description of the numerical scheme used to solve these coupled equations. In Chapter 5, we have implemented this procedure to give a detailed analysis of experimentally relevant quantities involving vortices including the effect of the individual collision terms of the quantum Boltzmann equation, on the decay rate of a vortex. We find that by not including *any* of the collision terms, the decay rate of the vortex is *significantly* reduced, especially at high temperatures, with the most dominant contribution to the decay being the particle-exchanging, thermal-condensate collisions.

That said, due to technical reasons for which we will address in Sec. 7.4.3, in Chapter 6 we present the effect of finite temperature on Josephson oscillations of an atom chip, double well experiment [34] in the *absence* of collisions and find that the decay rate of the population imbalance increases with temperature in a linear like manner, therefore, we would expect the decay rate to increase further when the collision dynamics are included in the simulations. In this experiment, the damping of population imbalance happens over a much shorter timescale than in our simulations. We expect that if we were to included the thermal-condensate particle exchanging terms in these simulations, we would also see damping over a shorter timescale.

These results reiterate the importance of including collisions when modelling atomic condensates at finite temperature. In many other finite temperature theories, for example the stochastic Gross-Pitaevskii equation [186, 188], and c-field techniques (see [180] and [54] for related reviews of finite temperature models), there are approximations made on the thermal cloud. Furthermore, due to the nature of the coupled equations in the ZNG formalism, the condensate and thermal cloud are two distinct components which are easily distinguished from each other, hence, both coherent and individual dynamics can be studied.

In this concluding chapter, we aim to summarise the main results of each of these topics and present prospects for future investigation.

7.1 Long-range, sound mediated dark soliton interactions

Dark solitons are prone to acceleration when propagating in an inhomogeneous system. In a harmonic trap, there exists a unique relationship between the frequency of the trap (ω_z) and that of the soliton ($\omega_z/\sqrt{2}$), which enables re-interaction of the soliton with the

sound it has emitted such that, solitons are stable against decay via sound emission in harmonic traps. When two identical solitons are placed in a harmonic trap, small amplitude oscillations appear on the trajectories of both, hinting to emission and reabsorption of energy throughout their motion. When these solitons are non-identical, both trajectories are significantly modified periodically. This is because solitons of different speeds emit and absorb energy at different rates. When the solitons are spatially confined to separate subregions of an idealised double well trap, eliminating direct collisions between them, this effect can be magnified. By placing a black (stationary) soliton in one well and a moving soliton in the other and ensuring that the barrier between the wells is sufficient to let energy pass between the wells ($V_0 \simeq \mu$) but not the soliton, the sound emitted by the moving soliton can travel into the well containing the black soliton and perturb it such that it begins to move and in turn also emit sound. The sound it emits can move into the other well and be absorbed by that soliton. Over a long period of time this emission and reabsorption results in identity reversal between the two solitons whereby the initially moving soliton becomes stationary and the black soliton moves at the initial speed of the other. This perfect reversal of characteristics happens periodically, however, it takes tens of soliton oscillations which is a long time with respect to current soliton experiments, since other decay mechanisms are present in the system and occur on shorter timescales.

We presented two systems in which this effect could be observed experimentally. The first was a harmonic trap split by a Gaussian barrier in which the presence or absence of soliton located in the one half of the trap significantly affects the motion of the soliton in the other. The other was a large periodicity optical lattice in which we observed solitons acting as both absorbers and emitters of energy: the motion of solitons at opposite wells of this optical lattice depend sensitively on whether the intermediate sites contain solitons or not.

Further to this, we briefly presented the results of some recent simulations by Nick Parker in which a similar mechanism of interaction is observed between vortices, thereby strengthening the general nature of this effect. When a double well trap in two dimensions contains vortices of the same polarity in both wells, at different initial radial positions, the motion of one significantly affects the motion of the other. A similar periodic cycle of characteristics as in the case of solitons is observed. When the vortices are of opposite polarity however, the motion of each vortex remain unaffected by the presence of the other.

The energy exchange between vortices happens over a much quicker timescale than for solitons, taking only ~ 10 oscillations in the trap before a significant change in the vortex radial coordinate can be observed. Therefore, vortices are likely to be a better candidate for the experimental observation of this effect.

7.2 Finite temperature vortex dynamics

As a result of finite temperature, a vortex loses energy and this causes it to spiral radially out of a condensate. We investigated this using the ZNG scheme. Advantages to this scheme include: the thermal cloud and condensate densities can be observed separately and the effect of the individual collision processes on the dynamics in question can be assessed.

We investigated the rate of decay of vortices as a function of temperature, in a pancake shaped geometry. We found that the rate of decay of a vortex is not only dependent on the temperature of the system but also on its initial position due to the system inhomogenity. As the temperature of the system increased, the rate of decay of a vortex increased. At the higher temperatures we investigated, it also became apparent that by increasing the vortex radial coordinate the decay rate of the vortex is also significantly increased, as a result of the increasing density of the thermal cloud closer to the edge of the condensate. When these simulations were repeated with or without the collisions, we observed that the absence of any of the collision processes in the simulations reduces the rate of decay of the vortex, most significantly so when the particle-exchanging, thermal-condensate collisions are neglected. The remaining finite temperatures vortex results were obtained with the inclusion of all collision terms.

The precession frequency of a vortex for the same geometry increased with temperature. This was confirmed for trapping parameters of a recent experiment [31]. These simulations were repeated for various atom numbers and trapping potentials, and similar agreement was found for all temperatures. The vortex core brightness, a quantity which has previously been suggested would be a possible mechanism for thermometry in a system such as this [235], was also seen to increase with temperature and again good agreement was observed between different atom numbers and trapping frequencies. More analysis is required however, before this becomes a tool for thermometry.

In the final part of this chapter, we investigated how rotating the thermal cloud could be used as a method to move a vortex to a predetermined position. We presented initial findings, using the parameters of an experiment which is in the early stages of investigating rotating the thermal cloud in the same sense of the vortex precession in order to move the vortex towards the centre of the condensate [236]. We found that the translation occurs over a much longer time scale than the preliminary experimental results. We understand, through correspondence with the experimental group that throughout the duration of the experiment, the temperature rises and atoms are lost from the system. Further investigation is required by both the experimental group and us in order to understand how to accurately model this experiment.

7.3 Finite temperature double well dynamics

In a recent experiment in which a double well is formed on the underside of an atom chip [34], the oscillations of population imbalance suffered significant damping over a short period of time. This motivated our study of the effect of finite temperature on double well dynamics. All results presented for double wells are in the absence of collisions, due to technical reasons in our code which we will address in Sec. 7.4.3.

We initially analysed a symmetric double well formed by imposing an optical potential in one direction of a harmonic trap [154]. For finite temperatures, due to the presence of thermal atoms in the system we measured the *total*, *thermal* as well as the *condensate* population imbalance and found that, as the result of the mean-field potential of the condensate on the thermal cloud the amplitude of oscillation of the total population imbalance is less than that for the condensate imbalance. From the Fourier spectrum of these oscillations, we found that all the aforementioned population imbalances oscillate with the same frequency, this included the evolution of phase difference between the two wells. We observed increased damping and phase shift on the Josephson oscillations, as the temperature is increased.

Repeating the analysis on the complicated atom chip double well, we found the population oscillations in this trap have two dominant frequencies as observed experimentally. When the temperature is increased, we observed damping of the population dynamics but on a much longer timescale than that observed in the experiment. We stress the fact that collisions were neglected in this analysis and since we have previously seen an increased rate of decay in the case of a vortex, we would expect the damping rate of population imbalance to also increase if collision dynamics were included in these simulations.

7.4 Further work

7.4.1 Vortex quantities at finite temperature

In Chapter 5 we presented the effect of temperature on precession frequencies and vortex core brightness. We found similar behaviour with increasing temperature for the different atom numbers and trapping frequencies. In Sec. 5.5 we discussed the suggestion of vortex core brightness as a quantity to determine the temperature of a system [235]. We propose that both *precession frequency* and *vortex core brightness* could be used in conjunction as a thermometer for such systems. This would mean an extensive sweep of trapping parameters, atom number and vortex radial coordinate in order to understand the behaviour and dependence of these quantities on such parameters, as well as temperature.

An ongoing investigation is the rotation of the thermal cloud in order to manipulate the position of the vortex to compare with preliminary data from a recent experiment [236]

for which we presented early findings in Sec. 5.6. This could be a useful method for experimentally manipulating a vortex into the desired position, particularly, since it is difficult to predetermine the position of a vortex when it is being generated (see Chapter 1 Sec. 1.3.2). Our current results show a much slower motion of the vortex towards the centre of the trap than has been seen so far in these experiments, however, since atoms are lost and the temperature rises during the experiment, we need to do more investigation into modelling this accurately.

7.4.2 Multiple vortices

In Chapter 3, we demonstrated a sound mediated interaction mechanism between solitons at zero temperature and briefly introduced work done by Nick Parker to observe a similar exchange of characteristics between vortices. Then, in Chapter 5, we assessed the effect of finite temperature on a single vortex in a harmonic trap. In the future we would like to combine these two topics and model more than one vortex in a harmonic trap and understand how the trajectories are modified by each other, as well as the effect finite temperature has on their dynamics.

This investigation would be experimentally relevant since, during vortex creation, it is possible that more than one vortex enters the system. Using the ZNG scheme enables us to easily view the condensate and thermal cloud densities separately. In Fig. 7.1 we show snapshots in time of an axial view of a condensate in a harmonic trap ($\omega_\perp = 2\pi \times 129$ Hz, $\omega_z = \sqrt{8}\omega_\perp$), containing two off-centred vortices at positions $r_{v_1} \simeq 0.5 l_\perp$ and $r_{v_2} \simeq 1.2 l_\perp$ at the temperature $0.3T_c$. The vortices are created by multiplying the condensate wavefunction by a phase factor (Chapter 5, Eq. 5.9) at all the points in which we want to create a vortex.

The peaks in the thermal cloud density corresponding to the positions of the vortices in the condensate can be clearly seen.

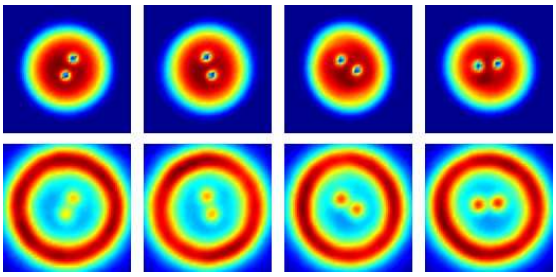

Figure 7.1: Density cross sections of the condensate (top) and thermal cloud (bottom) ($N_{\mathrm{TOT}} = 10000$, $T = 0.3T_c$) at times (from left to right) $1\omega_\perp^{-1}$, $2\omega_\perp^{-1}$, $3\omega_\perp^{-1}$ and $4\omega_\perp^{-1}$.

In Fig. 7.2 we plot the x-position of these vortices over time. The amplitude of these oscillations are significantly modified due to the presence of the other vortex in the system

with each vortex oscillating between two radial positions. These results are for the low temperature of $0.3T_c$ and much investigation needs to be carried out at higher temperatures to assess the dependence of this interaction on the presence of thermal atoms in the system.

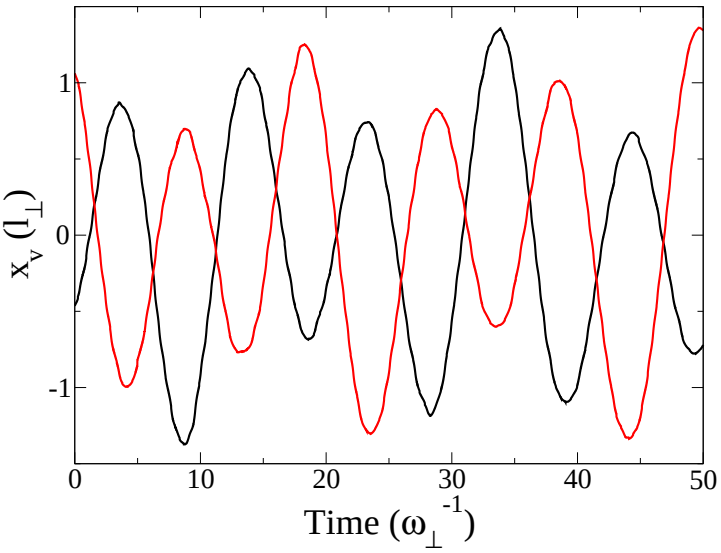

Figure 7.2: x-position of vortices vs. time. Initial positions $r_{v_1} \simeq 0.5l_\perp$ and $r_{v_2} \simeq 1.2l_\perp$, $N_{\rm TOT} = 10000$.

When we have assessed the temperature dependence of this interaction mechanism between two vortices, we would like to extend the analysis to multiple vortices and finally a lattice.

Vortex Lattice

If a condensate is rapidly rotated, a vortex lattice can form [220]. Large lattices of this type have been observed experimentally [115] as well as their subsequent decay [49]. These lattices are highly regular, resembling the triangular flux-line Abrikosov lattices in type-II superconductors [242]. Collective elliptical oscillations of vortices about their equilibrium positions called Tkachenko oscillations [243], have been predicted to occur (see [79] for a review) and subsequently observed in atomic condensates [244].

In Fig. 7.3 we show a small lattice of 12 vortices, in a system with $N_{\rm TOT} = 10000$ atoms with the same trapping parameters as in Figs. 7.1 and 7.2 at a temperature of $T = 0.6T_c$.

In summary, we aim to extend our analysis of single vortices at finite temperature to multiple vortices as well as large vortex lattices in which Tkachenko oscillations can be observed, to understand how their interactions are affected by the presence of a thermal cloud.

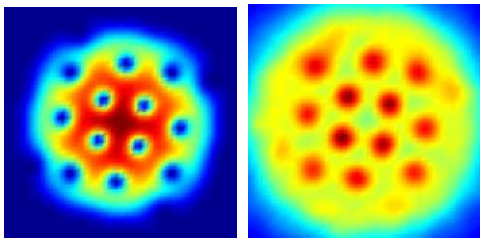

Figure 7.3: Density cross sections of the condensate (left) and thermal cloud (right) of a small vortex lattice with 12 vortices. The axes are the same in both directions with the range $-7.5 \geq x, y \leq 7.5$. $T = 0.6T_c$, $N_{\mathrm{TOT}} = 10000$.

7.4.3 Implementation of the ZNG equations for other geometries

The version of the code which we are currently using to solve the coupled ZNG equations makes use of cylindrical symmetry in order to increase numerical efficiency (as has been highlighted in Chapter 4). This works well for geometries which have such symmetry, for example the harmonic trapping potential used in Chapter 5. However, when geometries which are asymmetric in the x and y direction are investigated, the code may run into numerical difficulties. It is for this reason which we were unable to solve the full dynamical equations, i.e. including collision terms for the double well geometries in Chapter. 6.

In Chapter 4 Sec. 4.2.1 we gave a detailed explanation of how cylindrical symmetry is used to assign position and momenta to test particles during initialisation. We have already adapted this to make it fully 3D for the geometries presented in Chapter 6. When the test particles are binned however, they are done so in radial and axial bins (see Sec. 4.2.2) which are subdivided further into cells for the collisions to happen (see Sec. 4.3.1). This is not the optimal way of binning the test particles when the geometry is not of a cylindrically symmetric form.

We aim to develop the code such that the cells in which the test particles are binned in are square such that any geometry can be studied. Square bins have been implemented for solving the Boltzmann this way in [215] in which the further step of having dynamical binning has been undertaken, however, the thermal-condensate, particle exchanging collisions are ignored in this work.

Appendix A

Derivation of the Gross-Pitaevskii and Bogoliubov Equations

A.1 Derivation of the Gross-Pitaevskii equation

The second quantised Hamiltonian has the form:

$$\hat{H} = \int d\mathbf{r}\hat{\Psi}^\dagger(\mathbf{r})\left[-\frac{\hbar^2}{2m}\nabla^2 + V_{\text{ext}}(\mathbf{r})\right]\hat{\Psi}(\mathbf{r}) \tag{A.1}$$

$$+ \frac{1}{2}\int d\mathbf{r}\int d\mathbf{r}'\hat{\Psi}^\dagger(\mathbf{r})\hat{\Psi}^\dagger(\mathbf{r}')V(\mathbf{r}-\mathbf{r}')\hat{\Psi}(\mathbf{r}')\hat{\Psi}(\mathbf{r}). \tag{A.2}$$

For the purpose of conserving space in this appendix we will furthermore denote the terms in the square brackets as $\hat{h}_0$ and replace the exact interatomic interaction by a contact interaction (as in Chapter 2, Eq. (2.6)), the Hamiltonian becomes,

$$\hat{H} = \int d\mathbf{r}\hat{\Psi}(\mathbf{r},t)\hat{h}_0\Psi(\mathbf{r},t) + \frac{g}{2}\int d\mathbf{r}\hat{\Psi}^\dagger(\mathbf{r},t)\Psi^\dagger(\mathbf{r},t)\Psi(\mathbf{r},t)\Psi(\mathbf{r},t). \tag{A.3}$$

We substitute $\hat{\Psi}(\mathbf{r},t) = \phi(\mathbf{r},t) + \hat{\psi}(\mathbf{r},t)$ into this Hamiltonian and get

$$\begin{aligned}
\hat{H} &= \int d\mathbf{r}(\phi^* + \hat{\psi}^\dagger)\hat{h}_0(\phi + \hat{\psi}) \\
&+ \frac{g}{2}\int d\mathbf{r}(\phi^* + \hat{\psi}^\dagger)(\phi^* + \hat{\psi}^\dagger)(\phi + \hat{\psi})(\phi + \hat{\psi}) \\
&= \int d\mathbf{r}(\phi^*\hat{h}_0\phi + \phi^*\hat{h}_0\hat{\psi} + \hat{\psi}^\dagger\hat{h}_0\phi + \hat{\psi}^\dagger\hat{h}_0\hat{\psi}) \\
&+ \frac{g}{2}\int d\mathbf{r}(\phi^*\phi^* + 2\phi^*\hat{\psi}^\dagger + \psi^\dagger\psi^\dagger)(\phi^2 + 2\phi^*\hat{\psi} + \hat{\psi}\hat{\psi})
\end{aligned} \tag{A.4}$$

where the explicit dependence of ϕ and ψ on position and time is assumed.
The Hamiltonian can now be separated into parts according to the dependence of ψ, the

fluctuation term.

$$\hat{H} = H_0 + \hat{H}_1 + \hat{H}_2 + \hat{H}_3 + \hat{H}_4$$

where the contributions are,

$$H_0 = \int d\mathbf{r}\big(\phi^* \hat{h}_0 \phi + \frac{g}{2}|\phi|^4\big) \tag{A.5}$$

$$\hat{H}_1 = \int d\mathbf{r}\big[\hat{\psi}^\dagger\big(\hat{h}_0\phi + g|\phi|^2\big)\phi + \phi^*\big(\hat{h}_0 + g|\phi|^2\big)\hat{\psi}\big] \tag{A.6}$$

$$\hat{H}_2 = \int d\mathbf{r}\big[\hat{\psi}^\dagger\big(\hat{h}_0 + 2g|\phi|^2\big)\hat{\psi} + \frac{g}{2}\big((\phi^*)^2\hat{\psi}\hat{\psi} + \phi^2\psi^\dagger\psi^\dagger\big)\big] \tag{A.7}$$

$$\hat{H}_3 = g\int d\mathbf{r}\big[\phi\hat{\psi}^\dagger\hat{\psi}^\dagger\hat{\psi} + \phi^*\hat{\psi}^\dagger\hat{\psi}\psi\big] \tag{A.8}$$

$$\hat{H}_4 = \frac{g}{2}\int d\mathbf{r}\big(\hat{\psi}^\dagger\hat{\psi}^\dagger\hat{\psi}\hat{\psi}\big) \tag{A.9}$$

H_0 has no operator dependence i.e. it is a purely classical quantity.

If the Hamiltonian is approximated by H_0 (i.e. all the atoms are assumed to be in the condensate, therefore $\hat{\psi} = 0$), when it is substituted into the Heisenberg equation of motion (as in Sec. 2.1) the resulting evolution equation is the GPE which is accurate at zero temperature and is written,

$$i\hbar\frac{\partial\phi(\mathbf{r},t)}{\partial t} = \left[-\frac{\hbar^2}{2m}\nabla^2 + V_{\text{ext}}(\mathbf{r},t) + g|\phi(\mathbf{r},t)|^2\right]\phi(\mathbf{r},t). \tag{A.10}$$

A.2 The dimensionless Gross-Pitaevskii equation

The Gross-Pitaevskii equation in 1D is written as follows

$$i\hbar\frac{\partial\phi(z,t)}{\partial t} = \left(-\frac{\hbar^2}{2m}\frac{\partial^2}{\partial z^2} + V(z) + g|\phi(z,t)|^2 - \mu\right)\phi(z,t)\ . \tag{A.11}$$

where it is convenient to work with a complex wavefunction $\phi(z,t)$, which is normalised to unity i.e.

$$\int |\phi(z,t)|^2 dz = 1. \tag{A.12}$$

To nondimensionalise Eq. (A.11) in terms of the length scale of the system, i.e. the harmonic oscillator length $l_\perp = \sqrt{\hbar/(m\omega_\perp)}$, we introduce the rescalings

$$\phi_{\text{HO}}(z,t) = l_\perp\phi(z,t), \qquad t_{\text{HO}} = \omega_\perp t, \qquad z_{\text{HO}} = \frac{z}{l_\perp} \tag{A.13}$$

where the subscript HO denotes the nondimensional quantity. In these units, the energy is rescaled in units of $\hbar\omega_\perp$.

The resulting, nondimensional equation is written as

$$i\frac{\partial\phi_{\rm HO}}{\partial t_{\rm HO}} = \left(-\frac{1}{2}\frac{\partial^2}{\partial z_{\rm HO}^2} + V_{\rm HO} + g_{\rm HO}|\phi_{\rm HO}|^2 - \mu_{\rm HO}\right)\phi_{\rm HO} \tag{A.14}$$

where $V_{\rm HO} = 0.5z_{\rm HO}^2$, $g_{\rm HO} = g_{1D}/(\hbar\omega_\perp l_\perp)$, $\mu_{\rm HO} = \mu/(\hbar\omega_\perp)$ and we have assumed the explicit dependence on z and t.

Using similar arguments, the 3D GPE can be reduced to dimensionless form.

A.3 The Bogoliubov equations for condensate excitations

At zero temperature, excitations of the condensate can be obtained by accounting for perturbations around the condensate ground state via

$$\phi(\mathbf{r},t) = e^{-i\mu t/\hbar}[\phi_0(\mathbf{r}) + \delta\phi(\mathbf{r},t)] \tag{A.15}$$

$\delta\phi$ represents condensate fluctuations around the ground state ϕ_0. Substituting (A.15) into the GPE A.10, subtracting the time independent GPE (Chapter 2 Eq. (2.19)) and linearising results in the an equation for the excitations around the ground state of the condensate,

$$i\hbar\frac{\partial}{\partial t}\delta\phi(\mathbf{r},t) = [\hat{h}_0 + 2g|\phi_0(\mathbf{r},t)|^2 - \mu]\delta\phi(\mathbf{r},t) + g\phi_0^2\delta\phi^*(\mathbf{r},t). \tag{A.16}$$

To solve for the collective modes of the system, we look for solutions of the form

$$\delta\phi(\mathbf{r},t) = \sum_i [u_i(\mathbf{r})e^{-i\omega_i t} + v_i^*(\mathbf{r})e^{i\omega_i t}]. \tag{A.17}$$

where i labels the different modes and ω_i are the respective frequencies. This is substituted into Eq. (A.16) and after the prefactors of the exponentials have been collected we get two coupled equations. These equations are commonly known as the Bogoliubov equations (analogous to the Bogoliubov de Gennes equations in superconductivity).

$$(\hat{h}_0 + 2g|\phi_0(\mathbf{r})|^2 - \mu)u_i(\mathbf{r}) + g[\phi_0(\mathbf{r})]^2 v_i(\mathbf{r}) = \varepsilon_i u_i(\mathbf{r}) \tag{A.18}$$

$$(\hat{h}_0 + 2g|\phi_0(\mathbf{r})|^2 - \mu)v_i(\mathbf{r}) + g[\phi_0(\mathbf{r})]^2 u_i(\mathbf{r}) = -\varepsilon_i v_i(\mathbf{r}) \tag{A.19}$$

$\varepsilon_i = \hbar\omega_i$ are the dressed/quasiparticle energies (since these are zero temperature equations, the dressing arises from mean-field coupling).

These equations can be represented in matrix notation by

$$\begin{pmatrix} \hat{L}(\mathbf{r}) & \hat{M}(\mathbf{r}) \\ -\hat{M}^*(\mathbf{r}) & -\hat{L}^*(\mathbf{r}) \end{pmatrix} \begin{pmatrix} u_i(\mathbf{r}) \\ v_i(\mathbf{r}) \end{pmatrix} = \varepsilon_i \begin{pmatrix} u_i(\mathbf{r}) \\ v_i(\mathbf{r}) \end{pmatrix} \tag{A.20}$$

where $\hat{h}_0 + 2g|\phi_0(\mathbf{r})|^2 - \mu = \hat{L}(\mathbf{r})$ and $g[\phi_0(\mathbf{r})]^2 = \hat{M}(\mathbf{r})$.

Appendix B

Density Matrix

A density matrix is a useful phase space probability measure (the quantum analog to distribution functions in classical mechanics) for systems which are described by a superposition of many states. i.e. a mixed state.

We provide an example where the equation for the expectation value of an operator $\hat{A}$, for a state in which the system in the state $|\psi_i\rangle$, with probability ω_i can be written using a density matrix.

$$\langle \hat{A} \rangle = \mathrm{Tr}\hat{\rho}\hat{A} \tag{B.1}$$

where the density matrix is given by $\hat{\rho} = \sum_i \omega_i |\hat{\psi}_i\rangle\langle\psi_i|$.
Since the Trace of a matrix is a summation over all the diagonal elements of the operator e.g. $\mathrm{Tr}\hat{B} = \sum_{j=1}^{n} \langle j|\hat{B}|j\rangle = B_{jj}$, where $|j\rangle$ is an orthonormal basis set, we have

$$\begin{aligned}
\mathrm{Tr}(\hat{\rho}\hat{A}) &= \sum_{j=1}^{n}\sum_{i=1}^{n} \omega_i \langle j|\psi_i\rangle\langle\psi_i|\hat{A}|j\rangle & \text{(B.2)}\\
&= \sum_{j=1}^{n}\sum_{i=1}^{n} \omega_i \langle\psi_i|\hat{A}|j\rangle\langle j|\psi_i\rangle & \text{(B.3)}\\
&= \sum_{j=1}^{n}\sum_{i=1}^{n} \omega_i \langle\psi_i|\hat{A}|\psi_j\rangle & \text{(B.4)}
\end{aligned}$$

as $\sum |j\rangle\langle j| = I$, the identity.

Appendix C

Determination of Collision Probabilities

The number of particles leaving the phase space volume element $d\mathbf{r}d\mathbf{p}/(2\pi\hbar)^3$ per unit time as a result of collisions involving either condensate or test particles is given as $d\mathbf{r}d\mathbf{p}/(2\pi\hbar)^3 C_{ij}^{\rm out}$ where ij stands for either 12 or 22 to denote the collision type. Therefore, the average number of particles undergoing a collision in the space $d\mathbf{r}$ per unit time is given by integrating over momenta. To achieve the average number of atoms undergoing a collision per unit volume and time at a *particular* point in space, $\mathbf{r}$ it is necessary to compute

$$\Gamma_{ij}^{\rm out}(\mathbf{r},t) = \int \frac{d\mathbf{p}}{(2\pi\hbar)^3} C_{ij}^{\rm out}, \tag{C.1}$$

and the same is true of 'in' collisions of either nature.
If the average time between collisions is given by τ_{ij}, then the probability that a collision has occurred for a single test particle in the time step dt is

$$P_{ij} = \frac{dt}{\tau_{ij}}. \tag{C.2}$$

This means, that in a single volume $d\mathbf{r}$ the number of atoms experiencing a collision in the time interval dt, is given by the number of atoms in the volume element i.e. $\tilde{n}(\mathbf{r},t)d\mathbf{r}$, multiplied by the probability that a collision has occurred for each particle,

$$\tilde{n}(\mathbf{r},t)d\mathbf{r}\frac{dt}{\tau_{ij}}. \tag{C.3}$$

Now we have a new expression for the average number of atoms suffering a collision per unit volume and per unit time at the point $\mathbf{r}$,

$$\Gamma_{ij}^{\text{out}} = \frac{\tilde{n}(\mathbf{r},t)}{\tau_{ij}}, \tag{C.4}$$

and have two relations for Γ_{ij}^{out}. The same analysis can be applied to obtain a similar relationship for Γ_{ij}^{in}.
If we specifically now look at the C_{12}^{out} collisions we can determine this probability. We have,

$$\Gamma_{12}^{\text{out}}(\mathbf{r},t) \;=\; \int \frac{d\mathbf{p}}{(2\pi\hbar)^3} C_{12}^{\text{out}} = \frac{\tilde{n}(\mathbf{r},t)}{\tau_{12}} \tag{C.5}$$

and we know that

$$\tilde{n}(\mathbf{r},t) \;=\; \int \frac{d\mathbf{p}}{(2\pi\hbar)^3} f(\mathbf{p},\mathbf{r},t). \tag{C.6}$$

where the scattering cross section is given by $\sigma = 8\pi a_s^2$.
From the relations above, we can deduce that the rate of increase in the number of thermal atoms per unit volume and per unit time as a result of the collision with a condensate atom is given by

$$\Gamma_{12}^{\text{out}} = \frac{\sigma n_c}{\pi m^2 (2\pi\hbar)^3} \int d\mathbf{p}_1 \int d\mathbf{p}_2 \int d\mathbf{p}_3 \delta(\mathbf{p}_c + \mathbf{p}_1 - \mathbf{p}_2 - \mathbf{p}_3)\delta(\varepsilon_c + \tilde{\varepsilon}_1 - \tilde{\varepsilon}_2 - \tilde{\varepsilon}_3) \times f_1(1+f_2)(1+f_3). \tag{C.7}$$

The rate of decrease of the number of thermal atoms per unit volume per unit time as a result of collisions with condensate atoms is given as

$$\Gamma_{12}^{\text{in}}(\mathbf{r},t) = -\frac{\sigma n_c}{\pi m^2 (2\pi\hbar)^3} \int d\mathbf{p}_1 \int d\mathbf{p}_2 \int d\mathbf{p}_3 \delta(\mathbf{p}_c + \mathbf{p}_1 - \mathbf{p}_2 - \mathbf{p}_3)\delta(\varepsilon_c + \tilde{\varepsilon}_1 - \tilde{\varepsilon}_2 - \tilde{\varepsilon}_3) \times (1+f_1) f_2 f_3. \tag{C.8}$$

Similarly the rate of collisions between thermal atoms (C_{22} collisions) is given by

$$\Gamma_{22}^{\text{out}}(\mathbf{r},t) = \frac{\sigma}{\pi m^2 (2\pi\hbar)^6} \int d\mathbf{p}_1 \int d\mathbf{p}_2 \int d\mathbf{p}_3 \int d\mathbf{p}_4 \delta(\mathbf{p}_1 + \mathbf{p}_2 - \mathbf{p}_3 - \mathbf{p}_4)\delta(\tilde{\varepsilon}_1 + \tilde{\varepsilon}_2 - \tilde{\varepsilon}_3 - \tilde{\varepsilon}_4) \times f_1 f_2 (1+f_3)(1+f_4). \tag{C.9}$$

Our final rates of collisions are given, with interchanged atom indices for uniformity, by

$$\begin{aligned}\Gamma_{12}^{\text{out}}(\mathbf{r},t) =& \frac{\sigma n_c}{\pi m^2 (2\pi\hbar)^3} \int d\mathbf{p}_2 \int d\mathbf{p}_3 \int d\mathbf{p}_4 \\ & \times \delta(\mathbf{p}_c + \mathbf{p}_2 - \mathbf{p}_3 - \mathbf{p}_4)\delta(\varepsilon_c + \tilde{\varepsilon}_2 - \tilde{\varepsilon}_3 - \tilde{\varepsilon}_4) \\ & \times f_2(1+f_3)(1+f_4). \end{aligned} \tag{C.10}$$

$$\begin{aligned}\Gamma_{12}^{\text{in}}(\mathbf{r},t) =& \frac{\sigma n_c}{\pi m^2 (2\pi\hbar)^3} \int d\mathbf{p}_2 \int d\mathbf{p}_3 \int d\mathbf{p}_4 \\ & \times \delta(\mathbf{p}_c + \mathbf{p}_3 - \mathbf{p}_2 - \mathbf{p}_4)\delta(\epsilon_c + \tilde{\varepsilon}_3 - \tilde{\varepsilon}_2 - \tilde{\varepsilon}_4) \\ & \times f_2(1+f_3)f_4. \end{aligned} \tag{C.11}$$

$$\begin{aligned}\Gamma_{22}^{\text{out}}(\mathbf{r},t) =& \frac{\sigma}{\pi m^2 (2\pi\hbar)^6} \int d\mathbf{p}_1 \int d\mathbf{p}_2 \int d\mathbf{p}_3 \int d\mathbf{p}_4 \\ & \times \delta(\mathbf{p}_1 + \mathbf{p}_2 - \mathbf{p}_3 - \mathbf{p}_4)\delta(\tilde{\varepsilon}_1 + \tilde{\varepsilon}_2 - \tilde{\varepsilon}_3 - \tilde{\varepsilon}_4) \\ & \times f_1 f_2(1+f_3)(1+f_4). \end{aligned} \tag{C.12}$$

These expressions all contain integrals over momenta. The technique of Monte Carlo sampling is a useful tool to approximate integrals when the integrand of a multidimensional integral has a complicated shape but is not strongly peaked in local regions. Sampling over momentum space is how the link between the expressions (C.10) and (C.12) is made to probabilities which we can calculate numerically.

The Monte Carlo probability expressions, which we quote in Chapter 4, Sec. 4.3.2, have been derived both in [59, 159].

Appendix D

Experimental Trapping Potential

D.1 The double well trap

This appendix reproduces details of the double well potential used in the experiment of Thywissen [34], as explicitly discussed in [240]. The trapping potential is formed on the underside of an atom chip through coupling of Ioffe-Pritchard style static magnetic trap with radio frequency (rf) magnetic fields. This combination has been recently developed to overcome the rigidity of the usual static magnetic trap and allow more complex systems such as atom interferometers and beam splitters to be investigated [238].

The rotating wave approximation is used to derive an analytic form of the double well. This is a common approximation used in dressed states which is valid when the dressing intensity is weak. The trapping potential is given by

$$U(\mathbf{r}) = m'_F \sqrt{[\hbar\omega_{\rm rf} - g_F \mu_B B_s(\mathbf{r})]^2 + \left[\frac{g_F \mu_B B_{{\rm rf},\perp}(\mathbf{r})}{2}\right]^2} \tag{D.1}$$

where the static magnetic field, $B_s(\mathbf{r})$, is a Ioffe Pritchard style trap in which no atoms are lost through Majorana losses since $B \neq 0$. Bars create a radial quadrupole magnetic field and coils in the centre of these bars create and offset in the field which prevent this. The static trap has components

$$\mathbf{B_s} = B_x \hat{\mathbf{x}} + B_y \hat{\mathbf{y}} + B_z \hat{\mathbf{z}}, \tag{D.2}$$

$$B_x(x,z) = B' x - \frac{B''}{2} xy, \tag{D.3}$$

$$B_y(x,y,z) = B_s(0) + \frac{B''}{2}(y^2 - \frac{1}{2}(x^2 + z^2)), \tag{D.4}$$

$$B_z(y,z) = -B' z - \frac{B''}{2} yz, \tag{D.5}$$

$$B_{dc} = \sqrt{{B_x}^2 + {B_y}^2 + {B_z}^2} \tag{D.6}$$

with the quantities

$$B_s(0) = \frac{2\hbar\nu_{TB}}{m'_F g_F \mu_B} \quad \text{static-trap bottom} \tag{D.7}$$

$$B' = \sqrt{\frac{mB_s(0)}{m'_F g_F \mu_B}\left(\omega_{\mathrm{x,z}}^2 + \frac{\omega_{\mathrm{y}}^2}{2}\right)}, \quad \text{gradient} \tag{D.8}$$

$$B'' = \frac{m\omega_{\mathrm{y}}^2}{m'_F g_F \mu_B} \quad \text{curvature.} \tag{D.9}$$

and trap bottom frequency, ν_{TB}.
The magnitude of the oscillating field perpendicular to the static field at each point $\mathbf{r}$ is given by

$$B_{\mathrm{rf},\perp}(\mathbf{r}) = |\mathbf{B_s} \times \mathbf{B}_{\mathrm{rf}}(\mathbf{r})|/|\mathbf{B}_s(\mathbf{r})|. \tag{D.10}$$

Since the rf oscillates in the $\hat{\mathbf{x}}$ direction, $\mathbf{B}_{\mathrm{rf}} = B_{\mathrm{rf}}\hat{\mathbf{x}}$; therefore, the component of the oscillating field perpendicular to the static field is:

$$B_{\mathrm{rf},\perp}(x,y,z) = B_{\mathrm{rf}}\sqrt{1 - \left(\frac{B_x(x,z)}{B_{\mathrm{dc}}(x,y,z)}\right)}. \tag{D.11}$$

The potential can now be written as:

$$U_{\mathrm{ext}}(x,y,z,\delta) = \frac{1}{h}\sqrt{(m_F g_F \mu_B B_{\mathrm{dc}}(x,y,z) - 2h(\delta + \nu_{TB}))^2 + \left(\frac{m_F g_F \mu_B B_{\mathrm{rf},\perp}(x,y,z)}{2}\right)^2} \tag{D.12}$$

Additionally the cloud is compressed in the weak direction to prevent the atoms from falling under gravity. The beam is much larger than the condensate size and so the trapping in the z direction takes the form of a harmonic potential which is added to the effective potential. The frequency of this is measured and denoted by, ω_{z0}. The potential value at the centre of the trap is subtracted ($\mu_B B_{\mathrm{dc}}(0,0,0) = 2h\nu_{\mathrm{TB}}$ and $B_{\mathrm{rf},\perp}(0,0,0) = B_{\mathrm{rf}}$). The final analytic expression for the trapping potential has the form [34, 240]:

$$V_{\mathrm{ext}}(x,y,z,\delta) = \frac{1}{h}\sqrt{(\mu_B B_{\mathrm{dc}}(x,y,z) - 2h(\delta + \nu_{TB})^2) + \left(\frac{\mu_B B_{\mathrm{rf},\perp}(x,y,z)}{2}\right)^2} - \frac{1}{h}\sqrt{(2h\delta)^2 + \left(\frac{\mu_B B_{\mathrm{rf}}}{2}\right)^2} + \frac{1}{2}m\omega_{z0}^2 z^2. \tag{D.13}$$

Bibliography

[1] C. Pethick and H. Smith, *Bose-Einstein condensation in dilute gases* (Cambridge University Press, 2002).

[2] L. P. Pitaevskii and S. Stringari, *Bose-Einstein Condensation* (Oxford University Press, Great Clarendon Street, Oxford, 2003).

[3] D. Tilley and J. Tilley, *Superfluidity and Superconductivity* (Institute of Physics Publishing, London, 1994), 3rd ed.

[4] S. Bose, Z. Phys. **26**, 178 (1924).

[5] A. Einstein, Sitzber. Kgl. Preuss. Akad. Wiss. **23**, 3 (1925).

[6] F. London, Nature **141**, 643 (1938).

[7] A. E. Leanhardt, T. A. Pasquini, M. Saba, A. Schirotzek, Y. Shin, D. Kielpinski, D. E. Pritchard, and W. Ketterle, Science **301**, 1513 (2003).

[8] M. H. Anderson, J. Ensher, M. R. Matthews, and C. E. Wiemann, Science **269**, 198 (1995).

[9] K. B. Davis, M. O. Mewes, M. R. Andrews, N. J. van Druten, D. S. Durfee, D. M. Kurn, and W. Ketterle, Phys. Rev. Lett. **75**, 3969 (1995).

[10] C. C. Bradley, C. A. Sackett, J. J. Tollett, and R. G. Hulet, Phys. Rev. Lett. **79**, 1170 (1997).

[11] C. C. Bradley, C. A. Sackett, J. J. Tollett, and R. G. Hulet, Phys. Rev. Lett. **75**, 1687 (1995).

[12] *"The Nobel Prize in Physics 2001" Nobelprize.org* (The Royal Swedish Academy of Sciences, 2001).

[13] C. E. Hecht, Physica **25**, 1159 (1959).

[14] D. G. Fried, T. C. Killian, L. Willmann, D. Landhuis, S. C. Moss, D. Kleppner, and T. J. Greytak, Phys. Rev. Lett. **81**, 3811 (1998).

[15] H. F. Hess, Phys. Rev. B **34**, 3476 (1986).

[16] S. L. Cornish, N. R. Claussen, J. L. Roberts, E. A. Cornell, and C. E. Wieman, Phys. Rev. Lett. **85**, 1795 (2000).

[17] G. Modugno, G. Ferrari, G. Roati, R. Brecha, A. Simoni, and M. Inguscio, Science **294**, 1320 (2001).

[18] A. Robert, O. Sirjean, A. Browaeys, J. Poupard, S. Nowak, D. Boiron, C. Westbrook, and A. Aspect, Science **292**, 5516 (2001).

[19] Y. Takasu, K. Maki, K. Komori, T. Takano, K. Honda, M. Kumakura, T. Yabuzaki, and Y. Takahashi, Phys. Rev. Lett. **91**, 040404 (2003).

[20] T. Weber, J. Herbig, M. Mark, H. Nägerl, and R. Grimm, Science **299**, 232 (2003).

[21] A. Griesmaier, J. Werner, S. Hensler, J. Stuhler, and T. Pfau, Phys. Rev. Lett. **94**, 160401 (2005).

[22] S. Stellmer, M. K. Tey, B. Huang, R. Grimm, and F. Schreck, Phys. Rev. Lett. **103**, 200401 (2009).

[23] Y. N. M. de Escobar, P. G. Mickelson, M. Yan, B. J. DeSalvo, S. B. Nagel, and T. C. Killian, Phys. Rev. Lett. **103**, 200402 (2009).

[24] S. Stellmer, M. K. Tey, R. Grimm, and F. Schreck, Phys. Rev. A **82**, 041602 (2010).

[25] P. G. Mickelson, Y. N. Martinez de Escobar, M. Yan, B. J. DeSalvo, and T. C. Killian, Phys. Rev. A **81**, 051601 (2010).

[26] S. Kraft, F. Vogt, O. Appel, F. Riehle, and U. Sterr, Phys. Rev. Lett. **103**, 130401 (2009).

[27] M. Lu, N. Q. Burdick, S. H. Youn, and B. L. Lev, Phys. Rev. Lett. **107**, 190401 (2011).

[28] R. Donnelly, *Quantized Vortices in Helium II* (Cambridge University Press, Cambridge, 1991).

[29] C. Henkel, J. Schmiedmayer, and C. Westbrook, Eur. Phys. J. D. **35**, 1 (2005).

[30] T. W. Neely, E. C. Samson, A. S. Bradley, M. J. Davis, and B. P. Anderson, Phys. Rev. Lett. **104**, 160401 (2010).

[31] D. V. Freilich, D. M. Bianchi, A. M. Kaufman, T. K. Langin, and D. S. Hall, Science **329**, 1182 (2010).

[32] T. G. Tiecke, M. Kemmmann, C. Buggle, I. Shvarchuck, W. von Klitzing, and J. T. M. Walraven, J. Opt. B: Quantum Semiclass **5**, S119 (2003).

[33] M. Albiez, R. Gati, J. Fölling, S. Hunsmann, M. Cristiani, and M. K. Oberthaler, Phys. Rev. Lett. **95**, 010402 (2005).

[34] L. J. LeBlanc, A. B. Bardon, J. McKeever, M. H. T. Extavour, D. Jervis, J. H. Thywissen, F. Piazza, and A. Smerzi, Phys. Rev. Lett. **106**, 025302 (2011).

[35] M. Greiner, O. Mandel, T. Esslinger, T. W. Hansch, and I. Bloch, Nature **415**, 39 (2002).

[36] C. Ryu, M. F. Andersen, P. Cladé, V. Natarajan, K. Helmerson, and W. D. Phillips, Phys. Rev. Lett. **99**, 260401 (2007).

[37] A. Ramanathan, K. C. Wright, S. R. Muniz, M. Zelan, W. T. Hill, C. J. Lobb, K. Helmerson, W. D. Phillips, and G. K. Campbell, Phys. Rev. Lett. **106**, 130401 (2011).

[38] K. Henderson, C. Ryu, C. MacCormick, and M. Boshier, New J. Phys. **11**, 043030 (2009).

[39] S. Inouye, M. R. Andrews, J. Stenger, H.-J. Miesner, D. M. Stamper-Kurn, and W. Ketterle, Nature **392**, 151 (1998).

[40] M. Greiner, C. A. Regal, and D. S. Jin, Nature **426**, 537 (2003).

[41] J. L. Roberts, N. R. Claussen, J. P. Burke, C. H. Greene, E. A. Cornell, and C. E. Wieman, Phys. Rev. Lett. **81**, 5109 (1998).

[42] D. S. Jin, J. R. Ensher, M. R. Matthews, C. E. Wieman, and E. A. Cornell, Phys. Rev. Lett. **77**, 420 (1996).

[43] M.-O. Mewes, M. R. Andrews, N. J. van Druten, D. M. Kurn, D. S. Durfee, C. G. Townsend, and W. Ketterle, Phys. Rev. Lett. **77**, 988 (1996).

[44] O. M. Maragò, S. A. Hopkins, J. Arlt, E. Hodby, G. Hechenblaikner, and C. J. Foot, Phys. Rev. Lett. **84**, 2056 (2000).

[45] D. S. Jin, M. R. Matthews, J. R. Ensher, C. E. Wieman, and E. A. Cornell, Phys. Rev. Lett. **78**, 764 (1997).

[46] M. R. Andrews, C. G. Townsend, H. J. Miesner, D. S. Durfee, D. M. Kurn, and W. Ketterle, Science **275**, 637 (1997).

[47] S. Burger, K. Bongs, S. Dettmer, W. Ertmer, K. Sengstock, A. Sanpera, G. V. Shlyapnikov, and M. Lewenstein, Phys. Rev. Lett. **83**, 5198 (1999).

[48] P. Rosenbusch, V. Bretin, and J. Dalibard, Phys. Rev. Lett. **89**, 200403 (2002).

[49] J. R. Abo-Shaeer, C. Raman, and W. Ketterle, Phys. Rev. Lett. **88**, 070409 (2002).

[50] B. P. Anderson, P. C. Haljan, C. E. Wieman, and E. A. Cornell, Phys. Rev. Lett. **85**, 2857 (2000).

[51] D. M. Stamper-Kurn, H.-J. Miesner, S. Inouye, M. R. Andrews, and W. Ketterle, Phys. Rev. Lett. **81**, 500 (1998).

[52] O. Maragò, G. Hechenblaikner, E. Hodby, and C. Foot, Phys. Rev. Lett. **86**, 3938 (2001).

[53] F. Chevy, V. Bretin, P. Rosenbusch, K. W. Madison, and J. Dalibard, Phys. Rev. Lett. **88**, 250402 (2002).

[54] N. P. Proukakis and B. Jackson, Journal of Physics B: Atomic, Molecular and Optical Physics **41**, 203002 (2008).

[55] T. R. Kirkpatrick and J. R. Dorfman, Phys. Rev. A **28**, 2576 (1983).

[56] T. R. Kirkpatrick and J. R. Dorfman, Journal of Low Temperature Physics **58**, 399 (1985).

[57] T. R. Kirkpatrick and J. R. Dorfman, Journal of Low Temperature Physics **58**, 301 (1985).

[58] T. R. Kirkpatrick and J. R. Dorfman, Journal of Low Temperature Physics **59**, 1 (1985).

[59] A. Griffin, T. Nikuni, and E. Zaremba, *Bose-condensed gases at finite temperatures* (Cambridge University Press, 2009).

[60] A. Griffin, *Excitations in a Bose-condensed liquid*, Cambridge studies in low temperature physics (Cambridge University Press, 1993).

[61] R. Walser, J. Williams, J. Cooper, and M. Holland, Phys. Rev. A **59**, 3878 (1999).

[62] R. Walser, J. Cooper, and M. Holland, Phys. Rev. A **63**, 013607 (2000).

[63] R. Meppelink, S. B. Koller, J. M. Vogels, H. T. C. Stoof, and P. van der Straten, Phys. Rev. Lett. **103**, 265301 (2009).

[64] J. E. Williams and A. Griffin, Phys. Rev. A **63**, 023612 (2001).

[65] B. Jackson and E. Zaremba, Phys. Rev. Lett. **87**, 100404 (2001).

[66] B. Jackson and E. Zaremba, Laser Phys. **12**, 93 (2002).

[67] B. Jackson, N. P. Proukakis, and C. F. Barenghi, Phys. Rev. A **75**, 051601 (2007).

[68] B. Jackson, N. P. Proukakis, C. F. Barenghi, and E. Zaremba, Phys. Rev. A **79**, 053615 (2009).

[69] E. Zaremba, T. Nikuni, and A. Griffin, Journal of Low Temperature Physics **116**, 277 (1999).

[70] T. Nikuni, E. Zaremba, and A. Griffin, Phys. Rev. Lett. **83**, 10 (1999).

[71] T. Nikuni and A. Griffin, Phys. Rev. A **63**, 033608 (2001).

[72] T. Nikuni and A. Griffin, Phys. Rev. A **65**, 011601 (2001).

[73] T. Nikuni and A. Griffin, Journal of Low Temperature Physics **111**, 793 (1998).

[74] T. Nikuni, Phys. Rev. A **65**, 033611 (2002).

[75] A. Griffin and E. Zaremba, Phys. Rev. A **56**, 4839 (1997).

[76] T. Nikuni and A. Griffin, Phys. Rev. A **69**, 023604 (2004).

[77] E. Zaremba, A. Griffin, and T. Nikuni, Phys. Rev. A **57**, 4695 (1998).

[78] P. G. Kevrekidis, D. J. Frantzeskakis, and R. Carretero-Gonzalez, eds., *Emergent Nonlinear Phenomena in Bose-Einstein Condensates: Theory and Experiment*, vol. Springer Series on Atomic, Optical, and Plasma Physics Vol. 45 (Springer, Berlin, 2008). (Springer, Berlin, 2008).

[79] A. L. Fetter, Rev. Mod. Phys. **81**, 647 (2009).

[80] D. Frantzeskakis, J. Phys. A: Math. Theor. **43**, 213001 (2010).

[81] R. K. Dodd, J. Eilbeck, J. Gibbon, and H. Morris, *Solitons and Nonlinear Wave Equations* (Academic, London, 1982).

[82] Y. S. Kivshar and B. Luther-Davies, Phys. Rep. **298**, 81 (1998).

[83] J. Denschlag, J. E. Simsarian, D. L. Feder, C. W. Clark, L. A. Collins, J. Cubizolles, L. Deng, E. W. Hagley, K. Helmerson, W. P. Reinhardt, et al., Science **287**, 97 (2000).

[84] C. Becker, S. Stellmer, P. Soltan-Panahi, S. Dörscher, M. Baumert, E.-M. Richter, J. Kronjäger, K. Bongs, and K. Sengstock, Nat. Phys. **4**, 496 (2008).

[85] A. Weller, J. P. Ronzheimer, C. Gross, J. Esteve, M. K. Oberthaler, D. J. Frantzeskakis, G. Theocharis, and P. G. Kevrekidis, Phys. Rev. Lett. **101**, 130401 (2008).

[86] S. Stellmer, C. Becker, P. Soltan-Panahi, E.-M. Richter, S. Dörscher, M. Baumert, J. Kronjäger, K. Bongs, and K. Sengstock, Phys. Rev. Lett. **101**, 120406 (2008).

[87] D. Dries, S. E. Pollack, J. M. Hitchcock, and R. G. Hulet, Phys. Rev. A **82**, 033603 (2010).

[88] V. Tikhonenko, J. Christou, B. Luther-Davies, and Y. S. Kivshar, Opt. Lett. **21**, 1129 (1996).

[89] Z. Dutton, M. Budde, C. Slowe, and L. V. Hau, Science **293**, 663 (2001).

[90] P. Engels and C. Atherton, Phys. Rev. Lett. **99**, 160405 (2007).

[91] G. Jo, J.-H. Choi, C. A. Christensen, Y. Lee, T. A. Pasquini, W. Ketterle, and D. E. Pritchard, Phys. Rev. Lett. **99**, 240406 (2007).

[92] B. Damski and W. H. Zurek, Phys. Rev. Lett. **104**, 160404 (2010).

[93] N. P. Proukakis, N. G. Parker, D. J. Frantzeskakis, and C. Adams, J. Opt. B: Quantum Semiclass **6**, S380 (2004).

[94] T. Busch and J. R. Anglin, Phys. Rev. Lett. **84**, 2298 (2000).

[95] D. L. Feder, M. S. Pindzola, L. A. Collins, B. I. Schneider, and C. W. Clark, Phys. Rev. A **62**, 053606 (2000).

[96] J. Brand and W. P. Reinhardt, Phys. Rev. A **65**, 043612 (2002).

[97] A. Muryshev, G. V. Shlyapnikov, W. Ertmer, K. Sengstock, and M. Lewenstein, Phys. Rev. Lett. **89**, 110401 (2002).

[98] A. E. Muryshev, H. B. van Linden van den Heuvell, and G. V. Shlyapnikov, Phys. Rev. A **60**, R2665 (1999).

[99] N. P. Proukakis, N. G. Parker, C. F. Barenghi, and C. S. Adams, Phys. Rev. Lett. **93**, 130408 (2004).

[100] L. D. Carr, M. A. Leung, and W. P. Reinhardt, J. Phys. B **33**, 3983 (2000).

[101] I. Shomroni, E. Lahoud, S. Levy, and J. Steinhauer, Nat. Phys. **5**, 193 (2009).

[102] P. O. Fedichev, A. E. Muryshev, and G. V. Shlyapnikov, Phys. Rev. A **60**, 3220 (1999).

[103] B. Jackson, C. Barenghi, and N. Proukakis, J. Low Temp. Phys. **148**, 387 (2007).

[104] J. Dziarmaga, Z. P. Karkuszewski, and K. Sacha, Journal of Physics B: Atomic, Molecular and Optical Physics **36**, 1217 (2003).

[105] G. Theocharis, A. Weller, J. P. Ronzheimer, C. Gross, M. K. Oberthaler, P. G. Kevrekidis, and D. J. Frantzeskakis, Phys. Rev. A **81**, 063604 (2010).

[106] N. G. Parker, N. P. Proukakis, M. Leadbeater, and C. S. Adams, Phys. Rev. Lett. **90**, 220401 (2003).

[107] N. G. Parker, N. P. Proukakis, and C. S. Adams, Phys. Rev. A **81**, 033606 (2010).

[108] J. Spreiter and A. Sacks, J. Aeronaut. Sci **18**, 21 (1951).

[109] T. Kibble, J. Phys. A: Math. Gen. **9**, 1387 (1976).

[110] W. H. Zurek, Nature **317**, 505 (1985).

[111] J. R. Anglin and W. H. Zurek, Phys. Rev. Lett. **83**, 1707 (1999).

[112] A. L. Fetter and A. A. Svidzinsky, J. Phys.: Condens. Matter **13**, R135 (2001).

[113] C. Weiler, T. W. Neely, D. R. Scherer, A. S. Bradley, M. J. Davis, and B. P. Anderson, Nature **455**, 948 (2008).

[114] K. W. Madison, F. Chevy, W. Wohlleben, and J. Dalibard, Phys. Rev. Lett. **84**, 806 (2000).

[115] J. R. Abo-Shaeer, C. Raman, J. M. Vogels, and W. Ketterle, Science **292**, 476 (2001).

[116] E. Hodby, G. Hechenblaikner, S. A. Hopkins, O. M. Maragò, and C. J. Foot, Phys. Rev. Lett. **88**, 010405 (2001).

[117] M. R. Matthews, B. P. Anderson, P. C. Haljan, D. S. Hall, C. E. Wieman, and E. A. Cornell, Phys. Rev. Lett. **83**, 2498 (1999).

[118] L. Dobrek, M. Gajda, M. Lewenstein, K. Sengstock, G. Birkl, and W. Ertmer, Phys. Rev. A **60**, R3381 (1999).

[119] A. E. Leanhardt, A. Görlitz, A. P. Chikkatur, D. Kielpinski, Y. Shin, D. E. Pritchard, and W. Ketterle, Phys. Rev. Lett. **89**, 190403 (2002).

[120] C. Raman, J. R. Abo-Shaeer, J. M. Vogels, K. Xu, and W. Ketterle, Phys. Rev. Lett. **87**, 210402 (2001).

[121] B. P. Anderson, P. C. Haljan, C. A. Regal, D. L. Feder, L. A. Collins, C. W. Clark, and E. A. Cornell, Phys. Rev. Lett. **86**, 2926 (2001).

[122] K. W. Madison, F. Chevy, V. Bretin, and J. Dalibard, Phys. Rev. Lett. **86**, 4443 (2001).

[123] Y. Shin, M. Saba, M. Vengalattore, T. A. Pasquini, C. Sanner, A. E. Leanhardt, M. Prentiss, D. E. Pritchard, and W. Ketterle, Phys. Rev. Lett. **93**, 160406 (2004).

[124] P. Engels, I. Coddington, P. C. Haljan, V. Schweikhard, and E. A. Cornell, Phys. Rev. Lett. **90**, 170405 (2003).

[125] E. A. L. Henn, J. A. Seman, G. Roati, K. M. F. Magalhães, and V. S. Bagnato, Phys. Rev. Lett. **103**, 045301 (2009).

[126] S. Sinha and Y. Castin, Phys. Rev. Lett. **87**, 190402 (2001).

[127] M. Tsubota, K. Kasamatsu, and M. Ueda, Phys. Rev. A **65**, 023603 (2002).

[128] N. G. Parker, N. P. Proukakis, C. F. Barenghi, and C. S. Adams, Phys. Rev. Lett. **92**, 160403 (2004).

[129] S. I. Davis, P. Hendry, and P. McClintock, Physica B **280**, 43 (2000).

[130] C. Nore, M. Abid, and M. E. Brachet, Phys. Rev. Lett. **78**, 3896 (1997).

[131] D. C. Samuels and C. F. Barenghi, Phys. Rev. Lett. **81**, 4381 (1998).

[132] M. Leadbeater, T. Winiecki, D. C. Samuels, C. F. Barenghi, and C. S. Adams, Phys. Rev. Lett. **86**, 1410 (2001).

[133] M. Leadbeater, D. C. Samuels, C. F. Barenghi, and C. S. Adams, Phys. Rev. A **67**, 015601 (2003).

[134] P. O. Fedichev and G. V. Shlyapnikov, Phys. Rev. A **60**, R1779 (1999).

[135] R. A. Duine, B. W. A. Leurs, and H. T. C. Stoof, Phys. Rev. A **69**, 053623 (2004).

[136] H. Schmidt, F. Goral, K. Floegel, M. Gajda, and K. Rzazewski, J. Opt. B: Quantum Semiclass **5**, S96 (2003).

[137] T. M. Wright, A. S. Bradley, and R. J. Ballagh, Phys. Rev. A **80**, 053624 (2009).

[138] T. M. Wright, A. S. Bradley, and R. J. Ballagh, Phys. Rev. A **81**, 013610 (2010).

[139] S. J. Rooney, A. S. Bradley, and P. B. Blakie, Phys. Rev. A **81**, 023630 (2010).

[140] B. Josephson, Physics Letters **1**, 251 (1962).

[141] P. W. Anderson and J. M. Rowell, Phys. Rev. Lett. **10**, 230 (1963).

[142] S. V. Pereverzev, A. Loshak, S. Backhaus, J. C. Davis, and R. E. Packard, Nature **388**, 449 (1997).

[143] S. Backhaus, S. V. Pereverzev, A. Loshak, J. C. Davis, and R. E. Packard, Science **278**, 1435 (1997).

[144] K. Sukhatme, Y. Mukharsky, T. Chui, and D. Pearson, Nature **411**, 280 (2001).

[145] J. Javanainen, Phys. Rev. Lett. **57**, 3164 (1986).

[146] N. R. Newbury, C. J. Myatt, E. A. Cornell, and C. E. Wieman, Phys. Rev. Lett. **74**, 2196 (1995).

[147] F. Cataliotti, S. Burger, C. Fort, P. Maddaloni, F. Minardi, A. Trombettoni, A. Smerzi, and M. Inguscio, Science **293**, 843 (2001).

[148] M. W. Jack, M. J. Collett, and D. F. Walls, Phys. Rev. A **54**, R4625 (1996).

[149] A. Smerzi, S. Fantoni, S. Giovanazzi, and S. R. Shenoy, Phys. Rev. Lett. **79**, 4950 (1997).

[150] G. J. Milburn, J. Corney, E. M. Wright, and D. F. Walls, Phys. Rev. A **55**, 4318 (1997).

[151] I. Zapata, F. Sols, and A. J. Leggett, Phys. Rev. A **57**, R28 (1998).

[152] S. Raghavan, A. Smerzi, S. Fantoni, and S. R. Shenoy, Phys. Rev. A **59**, 620 (1999).

[153] R. Gati, B. Hemmerling, J. Fölling, M. Albiez, and M. K. Oberthaler, Phys. Rev. Lett. **96**, 130404 (2006).

[154] A. Collin and E. Zaremba, Preprint (2011).

[155] J. Ruostekoski and D. F. Walls, Phys. Rev. A **58**, R50 (1998).

[156] S. Levy, E. Lahoud, I. Shomroni, and J. Steinhauer, Nature **449**, 579 (2007).

[157] J. Esteve, T. Schumm, J. B. Trebbia, I. Bouchoule, A. Aspect, and C. I. Westbrook, Eur. Phys. J. D. **35**, 141 (2005).

[158] N. G. Parker, A. J. Allen, C. F. Barenghi, and N. P. Proukakis, arXiv:1109.0039v1 (2011).

[159] B. Jackson and E. Zaremba, Phys. Rev. A **66**, 033606 (2002).

[160] E. P. Gross, Journal of Mathematical Physics **4**, 195 (1963).

[161] E. P. Gross, Il Nuovo Cimento, (Italian Physical Society) **20**, 454 (1961).

[162] L. P. Pitaevskii, Zh. Eksp. Teor. Fiz. **40**, 646 (1961).

[163] C. W. Gardiner, Phys. Rev. A **56**, 1414 (1997).

[164] Y. Castin and R. Dum, Phys. Rev. A **57**, 3008 (1998).

[165] S. A. Gardiner and S. A. Morgan, Phys. Rev. A **75**, 043621 (2007).

[166] G. Baym and C. J. Pethick, Phys. Rev. Lett. **76**, 6 (1996).

[167] N. P. Proukakis and K. Burnett, J. Res. Natl. Inst. Stand. Technol. **101**, 457 (1996).

[168] A. Griffin, Phys. Rev. B **53**, 9341 (1996).

[169] N. P. Proukakis, Ph.D. thesis, University of Oxford (1997).

[170] N. P. Proukakis, K. Burnett, and H. T. C. Stoof, Phys. Rev. A **57**, 1230 (1998).

[171] J. Binney, *The Theory of critical phenomena: an introduction to the renormalization group*, Oxford science publications (Clarendon Press, 1992).

[172] H. Shi and A. Griffin, Physics Reports **304**, 1 (1998).

[173] D. A. W. Hutchinson, E. Zaremba, and A. Griffin, Phys. Rev. Lett. **78**, 1842 (1997).

[174] D. A. W. Hutchinson, K. Burnett, R. J. Dodd, S. A. Morgan, M. Rusch, E. Zaremba, N. P. Proukakis, M. Edwards, and C. Clark, Journal of Physics B: Atomic, Molecular and Optical Physics **33**, 3825 (2000).

[175] M. Hillery, R. F. O'Connell, M. O. Scully, and E. P. Wigner, Physics Reports **106**, 121 (1984).

[176] D. Jaksch, C. W. Gardiner, and P. Zoller, Phys. Rev. A **56**, 575 (1997).

[177] O. J. Luiten, M. W. Reynolds, and J. T. M. Walraven, Phys. Rev. A **53**, 381 (1996).

[178] M. Holland, J. Williams, and J. Cooper, Phys. Rev. A **55**, 3670 (1997).

[179] S. Giorgini, L. Pitaevskii, and S. Stringari, Journal of Low Temperature Physics **109**, 309 (1997).

[180] P. B. Blakie, A. S. Bradley, M. J. Davis, R. J. Ballagh, and C. W. Gardiner, Advances in Physics **57**, 363 (2008).

[181] M. Brewczyk, M. Gajda, and K. Rzazewski, Journal of Physics B: Atomic, Molecular and Optical Physics **40**, R1 (2007).

[182] M. J. Steel, M. K. Olsen, L. I. Plimak, P. D. Drummond, S. M. Tan, M. J. Collett, D. F. Walls, and R. Graham, Phys. Rev. A **58**, 4824 (1998).

[183] M. J. Davis, S. A. Morgan, and K. Burnett, Phys. Rev. A **66**, 053618 (2002).

[184] M. J. Davis, S. A. Morgan, and K. Burnett, Phys. Rev. Lett. **87**, 160402 (2001).

[185] P. B. Blakie and M. J. Davis, Phys. Rev. A **72**, 063608 (2005).

[186] H. T. C. Stoof, Journal of Low Temperature Physics **114**, 11 (1999).

[187] H. T. C. Stoof, Phys. Rev. Lett. **78**, 768 (1997).

[188] C. W. Gardiner and M. J. Davis, J. Phys. B: At. Mol. Opt. Phys. **36**, 4731 (2003).

[189] H. T. C. Stoof and M. J. Bijlsma, J. Low Temp. Phys. **124**, 431 (2001).

[190] R. A. Duine and H. T. C. Stoof, Phys. Rev. A **65**, 013603 (2001).

[191] S. P. Cockburn, H. E. Nistazakis, T. P. Horikis, P. G. Kevrekidis, N. P. Proukakis, and D. J. Frantzeskakis, Phys. Rev. Lett. **104**, 174101 (2010).

[192] G. Huang, M. G. Velarde, and V. A. Makarov, Phys. Rev. A **64**, 013617 (2001).

[193] D. E. Pelinovsky, D. J. Frantzeskakis, and P. G. Kevrekidis, Phys. Rev. E **72**, 016615 (2005).

[194] A. D. Martin and J. Ruostekoski, Phys. Rev. Lett. **104**, 194102 (2010).

[195] D. M. Gangardt and A. Kamenev, Phys. Rev. Lett. **104**, 190402 (2010).

[196] V. E. Zakharov and A. B. Shabat, Sov. Phys. JETP **34**, 823 (1973).

[197] N. G. Parker, N. P. Proukakis, M. Leadbeater, and C. S. Adams, Journal of Physics B: Atomic, Molecular and Optical Physics **36**, 2891 (2003).

[198] K. J. Blow and N. Doran, Phys. Lett. A **107**, 55 (1985).

[199] D. J. Frantzeskakis, G. Theocharis, F. K. Diakonos, P. Schmelcher, and Y. S. Kivshar, Phys. Rev. A **66**, 053608 (2002).

[200] G. Theocharis, P. Schmelcher, M. K. Oberthaler, P. G. Kevrekidis, and D. J. Frantzeskakis, Phys. Rev. A **72**, 023609 (2005).

[201] V. V. Konotop and L. Pitaevskii, Phys. Rev. Lett. **93**, 240403 (2004).

[202] D. Pelinovsky and P. G. Kevrekidis, AMS Contemp. Math. **473**, 159 (2008).

[203] N. G. Parker, Ph.D. thesis, Durham University (2004).

[204] T. Anker, M. Albiez, R. Gati, S. Hunsmann, B. Eiermann, A. Trombettoni, and M. K. Oberthaler, Phys. Rev. Lett. **94**, 020403 (2005).

[205] O. Morsch and M. Oberthaler, Rev. Mod. Phys. **78**, 179 (2006).

[206] G. Birkl, F. B. J. Buchkremer, R. Dumke, and W. Ertmer, Optics Communications **191**, 67 (2001).

[207] E. Bolda and D. Walls, Phys. Rev. Lett. **81**, 5477 (1998).

[208] B. Jackson, J. F. McCann, and C. S. Adams, Phys. Rev. A **61**, 013604 (1999).

[209] E. Lundh and P. Ao, Phys. Rev. A **61**, 063612 (2000).

[210] W. F. Vinen, Phys. Rev. B **64**, 134520 (2001).

[211] A. Martin, *Private communication.*

[212] M. Fromhold, *Private communication.*

[213] C. Eltschka and P. Schlagheck, Phys. Rev. Lett. **94**, 014101 (2005).

[214] B. Jackson and E. Zaremba, Phys. Rev. Lett. **88**, 180402 (2002).

[215] A. C. J. Wade, D. Baillie, and P. B. Blakie, Phys. Rev. A **84**, 023612 (2011).

[216] W. Press, S. Teukolsky, W. Vetterling, and B. Flannery, *Numerical Recipies in FORTRAN* (Cambridge University Press, 1992).

[217] R. W. Hockney and J. W. Eastwood, *Computer simulation using particles* (McGraw-Hill, New York, 1981).

[218] B. Jackson and C. S. Adams, Phys. Rev. A **63**, 053606 (2001).

[219] L. Onsager, "Statistical Hydrodynamics", Nuovo Cimento **6**, 279 (1949).

[220] R. Feynman, *Chapter II Application of Quantum Mechanics to Liquid Helium*, vol. 1 of *Progress in Low Temperature Physics* (Elsevier, 1955).

[221] W. F. Vinen, Proc. R. Soc. A **260**, 218 (1961).

[222] H. Pu, C. K. Law, J. H. Eberly, and N. P. Bigelow, Phys. Rev. A **59**, 1533 (1999).

[223] Y. Kawaguchi and T. Ohmi, Phys. Rev. A **70**, 043610 (2004).

[224] F. Chevy, K. W. Madison, and J. Dalibard, Phys. Rev. Lett. **85**, 2223 (2000).

[225] R. J. Dodd, K. Burnett, M. Edwards, and C. Clark, Phys. Rev. A **56**, 587 (1997).

[226] D. E. Sheehy and L. Radzihovsky, Phys. Rev. A **70**, 063620 (2004).

[227] D. E. Sheehy and L. Radzihovsky, Phys. Rev. A **70**, 051602 (2004).

[228] D. S. Rokhsar, Phys. Rev. Lett. **79**, 2164 (1997).

[229] T. Isoshima, J. Huhtamäki, and M. M. Salomaa, Phys. Rev. A **69**, 063601 (2004).

[230] B. G. Wild and D. A. W. Hutchinson, Phys. Rev. A **80**, 035603 (2009).

[231] W. Thomson (Lord Kelvin), Philos. Mag. **10**, 155 (1880).

[232] B. Svistunov, Phys. Lett. A **287**, 169 (2001).

[233] A. L. Fetter, J. Low Temp. Phys. **161**, 445 (2010).

[234] J. R. Ensher, D. S. Jin, M. R. Matthews, C. E. Wieman, and E. A. Cornell, Phys. Rev. Lett. **77**, 4984 (1996).

[235] I. Coddington, P. C. Haljan, P. Engels, V. Schweikhard, S. Tung, and E. A. Cornell, Phys. Rev. A **70**, 063607 (2004).

[236] T. Langin, Master's thesis, Department of Physics of Amherst College (2011).

[237] S. Aubin, S. Myrskog, M. H. T. Extavour, L. J. LeBlanc, D. McKay, A. Stummer, and J. H. Thywissen, Nat. Phys. **2**, 384 (2006).

[238] I. Lesanovsky, T. Schumm, S. Hofferberth, L. M. Andersson, P. Krüger, and J. Schmiedmayer, Phys. Rev. A **73**, 033619 (2006).

[239] C. Cohen-Tannoudjii, J. Dupont-Roc, and G. Grynberg, *Atom-Photon Interactions* (A Wiley-Interscience publication, U.S.A, 1933).

[240] L. J. LeBlanc, Ph.D. thesis, Graduate Department of Physics, University of Toronto (2010).

[241] J. H. Thywissen, *Private communication*.

[242] A. A. Abrikosov, Zh. Eksp. Teor. Fiz. **32**, 1442 (1957).

[243] V. K. Tkachenko, Zh. Eksp. Teor. Fiz. **50**, 1573 (1966).

[244] I. Coddington, P. Engels, V. Schweikhard, and E. A. Cornell, Phys. Rev. Lett **91**, 100402 (2003).